Gravitational Waves from Black Hole Binaries in the Point-Particle Limit

seit 1558

Dissertation
zur Erlangung des doctor rerum naturalium (Dr. rer. nat.)

vorgelegt dem Rat der physikalisch-astronomischen Fakultät
der Friedrich-Schiller-Universität Jena

von MSc. Enno Harms
geboren am 06.05.1987 in Wittingen

Contents

Introduction

This thesis is, in a broad sense, about modelling black hole (BH) binaries within the framework of General Relativity (GR). We will be dealing with the problem of finding solutions to Einstein's equations

$$G_{\mu\nu} = 8\pi T_{\mu\nu} \tag{1.1}$$

by means of computer simulations, i.e. within Numerical (General) Relativity (NR). Eq.'s (1.1) constitute the core of Einstein's theory of gravitation [1, 2]. In essence, solving Einstein's equations means to find solutions for the coupled system of variables $(g_{\mu\nu}, T_{\mu\nu})$, where $g_{\mu\nu}$ is the metric tensor, which fixes the Einstein tensor $G_{\mu\nu}$, and $T_{\mu\nu}$ is the energy-momentum tensor, which determines the distribution of matter/energy.

Despite the elegant appearance of Eq.'s (1.1), only a few astrophysically relevant analytical solutions are known today. These are usually based on assumptions of high symmetry, like the famous BH solutions of Schwarzschild [3] and Kerr [4], for vacuum, or the Tolman-Oppenheimer-Volkoff [5] solution, for matter. With state-of-the-art numerical algorithms and high-performance computers NR is nowadays able to find solutions to Eq.'s (1.1) for complicated configurations (see, e.g., [6, 7, 8, 9, 10]). A major interest is in the prediction of radiation which might be emitted from such systems and, once observed on Earth, disclose interesting physical information. In particular, Eq.'s (1.1) predict the existence of gravitational waves (GWs); small perturbations of a given metric $g_{\mu\nu}$, which travel at the speed of light c. Observations of radio pulses from the Hulse-Taylor binary pulsar [11] allow the deduction of the orbital decay of the system, and, indeed, it agrees with the one expected from energy losses through GW emission. A direct detection of GWs, however, has not been possible so far, but it is highly desirable because systematic detections would open up a new window for astrophysical observations, complementary to the electromagnetic channel. Moreover, the observation of GWs would further confirm the efficiency of GR as a good theory of gravitation. In the search for GWs, one of the most promising sources strong enough to be detected on Earth is the merger of compact binaries. As advanced GW-detectors [12, 13, 14] will reach the needed sensitivity in the near future, accurate predictions for the expected waveforms are more than ever needed.
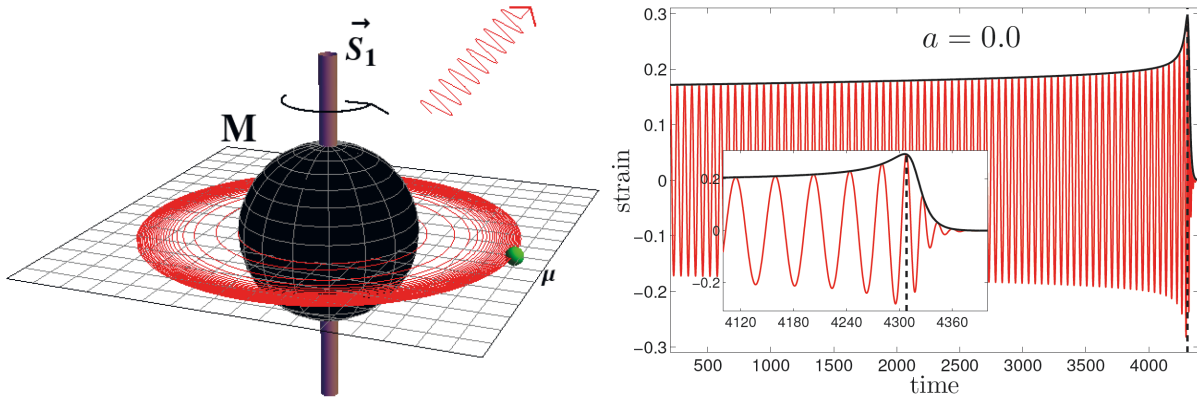
Figure 1.1: Illustration of the central topic of this thesis: Gravitational waves from binaries in the test-particle approximation. The left panel illustrates the configuration of a small mass μ orbiting a black hole of mass $M \gg \mu$, and of spin $|\vec{S}_1| = aM$. The system emits gravitational waves, which can, in principle, be measured on Earth as gravitational strains. To detect these strains, numerical simulations need to provide highly accurate templates to help distinguish physics from noise. The right panel shows a typical prediction for the waveform, with a maximum at merger (time ~ 4300) and a raise of the frequency and the amplitude ("chirp") during the inspiral.

Topics of this thesis

In this thesis we will study the GWs produced from a compact binary system in the test-particle approximation. In this approximation the binary system is modelled as a central, non-moving BH of mass M and a small, almost structureless companion of mass $\mu \ll M$ (see illustration in Fig. 1.1). To understand the applicability of our results, let us point out the assumptions of the test-particle model. First, the influence of the small companion on the metric is negligible, i.e. the system can be described by a fixed background metric $g_{\mu\nu}$, defined by the big companion, plus a perturbation field $h_{\mu\nu}$, produced by the particle, propagating upon the background. Second, concerning the dynamics of the particle, the perturbations are ignored at any order, i.e. the gravitational self-force is not taken into account and the particle is assumed to move along geodesics of the background spacetime. For a stationary background, like the rotating Kerr BH, geodesic motion implies the existence of a conserved total energy of the particle and thus we call such motion "conservative". In view of the fact that the small body is assumed to be a compact object, which could be a BH as well, the negligence of the self-force requires an additional argument; namely, that we restrict to relatively short-time scenarios, in which effects of the self-force do not manifest themselves noticeably, due to $\mu \ll M$. Note, though, that in many experiments we may deviate from the strict geodesic test-particle motion by including a hand made radiation reaction (RR) term, which takes into account radiative energy losses. Like the self-force the RR leads to deviations from geodesics of the background, but it is conceptually different, being confined to an energy balance argument. Third, regarding the evolution of the perturbations $h_{\mu\nu}$, all non-linearities are neglected, i.e. we will restrict ourselves to a fully linear treatment. The relevant equations

of linear BH perturbation theory are the Regge-Wheeler-Zerilli (RWZ) equations [15, 16], in case the central BH is non-rotating, and the Teukolsky equation (TKEQ) [17, 18], in case the central BH rotates with angular momentum $|\vec{S}_1| = a\, M$. Finally, note that the test-particle model, which is also called the "particle limit", is a quantitative description only if $\mu \to 0$. In practice, one regards this to hold when binaries are in an extreme mass-ratio (EMR), typically defined by $\mu/M \lesssim 10^{-6}$.

In the following we will mainly work with the TKEQ. A new algorithm to find its numerical solutions in the time-domain will be developed, tested, and finally applied to compute GWs from a particle orbiting a Kerr BH. Our realisation of the new approach in a computer code is called the "*teukode*". We will prove that the implementation in the *teukode* is successful; all comparisons against the literature are passed consistently. We have also been able to add new knowledge to the literature concerning topics like the structure of merger waveforms, GW energy fluxes, consistency of RR models, kick and antikick velocities, and GWs from a spinning particle. Our work in the particle limit is relevant because, (i) such systems are promising sources for GW detectors [19], (ii) in this limit nearly-extremal mass ratios and spins can be treated, which is complementing NR information, and (iii) (semi-)analytical models like the effective-one-body (EOB) model rely on information from the particle limit. Many of our results have been already published in [H1, H2, H3], and others will be published in the near future [H4].

The plan of the thesis is roughly divided into (a) theoretical concepts, (b) implementation details and validation, and (c) new results. We start with the discussion of the dynamics of a test-particle in Ch. 2. This includes the well-known theory on "spinning" particles in GR, and on EOB-dynamics with a RR. In Ch. 3 the "Teukolsky formalism" is reviewed, with focus on the traditional routes to solve the TKEQ. In Ch. 4 we discuss our innovative time-domain approach for solving the TKEQ with a spinning-particle-source-term in a hyperboloidal and horizon-penetrating coordinate system. After the theoretical part we will describe our implementation, the *teukode*, in Ch. 5, which also contains numerous confirmations of the correctness of our results; among them numerical convergence tests, replications of existing numerical experiments, and accuracy comparisons with the literature. Thus, the stage is set for the presentation of results which exceed previous literature knowledge. New results for the vacuum TKEQ, continuing the investigations of [H0], are gathered in Ch. 6. New results on GWs from point-particle inspirals on a BH are presented in Ch. 7. The studies presented in Ch. 7 are, as usual in the literature, neglecting the spin of the small body. In Ch. 8 we will present our latest development, i.e. preliminary results regarding GWs from a spinning particle on circular equatorial orbit. Finally, in Ch. 9 the conclusion is drawn and an outlook is given.

Throughout the thesis we will adopt geometric units $G = c = 1$. Often, mass-reduced quantities, denoted by a hat, are employed; e.g., $\hat{a} \equiv a/M \equiv |\vec{S}_1|/M^2$, or $\hat{r} \equiv r/M$.

Dynamics of a point-particle

In full nonlinear simulations of the Einsteins Equations (1.1) with some matter equations, at each evolution step, the metric affects the evolution of matter $T^{\mu\nu}$, and vice versa. The problem of motion, however, drastically simplifies when we can ignore the influence of the matter on the metric so that we can just evolve $T^{\mu\nu}$ on a fixed background metric. In the context of point particles, this is the "test-particle" limit, as described in Ch. 1. The GWs produced by such matter perturbations of the vacuum Kerr background can be found by solving the TKEQ with an appropriate source term. The information on the matter distribution enters that source term through the stress-energy tensor $T^{\mu\nu}$. Thus, the computation of GWs from test-particles consists of two separate steps. First, we compute the dynamics $T^{\mu\nu}(\tau, \rho, \theta, \varphi)$ for some interval $\tau \in (0, \tau_{\text{end}})$, where $(\tau, \rho, \theta, \varphi)$ denote the coordinates mainly used in this thesis, the HH-coordinates of [20] (cf. App. B for details). Second, evaluate the GWs produced from that dynamics, i.e. solve the TKEQ using that $T^{\mu\nu}$ in the source term.

Concerning the dynamics used in this work, we have restricted the motion of the particle to the equatorial plane because our preliminary tests on non-equatorial dynamics show a small uncertainty with respect to handling such motion in our implementation of the TKEQ (Sec. 5.2); a more thorough validation is postponed to the future. In this thesis, two different kinds of dynamics have been investigated within the equatorial plane. The first kind of dynamics are characterised by the tag "conservative", for there is a constant total energy of the particle along its worldline. In the case of a non-spinning particle this is just saying geodesic motions. In the case of a spinning particle (SP) the conservative motion is no longer geodesic but described by the Mathisson-Papapetrou equations (MPEQs) (see Eq.'s (2.6)). The dynamics for SPs employed here were produced by Dr. Lukes-Gerakopoulos [21]. The second kind of dynamics are "non-conservative"; the conservative equations of motion (EOM) are enhanced by an artificial radiation reaction (RR). We have used and investigated the effective-one-body (EOB) RR for a non-spinning particle (cf. Sec. 7.2). These "EOB-dynamics" were provided by Dr. Alessandro Nagar [22]. As yet, the EOB-dynamics are limited to non-spinning particles. The generalisation to SPs is one of the future goals and likely to be supported from the results of Ch. 8 and [H4].

The following review shall lay the basis for understanding the dynamics used in this thesis. In the first part, Sec.2.1, the formalism for "spinning particles" in GR is described, with focus on Mathisson's gravitational skeleton for the $T^{\mu\nu}$ of a small body and, in particular, on the pole-dipole approximation and the associated Mathisson-Papapetrou dynamics. In the second part, Sec.2.2, the EOB-dynamics and the RR are outlined. It is explained how Post-Newtonian (PN) results can be resummed to extend the range of applicability.

2.1   A spinning particle in GR

Intuitively, the motion of an extended body is separated into the motion of its center of mass (COM) as a whole and internal rotations of each element of the body about that center. Assuming that the body is rigid and all elements are rotating in the same manner about the COM, all internal rotations can be described by a single 3d "spin"-vector. In GR the such defined spin of a body is an ambiguous concept because the COM is observer dependent and, therefore, one has to pick some arbitrary frame before it can be defined. Nevertheless, an abstraction of the internal motions of the body's elements is indispensable for a physical model of compact binaries because these internal motions can have significant influence on the dynamics and GWs of compact binaries.

2.1.1   Ambiguity of spin in relativity

In order to understand the caveats related to SPs in GR, it is instructive to return, for a brief moment, to basic Newtonian physics in order to recollect the relevant notation.

Spin in a Newtonian binary
In Newtonian physics the location of the COM is observer independent. Thus, we can always separate the motion of an extended body into the motion of its COM and internal rotations of each element of the body about that center. We have conservation of energy, of linear momentum of the COM, and of angular momentum with respect to that center. Consider now a system of two such bodies with masses M_1 and $M_2 \ll M_1$, i.e. a binary in the special case that one of the two bodies is much heavier than the other one. This means we have an (almost) non-moving central object and a small orbiting object attracted by gravity. The COM of the total system, C_{tot}, coincides with the COM of the heavy body, C_1. Thus, the linear momentum of the system is vanishing. The problem of motion of such a binary system can be separated into several sub-problems,

  (i) the motion of the COM of the big body, C_1, about C_{tot}; for $M_2 \ll M_1$ absent,
  (ii) the motion of the COM of the small body, C_2, about C_{tot},
 (iii) the internal rotation of the big body about C_1,
 (iv) the internal rotation of the small body about C_2.

Since all of these motions can be described by conserved angular momenta, one can define a total angular momentum $\vec{J}$ which is as well conserved, by $\vec{J} = \vec{L} + \vec{S}$, with $\vec{L} = \vec{L}_2$ for $M_2 \ll M_1$ and $\vec{S} = \vec{S}_1 + \vec{S}_2$. It is conventional to call the internal rotations of the isolated bodies "spins", while the rotation of the one body around the other is called "orbital angular momentum" $\vec{L}$. Since there are two spins, one sometimes writes "spin(1)" and "spin(2)" for the spin of the central and the orbiting body respectively.

Ambiguity of the center of mass

The above separation of the conserved total angular momentum into its orbital and its spin contributions is manifestly bound to the notion of a COM. While the COM is an invariant location in Newtonian gravity, it is observer dependent already in special relativity. This is the origin of the ambiguities in the definition of spin in GR.

The observer dependence of the COM can be understood by imagining a homogeneous, two dimensional disc rotating about its geometrical center. An observer in this center sees an isotropic mass distribution and thus measures the COM right at his position. On the contrary, an observer moving past the disc, in the opposite direction of its rotation, will measure a higher velocity above the geometrical center than below. The equivalence of mass and energy, thus, results in a higher relativistic mass in the upper half than in the lower one. The two different centers are sometimes called "center of inertia" and "energetic center", respectively. A nice visualisation of this issue can be found, e.g., in the thesis of Steinhoff [23] (cf. also [24]).

The absence of a preferred point like the COM leads to a freedom in the definition of the spin of an extended body in GR. Nevertheless, one might hope that this freedom vanishes at least in the limit of a point-like body. Unfortunately, this hope is in vain since Møller [25] proved that any system with mass M and angular momentum S has a finite lower bound for its radial extension $R \geq S/(Mc)$. Consequently, a point-like spinning body can only be viewed as a mathematical model, which, however, cannot be considered the limit of any physically reasonable matter distribution [26]. Instead, a SP has to be understood as a very small, spinning body, and a physically reasonable description of this body has to account for the freedom in the choice of its COM. With this in mind, certain aspects of the formalism for SPs in GR, as reviewed below, become plausible.

2.1.2   Formalism for spinning particles

The treatment of SPs has a long history in special and general relativity [27, 28, 29]. Uncountable studies have developed the theory since; e.g., consult [30, 31, 23, 32] for more recent works. In the following we restrict to those aspects important for handling a SP within the Teukolsky formalism (see Ch. 3). This means to give an overview of the

prevalent model for the stress-energy tensor and the associated EOM. Also, the "spin-supplementary" conditions (SSC) shall be discussed with reference to the above mentioned ambiguities of spin.

Mathisson's gravitational skeleton

The standard model for the stress energy tensor of a SP is part of the "gravitational skeleton" approach devised by Mathisson [33] and developed in a series of works by Dixon [34, 35, 36, 37]. The basic idea is to replace the full energy-momentum tensor of a physical body by multipole moments defined only at a single reference point inside the body. Formally, the multipolar expansion of $T^{\mu\nu}$ reads

$$\sqrt{-g}T^{\mu\nu} = \int d\lambda \left[t^{\mu\nu}\delta^4 - \nabla_\alpha(t^{\mu\nu\alpha}\delta^4) + \frac{1}{2!}\nabla_\alpha\nabla_\beta(t^{\mu\nu\alpha\beta}\delta^4) - ... \right] \quad , \qquad (2.1)$$

where the $t^{\mu\nu..}$ terms are the "multipole moments" and g is the determinant of the background metric. The distributions $\delta^4 = \delta\left(x^0 - X^0(\lambda)\right) \delta\left(x^i - X^i(\lambda)\right)$, where x^μ are arbitrary coordinates, realise the reduction of the system onto the worldline $X^\mu(\lambda)$ of some yet undefined reference point inside the body, λ being the proper time (cf. [23, 38]). The n-th multipole moment, $t^{\alpha\beta\mu_1..\mu_n}$, represents spatial integrals on a given hypersurface over the actual stress-energy tensor of the considered body, weighted with the n-th power of the deviation from the worldline with respect to the chosen reference point, $\int T^{\alpha\beta}\delta x^{\mu_1}..\delta x^{\mu_n} dx^3$, with $\delta x^\mu = (x^\mu - X^\mu(\lambda))$ [39]. Following Dixon [35], physically meaningful quantities are standardly used nowadays to express the multipole moments (cf., e.g., Sec. II A in [40]). For instance, zeroth moments can be encoded in the linear four momentum [26]

$$p^\mu = \int\limits_{x^0=const.} T^{\mu 0} \sqrt{-g}d^3x \quad . \qquad (2.2)$$

Similarly, first moments can be encoded in the internal angular momentum tensor [30], or, perhaps more conventionally, the "spin tensor",

$$S^{\mu\nu} = \int\limits_{x^0=const.} \left(\delta x^\mu \, T^{\nu 0} - \delta x^\nu \, T^{\mu 0} \right) \sqrt{-g} \, d^3x \quad . \qquad (2.3)$$

In this definition the yet unspecified reference point tracked by $X^\mu(\lambda)$ is used as the center against which the spin is measured. The antisymmetry implies that there are six independent components for spin. These can be interpreted as being the components of a spatial spin vector in the well-known sense, plus the freedom of choosing the spatial center with respect to which the spin is defined. This center for the spin serves, at the same time, as the reference point whose worldline $X^\mu(\lambda)$ bears the gravitational skeleton (see [26]). Note that the spatial integrals of Eq.'s (2.2)&(2.3), in fact, only have to be computed for getting initial data for $p^\mu, S^{\mu\nu}$. Then, p^μ and $S^{\mu\nu}$ are used as worldline-variables which

are encoding zeroth and first moments respectively, and which are evolved according to some EOM (as introduced below).

The above description (2.1) of a physical body as a series of multipole moments becomes approximative by, (i) making a simplified consideration of the factual $T^{\mu\nu}$ when computing the integrals which define the moments, or the variables representing the moments $(p^\mu, S^{\mu\nu})$, and/or (ii) neglecting higher nonzero multipoles in the series. Note, however, that the representation can be very accurate when considering idealised bodies of small size and high symmetry, like a point-like mass or a spherical top. A point-like mass can be reduced to its monopole, with $t^{\mu\nu} = v^{(\mu}p^{\nu)}$. Here, $v^\mu(\lambda)$ is the tangent vector to the worldline $X^\mu(\lambda)$. Note that for multipolar bodies v^μ need not be parallel to p^μ, as we will discuss below (cf. Sec. 2.1.3). The dipole moment can be written in terms of the spin tensor $t^{\mu\nu\alpha} = S^{\alpha(\mu}v^{\nu)}$. Thus truncating Eq. (2.1) at the first order, we get the following "pole-dipole approximation" of a small body

$$\sqrt{-g}T^{\mu\nu} = \int d\lambda \; \left[v^{(\mu}p^{\nu)}\delta^4 - \nabla_\alpha(S^{\alpha(\mu}v^{\nu)}\delta^4) \right] \qquad , \qquad (2.4)$$

which is obviously linear in the spin. It is important to understand that this does not necessarily mean to neglect quadratic in spin information, nor, equivalently, second moments. One can easily imagine situations where monopole and dipole completely characterise the considered body; e.g., a spherical top. Loosely speaking, one cannot loose quadrupole information when there is none. In general, however, astrophysically relevant objects like a black hole may exhibit quadrupolar deformations, which can be written as a quadratic in spin term [41]. It, therefore, depends on the object that we want to subject to the pole-dipole representation whether this approximation is or is not neglecting relevant quadratic in spin information.

Equations of motion (EOM)

The problem of motion of a binary configuration in GR is, in general, too complex to be solved analytically from EOM for the metric and the energy-momentum tensor. In the limit of a fixed background gravitational field we can, however, find evolution equations for a matter perturbation $T^{\mu\nu}$ by demanding that the dynamical equation holds,

$$\nabla_\mu T^{\mu\nu} = 0 \qquad . \qquad (2.5)$$

In the case of a small body the gravitational skeleton representation of $T^{\mu\nu}$ is adequate. Inserting the skeleton Eq. (2.4) into Eq. (2.5), one obtains evolution equations for the multipole moments, or for the characteristic quantities used to encode the multipole moments $(p^\mu, S^{\mu\nu}$ in our case), rather than equations for the components of $T^{\mu\nu}$ themselves.

Restricting to a zeroth order description of $T^{\mu\nu}$, i.e. to the mass monopole, one obtains

the geodesic EOM (cf., e.g., Ex. 3 in Ch. 4 of Carroll's book [42]). Including the first order moments, i.e. representing a body in the pole-dipole approximation, Papapetrou derived the EOM for a spinning body [39]. Several rederivations, which were especially important with respect to the different choice of evolution variables, were performed in [38, 43, 26, 37]. Today's standard formulation is given in terms of $\{v^\mu, p^\mu, S^{\mu\nu}\}$ and reads

$$v^\alpha \nabla_\alpha\, p^\mu = -\frac{1}{2}\, R^\mu{}_{\nu\rho\sigma}\, v^\nu\, S^{\rho\sigma} \quad , \tag{2.6}$$

$$v^\alpha \nabla_\alpha\, S^{\mu\nu} = p^\mu v^\nu - p^\nu v^\mu \qquad , $$

where $R_{\alpha\beta\gamma\delta}$ is the Riemann tensor of the background. In this chapter we will sometimes denote $v^\alpha \nabla_\alpha$ by a dot on the respective quantity. This system of ordinary differential equations is manifestly linear, in the sense that no higher order terms of the variables appear. But, moreover, it is underdetermined; there are three degrees of freedom. The system has to be closed by some supplementary condition. The three degrees of freedom can be interpreted as the freedom in the choice for the reference point that is tracked by the EOM. Usually this reference point is chosen as the COM with respect to some preferred observer; which explains why it is reasonable to also use the worldline as the spatial center against which to measure the spin in Eq. (2.3). In this convention, a condition which fixes the notion of spin also fixes the location of the reference point. Such a condition is called a "spin-supplementary-condition" (SSC). Since Mathisson already derived Eq.'s (2.6) in a special SSC, one often sees them called "Mathisson-Papapetrou" equations (MPEQs). Sometimes even "Mathisson-Papapetrou-Dixon" equations to acknowledge the important reformulation of Dixon.

The validity of Eq.'s (2.6) can lead to some confusion and the literature is not always clear in that respect. The crucial point is to recall the conditions that were imposed in deriving Eq.'s (2.6). Most importantly, the energy-momentum tensor was assumed to be of pole-dipole form. Thus, the equations hold strictly only for those bodies which are, as a matter of fact, sufficiently, with respect to the physical context, described by their pole and dipole; i.e. as a spherical top. However, as usual in physics, the situation becomes more subtle when one wants to stretch the limits of the model; in particular, when one considers bodies which have, to a small extent, more structure than a spherical top, i.e. bodies which are significantly, with respect to the physical context, squeezable. Certainly, if one subjects such bodies to the pole-dipole model, the representation becomes approximative by neglecting at least second moments, which are expressible as quadratic in spin terms. Hence, the MPEQs are rigorous/quantitative only for bodies which are perfectly described by their pole and dipole. For bodies with quadrupolar or even higher order features the MPEQs are only a qualitative description of the evolution. This discussion will become

important in view of the meaningfulness of sustaining non-linearities introduced to the system by certain SSCs.

In general, the trajectories of SPs as obtained from Eq.'s (2.6) under some SSC deviate from geodesic motion but converge towards them for $S^{\mu\nu} \to 0$. The constants of motion for single pole particles, the energy $-p_t$ and the z-component of the orbital angular momentum p_ϕ, are no longer preserved for a pole-dipole particle evolving under Eq.'s (2.6). Instead, we have conservation of

$$E = -p_t + \frac{1}{2}S^{\mu\nu}\,\partial_\nu g_{t\mu}\,, \qquad J_z = p_\phi - \frac{1}{2}S^{\mu\nu}\,\partial_\nu g_{\phi\mu} \qquad , \qquad (2.7)$$

when considering a stationary and axisymmetric background like Kerr [30, 35], with standard Boyer-Lindquist coordinates (t, r, θ, ϕ). Without a SSC one cannot find a mass parameter which is conserved. The definitions $p^\mu p_\mu =: -\mu^2$ and $p_\mu v^\mu =: -m$ lead to $\frac{d}{d\lambda}\mu = \frac{\dot{p}_\rho\, p_\sigma\, \dot{S}^{\rho\sigma}}{m\,\mu}$, and $\frac{d}{d\lambda}m = \dot{u}_\rho\, u_\sigma\, \dot{S}^{\rho\sigma}$, respectively, which can both yield conservation given a suitable SSC [30]. In fact, μ is the rest mass of the body with respect to an observer with four velocity equal to the specific linear momentum $u_\nu = \frac{p_\nu}{\mu}$, while m is the rest mass with respect to an observer with four velocity equal to the tangent vector v^μ of the reference worldline. Furthermore, the conservation of the spin measure $2\,S^2 = S_{\mu\nu}S^{\mu\nu}$ depends, as well, on the SSC.

Before proceeding to the discussion of a common choice for the SSC, note that EOM for bodies with nonvanishing quadrupole or even higher moments can be derived following the same procedure of inserting the truncated gravitational skeleton into the dynamical equation, Eq. (2.5). Details can be found in [23, 44] and several works of Bini et al. [45, 46, 47].

2.1.3   Spin supplementary conditions (SSCs)

Among the infinite choices for closing the system (2.6) only those should be picked which lead to physically reasonable results. In principle, one could directly impose some relation between v^μ, p^μ and $S^{\mu\nu}$, but, in practice, this can lead to questionable motion of the reference point within the body (cf., e.g., [31, 48] for a detailed study of SSCs). To avoid this, the SSC is chosen such that the implied reference worldline tracks the COM of some physical observer (see beginning of Sec. 3 in [31]). For that choice of the spin the observer will measure a purely spacelike spin tensor, i.e. $S^{0\mu} = 0$. One can, in fact, show that for an observer with $S^{0\mu} = 0$ the COM coincides with the reference point tracked by v^μ in the MPEQs [31]. The covariant formulation of such a condition reads $\omega_\mu S^{\mu\nu} = 0$, where ω_μ is the four velocity of the chosen observer. In his rest frame we have $\omega_\mu = (\omega_0, 0, 0, 0)$. Notably, the imposition of such conditions reduces the independent components of $S^{\mu\nu}$ to

three, which allows the construction of a spin-vector as done below for a specific SSC.

One of the prevalent SSCs was suggested by Tulczyjew [38] (TUL-SSC)

$$p_\mu S^{\mu\nu} = 0 \quad , \tag{2.8}$$

and it will be the SSC chosen in this work. It features the strict conservation of $\mu^2 = -p_\mu p^\mu$, and allows the definition of the spin-vector $S^\alpha = \frac{1}{2}\epsilon^{\alpha\nu\rho\sigma}\frac{p_\nu}{\mu}S_{\rho\sigma}$, with a conserved spin measure $2S^2 = 2\,S^\mu S_\mu = S^{\mu\mu}S_{\mu\nu}$. Here, $\epsilon_{\mu\nu\rho\sigma} = \sqrt{-g}\tilde{\epsilon}_{\mu\nu\rho\sigma}$ is the Levi-Civita tensor with $\tilde{\epsilon}_{0123} = 1$. Condition (2.8) prescribes a unique relation between the tangent and the specific linear momentum

$$v^\mu = \frac{m}{\mu}\left(u^\mu + \frac{2\,S^{\mu\nu}R_{\nu\rho\kappa\lambda}u^\rho S^{\kappa\lambda}}{4\mu^2 + R_{\alpha\beta\gamma\delta}S^{\alpha\beta}S^{\gamma\delta}}\right) \quad , \tag{2.9}$$

where in this case m is not a constant of motion, but rather used as a correction factor which is set at every time step such that $v^\mu v_\mu = -1$ (cf. [21]). In general, Eq. (2.9) implies that v^μ and u^μ differ by terms of the order $\mathcal{O}(S^2)$, i.e. we have $v^\mu = u^\mu + \mathcal{O}(S^2)$.

Concerning the meaningfulness of $\mathcal{O}(S^2)$ terms, recall the discussion on the validity of Eq.'s (2.6). For bodies with more than dipolar structure the MPEQs are only a qualitative description; in particular, they are neglecting $\mathcal{O}(S^2)$ terms connected to the second moments of the body. For instance, if we consider BHs in the pole-dipole model, we are likely neglecting a quadrupole moment, i.e. quadratic in spin terms [23, 41]. Consequently, the evolution of a deformed BH is only qualitatively given by Eq.'s (2.6). In this case it would make no sense to sustain the $\mathcal{O}(S^2)$ terms in Eq. (2.9) introduced by the SSC. For such bodies the whole formalism is only a qualitative picture, which is consistent at linear order in the spin. Conversely, for bodies which are sufficiently described by the pole-dipole model the formalism has at no place neglected $\mathcal{O}(S^2)$ terms. Thus, the introduced quadratic in spin relation Eq. (2.9) has to be solved strictly. It would be a further linearisation/approximation to demand that $\mathcal{O}(S^2)$ terms can be neglected; for example, by virtue of the assumption that the body be slowly rotating, $S \ll 1$.

We do not linearize Eq.'s (2.6) with respect to the spin. The dynamics used in this work are produced solving the full, quadratic in spin relation Eq. (2.9). This means that our dynamics are rigorous for pole-dipole bodies while higher order bodies are not consistently described. Moreover, to obtain qualitative insights on the influence of spin, we study spin values of order $S/(\mu M) \sim \mathcal{O}(1)$, which are theoretically too high [30, 40]. Note that all relevant references used for comparisons made the same choice (cf. App. D).

2.2 Effective-one-body dynamics

This thesis is intimately related to the topic of EOB-dynamics because the considered realistic, non-geodesic trajectories of a nonspinning particle (cf. Fig. 2.1), as produced by Dr. Nagar [49], were obtained within the EOB formalism. The orbits are used in Ch. 7 in investigations of waveforms and fluxes from binaries in the point-particle limit. In the future it may be possible to use the results of this thesis for a SP (cf. Ch. 8) to improve the accuracy, or the range of validity, of the RR of the model; currently the RR is built in the non-spinning limit. Also, our numerical waveforms could be used to find the flexibility parameters of the EOB-model in the EMR limit. These tight relations and future prospects motivate a quick overview on the EOB-dynamics for a point particle. Especially, the procedure of recasting analytical PN-waveforms into a better-behaved multiplicative vesture and the implied improvement of the RR shall be demonstrated. We have, so far, only used EOB-dynamics for a nonspinning particle and equatorial motion. The discussion below is held within these limits.

The EOB model is probably the most advanced semi-analytical approach to the general relativistic two-body problem in the strong-field region. Originally introduced in [50], "the basic idea is to map the two-body problem (...) onto an effective-one-body problem, i.e. the motion of a test particle in some effective external metric". More precisely, the Hamiltonian dynamics of a compact binary with masses M_1 and M_2 are mapped onto those of an effective particle of mass $\mu = \frac{M_1 M_2}{M_1 + M_2}$, which moves on the background of a deformed Kerr metric with mass $M = M_1 + M_2$. The deformation parameter is the symmetric mass ratio $\nu = \frac{\mu}{M} = \frac{M_1 M_2}{(M_1 + M_2)^2}$. The EOM of the effective particle are obtained from an effective Hamiltonian, which is constructed from analytical information of PN theory. The waveform along the dynamics is computed as a PN multipolar waveform. In both, dynamics and the waveform, one applies certain *resummation* procedures to the expressions, which turn out to extend the validity of the employed PN results from the weak-field-slow-motion regime across almost the whole parameter space. The missing higher PN information are wrapped into a few flexibility parameters, which are finally computed by iterative comparison of the outcome with accurate numerical data. Since the EOB model aims at covering all mass-ratios, those comparisons need both data from full NR simulations and perturbative particle simulations. This directly explains part of the connection to a time-domain Teukolsky solver. The second connection is the RR. The limit $\nu \to 0$, for which the RR is given by the fluxes of a particle in circular orbit, is used as the starting point. With respect to this "fixed end" at $\nu \to 0$ the RR is suitably deformed in ν to agree with NR data for finite ν.

Working in the point-particle approximation, we are mostly interested in the EMR limit
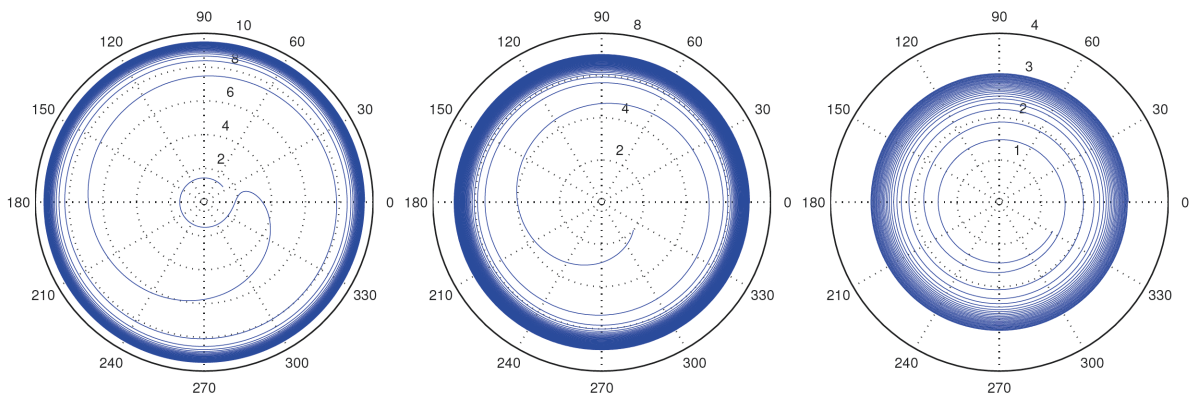
Figure 2.1: Examples of realistic trajectories $(r_p(t), \phi_p(t))$ of a non-spinning point particle in the equatorial plane, starting from circular motion with adiabatically shrinking radius and final plunge, as produced within the EOB formalism. The plots refer to a Kerr background with dimensionless spin $\hat{a} = -0.9$ (left), $\hat{a} = 0$ (center), and $\hat{a} = +0.9$ (right). Plot adopted from [H2].

of the model. In this case $M_1 \gg M_2$ and we have $M \approx M_1$, $\mu \approx M_2$. A test-particle does not deform the background. Thus we omit further details on the ν-dependent mappings (for more details on the deformation cf. [49]). It is enough to keep in mind here that they (i) deform the point particle Hamiltonian to the effective one, and (ii) deform the point particle RR to the NR-adapted one. We stress that the EOB-dynamics used in this work were created with $\mu/M = 10^{-3}$ in order to reduce the inspiral time. At this value the RR is noticeably deformed from the EMR limit, which means we consider a somewhat inconsistent trajectory for the test particle limit. That is why investigations like those of Sec. 7.2.2 have to probe this well-known procedure.

2.2.1 Equations of motion for a point particle

The conservative part of the dynamics of a nonspinning particle is the geodesic motion of a test-particle on the Kerr background. Geodesic motion can be described by the four-dimensional Hamiltonian $\mathcal{H} = -\frac{1}{2}\mu^2 = \frac{1}{2}g^{\alpha\beta}p_\alpha p_\beta$, where p_α are the conjugate momenta of the coordinates $q^\alpha(\lambda)$ (usually BL-coordinates (t, r, θ, ϕ)), with λ the proper time. Because λ does not appear explicitly in the system one can separately solve for $t(\lambda)$ and use t instead of λ as the integration parameter. The time component of the momenta, p_t, is a conserved quantity for geodesic motion on Kerr. Therefore, one can reduce the system and consider equivalently the three-dimensional Hamiltonian $H = -p_t$, which is the total energy of a test-particle on a geodesic. An explicit expression in terms of coordinates and momenta can be found from the normalisation $g^{\alpha\beta}\hat{p}_\alpha\hat{p}_\beta = -1$, where $\hat{p}_\alpha = p_\alpha/\mu$ are the momenta per unit mass, equal to the four-velocity $dq^\alpha/d\lambda$ for a nonspinning particle, and, then, solving for $\hat{p}_t$

$$\hat{H} \equiv H/\mu = -\hat{p}_t = \frac{g^{0i}\hat{p}_i}{g^{00}} + \left(\frac{g^{0i}\hat{p}_i}{g^{00}} - \frac{g^{ij}\hat{p}_i\hat{p}_j + 1}{g^{00}} \right)^{1/2} \quad , \quad (2.10)$$

where $g^{\mu\nu}$ is the inverse metric tensor. $\hat{H}$ is the conserved energy per unit mass for a test-mass. According to $\frac{dq^i}{dt} = \frac{\partial}{\partial \hat{p}_i} \hat{H}$ and $\frac{d\hat{p}_i}{dt} = -\frac{\partial}{\partial q^i} \hat{H}$ we thus obtain six Hamilton EOM. Two of them are trivial in the equatorial plane. At this point one can add, by hand, dissipative terms to account for the emission of GWs. In doing this we depart from the pure test-particle limit. The resulting EOM in the equatorial plane read

$$\dot{r} = \frac{\partial}{\partial \hat{p}_r} \hat{H} \quad , \quad \dot{\phi} = \frac{\partial}{\partial \hat{p}_\phi} \hat{H} = \hat{\Omega} \quad , \quad \dot{\hat{p}}_r = -\frac{\partial}{\partial r} \hat{H} + \hat{\mathcal{F}}_r \quad , \quad \dot{\hat{p}}_\phi = \hat{\mathcal{F}}_\phi \; , \qquad (2.11)$$

where the dot, differently from the notation used in Sec. 2.1.3, stands for differentiation with respect to t. We decided to set $\hat{\mathcal{F}}_r$ to zero because a robustly performing expression seems to be missing from the literature [51]. Eq.'s (2.11) are the ones used for producing what is called "realistic trajectories" in this thesis; orbits which evolve through a series of circular orbits with gradually shrinking radii until the orbit becomes unstable and the particle plunges geodesically into the BH (cf. Fig. 2.1). The piece driving the particle away from the geodesic motion is the RR, $\hat{\mathcal{F}}_\phi$. For EMRs $\hat{\mathcal{F}}_\phi$ is prescribed in analytical form by employing PN multipolar waveforms for a particle on circular orbits.

2.2.2 Multiplicative post-Newtonian multipolar waveforms

The PN waveform is an essential ingredient to the whole EOB formalism. It is used to generate the wave signal from the EOB dynamics. But, in addition, it is also important for the dynamics themselves, where it is used, in the specification to quasi-circular binaries, to build the EOB-RR. A RR is supposed to lead to adiabatic, quasi-circular inspiral motion. In the EOB formalism the RR is built on the basis of the test-particle energy fluxes; at each radius of a quasi-circular inspiral, the RR is demanded to coincide with the energy fluxes of a test-particle in circular orbit at that radius. To handle finite mass ratios ν, the such obtained RR is deformed in a suitable way, calibrated by NR simulations. The fluxes of a test-particle are available in analytic form in the PN-approximation. Pure PN-waveforms, however, fail to capture the numerical fluxes of a test-particle in the strong-field. As it turns out, rewriting the PN-information in a certain multiplicative way, together with doing new expansions, leads to a much better behaved analytical waveform for a test-particle. This idea was invented as the "multiplicative approach" for PN waveforms by Damour and Nagar [52, 53]. Below, the procedure to obtain the improved waveform from a given PN waveform in the case of a test-mass in circular orbit, shall be described.

Originally, any PN-approximation is a Taylor-expansion in $x \equiv (v/c)^2$, where v is the characteristic velocity of the system. The x^n term is named the "n-th order" PN term. Evidently, one has a sum of the Newtonian-approximation and corrections; more precisely, for the multipolar waveform we have $h_{\ell m}^{\mathrm{PN}} = h_{\ell m}^{\mathrm{N}} + h_{\ell m}^{\mathrm{1PN}} + h_{\ell m}^{\mathrm{1.5PN}} + h_{\ell m}^{\mathrm{2PN}} + \dots$. Note that $h_{\ell m}^{\mathrm{N}}$ already contains factors of v so that the PN corrections here are not actually ordered

like $v^1, v^2, ..$-terms but like successively higher powers of v, starting with the Newtonian-term-power of v plus 1. In [52, 53] Damour and Nagar proposed a rewriting of the PN-waveform which turns out to be much better converging towards numerical data. Later on, the convergence was further improved in [54], which the following overview leans on.

The basic idea is to replace the PN-sum in favour of a product of physically motivated contributions, wrapped up in a correction factor to the Newtonian part. Essentially, one writes $h_{\ell m} = h_{\ell m}^{(\mathrm{N},\epsilon)} \cdot \hat{h}_{\ell m}^{(\epsilon)}$, where ϵ denotes the parity of the multipole; for circular equatorial orbits simply $\epsilon = 0$ when $\ell + m$ even and $\epsilon = 1$ when $\ell + m$ odd. The leading term $h_{\ell m}^{(\mathrm{N},\epsilon)}$ is the Newtonian contribution. It is given by

$$h_{\ell m}^{(\mathrm{N},\epsilon)} = \frac{M\nu}{c^2 R} n_{\ell m}^{(\epsilon)} c_{\ell+\epsilon}(\nu)\, v^{\ell+\epsilon}\, Y_{0,\ell-\epsilon,-m}\left(\frac{\pi}{2},\phi\right) \quad , \tag{2.12}$$

with the relative distance R. The numerical values of the constants $n_{\ell m}^{(\epsilon)}$ and $c_{\ell+\epsilon}(\nu)$, are irrelevant for our discussion (cf. references [54, 55] for exact definitions). Inspecting Eq. (2.12), the meaning of the "characteristic" velocity v has to be fixed. In case of the particle limit there is a natural choice, i.e. the orbital velocity of the particle, on circular orbits $v_{\mathrm{orb}} \equiv r\Omega$. The angular velocity Ω is given by the geodesic equations. It reads $\Omega = \frac{d\phi}{dt} = \pm\frac{M^{1/2}}{r^{3/2}+aM^{1/2}}$, which can be rewritten as a Kepler-constraint for some modified radius $\tilde{r}$, $\Omega^2 \tilde{r}^3 = const.$ (see Eq. (54) in [H2]). For $a = 0$ and $M = 1$ this means we have $\Omega = r^{-3/2}$, and, thus, $v_{\mathrm{orb,a=0}} = \Omega^{\frac{1}{3}}$. If we use v_{orb} as the PN-parameter v, we get $x \equiv v^2 = \Omega^{\frac{2}{3}} = 1/r$. Proceeding to $a \neq 0$, one has to take special care when choosing what exactly the PN ordering parameter $v \equiv x^{1/2}$ shall refer to. Some confusion enters the field because one might use, (i) $v^2 = 1/r$ (e.g., in [56, 57]), (ii) $v^2 = \Omega^{2/3}$ (cf. [55, 58]), both of which choices are motivated by being the orbital velocity in case of Schwarzschild, or (iii) strictly $v = v_{\mathrm{orb}} = r\Omega$.

Let us come to the correction factor $\hat{h}_{\ell m}^{(\epsilon)} = 1 + \mathcal{O}(x)$. This correction is further decomposed into a product of factors, which are given as resummed PN-terms, as well of the form $\sim 1 + \mathcal{O}(x)$. First, there is a contribution called the "source of gravitational radiation". Since its leading order is the energy density, one defines $\hat{S}_{\mathrm{eff}}^{(\epsilon=0)} = \hat{H}_{\mathrm{eff}}$, where $\hat{H}_{\mathrm{eff}}$ is the effective Hamiltonian. In our case the "effective" can be dropped; the Hamiltonian for a test-particle in circular orbit about Kerr is known in closed form. The specific version reads

$$\hat{S}_{\mathrm{eff}}^{(\epsilon=0)} = \hat{H}(r) = \frac{1 - \frac{2M}{r} + \frac{aM^{1/2}}{r^{3/2}}}{\sqrt{1 - \frac{3M}{r} + \frac{2aM^{1/2}}{r^{3/2}}}} \quad . \tag{2.13}$$

For odd parity modes another choice performs better, namely identifying the angular

momentum as the source and normalising it by the Newtonian value. In our case this is

$$\hat{S}_{\text{eff}}^{(\epsilon=1)} = \frac{L_z(r)}{L_z^N} = \frac{\mu M}{L_z^N} \sqrt{\frac{r}{M}} \; \frac{1 - \frac{2aM^{1/2}}{r^{3/2}} + \frac{a^2}{r^2}}{\sqrt{1 - \frac{3M}{r} + \frac{2aM^{1/2}}{r^{3/2}}}} \quad , \tag{2.14}$$

where $L_z^N = \mu M/v$ is the Newtonian angular momentum (cf. Eq. (24) and Eq.(25) in [55]). The second physical contribution to the waveform is assigned to the backscattering of radiation on its journey towards future null infinity. This backscattering is encoded in the "tail factor" $T_{\ell m}$. The standard form for this factor is given in terms of the Γ-function

$$T_{\ell m} = \frac{\Gamma(\ell + 1 - 2i\,\hat{\hat{k}})}{\Gamma(\ell + 1)} e^{\pi \hat{\hat{k}}} \, e^{2i\,\hat{\hat{k}}\,\log(4m\Omega M/\sqrt{e})} \quad , \tag{2.15}$$

where $\hat{\hat{k}} = M\, m\Omega$ (cf. Eq. (26) in [55]).

Of course, these two physically identified contributions can not make the complete picture. Thus, one allows for residual correction factors in amplitude, $f_{\ell m}$, and in phase, $e^{i\delta_{\ell m}}$. As shown in [54, 55], the replacement $\rho_{\ell m} = f_{\ell m}^{1/\ell}$ leads to further improvements. Assembling all the pieces, the final decomposition of the waveform into multiplicative factors reads

$$h_{\ell m} = h_{\ell m}^{(\text{N},\epsilon)} \cdot \hat{S}_{\text{eff}}^{(\epsilon)} \, T_{\ell m} \, e^{i\delta_{\ell m}} \, (\rho_{\ell m})^{\ell} \quad . \tag{2.16}$$

Since in the particle limit $\hat{S}_{\text{eff}}^{(\epsilon)}$ and $T_{\ell m}$ are given in closed form, the task of deducing the multiplicative waveform from a given "exact" waveform, either some PN-waveform or a numerical one, consists of determining the residual corrections $\delta_{\ell m}, \rho_{\ell m}$. With respect to using the waveform for energy fluxes from circular orbits even the phase is irrelevant. We only need to compute the amplitude corrections $\rho_{\ell m}$.

2.2.3   Resummed energy fluxes and $\rho_{\ell m}$ corrections

The $\rho_{\ell m}$ corrections at a given PN order can be computed from the respective PN expression, either for the waveform or the energy fluxes. Here we assume to be given energy fluxes. The following procedure was adopted in [55] by employing 5.5PN results for energy fluxes of a non-spinning particle on Schwarzschild [59] together with 4PN-results on Kerr [61] (apparently some results were not published explicitly, cf. App. C of [62]). The $\rho_{\ell m}$'s of [55] were adopted in this thesis for the EOB-dynamics.

The energy fluxes of a particle in circular orbit follow from the strain as

$$\frac{d}{dt}E = \frac{1}{16\pi} \int |r\dot{h}|^2 \, \sin\theta \, d\theta \, d\phi \, , \tag{2.17}$$
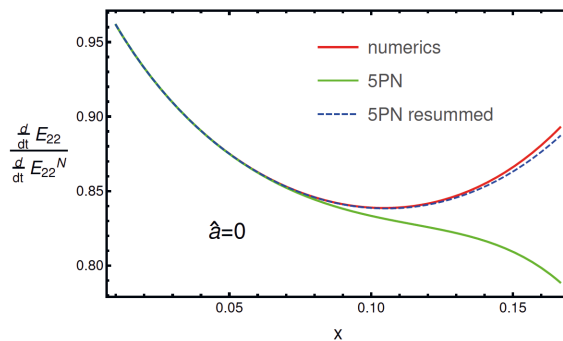
Figure 2.2: Performance of analytical models for the energy fluxes of a particle in circular equatorial orbit on Schwarzschild. For large distances $x \equiv 1/\hat{r} \to 0$ the 5PN energy flux (green) converges towards the numerical data (red). Close to the last-stable-orbit, at $x = 1/6$, the PN-result deviates from the numerics. The resummation procedure (see text) can help to yield a better agreement (blue dashed). The formulas for the analytic fluxes are given in [59] together with detailed assessments of the improvements due to resummation. The numerical fluxes are provided by a frequency domain code of Hughes [60], but, at slightly worse accuracy, can also be computed with the *teukode* (cf. Sec. 5).

which can be decomposed into modes

$$
\frac{d}{dt}E = \sum_{\ell=2}^{\ell_{max}} \sum_{m=1}^{\ell} \frac{d}{dt}E_{\ell m} = \frac{2}{16\pi} \sum_{\ell=2}^{\ell_{max}} \sum_{m=1}^{\ell} |r\dot{h}_{\ell m}|^2 = \frac{2}{16\pi} \sum_{\ell=2}^{\ell_{max}} \sum_{m=1}^{\ell} (m\,\Omega)^2 |rh_{\ell m}|^2 \qquad , \quad (2.18)
$$

where the term $\frac{d}{dt}E_{\ell m}$ is often called $F_{\ell m}$, and it wraps up both $\pm m$ contributions. Here one could simply insert the PN-waveform at some order to get the corresponding PN-fluxes. For the sake of extending the reliability of the fluxes, one can rewrite the PN-waveform in the form of Eq. (2.16). The modulus in the fluxes actually allows to forget about phase corrections.

Using energy fluxes instead of the waveform for the computation of the $\rho_{\ell m}$, first note that $|h_{\ell m}| \sim \sqrt{F_{\ell m}}$. Normalising with the leading order term, we get equality, $\frac{|h_{\ell m}|}{h_{\ell m}^N} = \sqrt{\frac{F_{\ell m}}{F_{\ell m}^N}}$, with, e.g., $F_{22}^N = \frac{32}{5}v^{10}$. Reorganising Eq. (2.16) and using this relation, the expansion $f_{\ell m} = \text{Taylor}\left(\sqrt{\frac{F_{\ell m}^{\text{PN}}}{F_{\ell m}^{\text{N},\epsilon}(\hat{S}_{\text{eff}}^{(\epsilon)}|T_{\ell m}|)^2}}\,, v, v_0 = 0 \right)$ gives the wanted corrections. The expansion can be equivalently performed in $x \equiv v^2$. Of course, one has to truncate at the order dictated by the given PN-flux. At high orders this expansion can get involved. In checking the herein used results of [55] we employed *mathematica's* "Series[..]" command. This allows to separately expand the pieces, and to afterwards multiply the results. Finally, to further improve the performance, one computes $\rho_{\ell m} = \text{Taylor}\left(f_{\ell m}^{1/\ell}, v, v_0 = 0 \right)$. The explicit expressions of the $\rho_{\ell m}$'s as series in v are given in Eq.'s (29a-29i) of [55]. To convince ourselves of the improved performance one can compare the pure-PN fluxes with the ones obtained after the above procedure. Fig. 2.2 gives an impression of the amendment due to the resummation at 5PN. Detailed comparisons of PN-fluxes and their resummed versions can be found in [55, 59].

Teukolsky formalism

The Teukolsky Equation (TKEQ) describes the evolution of linear perturbations on a rotating BH background. It is essentially the result of linearizing the Bianchi-identities, $R_{\alpha\beta[\gamma\delta;\mu]} = 0$, where the semicolon denotes a covariant derivative and $R_{\alpha\beta\gamma\delta}$ the Riemann tensor, written in tetrad notation [63], and imposing the Einstein Eq.'s (1.1). Mathematically the TKEQ is a linear partial differential equation (PDE) of second order with a wave-equation-like structure for the variable $\Psi(t, r, \theta, \phi)$, written in Boyer-Lindquist (BL) coordinates. Depending on the character of the considered perturbation (gravitational, electromagnetic, neutrino or scalar), Ψ represents different fields which contain full information on the respective perturbation. The TKEQ was derived by Teukolsky in 1972 [17, 18, 64] and used in a first study to show that a rotating BH spacetime is dynamically stable against linear perturbations. Besides stability studies [65, 66, 67], the TKEQ finds important application in the computation of quasi-normal modes [68, 69, 70, 71, 72], GWs of EMR systems [73, 74, 75, 76, 77] and effects of the self-force [78, 79].

We start in Sec. 3.1 by quoting the explicit TKEQ in BL coordinates. Sec. 3.2 outlines the traditional route to find its numerical solutions in the frequency-domain, which is often called the "Teukolsky formalism". It is, however, also possible to solve the TKEQ in the time-domain. We will review the one and only, besides that used in this thesis, published time-domain approach of Krivan et al. [80] in Sec. 3.3, and also describe its development and applications over the last twenty years.

Additionally, App. A describes the derivation of the gravitational TKEQ within the "Newman-Penrose" (NP) formalism. For our purpose here it is enough to note just a few things. First, Teukolsky's "master-equation", Eq. (3.3) below, represents a family of evolution equations. All of these evolution equations share a similar form and are parameterised in the TKEQ by the spin weight s of the considered field: the field represented by Ψ has the spin weight, (i) $s = 0$ in the scalar case, (ii) $|s| = 1/2$ in the neutrino case, (iii) $|s| = 1$ in the electromagnetic case, and (iv) $|s| = 2$ in the gravitational case (cf. Sec. A.3). Second, for a given s each of the explicit equations follows from certain more general perturbation equations for tetrad scalars, i.e. for the Weyl scalars Ψ_4 and Ψ_0 in

the gravitational case, by specifying some key ingredients to the Kerr background: the coordinate system and the null-tetrad basis.

3.1 Explicit Teukolsky Equation

In App. A we have quoted Teukolsky's decoupled gravitational perturbation equations for Ψ_4 and Ψ_0, Eq.'s (A.16)-(A.19) respectively. These equations are written in tetrad notation and are more general than the explicit TKEQ because they hold for arbitrary vacuum type D spacetimes and for arbitrary choices of the tetrad and the coordinates. To arrive at the explicit TKEQ below, one specifies these equations to the Kerr background and then follows Teukolsky's choices [18] for the tetrad and the coordinate system.

The explicit TKEQ uses the Kerr metric in BL coordinates $\{t, r, \theta, \phi\}$

$$ds_{\mathrm{BL}}^2 = -\left(1 - \frac{2Mr}{\Sigma}\right) dt^2 - \frac{4aMr}{\Sigma} \sin^2\theta\, dt\, d\phi + \frac{\Sigma}{\Delta}\, dr^2 \tag{3.1}$$
$$+ \Sigma\, d\theta^2 + \left(r^2 + a^2 + \frac{2Ma^2 r \sin^2\theta}{\Sigma}\right) \sin^2\theta\, d\phi^2 \ ,$$

where the two parameters are the mass of the Kerr spacetime M and its spin parameter a. We further have $\Sigma \equiv r^2 + a^2 \cos^2\theta$ and $\Delta \equiv r^2 + a^2 - 2Mr = (r - r_+)(r - r_-)$, which defines the horizons $r_\pm$. A well-known null-tetrad basis for the Kerr metric is given by the Kinnersley null-tetrad [81], defined in BL coordinates as

$$\ell^\mu = \frac{(r^2 + a^2, \Delta, 0, a)}{\Delta}\ , \ n^\mu = \frac{(r^2 + a^2, -\Delta, 0, a)}{2\Sigma}\ , \ m^\mu = \frac{(\mathrm{i}a\sin\theta, 0, 1, \mathrm{i}\csc\theta)}{\sqrt{2}(r + \mathrm{i}a\cos\theta)}\ . \tag{3.2}$$

With these choices Eq.'s (A.16)-(A.19) can be made explicit. Then, deriving the TKEQ is just a matter of computing the respective spin coefficients Eq.'s (A.13), and the directional derivatives Eq.'s (A.12). To arrive at the exact form given by Teukolsky, one has to be mindful of the meaning of the master variable Ψ in the different spin-weight cases, as listed in Table 1 of [18]. The TKEQ does, for example, not consider Ψ_4 directly but, for the sake of achieving separability, $\Psi = \rho^{-4}\,\Psi_4 = (r - \mathrm{i}\,a\cos\theta)^4\Psi_4$. The resulting equations are summarised, together with the analogous equations for electromagnetic, neutrino and scalar field perturbations, to Teukolsky's master equation. In BL-coordinates it reads

$$\left[\frac{r^2 + a^2}{\Delta} - a^2 \sin^2\theta\right] \partial_{tt}\Psi + \frac{4aMr}{\Delta}\, \partial_{\phi t}\Psi - \Delta^{-s}\partial_r(\Delta^{s+1}\partial_r \Psi) - \frac{1}{\sin\theta}\, \partial_\theta(\sin\theta\, \partial_\theta \Psi)$$
$$+ \left(\frac{a^2}{\Delta} - \frac{1}{\sin^2\theta}\right) \partial_{\phi\phi}\Psi - 2s\left(M\frac{r^2 - a^2}{\Delta} - (r + \mathrm{i}\,a\cos\theta)\right) \partial_t \Psi$$
$$- 2s\left(\frac{a(r - M)}{\Delta} + \mathrm{i}\,\frac{\cot\theta}{\sin\theta}\right) \partial_\phi \Psi + s\,(s\cot^2\theta - 1)\,\Psi = 4\,\pi\,\Sigma\,T \qquad , \tag{3.3}$$

which gives the gravitational equations for $\Psi = \Psi_0$ for $s = +2$, and for $\Psi = \rho^{-4}\Psi_4$ for $s = -2$. To avoid confusion note that $\Psi_{0/4}$ actually means $\Psi_{0/4}^B$ in the notation of App. A, where the superscript B denotes that this is a perturbation. Furthermore, it includes the equations for perturbations of the electromagnetic field for $|s| = 1$, for neutrino fields for $|s| = 1/2$, and for scalar fields $s = 0$, in which case it just becomes the scalar wave equation on Kerr spacetime. The source term T has different meanings accordingly. For instance, in the $s = +2$ case it becomes $T = 2\,T_0$, and for $s = -2$ it becomes $T = 2\,(r - \mathrm{i}\,a\cos\theta)^4\,T_4$, where the scalars $T_{0/4}$ are built from $T^{\mu\nu}$ and quoted in Eq.'s (A.17)&(A.19). In the remainder of this thesis only the gravitational case $|s| = 2$ will be of interest.

3.2 Separability in the frequency domain

The 1973 Teukolsky paper [18] contained several useful new results. First, the bare derivation of decoupled gravitational perturbation equations for arbitrary vacuum Petrov-type D backgrounds. Second, the insight that the analogy with electromagnetic, neutrino and scalar perturbations allowed to summarise all of them to a single master equation ordered by the spin-weight character of the field. The probably most surprising finding was the possibility to derive equations which are separable to ordinary differential equations (ODEs). As noted in [82], it was clear that t and ϕ can be separated out, but there was "no obvious reason why the r and θ dependence would separate". Yet, it turned out to be possible. The previously mentioned change of variables to a rescaled version, $\Psi_4 \to \Psi$, led to the explicit form Eq. (3.3).

Let us follow the procedure to separate the master equation Eq. (3.3) into ODEs, which is not difficult, as it was constructed for that purpose. By Fourier decomposition in time and azimuthal direction $\Psi = e^{-\mathrm{i}\omega t}\,e^{\mathrm{i}m\phi}\,f(r,\theta)$, two dependencies become trivial by virtue of $\partial_t \to -\mathrm{i}\omega$ and $\partial_\phi \to im$. Then, assuming that the radial and the polar dependencies separate as well, one can insert the ansatz

$$\Psi = e^{-\mathrm{i}\omega t}\,e^{\mathrm{i}m\phi}\,S_{s\ell m}^{a\omega}(\theta)\,R_{\omega\ell m}(r) \tag{3.4}$$

into the master equation for vacuum. This is enough to have the equation separate nicely into two ODEs. The sub- and superscripts on $S_{s\ell m}^{a\omega}$ and $R_{\omega\ell m}$ already display the different parameters in the explicit definition equations below. Without that knowledge one would just have called them $S(\theta)$ and $R(r)$, and for brevity we will do so sometimes. The radial equation takes effective potential form and reads

$$\Delta^{-s}\frac{d}{dr}\left(\Delta^{s+1}\frac{d}{dr}R(r)\right) + V(r)R(r) = 0 \qquad , \tag{3.5}$$

with the "potential" $V(r) = \left(\frac{K^2 - 2\,\mathrm{i}\,s\,(r-M)\,K}{\Delta} + 4\,\mathrm{i}\,s\,\omega\,r - \lambda\right)$. The appearing quantities are $K = (r^2 + a^2)\omega - a\,m$, $\lambda = \mathcal{E}_{s\ell m} + a^2\,\omega^2 - 2\,a\,m\,\omega - s(s+1)$, whereat the $\mathcal{E}_{s\ell m}$ will be specified momentarily. This potential is complex and, in contrast to the RWZ-equations, not short-ranged. The angular equation as written in [83] is

$$\frac{1}{\sin\theta}\frac{d}{d\theta}\left(\sin\theta\frac{d}{d\theta}S(\theta)\right)$$
$$+ \left(a^2\,\omega^2\,\cos^2\theta - \frac{m^2}{\sin^2\theta} - 2\,a\,\omega\,s\,\cos\theta - \frac{2\,m\,s\,\cos\theta}{\sin^2\theta} - s^2\,\cot^2\theta + \mathcal{E}_{s\ell m} - s^2\right)S(\theta) = 0\,.$$

$$(3.6)$$

For fixed $\{s, a\omega, m\}$ the latter equation can be seen as an eigenvalue problem for an angular operator. This operator has eigenvalues $\mathcal{E}_{s\ell m}(s, a\omega)$ and eigenfunctions $S_{s\ell m}^{a\omega}(\theta)$, which are called "spin-weighted spheroidal harmonics", see App. F for an algorithm to compute these functions. In the limit of $a\omega = 0$, the operator is just the angular part of the wave-operator in spherical coordinates. In that limit the eigenfunctions reduce to the well-known spin-weighted spherical harmonics $Y_{s\ell m}$. Like the $Y_{s\ell m}$ the $S_{s\ell m}$ form a complete set of basis functions. Thus, we can reconstruct our full solution for $s = -2$ as

$$\Psi_4 = (r - \mathrm{i}\,a\cos\theta)^{-4}\int_{-\infty}^{\infty}\left(\sum_{\ell m}R_{\omega\ell m}(r)\,S_{-2\ell m}^{a\omega}(\theta)\,e^{-\mathrm{i}\,\omega\,t}\,e^{\mathrm{i}\,m\,\phi}\right)d\omega\,, \qquad (3.7)$$

which means we have to combine the solutions for $R_{\omega\ell m}(r)$ and $S_{-2\ell m}^{a\omega}(\theta)$ for all relevant ℓ, m and ω to obtain the full solution. Note that this procedure is ultimately effective if the physical solution consists of a single discrete frequency, in which case the integration over $d\omega$ becomes trivial. Moreover, note that the $S_{-2\ell m}^{a\omega}(\theta)$ can be computed independently of a possible matter source, whereas the $R_{\omega\ell m}$ have to account for the source. In this case one has to expand the source term using the pre-computed $S_{-2\ell m}^{a\omega}(\theta)$ functions

$$4\,\pi\,\Sigma\,T = \int_{-\infty}^{\infty}\left(\sum_{\ell m}G_{\omega\ell m}(r)\,S_{-2\ell m}^{a\omega}(\theta)\,e^{-\mathrm{i}\,\omega\,t}\,e^{\mathrm{i}\,m\,\phi}\right)d\omega\,, \qquad (3.8)$$

with the result that Eq. (3.5) is enhanced by the source term $G_{\omega\ell m}(r)$ on the right-hand-side. Thus, the effort of solving the TKEQ mainly resides in solving the radial equation (3.5), which is, therefore, often referred to as *the* TKEQ.

Solving the radial equation turns out to be rather difficult. As described by Sasaki and Nakamura [84], see also [60] for a more recent work, the problem originates from the long-range character of the potential $V(r)$ and from the divergence of the source term $G_{\omega\ell m}(r)$ at large distances. The first problem can be surmounted by a suitable transformation of the function $R(r)$, which results in an equivalent formulation with a short-ranged

potential [85, 86]. The second problem was tackled by Sasaki and Nakamura [84], who succeeded in transforming the equation for $R(r)$ to one which is governed by a short-ranged potential and a non-divergent source term. Until ca. 2010, numerical frequency domain solutions of the TKEQ were usually found by solving the Sasaki-Nakamura equation and transforming back the solution to $R(r)$ [87, 88, 60]. Today, expansion-techniques in terms of hypergeometric functions dominate the community [89, 59, 58, 57] and set the literature benchmarks for the highest accuracy.

3.3   Traditional time domain approach

In general, a solution to the TKEQ consists of a wide range of frequencies ω, which makes the frequency domain approach computationally expensive. Therefore, it becomes very appealing to have a time-domain solver of the TKEQ. The problem is still only 2+1 dimensional because, given coordinates that manifest the symmetry, one can exploit the axisymmetry of the background by a Fourier-ansatz in azimuthal direction

$$\Psi(t, r, \theta, \varphi) = \sum_m e^{\mathrm{i}\, m\, \varphi} \Psi_m(t, r, \theta) \quad . \tag{3.9}$$

For the situations considered in this thesis we estimate that evolving for $m \in \{0, .., 6\}$ yields $\gtrsim 95\%$ of the full signal, as observed in a few test cases. Here, one should note here that Teukolsky was using the standard BL coordinate ϕ, whereas the above used φ anticipates the change of coordinates $\phi \to \varphi$, Eq. (3.10). Due to $\partial_\phi = \partial_\varphi$ the symmetry remains manifest in the new coordinate and the obtained 2+1 equation's coefficients are independent of φ. Since the master equation is also a linear PDE, the different $(..)e^{im\varphi}\Psi_m$ terms do not mix and the equation can be decomposed into separate sub-equations for the Ψ_m. For the full equation to hold, each of the single Ψ_m-equations has to hold independently. Thus, the evolutions of different m-modes completely decouple. For every m-mode equation the only remaining φ appearance is in the overall factor $e^{\mathrm{i}\, m\, \varphi}$, which can consequently be discarded; in vacuum the factor is irrelevant because the equation can trivially be divided by the $e^{\mathrm{i}\, m\, \varphi}$; in case of a matter perturbation one has to Fourier-expand the source term as well in order to make $e^{\mathrm{i}\, m\, \varphi}$ an overall term.

The first and to our knowledge only one successful scheme for such numerical time-domain integration of the 2+1 TKEQ for gravitational perturbations was introduced by Krivan et al. in [80]. The authors discussed severe numerical instabilities in case of a straightforward implementation in BL-coordinates. They were able to suppress those by a certain reformulation. First, the azimuthal BL coordinate leads to numerical problems at the horizon, even in the case of scalar perturbations [90]. These can be easily cured by transforming to the azimuthal Kerr-ingoing coordinate. Additionally, the tortoise radial coordinate

is used in order to push the horizon to minus infinity, $r^* \xrightarrow[r \to r_+]{} -\infty$. Together these transformations read $d\varphi = d\phi + \frac{a}{\Delta} dr$, $dr^* = \frac{r^2 + a^2}{\Delta} dr$ (cf. Eq.'s (2.4)-(2.7) in [91]), or explicitly

$$\varphi = \phi + \frac{a}{r_+ - r_-} \log\left(\frac{r - r_+}{r - r_-}\right) \ , \ r^* = r + \frac{2Mr_+}{r_+ - r_-} \log \frac{r - r_+}{2M} - \frac{2Mr_-}{r_+ - r_-} \log \frac{r - r_-}{2M} \ .$$
(3.10)

The $r \to \infty$ behaviour of the variable Ψ was given by Teukolsky as $\lim_{r \to \infty} \Psi(t, r, \theta, \phi) \sim r^3$ for $s = -2$, which invokes the rescaling of the field variable $\Psi_m(t, r^*, \theta) \to r^3 \Phi_m(t, r^*, \theta)$, to avoid the growth for large r. Unfortunately, these modifications are not yet enough to avoid numerical instabilities when implementing the 2+1-reduced TKEQ for $s = -2$ as a second order in time and space equation. The particular first order reduction $\Pi = \partial_t \Phi + \frac{r^2 + a^2}{(r^2 + a^2)^2 - a^2 \Delta \sin^2 \theta} \partial_{r^*} \Phi$ was found to allow stable simulations; however, apparently only in combination with a modified Lax-Wendroff time integration scheme of second order. Spatial derivatives were approximated by centered finite differences of second order. The grid in θ direction was staggered to avoid problems at the axis. The boundary conditions on the axis were imposed by $\Phi = 0$ for even m and $\partial_\theta \Phi = 0$ for odd m. This originates from the parity behaviour of the spheroidal harmonic associated with the considered m mode and spin weight s (see, e.g., the discussion on boundary conditions in [92]). At the inner radial boundary the fields were set to $\Phi = \Pi = 0$ in order to have no propagation of the fields close to the horizon, i.e. no outgoing radiation. At the outer radial boundary one would need a purely outflow boundary condition. In a numerical approximation boundary conditions can lead to small reflections, which gradually pollute the simulation. Without the hope of a clean outer boundary the fields were set to $\Phi = \Pi = 0$ as well. The expected unphysical reflections were made tolerable by pushing out the boundary so far that the physically relevant part of the simulation ended before the first reflections reached the extraction zone.

3.3.1 Applications and upgrades

Krivan et al.'s time-domain approach [80] from 1997 was a great advance at the time, for it allowed stable simulations at the order of $\sim 1000M$. The reported usual resolution was $N_{r^*} \times N_\theta = 8000 \times 32$ grid points, on the domain $r^* \in [-100M, 500M]$ and $\theta \in [0, \pi]$. Second order convergence was found for $t < 50M$, with a subsequent drop of the convergence to ~ 1.3. For the first time it was possible to measure power-law decay rates for $s = -2$ fields on Kerr in a numerical time-domain approach. The main limitations of the scheme were the second order accuracy inherited from the special Lax-Wendroff integration algorithm and the outer boundary problem. The latter required huge computational domains for the radiation extraction to be not too close to the BH (at a radius $r^* = 20M$). Thus,

extrapolation errors were induced when computing the relevant information at future null infinity. Furthermore, the approach was tailored for $s = -2$ gravitational perturbations. The very interesting ingoing radiation, which in general has to be computed from $s = +2$ perturbations, is not treatable in BL-coordinates. Note that, when speaking of the "BL" version of the Krivan et al. scheme, it has to be understood as including the necessary transformations to the tortoise coordinate and to the well-behaved azimuthal coordinate. As discussed above, pure BL coordinates are not suitable at all.

In the almost 20 years from the development of this scheme until now several follow-up works have adopted and enhanced it. The algorithm was initially developed for evolutions of scalar fields [90, 93], and used in this context in 2001 to crosscheck the analytically found superradiance resonance of a scalar field around a nearly-extremal Kerr BH [94, 95, 96]. A few months after the original paper [80] the Krivan et al. code was used in [97] to crosscheck a time-domain Zerilli-Equation solver. Krivan and Price [98] performed simulations in the "close-limit" of two black holes. Surprisingly, besides the above references, there are no further publications on the basis of Krivan et al.'s code. In 2000 Campanelli, Khanna et al. [99] transformed the TKEQ to ingoing Kerr-Schild coordinates, but otherwise adopted the Krivan et al. scheme into a code named "penetrating Teukolsky Code". In January 2002, Khanna used this code to evolve two-black hole initial data [100]. Later in 2002 the same code was used by Burko and Khanna [101] to investigate power-law decay rates of generic spin, including also $s = +2$, and to compare the numerical results with the analytic predictions of Hod [102, 103, 104] and Barack and Ori [105, 106, 107][1]. In 2004 the penetrating Teukolsky code was used in an analysis of scalar fields [108].

After [108] the focus of the research moved away from the penetrating Teukolsky code back towards the standard BL-coordinate scheme of Krivan et al.. The first step in this direction was done by Lopez-Aleman, Khanna and Pullin in 2003 [109]. In their study a nonspinning point-particle perturbation was added as a source term to the TKEQ. This might explain the return to BL coordinates since the source term requires the computation of orbits, and typically codes will produce orbits in BL coordinates. That implementation has been used and developed steadily ever since. To date it is probably the most advanced time-domain Teukolsky solver, besides ours, and the following review on developments is almost exclusively related to that code.

In their first study [109] the authors considered a source term with a stress-energy tensor that models a point-particle on circular, equatorial geodesics. The distributional character of the particle was represented by narrow Gaussian functions. The code was found to be second order convergent up to $500M$ and reproduced energy fluxes obtained

---

[1]A detailed review on the topic of late-time tail decay rates, including scalar field studies, can be found in [H0, H1].

from frequency-domain calculations, though with significant deviations (around 30%) at the stated typical resolution of 6400 × 60 grid-points. Later on the authors noted in [110] that Eq. (20) of [109] was unnecessary and largely responsible for the inaccuracy. In September 2003, Khanna enhanced the study of gravitational radiation from a point-particle to elliptic and inclined orbits [111]. Besides Khanna's implementation also Pazos-Avalos&Lousto [92] adopted Krivan et al.'s approach and developed a code with a modified fourth-order Lax-Wendroff algorithm in 2004. The expected convergence rate was sustained up to $\sim 1000M$. The authors were able to accurately compute quasi-normal modes' frequencies and power-law decay rates and reported a significant gain in accuracy; they did, however, not embark into modelling a point particle. It is noteworthy to mention that Pazos-Avalos&Lousto's development of a fourth order accurate scheme seems not to have been ported to the code of Khanna et al.. In 2007 Burko and Khanna [110] improved the accuracy of their code to a level of $\sim 1\%$ difference for energy fluxes of a particle in circular equatorial orbit (CEO). The improvement was assigned to the correction of two errors in the source computation and a higher grid resolution, by a factor ~ 3 in radial direction compared to [109]. Additionally, the authors investigated waveforms emitted from "zoom-whirl" orbits. In 2008 a major progress was made by the fabrication of a few-point numerical delta-function that mimics a delta-distribution in its integral properties [91]. Using resolutions of $N_{r*} \times N_\theta = 9600 \times 40$ grid points, the new delta representation allowed to reproduce energy fluxes for CEOs computed in the frequency domain with deviations $< 1\%$. In case of more generic orbits the new delta-representation was found to produce high-frequency noise [112]. By enlarging the support of the delta, raising the order of the interpolation used in the derivation, and by applying a low-pass filter it was possible to remove the noise and to reproduce frequency-domain waveforms for eccentric, inclined orbits. Furthermore, a hybrid method was devised, which consists of, (i) computing the energy fluxes for CEOs within the frequency domain [113, 114], (ii) adding the energy losses as a RR force to a geodesic solver, and (iii) feeding the obtained quasi-circular-inspiral+plunge trajectory to the time-domain code in order to produce the waveform. Building on such realistic trajectories, the authors investigated recoil velocities in the particle limit over the spin range $\hat{a} \in [-0.9, 0.9]$ [115]. In 2009 Burko and Khanna [116] revisited the homogeneous TKEQ and studied the influence of BL and ingoing-Kerr slicing on the late-time decay rates of scalar fields by reviving the penetrating Teukolsky code. Further investigations of tails of scalar fields followed in [117] within the BL code, enhanced by quadruple precision, sixth-order finite differences in angular direction and resolutions up to 64000 × 64 grid points. Also, starting from 2009 [118, 119, 120] the code was developed in the direction of high performance parallel computing on the basis of a domain decomposition strategy realised with either OPENMPI or corresponding libraries on graphics processing units. In 2011 significant

conceptual progress was achieved by remediating the outer boundary problem of Krivan et al.'s scheme through the application of the hyperboloidal layer technique [75], as developed in [121, 122, 123, 124, 125, 126]. This drastically reduced the computational costs. For example, a small resolution of only 3125×32 grid points still reduced the deviations in CEO energy fluxes to the level of $\sim 0.05\%$. Remarkably, the simulation of a long-scale $t \sim 10^6 M$ inspiral within the hyperboloidal layer code only took ~ 1 day when run on 1000 cores. The boundary problem at the horizon was resolved analogously with a layer technique in [127].

Around 2010 the effective-one-body models for spinning binaries [49, 128, 129] became sufficiently mature to stimulate the onset of comparisons against numerical data in the particle limit also for Kerr. For Schwarzschild the strategies of informing the EOB-model by computing the GWs from a particle on quasi-circular orbits that are slowly shrinking due to an EOB RR force until merger, were developed by Damour, Nagar, Bernuzzi et al. in [22, 52, 130, 131, 132, 133]. For Kerr the comparison against frequency-domain Teukolsky solvers [134, 74] was limited to slowly evolving CEOs, until in 2011 Barausse et al. [135] complemented the comparison using Khanna et al.'s time-domain code to tackle inspiral trajectories. Besides improving the EOB model in this direction, Barausse's study comprised of interesting analyses of certain characteristics of the multipolar waveforms such as the hierarchy of the dominant modes. For completeness note that this study was not yet employing the simultaneously integrated hyperboloidal layer technique. In 2012 Taracchini et al. incorporated these numerical results to a prototype EOB model [136]. In 2014 Taracchini et al. [76] performed a detailed analysis of merger waveforms in the particle limit using energy fluxes from the frequency-domain as a RR instead of the EOB one. The study focused in particular on nearly extremal configurations with $|\hat{a}| = 0.99$, and found interesting features such as the flattening of the waveform for $\hat{a} \to 1$. Apart from the EOB applications, a theoretical interest in time-domain numerical data was ignited by the study of self-force effects. From 2012 on the time-domain code was used for producing waveforms from orbits around Schwarzschild spacetime that accounted for self-force effects [137], and in the context of overspinning an extremal Kerr BH [138, 139]. In 2015 the latest work in this direction accounted for spin-orbit coupling effects in producing the orbit, though neglecting the spin of the particle in the source term of the TKEQ [140]. Finally, another recent application of Krivan et al.'s scheme was a time domain code that evolves a scalar field in the spacetime of a Kerr Anti-de-Sitter BH [141].

A new time-domain approach to the Teukolsky Equation

As described in the previous chapter, the traditional time-domain approach to the TKEQ due to Krivan et al. [80] has been developed by Khanna and collaborators to an extreme accuracy and utility. Nonetheless, there is room for further improvements. This chapter presents an alternative approach to the numerical solution of the TKEQ in the time-domain, which is based on a reformulation of the TKEQ using hyperboloidal, horizon penetrating coordinates and a suitably rotated null-tetrad. This idea has been followed, though unknowingly, as explained below, already in [H0] for the homogeneous TKEQ (see Ch. 6 and [H1]), and is extended here to the case of a point-particle source term.

A key feature of the new approach is the use of hyperboloidal, horizon-penetrating coordinates, which allow a perfect boundary treatment at both the outer and the inner radial boundary and the elimination of extrapolation errors for waves at scri. For certain important applications the new approach is advantageous over Krivan et al.'s original scheme, even after the multiple amendments of the last years; namely, our approach allows the computation of ingoing gravitational radiation from $s = +2$ simulations, and, it yields well-behaved numerics when implemented with standard numerical techniques (cf. Sec. 5.1 for details on our implementation). This is important because it opens the door for higher order algorithms and greatly simplifies possible future implementations. Notably, our simulations, apart from the most challenging cases of spin parameter values $|\hat{a}| \to 1$, do not require the numerical Kreiss-Oliger dissipation [142].

First, we explain in Sec. 4.1 how a regular form of the TKEQ in hyperboloidal, horizon-penetrating coordinates can be obtained. Two apparently different approaches are compared and shown to be equivalent. For readers interested in more details, the main ideas of the hyperboloidal compactification technique in the context of BH perturbation theory are gathered in Appendix B. In this work two such hyperboloidal coordinate systems are used; mainly, the HH-coordinates $(\tau, \rho, \theta, \varphi)$ (cf. Sec.B.2) and the RT-coordinates (T, R, θ, φ) (cf. Sec.B.3). In Sec. 4.2 we collect the relevant formulas for computing en-

ergy and angular momentum fluxes from our evolution variable ψ. Finally, in Sec. 4.3 the calculation of the TKEQ source term will be sketched, which also gives the opportunity to describe the derivation of the explicit energy-momentum tensor for a spinning particle (cf. Ch. 2).

The following discussion assumes basic knowledge of tetrad calculus and the Newman-Penrose (NP) formalism; especially of terminology like spin coefficients, NP-operators, and a null-rotation. A short reminder on these topics can be found during the discussion of the derivation of the TKEQ in App. A. In addition, basic knowledge on the hyperboloidal coordinate systems is required; most notably, that future null infinity $\mathcal{J}^+$ ("scri") is part of the domain. In the here used HH-coordinates the radial coordinate value of scri is denoted by $\rho_{\mathrm{scri}} = S$. (Not to be confused with the spin magnitude, which is also labelled by S in the relevant sections treating spinning particles.)

4.1   Regular TKEQ in hyperboloidal coordinates

For many purposes hyperboloidal, horizon penetrating coordinates are known to have the mentioned favourable properties. Therefore, we would like to apply such coordinates, more precisely, the HH-coordinates to the TKEQ. An explicit reformulation which is regular at the horizon and scri, and thus suitable for numerical simulations, shall be derived. There are two mathematically equivalent ways of obtaining a regular form, and both shall be explained here. It turns out that one of them is preferable when considering a source term that is non-vanishing at the horizon.

4.1.1   Approach 1

Transformation of coordinate basis and rescaling of field variable:
The intuitive way of obtaining a regular version of the TKEQ in HH-coordinates starts from the explicit TKEQ (3.3) as derived in BL-coordinates and in the Kinnersley null-tetrad. Then transform the coordinate basis in the usual manner $\frac{\partial}{\partial x^\mu} = \frac{\partial \tilde{x}^\nu}{\partial x^\mu} \frac{\partial}{\partial \tilde{x}^\nu}$, where $\tilde{x}^\mu$ shall label the new hyperboloidal coordinates and x^μ the BL-coordinates. The Jacobians $\frac{\partial \tilde{x}^\nu}{\partial x^\mu}$ can be read off from the explicit transformations (B.1) specified to (B.6). Inserting these into (3.3) brings us half way to the desired reformulation. The second half consists of finding a cure for the fact that some coefficients of the resulting equation are singular at the horizon and others at future null infinity. Fortunately, these singularities can be directly attributed to the behaviour of the considered field variables in the asymptotic regions $r \to \infty$ and $r \to r_+$. Moreover, the behaviour of the field can be classified by the spin weight s. Already in the original work of Teukolsky [18] (specifically after Eq. (5.3)

and in Eq. (5.6)) we find the asymptotic behaviour of the master variable

$$\Psi \xrightarrow[r \to r_+]{} \Delta^{-s} \quad , \quad \Psi \xrightarrow[r \to \infty]{} r^{-(2s+1)} \qquad . \tag{4.1}$$

Note that this is consistent with the fact that Ψ_4 falls off as r^{-1} since the master variable for $s = -2$ is $\Psi = (r - i\,a\cos\theta)^4\,\Psi_4$. In order to get rid off the unwanted behaviour of Ψ, one can simply consider a rescaled field variable. Note that this is only necessary because the horizon and scri are part of the domain, whereas in the standard BL-approach these delicate points are not included. Noting that asymptotically $\Delta \sim r^2$ leads to the combined rescaling

$$\Psi = \Delta^{-s}r^{-1}\psi\,, \tag{4.2}$$

with the new master variable ψ. Indeed, this yields the desired regularity of the coefficients in the entire domain $\rho \in [\rho_+, S]$. After the reduction to 2+1 form by Fourier-decomposition of ψ in azimuthal direction (3.9), the equation schematically takes the form

$$C_{\tau\tau}\partial_{\tau\tau}\psi + C_{\tau\rho}\partial_{\tau\rho}\psi + C_{\rho\rho}\partial_{\rho\rho}\psi + C_{\theta\theta}\partial_{\theta\theta}\psi + C_{\tau}\partial_{\tau}\psi + C_{\theta}\partial_{\theta}\psi + C_{\rho}\partial_{\rho}\psi + C_0\psi = S_s\,, \tag{4.3}$$

where ψ now abbreviates the Fourier-mode contribution ψ_m and S_s represents the spin-weight dependent source term. The coefficients in HH-coordinates are given in explicit form in Appendix C.

While this approach is perfectly working in the case of the homogeneous TKEQ, one encounters problems once $S_s(\rho_+) \neq 0$. To understand the issue, note that the coefficients of Eq. (4.3) obtained following the above steps contain an overall factor, which, depending on s, vanishes or explodes at the horizon. The reason for the appearance of this factor is the rescaling with Δ^{-s}, where the trouble is $\Delta(\rho_+) = 0$. On a more abstract level, the reason is the use of the Kinnersley tetrad, which is singular at ρ_+. To relieve the equation of this factor, we multiplied $(\Delta^s\,r(\rho)\,S^2)$ to the whole equation, which results in the coefficients stated in App. C. As a consequence, in the inhomogeneous case that factor is absorbed by the source term. For example, looking at the $s = -2$ case, the multiplication will introduce an overall Δ^{-2} to the source S_{-2}. Thus, the source is corrupted at the horizon unless one can find a corresponding Δ^2 in the many pieces that form S_{-2}. In practice, this is cumbersome and we were not able to find all potentially hidden factors of Δ^2 to cancel out the singular factor. Note that the same argumentation holds for the analogous transformations to RT-coordinates (cf. [H1]), in which case the overall factor $\left(\frac{\Delta^s\,r(R)}{R}\right)$ was multiplied to the equation. In conclusion, this makes the above procedure unwieldy for a point-particle perturbation which reaches the horizon.

4.1.2 Approach 2

Rotation of null-tetrad and rederivation of the TKEQ:

A slightly different approach goes back to the decoupled equations for Ψ_0 and Ψ_4 (and the analogous scalars for the other cases), i.e. to the state before these equations were specified to the Kerr background, a tetrad and a coordinate system. For clarity let us follow this approach on the example of the $s = -2$ equation (A.18) with the source term (A.19). The idea is to replace the Kinnersley-tetrad by a tetrad that is well-behaved on the horizon as motivated by Teukolsky in examinations of horizon fluxes [83]. The reasoning is that if the tetrad legs are regular, the corresponding NP-operators will be so, and after some algebra we are bound to obtain a TKEQ that is regular by construction also in the source term.

The Kinnersley null-tetrad (3.2) can be rotated according to a null rotation of class three (cf. Eq. (A.10)) to become, once rewritten with respect to horizon-penetrating coordinates, regular at the horizon. The choice $\Lambda = \frac{\Delta}{2(r^2 + a^2)}$ and $\Theta = 0$ corresponds to the "Hawking-Hartle"-tetrad [143] and was adopted by Teukolsky. We basically follow this procedure with the restriction to its essential part, i.e. we rotate by $\Lambda = \Delta$ following Campanelli et al. [99][1]. The resulting tetrad, written with respect to the iK-coordinate basis, has the same $\vec{m}$-leg as the Kinnersley tetrad in BL coordinates. The components of $\vec{l}, \vec{n}$ read

$$\vec{l} = (\Delta + 4Mr, \Delta, 0, 2a), \quad \vec{n} = \frac{(1, -1, 0, 0)}{2\Sigma}, \tag{4.4}$$

which are manifestly well-behaved at the horizon, $\Delta = 0$. Subsequently, the tetrad is transformed to the HH-coordinate basis and written in terms of the new radial coordinate ρ. The explicit expressions of these legs are a bit lengthy and not quoted here since they are irrelevant for the argument. Before computing the spin coefficients needed for the NP-operators (A.13), one should recall that they are tetrad scalars. This means they are independent of the coordinate system but dependent on the tetrad. Therefore, we can compute the NP-operators of the rotated tetrad written in simple coordinates; for instance, just take the iK-coordinate expressions (4.4), and in the end switch the coordinates by letting $r \to r(\rho)$. In order to convince oneself of the correctness of the above procedure, one may want to cross-check some expressions and repeat the computation of the spin-coefficients starting directly from the legs in the HH-coordinate basis. In doing this it is advisable to avoid the lengthy covariant derivatives appearing in the definition equation (A.4) by rather consulting Ch. 1 of Chandrasekhar's book [144]. Eq. (265) therein provides an equivalent but more convenient definition of the spin-coefficients in terms of

---

[1]Note that in rederiving the TKEQ we found slight disagreements with Eq. (31) of [99]. More precisely, there seem to be typos in the imaginary part of the non-derivative coefficient and in the ∂_τ^2 coefficient.

the λ-symbols $\lambda_{abc} = e_{(b)i,j} \left[e_{(a)}{}^i e_{(c)}{}^j - e_{(a)}{}^j e_{(c)}{}^i \right]$, where the round brackets denote that these indices run over the different tetrad legs rather than their components. Following Eq. (268) in [144], the λ symbols yield the spin-coefficients via $\gamma_{abc} = \frac{1}{2} \left[\lambda_{abc} + \lambda_{cab} - \lambda_{bca} \right]$.

After some algebra, the insertion of the tetrad-legs written in the HH-coordinate basis and of the associated NP-operators into the decoupled equation Eq. (A.18) gives an explicit equation, which is obviously different from the explicit result of approach 1, Eq. (4.3). Evidently, the disparity is due to the different field variables considered. Recall that in approach 1 the additional rescaling used by Teukolsky, in order to obtain from Eq. (A.18) a separable equation when specified to Kerr, reads $\Psi = \rho^{-4} \Psi_4$. To check if approach 2 can give the same result, we name our master variable ψ and rescale accordingly $\Psi_4 = \rho^4 \psi$. This yields, indeed, a form of the equation which is, at first sight, quite similar (many coefficients agree) to the explicit TKEQ in HH-coordinates, Eq. (4.3). Recapitulating the procedures, this similarity may sound odd because in approach 1 we had additionally rescaled the field variable with factors of Δ, which are apparently missing in approach 2. The puzzling similarity will be explained in a moment. First, let us mention that even the small remaining differences with respect to Eq. (4.3) can be removed. The main difference is that, in approach 2, some coefficients are still singular at scri. This makes sense because in rotating the tetrad we were only concerned with the horizon. Addressing scri, the remaining singularities disappear by virtue of the rescaling $\psi_{\text{old}} = r^{-1} \psi_{\text{new}}$. In fact, once one multiplies the equation with the overall factor $r S^2$, or with $\frac{r(R)}{R}$ in case of RT-coordinates, approach 2 results in exactly the same equation (4.3) which was obtained in approach 1, i.e. with exactly the same coefficients given in Appendix C.

While this may come as a surprise, one can actually comprehend the equivalence of the two approaches. Recall the consequences of null rotations of class three on the considered field variable (cf. Eq. (A.11)). A null rotation of the tetrad with $\Lambda = \Delta$ implies for a spin-weight s field that $\psi_{\text{new}} = \Delta^s \psi_{\text{old}}$, i.e. , e.g., for $s = -2$ we have $\psi_{\text{new}} = \Delta^{-2} \psi_{\text{old}}$. A rescaling of the field and a tetrad rotation are thus equivalent. This means that the considered field variable ψ_{new} is exactly the same in both approaches. Consequently, the equations have to coincide. Actually, the rescaling of the field with r^{-1} in approach 2 could have been as well wrapped in a second null rotation. The simpler rescaling just works as fine because the inherited overall factor in the source term is well-behaved, except for scri. (We do not care about the regularity of the source at scri, for there is anyway no chance to consider sources which are non-vanishing at scri.)

Even though the resulting homogeneous parts of the equations are the same in both approaches, the source term is artificially different. It is explicitly regular at the horizon only in the second approach. In the first approach the source term S_s must be implicitly regular

as well, but the explicit cancellation of the $\frac{1}{\Delta^2}$ factor with hidden Δ^2 factors is practically impossible. Since the computation of S_s (sketched below) involves lengthy algebra it is invaluable to have the complete expression regular at the horizon by construction, i.e. given of course a regular behaviour of $T_{\mu\nu}$. In our case this is needed to track the particle until it reaches the horizon. This is, by the way, an interesting difference compared to Krivan et al.'s time-domain approach to the TKEQ in BL-coordinates (Sec. 3.3). As mentioned several times in the literature (e.g., in the last part of Sec. III A of [135]), the TKEQ source term for a point-particle which approaches the horizon in BL-coordinates is smoothly "red-shifted". That is to say it vanishes due to the factor $\frac{dt}{d\lambda} \xrightarrow[r \to r_+]{} \infty$, with λ the proper time, in the denominator of $T_{\mu\nu}$. On the contrary, using horizon penetrating coordinates like the HH-coordinates, $\frac{d\tau}{d\lambda}$ remains finite, and we observe nothing special at the horizon crossing.

4.1.3   Related quantities

For many practical purposes our evolution variable ψ has to be converted to related quantities. Here, we describe the relevant relations for $s = \pm 2$. Note that in our 2+1-approach we actually solve for the m-mode of ψ, and the following relations are employed in terms of the m-modes of the respective quantities.

To compare with other perturbation approaches, it is useful to compute the metric perturbations $h_{\mu\nu}$ in the transverse-traceless gauge. In fact, we just have to integrate the relation $h = 2 \int \int \psi_4 dt' dt''$ to obtain the strain $h = h_+ - i h_\times$ (cf. Eq. (A.9)), but note that this only holds asymptotically. For a better physical intuition it is useful to decompose the perturbation with respect to the spin-weighted spherical harmonic basis functions, $Y_{s\ell m}(\theta, \phi)$ (see, e.g., Sec.3.3 in [145]). We will call the coefficients $h_{\ell m}$ of the following expansion

$$r\, h(t, \theta, \phi) = \sum_{\ell=2}^{\infty} \sum_{m=-\ell}^{\ell}\; r\, h_{\ell m}(t)\, Y_{-2\ell m}(\theta, \phi) \quad , \tag{4.5}$$

the "multipoles" or "modes" of h. Multipoles of related quantities like Ψ_4 are defined analogously. To compute these modes we evaluate the inner products of h and $Y_{s\ell m}$, i.e. we integrate over θ and ϕ. Since we are working in an azimuthal mode-decomposed approach, a single simulation will only yield the (distance scaled) Fourier-m-mode contribution rh_m, which is defined like $rh(t, \theta, \phi) = \sum\limits_{m=-\infty}^{\infty} rh_m(t, \theta)e^{im\phi}$. In practice we therefore only project $r\, h_m(t, \theta)$ in the θ-direction, i.e. against $\tilde{Y}_{-2\ell m}(\theta)$, with $Y_{-2\ell m}(\theta, \phi) = \tilde{Y}_{-2\ell m}(\theta)e^{im\phi}$. The multipoles $h_{\ell m}$ can as well be connected to the "+"/"$\times$" polarisations via $r\, h_{\ell m} = rh_{+,\ell m} -$

$i\,r\,h_{\times,\ell m}$. Let us also introduce another common normalisation convention,

$$r\,h(t,\theta,\phi) = r \sum_{\ell=2}^{\infty} \sum_{m=-\ell}^{\ell} \sqrt{\frac{(\ell+2)!}{(\ell-2)!}}\,\Psi_{\ell m}(t)\,Y_{-2\ell m}(\theta,\phi)\,, \qquad (4.6)$$

where, in a slight abuse of the symbol Ψ, the complex quantities $\Psi_{\ell m} = \Psi_{\ell m}^{(e)} + i\Psi_{\ell m}^{(o)}$ refer to the RWZ variables [146]. The explicit relations read $\mathcal{R}(h_{\ell m}) = h_{+,\ell m} = \sqrt{\frac{(\ell+2)!}{(\ell-2)!}}\Psi_{\ell m}^{(e)}$ and $\mathcal{I}(h_{\ell m}) = -h_{\times,\ell m} = \sqrt{\frac{(\ell+2)!}{(\ell-2)!}}\Psi_{\ell m}^{(o)}$. In fact, in [146] the $\Psi_{\ell m}$ were defined with respect to a slightly different convention of the $Y_{s\ell m}$, i.e. our $\Psi_{\ell m}$ are not exactly those of [146]. For completeness, let us mention how the exact quantity of [146] can be retrieved from ours, $\Psi_{\ell m, \text{orig}} = i^{-\text{mod}(\ell+m,2)}\,(-1)^m\Psi_{\ell m}$. In many plots we will use the RWZ-normalised version of $h_{\ell m}$, motivated from the ease of applying RWZ-equation-related formalisms and comparing waveforms.

For clarity, let us recall the now multiple appearances of the symbol Ψ. Teukolsky used Ψ as his master variable, which represents, depending on the actually considered spin-weight s perturbation, different quantities; e.g., for $s = 2$ simply $\Psi = \Psi_0$. In our approach described above we consider a further rescaled version of Ψ, and call the new master variable, i.e. our evolution variable, ψ. In the $s = -2$ case Ψ is asymptotically nothing else but $r\Psi_4$, the radius scaled fourth Weyl scalar in the Kinnersley tetrad. After two time integrations one obtains the strain $r\,h$. The RWZ-convention works in a RWZ-normalised form of $h_{\ell m}$, introduced in Eq. (4.6). Whenever we will speak of $\Psi_{\ell m}$, this will refer to the modes of the RWZ-normalised strain (not to modes of Teukolsky's master variable Ψ).

Knowing the relation between $h \leftrightarrow \Psi_4$, it remains to relate our evolution variable ψ to Ψ_4. Therefore, one has to relate ψ to Teukolsky's master variable Ψ, which reads $\Psi = \Delta^{-s}r^{-1}\psi$, and, then, to look up Table 1 of [18]. For $s = -2$ we concretely have $\psi = \Delta^{-2}r\rho^{-4}\Psi_4$ with ρ being a NP-operator and Ψ_4 referring to the Kinnersley tetrad as usual. Asymptotically $\Delta^{-2} \sim r^{-4}$ and $\rho^{-4} \sim r^4$, so extraction at scri means $\psi = r\Psi_4$. At scri, we thus just have to integrate the relation $r\ddot{h} = 2\psi$ to obtain the strain $r\,h(u,\theta)$ (cf. Eq. (A.9)).

For $s = +2$ our evolution variable is $\psi = r\Psi_{0,\text{Campa}}$, where the subscript stresses the usage of the Campanelli et al. [99] tetrad (see Eq. (4.4)). The time-domain flux formulas below will be given instead in terms of $\Psi_{0,\text{Hawk}}$. The "Hawking-Hartle" tetrad (see Eq.'s (4.14) in [83]) is trivially related to the Campanelli one. First, we have $\Psi_{0,\text{Hawk}} = \frac{\Delta^2}{4\,(r^2+a^2)^2}\,\Psi_0$ where Ψ_0 refers to the Kinnersley tetrad (cf. Eq. (4.43) in [83]). Note that Ψ_0 cannot be evaluated at the horizon while $\Psi_{0,\text{Hawk}}$ can be, once the tetrad is written in horizon penetrating coordinates; e.g., the Kerr-ingoing coordinates of Eq.'s (2.1) in [83] or the slightly different Kerr-ingoing coordinates of Eq.'s (B.2) (remember both coordinates give the same $\Psi_{0,\text{Hawk}}$

as it is a tetrad scalar). In the Campanelli tetrad we have $\Psi_{0,\text{Campa}} = \Delta^2 \Psi_0$. Hence, our $s = +2$ evolution variable connects to the relevant Hawking-Hartle tetrad scalar like $\psi = r \Psi_{0,\text{Campa}} = r \Delta^2 \Psi_0 = r \, 4 \, (r^2 + a^2)^2 \, \Psi_{0,\text{Hawk}}$. Specifically at the horizon, we have $\psi/(4r_+(r_+^2 + a^2)^2) = \Psi_{0,\text{Hawk}}$; note the factor r_+ that we have to divide by due to our rescaling for regularity at scri.

4.2 Flux computations

GWs carry away energy and angular momentum from the emitting system, say a compact binary. In general, this drives the motion from eccentric orbits towards quasi-circular motion [147, 148] and finally to merger. In the point-particle limit the focus of flux computations is usually on circular orbits because the corresponding fluxes can be used in some form, e.g., incorporated to analytic models or simply using the numerically found values, as a RR force on the basis of an energy balance argument. For example, one can enrich the equations of motion of a test-particle by the found radiative energy losses to obtain more realistic orbits with quasi-circular spiral, plunge and merger. Eventually, one can measure the fluxes for these realistic orbits, and assess the performance of the constructed radiation reaction by comparing with the produced fluxes.

4.2.1 Frequency domain formulas

Let us start with the most simple and yet relevant case of circular equatorial orbits. These orbits are special in the sense that they can be characterised by a single frequency Ω_ϕ of motion. Thus, we can employ in our time-domain approach formulas usually associated with the frequency-domain.

The possibility is appealing because, (i) it allows us to crosscheck the time-domain formulas, especially in the case of Poisson's untested time-domain method for computing horizon-fluxes [149] (see Sec.'s 4.2.2&5.2.2), (ii) the formulas can be written in terms of our field variable ψ, whereas the time-domain formulas below require to compute related quantities ($h \sim \int \int \psi d\tau$ at scri or $\Psi_{0,\text{Hawk}}(\tau)$ from $\tau = -\infty$ to $\tau = +\infty$ at the horizon), and (iii) one is able to compute horizon and infinity fluxes in a single $s = +2$ or $s = -2$ simulation exploiting a frequency-domain relation between Ψ_4 and Ψ_0.

The machinery for computing fluxes from the TKEQ in the frequency-domain was set up already in the 1974 Teukolsky paper [83]. With slight modifications, due to the differences between the master variables ψ and Ψ, we can use Eq.'s (4.12a) and (4.44) of [83]. For a given $Y_{s\ell m}$ contribution of our master variable ψ within the $s = -2$ version of the TKEQ, $\psi_{\ell m}$, the energy flux to infinity can be computed according to the first part of Eq. (4.12a)

of [83]

$$\frac{dE_{\ell m}^{\infty}}{dt} = \frac{1}{4\,\pi\,\omega^2}|\psi_{\ell m}|^2 \qquad , \qquad (4.7)$$

where $\omega = \Omega_\phi\, m$. Analogously, our full 2+1-variable ψ_m can be used to compute the full flux (including all l-modes) by

$$\frac{dE_m^{\infty}}{dt} = \int_0^{\pi} \frac{1}{2\,\omega^2}|\psi_m|^2 \sin\theta\, d\theta \qquad . \qquad (4.8)$$

The flux at the horizon is computed from the zeroth Weyl scalar in the "Hawking-Hartle" tetrad $\Psi_{0,\mathrm{Hawk}}$ (see Sec. 4.1.2). From a $s = +2$ TKEQ-simulation we obtain $\psi = r\Psi_{0,\mathrm{Campa}}$, where the subscript emphasises the use of the tetrad of Campanelli et al. [99]. This is related to the desired $\Psi_{0,\mathrm{Hawk}}$ by a trivial factor (see Sec. 4.1.3 for details). Accounting for an additional factor r, which is introduced by our rescaling for regularity at $\mathcal{J}^+$, we can use the first part of Eq. (4.44) in [83] for computing the ℓm-flux and the full-m fluxes[2]

$$\frac{dE_{\ell m}^H}{dt} = \frac{1}{2\,\pi}\, \frac{\omega}{32\,k\,(k^2 + 4\,\epsilon^2)\,(2\,M\,r_+)^3}\, \frac{|\psi_{\ell m}|^2}{r_+^2} \,, \qquad (4.9)$$

$$\frac{dE_m^H}{dt} = \frac{\omega}{32\,k\,(k^2 + 4\,\epsilon^2)\,(2\,M\,r_+)^3} \int_0^{\pi} \frac{|\psi_m|^2}{r_+^2} \sin\theta\, d\theta \qquad , \qquad (4.10)$$

where $k = \omega - \frac{m\,a}{2\,M\,r_+}$ (see after Eq. (2.11) in [83]) and $\epsilon = \sqrt{M^2 - a^2}/(4\,M\,r_+)$ (see Eq. (4.30) in [83]). Note that the above formulas also yield the angular momentum fluxes via the relation

$$\frac{dJ}{dt} = \frac{m}{\omega}\, \frac{dE}{dt} \qquad , \qquad (4.11)$$

cf. Eq. (4.13) in [83], which is why one often sees circular orbits fluxes being discussed in terms of either the energy or the angular momentum fluxes.

"Miraculous identities"

The title of this subsection is taken from the corresponding subsection in [82] because it seems to be the most adequate description for the following fact: "the decoupled components [Ψ_4 and Ψ_0] contain complete information about all nontrivial features of the full perturbed field" [18]. In other words, having solved the master equation for Ψ_4 allows to compute Ψ_0 without re-solving the master equation a second time, and vice versa. The reason is that the Einstein Equations imply certain relations $\Psi_4 \leftrightarrow \Psi_0$, which Chandrasekhar [144] called "Starobinsky-Teukolsky" identities [150] (see [82, 64, 83] for more details). These relations are more than unexpected, for one is used to think of Ψ_4 and

---

[2]These formulas are validated by our numerical tests. For completeness, note that in the step from (4.37) to (4.44) in [83] we could not follow the apparent cancellation of the factor $4(r^2 + a^2)^2$, which seems to appear last in (4.43).

Ψ_0 as outgoing and ingoing radiation respectively. The explicit relations are not quoted here because we do not employ them directly, but they can be found in Sec. III of [83]. Below we will only state the relevant implications for the energy fluxes.

Unfortunately, the conversion $\Psi_4 \leftrightarrow \Psi_0$ relies on the assumption of a discrete frequency solution, $\Psi_{4/0} = |\Psi_{4/0}|e^{i\omega\tau}$, so for us it is only useful in very restricted cases; namely, when the solution, as a matter of fact, consists of a single frequency, like for a point-particle on circular equatorial orbits. Moreover, the identities hold only for multipolar decompositions with respect to the eigenfunctions of the angular operator of the TKEQ, i.e. we have to work with the spin-weighted spheroidal harmonics $S_{s\ell m}^{a\omega}$ projection-modes of the solution. In addition, we need their eigenvalues. When $a = 0.0$ we can use the spin-weighted spherical harmonics with $\mathcal{E}_{s\ell m}(a\omega = 0) = \ell(\ell+1)$. For the algorithm used to compute the $S_{s\ell m}^{a\omega}$ consult Appendix F.

Teukolsky translated the relations $\Psi_4 \leftrightarrow \Psi_0$ into formulas for the energy fluxes of the corresponding $S_{s\ell m}$-modes (cf. also [60]). For $s = -2$ our field variable ψ corresponds to $\sim \Psi_4$ modulo some factors (emphatically not to $\sim \Psi_0$), but still we can use it at the horizon to compute

$$\frac{dE_{\ell m}^H}{dt} = \frac{\alpha_{s\ell m}}{4\pi\omega^2} \frac{|\psi_{\ell m}|^2}{r_+^2} \quad , \tag{4.12}$$

where, mentioned again for clarity, $\psi_{\ell m}$ refers to a projection against $S_{s\ell m}^{a\omega}$. The conversion coefficient $\alpha_{s\ell m}$ is given by Eq. (4.17) in [60],

$$\alpha_{s\ell m} = \frac{256\,(2Mr_+)^5\,k\,(k^2 + 4\epsilon^2)\,(k^2 + 16\epsilon^2)\,\omega^3}{|C_{s\ell m}|^2} \quad , \tag{4.13}$$

with k and ϵ as defined below Eq. (4.10), and with the Starobinsky constant[3]

$$|C_{s\ell m}|^2 = (Q^2 + 4a\omega\,m - 4a^2\omega^2)\left[(Q-2)^2 + 36a\omega\,m - 36a^2\omega^2\right] \tag{4.14}$$

$$+ (2Q-1)(96a^2\omega^2 - 48a\omega m) + 144\,\omega^2(M - a^2) \quad , \tag{4.15}$$

where $Q = \mathcal{E}_{s\ell m} - 2a\omega\,m + (a\omega)^2$, cf. Eq.'s (3.23)-(3.24) in [83]. Analogously, one can compute the multipolar infinity flux from a $s = +2$ simulation, where the field variable ψ is some form of $\sim \Psi_0$, using

$$\frac{dE_{\ell m}^\infty}{dt} = \frac{16\,\omega^6}{4\pi\,|C_{s\ell m}|^2}\,|\psi_{\ell m}|^2 \quad , \tag{4.16}$$

cf. Eq. (4.12a) in [83]. We have tested these relations for a point particle on circular

---

[3]Do not get confused when comparing this with Eq. (4.18) of [60], which employs the symbol $\lambda = Q - s(s+1)$ for the special case $s = -2$. Instead, Eq. (4.14) here holds for both $s = -2$ and $s = +2$.

orbits and found excellent agreement with the standard computations, but since we were also interested in the full-ℓ summed fluxes (not accessible by these conversions) we had to perform both $s = \pm 2$ simulations anyway. Thus, in practice, we could rarely exploit the relations except for cross-checks.

4.2.2 Time domain formulas

To compute the fluxes for arbitrary trajectories, which emit GWs over continuous frequency bands, we need time-domain formulas. These formulas are usually written in terms of the gravitational strain h and the Weyl scalar $\Psi_{0,\mathrm{Hawk}}$ (cmp. Sec. 3.3 of [H2]). Notably, $\Psi_{0,\mathrm{Hawk}}$ cannot be computed in a BL-approach at the horizon, and therefore the Poisson horizon-flux formalism is not applicable in BL-coordinates. On the contrary, our new time-domain approach enabled us to employ the formalism and to check its validity for the first time.

Let us first consider outgoing GWs at scri. Following [91] the energy flux is given by

$$\dot{E} = \frac{1}{16\pi} \int_{S_2} d\Omega \; |r\,\dot{h}|^2 = \frac{1}{16\pi} \sum_m \int_{-1}^{1} d\xi \; |r\,\dot{h}_m|^2 \; , \qquad (4.17)$$

where in the last expression we have used $\xi = \cos\theta$ and introduced the mode-decomposition of h to express the flux in terms of the 2+1 fields. The angular momentum $\vec{J} = (J_x, J_y, J_z)$ flux is given by

$$\dot{J}_i = -\frac{1}{16\pi} \Re \left\{ \int_{S_2} d\Omega \; (r\,\dot{h})^* \mathcal{J}_i (r\,h) \right\} \; , \qquad (4.18)$$

where $\mathcal{J}_i$ are the spin 2 quantum mechanical operators, in particular $\mathcal{J}_z = \partial_\phi$. For equatorial orbits $J_x = J_y = 0$, so the relevant quantity is

$$\dot{J}_z = \frac{1}{16\pi} \Im \left\{ \sum_m m \int_{-1}^{1} d\xi \; (r\,\dot{h}_m)^* (r\,h_m) \right\} \; . \qquad (4.19)$$

Similarly, the linear momentum $\vec{P} = (P_x, P_y, P_z)$ flux can be computed from

$$\dot{P}_i = \frac{1}{16\pi} \int_{S_2} d\Omega \; n_i |r\,\dot{h}|^2 \; , \qquad (4.20)$$

where $n_i = (\sin\theta\cos\phi, \sin\theta\sin\phi, \cos\theta)$. For equatorial orbits $P_z = 0$.

Coming to the horizon-absorbed energy and angular momentum fluxes, one starts from the first law of BH mechanics [143, 151]. This relates the horizon area A_{H} to the fluxes of mass/energy M_{H} and angular momentum J_{H}; more precisely, $\frac{\kappa}{8\pi}\dot{A}_{\mathrm{H}} = \dot{M}_{\mathrm{H}} - \Omega_{\mathrm{H}}\dot{J}_{\mathrm{H}}$, where $\kappa = (r_+ - M)/(r_+^2 - a^2)$ is the surface gravity and $\Omega_{\mathrm{H}} = a/(2Mr_+)$ is the angular velocity of the horizon. Following [83, 152, 149], the variation of the horizon mass and angular

momentum can be expressed as

$$\dot{M}_{\mathrm{H}} = \frac{1}{16\pi} \int dS \; \sigma^{AB} \mathcal{L}_t \gamma_{AB} \;\;, \;\; \dot{J}_{\mathrm{H}} = \frac{1}{16\pi} \int dS \; \sigma^{AB} \mathcal{L}_\phi \gamma_{AB} \;, \tag{4.21}$$

where dS is the horizon area element of the induced 2-metric γ^{AB}, σ^{AB} is the "shear tensor" (see Eq. (3.4) in [149]), and $\mathcal{L}_{t,\phi}$ are Lie derivatives with respect to the Killing vectors of the background. Poisson [149] gives the final flux equations for the 2+1 fields

$$\dot{M}_{\mathrm{H}} = \frac{r_+^2 + a^2}{4\kappa} \sum_m \left[2\kappa \int_{-1}^1 d\xi \; |f_{\mathrm{H}m}^+|^2 - \mathrm{i}m\Omega_{\mathrm{H}} \int_{-1}^1 d\xi \; \left(f_{\mathrm{H}m}^{+\,*} f_{\mathrm{H}m}^- - f_{\mathrm{H}m}^+ f_{\mathrm{H}m}^{-\,*} \right) \right] \;, \tag{4.22}$$

$$\dot{J}_{\mathrm{H}} = -\frac{r_+^2 + a^2}{4\kappa} \sum_m \mathrm{i}m \left[\int_{-1}^1 d\xi \; \left(f_{\mathrm{H}m}^{+\,*} f_{\mathrm{H}m}^- - f_{\mathrm{H}m}^+ f_{\mathrm{H}m}^{-\,*} \right) \right] \;. \tag{4.23}$$

The complex quantities $f_{\mathrm{H}m}^{\pm}$ are defined as integrals of the m-mode components of the Weyl scalar $\Psi_{0,\mathrm{Hawk}}$ at the horizon

$$f_{\mathrm{H}m}^+(v,\theta) = -e^{\kappa v} \int_v^\infty dv' e^{-(\kappa - \mathrm{i}m\Omega_{\mathrm{H}})v'} \Psi_{0,\mathrm{Hawk,\ m}}(v', r_+, \theta) \tag{4.24}$$

$$f_{\mathrm{H}m}^-(v,\theta) = -\int_{-\infty}^v dv' e^{\mathrm{i}m\Omega_{\mathrm{H}}v'} \Psi_{0,\mathrm{Hawk,\ m}}(v', r_+, \theta) \;, \tag{4.25}$$

where $v = t + \int dr \Delta^{-1}(r^2 + a^2)$ is the advanced time coordinate, see Eq. (B.8). Let us stress again that the needed $\Psi_{0,\mathrm{Hawk,\ m}}$ cannot be computed at the horizon in the traditional BL-approach to the TKEQ. Note also that $f_{\mathrm{H}m}^+(v)$ depends on the future behaviour $v' > v$ of the field, and can thus only be computed in post-processing. For this reason and in connection with the failure of computing the waveform at the particle's position, the formalism is not yet optimal for 2+1 simulations. We will come back to this issue when discussing the numerical experiments on horizon-fluxes for plunging orbits in Sec. 7.2.

4.3 Source term for a spinning particle

The derived reformulation of the homogeneous TKEQ in HH-coordinates, Eq. (4.3), is already useful for any kind of vacuum investigations like stability analyses of Kerr or measurements of quasi-normal modes and decay rates. To address matter perturbations, however, one needs to add the source term S_s, which is built from the energy momentum tensor appropriate for the considered scenario. For instance, the BH binary problem in the point-particle approximation requires to compute a $T_{\mu\nu}$ which corresponds to a "spinning particle" in orbit about Kerr. The aim of the following section is to provide such a $T_{\mu\nu}$, and to sketch the computation of S_s. We are interested in gravitational perturbations, and therefore the source term is implemented and discussed only for the $|s| = 2$ version of Eq. (4.3). For further details the interested reader might also want to have a look at the continuative comments in Appendix G.

4.3.1   Computing the source term from pieces

The source terms for the gravitational equations read

$$S_{-2} = 8\pi\Sigma \left(r - \mathrm{i}a\cos\theta\right)^4 T_4 \, , \qquad (4.26)$$

$$S_{+2} = 8\pi\Sigma\, T_0 \, , \qquad (4.27)$$

where T_4 and T_0 are the tetrad scalars defined in Eq.'s (A.19) and (A.17) respectively. The explicit form of these sources follows from straightforward algebra, but is too lengthy to be stated here. We will only outline a strategy of wrapping up different parts into smaller units, which can be handled more conveniently. We focus on T_4 but the discussion holds analogously for T_0.

The scalar T_4 is defined in terms of NP-operators like $\underline{\Delta}$ or δ^*, cf. Eq. (A.19) for the exact definition. Expanding the expressions by performing the multiplications of the NP-operators, one will obtain several products. Separate those, that contain derivative operators, i.e. $\underline{\Delta}^2, \delta^{*2}, \underline{\Delta}\delta^*, \gamma\delta^*, \mu\delta^*, \ldots$, from the non-derivative ones. Denoting with C non-derivative terms and with D derivative ones, we schematically get

$$T_4 = D_{nm^*}T_{nm^*} - D_{m^*m^*}T_{m^*m^*} - D_{nn}T_{nn} + C_{nm^*}T_{nm^*} - C_{m^*m^*}T_{m^*m^*} - C_{nn}T_{nn}, \quad (4.28)$$

where, e.g., $D_{nm^*}T_{nm^*}$ contains all pieces with derivatives of T_{nm^*}. Note that these terms are complex-valued. The explicit expressions in terms of $T_{nm^*}, \partial_\tau T_{nm^*}, \partial_\tau^2 T_{nm^*}, \partial_\rho T_{nm^*}, \ldots$ can be found with computer algebra. We made the overall choice to compute the stress energy-tensor (and its derivatives) in contravariant form $T^{\mu\nu}$, and the tetrad legs (and their derivatives) in covariant form n_μ, m_μ^*, l_μ ; for instance, $\partial_\rho T_{nn} = 2T^{\mu\nu}n_\mu\partial_\rho n_\nu + n_\mu n_\nu \partial_\rho T^{\mu\nu}$. Up to this point the calculation holds for arbitrary sources, and in a simulation the coefficients D_{xx}, C_{xx} can be computed once and for all in the initialisation. The information on what kind of perturbation is considered will be fixed by the determination of the energy-momentum tensor $T^{\mu\nu}$.

Besides from $T^{\mu\nu}$, the source term is built from the derivatives $\partial T^{\mu\nu}$ and $\partial\partial T^{\mu\nu}$, where ∂ can refer to any of our coordinates. In principle, the calculation of $T^{\mu\nu}, \partial T^{\mu\nu}, \partial\partial T^{\mu\nu}$ can be done in a pre-processing step for all relevant points $(\tau, \rho, \theta, \varphi)$, or (τ, ρ, θ) in a 2+1-approach, and, afterwards, be read into the simulation. In practice, this requires to know *a priori* the time steps τ_n and the grid setup $(\rho_i, \theta_j, \varphi_k)$ of the simulation, or, alternatively, a very dense, computationally expensive data set, which can be used for interpolation to the needed points. In our case of a point-particle perturbation we can find a better solution. The corresponding model for $T^{\mu\nu}$, which will be introduced in the following subsection, is of distributional form. Thus, $T^{\mu\nu}$ has a trivial spatial dependence. It is nonzero only

along the worldline of the particle. In this special case, we can assemble $T^{\mu\nu}(\tau_k, \rho_i, \theta_j, \varphi_k)$ for each evolution step τ_k at runtime from only a few characteristic quantities given along the worldline; namely, the particle's position, four velocity, linear momentum and spin tensor. We therefore call these quantities "the dynamics". The spatial dependence of $T^{\mu\nu}$ is solely determined by the numerical approximation of the distribution. Consequently, it is possible to not precompute $T^{\mu\nu}(\tau, \rho, \theta, \varphi)$ and its derivatives on dense 4D-grids, but only the dynamics for a dense set of coordinate time steps. The dynamics are, then, read into the code at the initialisation. At runtime and evolution step τ_k, the numerical energy-momentum distribution is computed by interpolating the dynamics to τ_k, and, finally, by "smearing" it over a few grid points according to the spatial profile of the numerical approximation of the distribution.

4.3.2 Explicit pole-dipole energy-momentum tensor

The physical core of the source term S_s is the energy-momentum tensor $T^{\mu\nu}$, in our case the one for a spinning particle. The formalism for "spinning particles" has been reviewed in Ch. 2. The main information to be used here is that the whole theory relies on Mathisson's "gravitational skeleton" representation of a small body (see Sec. 2.1.2). This means to reduce the body to quantities which define the moments of a multipole expansion of its energy-momentum tensor, and to track these along the worldline $X^{\mu}(\lambda)$, with λ the proper time, of a fixed reference point inside the body. Thus the corresponding energy-momentum tensor is of distributional form, containing $\delta^4 = \delta(x^0 - X^0(\lambda)) \, \delta^3(x^i - X^i(\lambda))$. In the "pole-dipole approximation" we content ourselves with accounting for the zeroth and the first moments, and the chosen quantities, which fix these moments, are usually $\{v^{\mu} = \frac{dX^{\mu}}{d\lambda}, p^{\mu}, S^{\mu\nu}\}$, i.e. the tangent, the linear momentum and the spin-tensor respectively. These dynamical quantities are defined only along the worldline. Concretely, the pole-dipole skeleton of $T^{\mu\nu}$ is given by Eq. (2.4). To employ this $T_{\mu\nu}$ in the source of the TKEQ, we have to process it to an explicit form. Then, it remains to insert the dynamical quantities $\{v^{\mu}, p^{\mu}, S^{\mu\nu}\}$, obtained after integrating the equations of motion, Eq. (2.5), into that $T_{\mu\nu}$ to compute the TKEQ source.

The energy momentum tensor of Eq. (2.4) can be made explicit by performing the integration over the worldline with affine parameter λ. The calculation starts by the trans-

formation $d\lambda \to dX^0 / \left(\frac{d}{d\lambda} X^0(\lambda) \right) = dX^0/v^0(\lambda)$ and the subsequent integration over X^0

$$\sqrt{-g}T^{\mu\nu} = \int \frac{dX^0}{v^0(\lambda)} \left[v^{(\mu}p^{\nu)}\delta\left(x^0 - X^0(\lambda)\right)\delta^3 - \nabla_\alpha \left(S^{\alpha(\mu}v^{\nu)}\delta\left(x^0 - X^0(\lambda)\right)\delta^3 \right) \right]$$

$$= \frac{v(\tau)^{(\mu}p(\tau)^{\nu)}}{v^0(\tau)}\delta^3\left(x^i - X^i(\tau)\right) - \int \frac{dX^0}{v^0(\lambda)}\nabla_\alpha \left(S^{\alpha(\mu}v^{\nu)}\delta\left(\tau - X^0(\lambda)\right)\delta^3 \right)$$

$$=: \sqrt{-g}T^{\mu\nu}_{NS} + \sqrt{-g}T^{\mu\nu}_{SP} \quad , \tag{4.29}$$

where we have used the symmetry $\int f(X^0)\delta(x^0 - X^0)dX^0 = \int f(X^0)\delta(X^0 - x^0)dX^0$ and named $x^0 = \tau$ according to our time coordinate in the HH-coordinate system. Note, however, that the computation shown here holds in any coordinate system. The part called $T^{\mu\nu}_{NS}$ is the stress-energy tensor for a monopole particle. The integration in $T^{\mu\nu}_{SP}$ is not straightforward due to the covariant derivative. Schematically, we can write

$$T^{\mu\nu}_{SP} = - \frac{1}{\sqrt{-g}}\int dX^0 \frac{1}{v^0(\lambda)} \Big\{$$

$$\partial_\tau \left[S^{0(\mu}v^{\nu)}\delta\left(\tau - X^0(\lambda)\right)\delta^3 \right] + \partial_i \left[S^{i(\mu}v^{\nu)}\delta\left(\tau - X^0(\lambda)\right)\delta^3 \right]$$

$$+ \Gamma^\mu_{\alpha\lambda}\left[S^{\alpha(\lambda}v^{\nu)}\delta\left(\tau - X^0(\lambda)\right)\delta^3 \right] + \text{index permuted } \Gamma \text{ terms} \Big\} , \tag{4.30}$$

where the Christoffel symbols $\Gamma^{\cdot}_{\cdot \cdot}$ are functions of the background and emphatically not of the worldline. This point of view is in contrast to the note in the discussion around Eq. (2.16) of reference [153], which treats the Christoffels as quantities only defined along the worldline. Certainly, one may argue that the presence of δ distributions allows the untroubled interchange of field and source points $x^\mu \longleftrightarrow X^\mu(\lambda)$. This is, however, strictly true only under a corresponding integral. But in our case the spatial delta-distributions are not integrated against and thus have to be understood as delta-functions that mimic the properties of distributions. We therefore prefer to not make use of the interchange of source and field points, in which case the Christoffels clearly remain background quantities. In the end, the whole discussion is anyway rather academic since a good delta-function representation will vanish except for a few field points close to the source points.

Coming back to Eq. (4.30), most of the terms can be trivially integrated. Special care has only to be taken of the ∂_τ term

$$\int dX^0 \frac{1}{v^0(\lambda)}\partial_\tau\left[S^{0(\mu}v^{\nu)}\delta\left(\tau - X^0(\lambda)\right)\delta^3 \right] = \int dX^0 \frac{1}{v^0(\lambda)} S^{0(\mu}v^{\nu)}\delta^3 \partial_\tau\left[\delta\left(\tau - X^0(\lambda)\right) \right] \quad , \tag{4.31}$$

where we have used that dynamical quantities along the worldline like $v^\mu, p^\mu, S^{\mu\nu}$ are λ-dependent but not τ-dependent unless the integration along the worldline is performed.

Now we want to exploit the defining property for the derivative of a δ distribution

$$\int f(X^0)\, \partial_{X^0} \left[\delta(X^0 - \tau) \right] dX^0 = - \int \left(\partial_{X^0}\, f(X^0) \right)\, \delta(X^0 - \tau) dX^0\,.$$

But inspecting Eq. (4.31), we face the problem that the integrand is not obeying the same form; the integration variable, X^0, is not the same as the one that the δ is differentiated with respect to, τ. Given that we want to keep the integration over X^0, we need to somehow transform the term $\partial_\tau \delta \left(\tau - X^0(\lambda) \right)$ to a derivative with respect to X^0. Since X^0 and τ are completely independent at this point, we only have a chance by exploiting some δ properties. The first property we need is $\int f(x)\partial_x\delta(x - y)dx = \int f(x)\partial_x\delta(y - x)dx$, which can be understood when replacing $\delta(x - y)$ by a narrow Gaussian (that in the limit of zero width defines a δ). Then, we have essentially $\int f(x)\partial_x\, e^{-0.5\,(x-y)^2}dx = -\int f(x) \left[(x - y)\, e^{-0.5\,(x-y)^2} \right] dx = \int f(x)\partial_x\, e^{-0.5\,(y-x)^2}dx$. Thus, we can write

$$\int dX^0 \frac{S^{0(\mu}v^{\nu)}\, \delta^3}{v^0(\lambda)} \left(\frac{\partial}{\partial\tau}\, \delta \left(\tau - X^0(\lambda) \right) \right) = \int dX^0 \frac{S^{0(\mu}v^{\nu)}\, \delta^3}{v^0(\lambda)} \left(\frac{\partial}{\partial\tau}\, \delta \left(X^0(\lambda) - \tau \right) \right) = (\star)\,. \tag{4.32}$$

Now, treating the distribution as a conventional function, $\partial_x\delta(y - x) = -\partial_y\delta(y - x)$, we may proceed as

$$(\star) = \int dX^0 \frac{S^{0(\mu}v^{\nu)}\, \delta^3}{v^0(\lambda)} \left(-\frac{\partial}{\partial X^0}\, \delta \left(X^0(\lambda) - \tau \right) \right), \tag{4.33}$$

which is finally of a form that we can handle. We can now exploit the defining property of the δ-distribution. Being mindful of the dependence of the dynamical quantities on X^0 through $\lambda(X^0)$, e.g., $v^\mu = v^\mu(\lambda(X^0))$, we can summarise the calculation starting from Eq. (4.31) up to here by the following result

$$\int dX^0 \frac{1}{v^0(\lambda)}\, \partial_\tau \left[S^{0(\mu}v^{\nu)}\delta \left(\tau - X^0(\lambda) \right) \delta^3 \right] = \cdots = \left[\frac{\partial}{\partial X^0} \left(\frac{S^{0(\mu}v^{\nu)}\, \delta^3}{v^0} \right) \right]_{X^0 = \tau}. \tag{4.34}$$

Thus, the hard part of Eq. (4.30) is resolved. After performing the integrations against X^0 in the remaining trivial parts of Eq. (4.30), which are of the form $\int f(\lambda(X^0))\delta(X^0 - \tau)\, dX^0 = f(\lambda(\tau))$, we can, at last, replace all λ-dependence by coordinate time τ dependence.

Assembling all the pieces together, we obtain the ready-to-use expression

$$T^{\mu\nu} = T^{\mu\nu}_{NS} + T^{\mu\nu}_{SP} = \frac{1}{\sqrt{-g}} \left\{ \frac{v^{(\mu}p^{\nu)}}{v^0}\, \delta^3 - \nabla_\alpha \left(\frac{S^{\alpha(\mu}v^{\nu)}}{v^0}\delta^3 \right) \right\}, \tag{4.35}$$

which coincides with the result (2.16) of [153]. Let us emphasise, for clarity, that the dynamical quantities are now coordinate time dependent $v^\mu(\tau), p^\mu(\tau), S^{\mu\nu}(\tau)$, as well as the

δ-functions $\delta^3 = \delta\left(\rho - \rho_p(\tau)\right) \delta\left(\theta - \theta_p(\tau)\right) \delta\left(\varphi - \varphi_p(\tau)\right)$, where the subscript p denotes the particle's coordinates. The factor from the volume element, $\sqrt{-g}$, is a function of the background; more precisely, $g_{BL} = -\sin^2\theta \, \Sigma^2$ and $g_{HH} = -\sin^2\theta \, \Sigma^2 (\frac{dr}{d\rho})^2$. Furthermore, in the non-spinning limit p^μ and v^μ are trivially related by the rest mass μ of the particle, i.e. $p^\nu = \mu v^\nu$.

Finally, let us describe how this $T_{\mu\nu}$ can be separated into pieces. While $T_{NS}^{\mu\nu}$ is rather short, $T_{SP}^{\mu\nu}$ is quite longish. Therefore, we split the spin-dependent part into $T_{SP}^{\mu\nu} = -\frac{1}{\sqrt{-g}} \left(Q_A^{\mu\nu} + Q_B^{\mu\nu} + Q_C^{\mu\nu} + Q_D^{\mu\nu}\right)$ with

$$Q_A^{\mu\nu} := \partial_\tau \left(S^{0(\mu}V^{\nu)} \, \delta^3\right) , \qquad Q_B^{\mu\nu} := S^{i(\mu}V^{\nu)} \, \partial_i \delta^3 ,$$
$$Q_C^{\mu\nu} := S^{\rho\mu} \, V^\sigma \Gamma_{\rho\sigma}^\nu \, \delta^3 , \qquad Q_D^{\mu\nu} := S^{\rho\nu} \, V^\sigma \Gamma_{\rho\sigma}^\mu \, \delta^3 , \qquad (4.36)$$

where we have introduced the coordinate velocities $V^\mu = v^\mu/v^\tau$ and exploited the antisymmetry of $S^{\mu\nu}$ in combination with the symmetry of $\Gamma_{\mu\nu}^\lambda$. As a matter of fact, in the code derivatives of $T_{SP}^{\mu\nu}$ are computed as sums of derivatives of the $Q_X^{\mu\nu}$. Then, one can build the tetrad contractions like, e.g., $T_{nn,SP}$, $T_{nn,NS}$,... and their derivatives, and, ultimately, bring them together as $T_{nn} = T_{nn,NS} + T_{nn,SP}$.

4.3.3 Numerical δ-functions and their derivatives

The energy momentum tensor of Eq. (4.35) contains distributional terms, like $\delta(x^i - X^i(\tau))$, and, in the spin-part $T_{SP}^{\mu\nu}$, also their derivatives, $\partial_\mu \delta(x^i - X^i(\tau))$. Once this $T^{\mu\nu}$ is inserted into the source term S_s of the TKEQ, it will be hit by all combinations of first and second partial derivatives with respect to the coordinate basis used. In a numerical approach we therefore have to approximate these distributions, and their derivatives up to third order, by some functions which mimic the distributional properties. This section will discuss two possible choices for such functions, a narrow Gaussian δ-function and a few-point discrete representation. A closer look at their numerical performance will follow in Sec. 5.2.4.

A natural choice for a numerical δ is the narrow Gaussian peak

$$\delta(x - X(\tau)) \; \longrightarrow \; \delta_\sigma(x - X(\tau)) = \frac{1}{\sigma\sqrt{2\pi}} \exp\left[-\frac{(x - X(\tau))^2}{2\sigma^2}\right] , \qquad (4.37)$$

where the width σ is chosen a multiple of the grid spacing h, i.e. $\sigma \sim n_\sigma h \ll M$, $n_\sigma \in \mathbb{N}$ (as in, e.g., [22, 130]). This function satisfies $\int \delta_\sigma dx = 1$ and it depends sensitively on the width σ. The method is very simple, smooth, and completely analytical but, in principle, computationally expensive because, (i) the Gaussian must be well resolved on the grid ($n_\sigma \gtrsim 4$), and (ii) exponential functions must be often evaluated during evolution.

The second method is a $2n$-points discrete δ-function as described in [154, 155, 91, 112]. The authors provided several slight modifications with respect to the choice for n and the order of accuracy. We focus here on sketching the main idea using the example of the $n = 1$ option (for more details the reader is referred to Sec. III.A of [91] and Sec. 4.3 of [H2]). Assume that the position of the particle α lies between two grid points, $\alpha \in [x_k, x_{k+1}]$. Then, the $n = 1$ discrete δ-function has support for maximally two points δ_i around α. These values are given requiring that the integral properties of the δ-function, e.g.,

$$f(\alpha) = \int dx f(x)\delta(x - \alpha) \approx \sum h f_i \delta_i \ , \tag{4.38}$$

be preserved also on the discrete level. If by chance $\alpha = x_k$, setting $\delta_k = 1/h$ and $\delta_i = 0$ elsewhere solves the problem. In general, α does not lie on a grid point, so interpolation has to be used. Considering the $n = 1$ option with linear interpolation at α and enforcing Eq. (4.38) leads to

$$\delta(x - X(\tau)) \longrightarrow \delta_d(x_j - X(\tau)) = \begin{cases} \gamma\, h^{-1} & , j = k \\ (1 - \gamma)\, h^{-1} & , j = k + 1 \\ 0 & , \text{otherwise} \ , \end{cases} \tag{4.39}$$

where $\gamma = (x_{k+1} - \alpha)/h$. Overall, this method is expected to be computationally more efficient than the Gaussian. However, too narrow a representation of the δ may lead to numerical instabilities (see discussions in Sec. 5.2.4 and [91, 112]). Note that similar formulas were derived for the first two derivatives [91], both of which take $(2n+2)$-points; the third derivative was not given, albeit in principle conceivable as well. Since for a spinning particle we have to handle third derivatives like $\partial_\mu \partial_\nu \partial_\eta \delta(x^i - X^i(\tau))$, we have used the δ_d-function only in the nonspinning limit.

Having introduced the employed numerical δ-representations, a short comment on how we handle derivatives of these δ-functions seems useful. For both δ representations the spatial derivatives are completely harmless because they are given analytically. Instead, time-derivatives deserve a moment of thought. The intuitive idea of treating the δ-function like a usual composite function $\delta(F(\tau, x))$ turns out to work fine. More precisely, in 1D, setting $F(\tau, x) := x - X(\tau)$ and using $\frac{\partial}{\partial x} = \frac{\partial F}{\partial x}\frac{\partial}{\partial F} = \frac{\partial}{\partial F}$ amounts to

$$\partial_\tau \delta(F(\tau, x)) = (\partial_\tau F(\tau, x))\, \partial_F \delta(F) = -(\partial_\tau X(\tau))\, \partial_x \delta(x - X(\tau)) \quad . \tag{4.40}$$

In this manner, time derivatives are converted to spatial derivatives. The time derivatives of the particle's position $\partial_\tau X^i(\tau)$ are provided in the dynamics.

Before proceeding, it may be helpful to stress here that the δ-functions under discussion are only needed in radial and polar direction. In a 2+1 approach, the δ-distribution in

azimuthal direction has to be handled by a Fourier decomposition, otherwise the coordinate φ can not be erased from the picture. We follow [91] and employ $\delta(\varphi - \varphi_p(\tau)) = \frac{1}{2\pi} \sum_m e^{\mathrm{i}\, m\,(\varphi - \varphi_p(\tau))}$ with $\partial_\varphi \to \mathrm{i}\, m$ and $\partial_\tau \to -\mathrm{i} m \partial_\tau \varphi_p(\tau)$. Thus, the source term contains the same overall factor $e^{\mathrm{i}\, m\, \varphi}$ that was contained in the homogeneous TKEQ after the 2+1 reduction; we simply have to multiply the inhomogeneous TKEQ by $e^{-\mathrm{i}\, m\, \varphi}$ to get rid of all φ appearances. What remains is only the information on the particle's φ position at a given time by virtue of the factor $\frac{1}{2\pi} e^{-\mathrm{i}\, m\, \varphi_p(\tau)}$. Note, however, that this assumes to use the same coordinates for the homogeneous TKEQ as for the source computation. If doing otherwise, consult the discussion on the coordinate invariance of the source term commented on in Appendix G.

4.3.4 Dynamics in HH-coordinates

The equations of motion for a test-particle (see Ch. 2) are conventionally integrated in BL-coordinates and, hence, one expects to be provided with dynamics in BL-coordinates. It remains to calculate the source term in HH-coordinates from the given BL-data. The source term requires the energy-momentum tensor with respect to the HH-coordinate basis, say $T_{HH}^{\mu\nu}$, or in case of a point particle the relevant quantities $\{v_{\mathrm{HH}}^\mu, p_{\mathrm{HH}}^\mu, S_{\mathrm{HH}}^{\mu\nu}\}$ to compute $T_{HH}^{\mu\nu}$. As tensorial quantities these can just be transformed from one to the other basis. However, the source computation for a spinning particle also requires the knowledge of up to third time derivatives of $\{X^\mu, v^\mu, p^\mu, S^{\mu\nu}\}$ with respect to the coordinate time. We shall briefly discuss how to analytically compute these derivatives in the HH-coordinate time from the given BL-data. Note that this concerns only the dynamics and can be done prior to the simulation.

The idea is to convert any HH-coordinate time τ derivative to an "eigentime" derivative. For example, seeking $\frac{\partial}{\partial\tau} p_{HH}^\mu$ we can exploit

$$\frac{\partial}{\partial\tau} p_{HH}^\mu = \left(\frac{\partial\tau(\lambda)}{\partial\lambda}\right)^{-1} \frac{\partial}{\partial\lambda} p_{HH}^\mu = \frac{\frac{\partial}{\partial\lambda} p_{HH}^\mu}{v_{HH}^\tau} \quad , \tag{4.41}$$

where v_{HH}^τ is obtained by transformation of v_{BL}^μ and it remains to compute $\frac{\partial}{\partial\lambda} p_{HH}^\mu$. Thus, consider the transformation $p_{HH}^\mu = \left(\frac{\partial x_{HH}^\mu}{\partial x_{iK}^\nu}\right) p_{iK}^\nu$, where p_{iK}^ν can be obtained from p_{BL}^ν analogously. The relevant non-vanishing Jacobian factors from BL to iK coordinates are

$$\frac{\partial\tilde{t}}{\partial t} = 1 \quad , \quad \frac{\partial\tilde{t}}{\partial r} = -\left(1 - \frac{r^2 + a^2}{\Delta}\right) \quad , \quad \frac{\partial r_{iK}}{\partial r} = 1 \quad , \quad \frac{\partial\theta_{iK}}{\partial\theta} = 1 \quad , \quad \frac{\partial\varphi}{\partial r} = \frac{a}{\Delta} \quad , \quad \frac{\partial\varphi}{\partial\phi} = 1 \quad . \tag{4.42}$$

The analogous factors from iK to HH coordinates are

$$\frac{\partial \tau}{\partial \tilde{t}} = 1 \quad , \quad \frac{\partial \tau}{\partial r} = \frac{4M\rho + \rho^2 - 4MS - 2\rho S}{S^2} \quad , \quad \frac{\partial \rho}{\partial r} = \frac{(\rho - S)^2}{S^2} \quad , \quad \frac{\partial \theta_{HH}}{\partial \theta_{iK}} = 1 \quad , \quad \frac{\partial \varphi_{HH}}{\partial \varphi_{iK}} = 1 \quad .$$
(4.43)

For completeness, we state the factors from iK to RT coordinates as well

$$\frac{\partial T}{\partial \tilde{t}} = 1 \quad , \quad \frac{\partial T}{\partial r} = \frac{2\,R\,(-1 + 2M(-1 + R^2))}{1 + R^2} \quad , \quad \frac{\partial R}{\partial r} = \frac{(-1 + R^2)^2}{2(1 + R^2)} \quad , \quad \frac{\partial \theta_{RT}}{\partial \theta_{iK}} = 1 \quad , \quad \frac{\partial \varphi_{RT}}{\partial \varphi_{iK}} = 1 \quad .$$
(4.44)

Coming back to the example of transforming the p^μ, we can write

$$p^\tau = p^{\tilde{t}} + \frac{4M\rho + \rho^2 - 4MS - 2\rho S}{S^2} p^r_{iK} \quad , \quad p^\rho = \frac{(\rho - S)^2}{S^2} p^r_{iK} \quad , \quad p^\theta_{HH} = p^\theta_{iK} \quad , \quad p^\varphi_{HH} = p^\varphi_{iK} \quad .$$
(4.45)

Note that for a test-particle the momenta are only defined along the worldline; in transforming these the coordinates have to be understood as the particle's position coordinates, i.e. actually $\rho \to \rho_p(\lambda)$ with λ the proper time. Then, we can compute the desired $\frac{\partial}{\partial \lambda} p^\mu_{HH}$. The ρ component, for example, reads

$$\frac{\partial}{\partial \lambda} p^\rho = \frac{(\rho_p - S)^2}{S^2} \frac{\partial}{\partial \lambda} p^r_{iK} + p^r_{iK} \frac{\partial}{\partial \lambda} \frac{(\rho_p(\lambda) - S)^2}{S^2} \quad ,$$
(4.46)

which only requires knowledge of proper time derivatives of the iK-momenta and of the iK-coordinates ($\rho_p(\lambda)$ can be expressed in terms of $r_p(\lambda)$). In the same manner, time derivatives of the iK-momenta can be computed from time derivatives of the BL-momenta and of the BL-coordinates. In practice, we need to compute up to ∂^3_τ derivatives of all quantities in the HH-system. In order to be able to calculate the third HH-time derivatives of all relevant quantities $\{X^\mu, v^\mu, p^\mu, S^{\mu\nu}\}$, the BL-data has to provide up to ∂^3_λ derivatives of these. Alternatively, if the data is densely sampled one can, of course, compute HH-time derivatives numerically.

The *teukode*

The previous chapter presented a new approach to the Teukolsky-Equation (TKEQ) using hyperboloidal, horizon-penetrating coordinates. The bottom line was a reformulated version of the TKEQ, Eq. (4.3), which is a wavelike partial differential equation (PDE) of second order in the HH-coordinates (τ, ρ, θ). This chapter describes our strategy of solving this PDE numerically. Our implementation in the C programming language is named the *teukode*. The code works with standard numerical algorithms, which will be quoted here, and, which shows that the new approach of Ch. 4 can be relatively simply realised. Note that the *teukode* was set up in collaboration with Dr. Bernuzzi, Dr. Nagar and Dr. Zenginoğlu in [H2]. Dr. Bernuzzi set up the infrastructure, Dr. Nagar provided guidelines comparing with the implementation of [132], and Dr. Zenginoğlu derived the explicit TKEQ in HH-coordinates. The author's main responsibility was to implement the TKEQ, especially the point-particle source term, and to conduct extensive numerical experiments in order to validate the code and to produce the new results.

Sec. 5.1 gives a description of the adopted numerical techniques. In Sec. 5.2 the correctness and the significance of the implementation is approved by performing standard convergence tests. Numerical experiments in terms of physical quantities which can be compared to the literature are presented. First, we shall recall experiments with the homogeneous TKEQ; more precisely, the measurement of decay-rates of initial perturbations. As a second step, we shall cross-check waveforms of a point particle against (i) results from a frequency domain code (with data kindly provided by Hughes [91, 62, 60]), (ii) a paper of Shibata [87], (iii) an existing Regge-Wheeler-Zerilli code (kindly provided by Bernuzzi, Nagar and Zenginoğlu [132]), and (iv) further frequency domain data kindly provided by Berti et al. [156]. Finally, Sec. 5.3 discusses the remaining limitations of the *teukode* with respect to stability and accuracy.

5.1   Numerical techniques and code details

For the numerical time-evolution the 2+1 TKEQ, Eq. (4.3), is written as a first-order in time and second-order in space system with reduction variables $\{\psi, \partial_\tau \psi\}$. We use a

standard method-of-lines approach and discretize the spatial domain $(\rho, \theta) \in [\rho_+, S] \times (0, \pi)$, where ρ_+ and S are the locations of the horizon and null infinity respectively, with a uniformly spaced grid of $N_\rho \times N_\theta$ points. At each grid point, the PDE is turned into an ODE in time by virtue of discrete representation of spatial derivatives; more precisely, finite differences up to eighth order of accuracy (though typically we use fourth and sixth order stencils). The stencils in the radial direction are centered in the bulk of the domain. At the boundaries one can either use lop-sided/sided stencils or ghost points filled by extrapolation. We observed no advantage in either of them, and decided, arbitrarily, to make (lop-)sided stencils our default choice. In angular direction the grid is staggered to avoid the well-known coordinate problems on the axis $\theta = 0$ or $\theta = \pi$. The polar direction is enhanced by ghost points to capture the boundary conditions on the axis. The ghost points are filled according to the parity condition $\pi = (-1)^{m+s}$, which mimics the behaviour of the spin-weighted spherical harmonics $Y_{s\ell m}$.

At each grid point, the fields are advanced in time by integrating the ODEs with a standard Runge-Kutta integrator of fourth order. The time step is chosen according to a CFL condition of type $\Delta t = C_{\mathrm{CFL}} \min(h_\rho, h_\theta)$, where h_x is the grid spacing in direction x and the factor C_{CFL} is restricted by the maximum coordinate speed of the PDE system. Usually there is a window $[C_{\mathrm{CFL,i}}, C_{\mathrm{CFL,f}}]$ which allows stable evolutions. The exact numerical values depend on the coordinate choice. As mentioned in Sec. B.4, our choice is the HH_{10}-system. For this choice simulations are stable in the range $C_{\mathrm{CFL}} \approx [1, 2.5]$ and our default choice is $C_{\mathrm{CFL}} = 2.0$. Instabilities arise for higher values but can be damped by artificial dissipation operators. These are implemented but in general not used for our simulations.

The computational costs of a simulation within the above outlined implementation depend on the numerical experiment. The homogeneous TKEQ allows very cheap simulations; at a reasonable resolution of $N_\rho \times N_\theta = 2400 \times 200$ points late times $\sim 1000M$ are reached within ~ 60 minutes on a standard Linux desktop computer using one core (3.2GHz) and the GNU C compiler. The nonspinning point particle simulations in the equatorial plane are relatively fast. For instance, the EOB inspiral experiments (see Sec. 5.2.3) required long simulations up to $\tau \sim 5000\,M$ and only took maximum runtimes of ~ 2 weeks at resolutions of $N_\rho \times N_\theta = 3600 \times 160$, which is the resolution standardly used in our science runs. Note that the relatively low number of points in θ direction relies on the use of very accurate discrete δ representations (see Sec's. 4.3.3 and 5.2.4). In contrast, spinning particle simulations are relatively expensive because they suffer from the algebraic complexity of the source term computation. In addition, such simulations require third derivatives of δ-functions, which can only be handled with the more expensive narrow Gaussian representation (see Sec. 4.3.3). Since the Gaussian is less accurate at a given

resolution, we usually employed resolutions of $N_\rho \times N_\theta = 4800 \times 400$ for those numerical experiments (see Ch. 8). To keep the runtimes reasonable at such high resolutions, we recently implemented the option to use parallel computing on multiple cores, using a standard grid decomposition strategy and the OPENMPI library. This process is still under development. Within this thesis only the experiments of Ch. 8 have been computed in parallel (8 cores). The runtimes for these experiments, which reach the needed $\tau \sim 500M$ in ~ 5 days using a single core, were thus reduced to ~ 2 days.

At this point a few words shall be spent on the methods used to convert our evolution variables $\{\psi,\ \partial_\tau \psi\}$ to directly related quantities of interest. For instance, there is the decomposition of the fields into their projections on spin-weighted spherical/spheroidal harmonics. For accuracy reasons, we want to employ all θ points for the required integration in θ-direction, i.e. this has to be done at runtime. Concretely, we interpolate the fields to a non-staggered uniform grid of $N_\theta + 1$ points and apply the Simpson rule. Further related quantities are the GW energy and angular momentum fluxes. For discrete-frequency solutions, like the waves from a particle in circular orbit, we can evaluate these in terms of the field variables with frequency domain formulas (cf. Sec. 4.2.1). This can easily be done at simulation time. The equivalent time-domain flux computations (see Sec. 4.2.2) are related to the gravitational strain, which can be computed at future null infinity from our evolution variable (cf. Sec. 4.1.3). To exploit the fine time-stepping, we perform this cumulative integration at runtime, using the trapezoidal rule and storing the concerned fields of the previous time step. The subsequent normalisation of the strain to the RWZ-convention (see Eq. (4.5)) is done in a post-simulation step using *matlab*. Furthermore, there are the time-domain absorbed fluxes (see Sec. 4.2.2). These stem, theoretically, from global time-integrals $f_{\mathrm{H}m}^+$; they cannot be evaluated at runtime. Instead, they require the complete output and, thus, have to be computed in a post-processing step. In practice, the exponentially decaying function in the integrals $f_{\mathrm{H}m}^+$ compresses the relevant information at a given time v_* to some interval $(v_* - \Delta v, v_* + \Delta v)$. We choose Δv such that the exponential satisfies $e^{-\kappa(v-v_*)} > 10^{-6}$, with $\kappa \in [0.25, 0.35]$ for $|\hat{a}| \in [0, 0.9]$. This typically amounts to intervals $v \in [v_* - 50M, v_* + 50M]$. Note that the accuracy of integrals in post-processing depends on the sampling of the output. To keep the amount of output reasonable, we implemented the option of interpolating to Gauss-Lobatto points for output in angular direction. This reduces the number of points needed for efficient angular integration to ~ 50.

5.1.1 A spectral version of the *teukode*

We have also implemented another version of the *teukode* which employs spectral differentiation in spatial directions. We use Chebyshev-polynomials on a Gauss-Lobatto grid in

radial direction and Fourier-modes on a staggered grid in polar direction. Apart from the discrete derivative approximation the main differences are, (i) the use of RT-coordinates instead of the HH-coordinates (see Sec. B.4), (ii) the implemented option of using quadruple precision, and (iii) the restriction to the vacuum TKEQ since the pseudo-spectral grid is not able to resolve a very localised structure like a point-particle. Referring to issue (iii), it might be noteworthy to mention that it would be conceivable, though, for the future to perform spectral simulations with a point-particle source term, after investing some time in technical developments like a mesh-refinement.

The spectral code was used in [H0] to conduct a proof of principle of the functionality of our new approach to the TKEQ in vacuum. In Ch. 6 the investigations in this direction will be completed with only those results which were found after the presentation of [H0]. Therefore, we will not go into further detail on this spectral implementation. Except, note that it was validated to be exponentially convergent (see Fig. 5 in [H1]) and capable of reproducing analytical and numerical predictions for late-time tail decay rates with high accuracy (cf. [H0, H1]).

5.2   Code validation

In this section the trust in the *teukode* shall be established. First, we recall that the code reproduces results obtained with the spectral implementation, which was validated already in [H1]. Second, we present convergence tests for the most interesting setup of a point particle on a realistic inspiral trajectory. After these intrinsic numerical tests, physical quantities, like waveforms and energy fluxes, are examined. These quantities are thoroughly studied in the literature, and thus give a further opportunity to assess the capabilities of the new approach and its implementation in the *teukode*.

5.2.1   Convergence

The numerical convergence of a code refers to the property of approaching towards a unique solution when the resolution is increased. This is important to guarantee the significance of the outcome and a higher accuracy at higher resolutions. There are several ways of assessing the convergence by examining the behaviour of "errors". When analytical solutions are known, one can simply measure the errors as deviations from the analytics, and monitor their decrease with higher resolutions. In our case we do not possess analytic solutions, but one can treat highly-accurate numerical solutions as such, at least to a reasonable extent. A first benchmark is obtained by comparing the *teukode* with the spectral code, which was validated in [H1]. In all cases tested, the *teukode* output was visually on top of the spectral code's output, even in the measurement of the challenging decay-rates (see Fig. 8 in [H1]). Thus, the *teukode* appears to function correctly at least
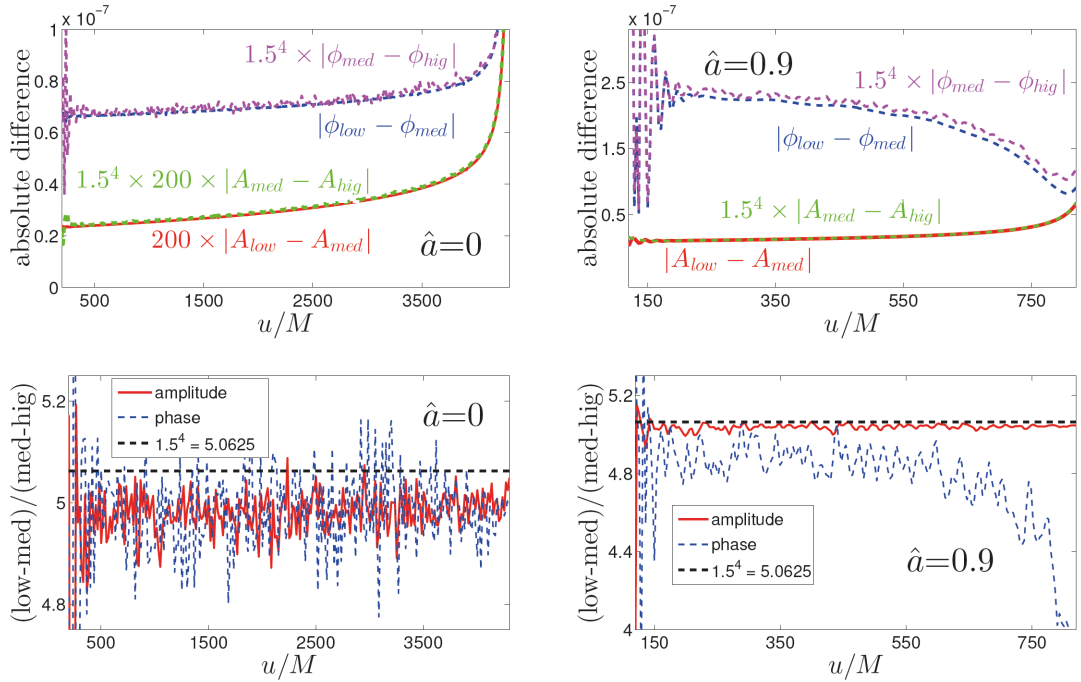
Figure 5.1: Self-convergence for the amplitude and phase of the waveform at the extraction point $(\rho, \theta) = (S = 10, \pi/2)$ for inspiral simulations on Kerr with $\hat{a} = 0$ (left) and $\hat{a} = 0.9$ (right). The merger is at $u/M \sim 4300$ and $u/M \sim 880$ respectively (not included in plots). The triplet uses radial resolutions $N_x = (400, 600, 900)$, with Gaussian widths $n_\sigma = (4, 6, 9)$ and $N_\theta = 30$. The expected scaling for the error is $1.5^4 \approx 5.0625$ for 4th-order finite differences. Top panels: absolute differences in phase $\Delta\phi$ and amplitude ΔA between various resolutions. The differences between medium and high resolution are rescaled by the expected factor assuming convergence and lay on top of the differences between low and medium resolution. For visualisation the differences in amplitude are rescaled by an arbitrary factor 200 in the left panel. Bottom panels: ratios of absolute differences. Plots adopted from [H2].

for the vacuum equation. Note, though, that it does not yet support quadruple precision, which prevents its usage in extensive late-time decay experiments. Another way to assess the convergence stems from the assumption that the numerical solution constitutes the analytical solution plus an error term proportional to a power of the grid-step, h^c. In this case a three-level self-convergence test would yield the order c by comparison of the outcomes at three resolutions. We have performed such a test for the most relevant setup of EOB-inspiral motion of a point particle at resolutions $N_\rho = (400, 600, 900)$. The number of points in polar direction is fixed at $N_\theta = 30$ because the motion of the particle takes place in radial direction only (plus azimuthal motion, but this is not part of the computational domain). The number of points for the Gaussian representation of the particle has to be adapted as well to see the expected order of convergence, i.e. the width is set to $\sigma = n_\sigma h_\rho$ with $n_\sigma = (4, 6, 9)$. Using 4th order finite differencing, one expects a convergence-order of $c = 4$. (Repeating the convergence test without adapting the size of the Gaussian leads to a different convergence rate, namely the one of the Gaussian representation, i.e. $c \sim 2$.) In Fig. 5.1 the results of our convergence tests for the phase and amplitude of the waveforms are shown. For Kerr parameters $\hat{a} = 0$ (left)

and $\hat{a} = 0.9$ (right) the two bottom panels display the expected fourth order convergence during the complete inspiral, but for the more challenging $\hat{a} = 0.9$ case we observe a loss of convergence towards the end of the inspiral. Due to the fast acceleration of the particle during the plunge phase, the experimental convergence rate starts to drift away from the expected fourth order some time before merger; for $\hat{a} = 0.9$ (right) this reflects in the gradual drop of the phase convergence (blue dashed). The absolute differences in phase and amplitude between the low and medium resolutions are at the level of $\Delta\phi \sim 10^{-7}$ and $\Delta A \sim 10^{-8}$ (top panel). After the merger (not shown in the plots) the fields decay exponentially during the ringdown phase and a clean convergence is totally lost. Hence, we expect larger relative errors after the merger and during the ringdown. Note that the science runs used for obtaining actual results employed a much higher resolution than the ones used for the convergence test.

5.2.2 Point-particle perturbations - geodesic motions

Having convinced ourselves of the intrinsic convergence properties, we proceed with numerical experiments which can be compared with the literature. First, we constrain ourselves to a nonspinning particle on circular orbits and compare the energy fluxes with data kindly provided to us by Prof. Hughes, using an improved version of his frequency domain code from [91, 62, 60]. Second, we treat inclined orbits, which can be compared to a paper of Hughes [60] and a paper of Shibata [87]. Third, we consider radial infalls on Schwarzschild, and compare the emitted waveforms with an existing RWZ solver [132]. For the scenario of a plunging particle we also compute the energy spectra and contrast our results with data kindly made available to us by Berti et al. [156].

Circular equatorial orbits

The measurement of energy fluxes from a particle on circular orbits is a thorough test for the correctness and the accuracy of the implementation. This check is especially helpful because one can use analytical solutions for the dynamics; circular motion features constant dynamics, except for the trivially time-dependent phase $\phi_p(t) = \Omega_\phi\, t$ (see, e.g., Sec.2 A in [60] for Ω_ϕ). In addition, it provides physical information for probing RR models (see Sec. 2.2.3).

Table I.1 in the Appendix I lists the results of our experiments at radii $\hat{r}_0 = 4, 6, 8, 10$, for $\hat{a} = 0, 0.9$ and $m = 2, 3$ obtained at resolutions of $N_\rho \times N_\theta = 2400 \times 200$. Note that, (i) such runs only take a few hours on one core (3.2GHz) of a standard desktop machine, and (ii) even resolutions of 1200×100 (~ 0.5 hours) would reproduce two digits of the target solution. The first vertical block of Tab. I.1 displays our fluxes at scri and the percental deviations from the extremely accurate frequency domain results of Hughes [91, 62]. As outlined in Sec. 4.2.1, our results can be equivalently obtained from

frequency domain and time-domain formulas and both yield the same $\sim 0.01\%$ agreement with the target solution. This beautiful coincidence is due to the nice features of the new approach; e.g., the direct extraction at scri and the possibility to use the few point discrete delta representation of [91] (see Sec. 4.3.3). The second vertical block of Tab. I.1 repeats the same analysis for fluxes at the horizon. In this case we show both the frequency-domain fluxes and the time-domain ones (in brackets) because they differ slightly. The frequency-domain numbers are again in agreement of $\sim 0.01\%$ with the target, while the results within Poisson's time-domain formalism are slightly off. The reason for the offset must likely be attributed to a lack of accuracy in our implementation of the time-domain algorithm devised by Poisson [149], which is employed here for the first time (see also Sec. 4.2.2). More precisely, our approximations of the appearing global time-integrals on finite intervals (see Sec. 5.1) and the time integration in post-processing seem to spoil the accuracy. The more important information is, however, that the formalism is approved to work in practice. Thus, we are equipped with a tool for measuring horizon fluxes from a particle on general trajectories, and we are not restricted to narrow-frequency-band orbits.

For completeness, let us support the expectation that the extraction at scri is important. For the $\ell = m = 2$ mode and the $\hat{r} = 6$ and $\hat{a} = 0.9$ case, Table I.2 in the appendix lists the energy fluxes computed from waveforms extracted at different finite radii and scri. We observe a significant loss of accuracy at small extraction radii. But assuming that the finite-radii waveform behaves like a Kth order polynomial in $1/r$, the extrapolation

$$f(u, r) = f^{(0)}(u) + \sum_{k=1}^{K} r^{-k} f^{(k)}(u) \,, \tag{5.1}$$

where we have chosen $K = 2$ leads to the "correct" result (see Sec.7.4 in [H2] for a discussion on extrapolation with other choices for K).

Circular inclined orbits

A future prospect is to generalise the equatorial motion investigated in this thesis to arbitrary trajectories, especially when non-aligned spins come into play. The *teukode* has already passed some preliminary tests for non-equatorial motion, which shall be presented here. The first level of complication is to treat tilted circular motion. On a Schwarzschild background the spherical symmetry would allow to view any circular orbit as an equatorial one (by adopting the coordinate system appropriately), but, of course, one can also choose to make the orbit non-equatorial. Such a tilted circular orbit is shown in the left panel of Fig. 5.2. For $\hat{a} = 0$ the inclined circular orbit stays closed or equivalently the fundamental orbital frequencies Ω_ϕ and Ω_θ of motion are integer multiples of one another. Instead looking at the right panel of the same figure for $\hat{a} \neq 0$, one sees the orbital axis precessing.
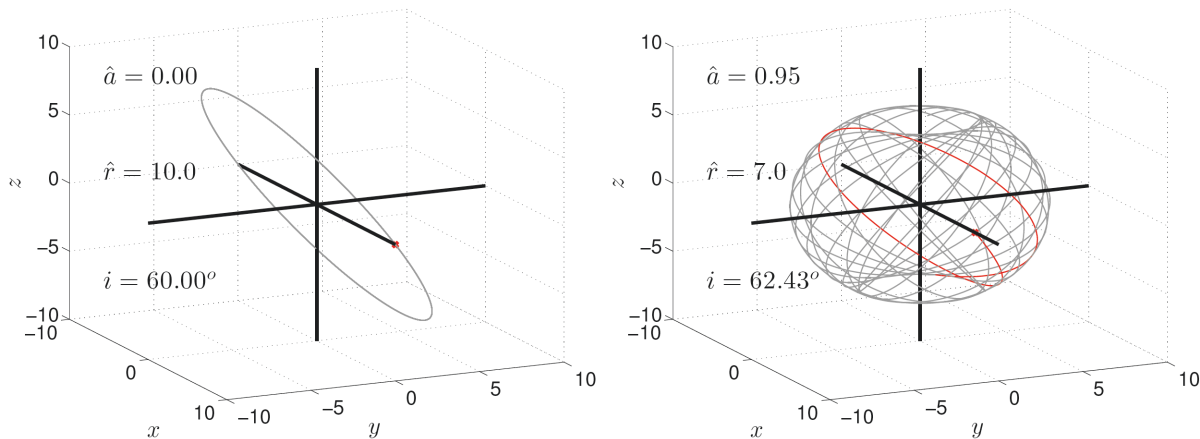
Figure 5.2: Visualisation of inclined circular orbits, see text for definition of the inclination angle i. Orbits start at $\theta = \pi/2, \phi = 0$ (marked as a red cross). On Schwarzschild $\hat{a} = 0$ (left) any inclination is artificial in the sense that the coordinate system could be adapted to make it equatorial again. The orbit is closed, i.e. the frequencies of motion Ω_ϕ and Ω_θ coincide modulo integer multiples. On Kerr $\hat{a} = 0.9$ (right) the orbits do not close. Instead, one observes a precession of the orbital axis around the spin axis of the BH. We have highlighted the whole first revolution of the orbit in red to demonstrate the deviation from closure.

At this point it seems constructive to briefly describe how one obtains such orbits in BL-coordinates. The equations of motion (EOM) are most conveniently derived from a Hamiltonian approach[1] with $\mathcal{H} = 0.5 \, g^{\alpha\beta} p_\alpha p_\beta$. Since the mass $\mu = \sqrt{-p_\mu p^\mu}$ is only a scale parameter, it is convenient to use the dimensionless version $\hat{\mathcal{H}} = 0.5 \, g^{\alpha\beta} \hat{p}_\alpha \hat{p}_\beta$ with $\hat{p}_\alpha = g_{\alpha\beta}/\mu \frac{d}{d\lambda} x_p^\beta(\lambda)$, where $x_p^\mu(\lambda)$ denotes the sought-after worldline with proper time λ. Employing the classical Hamilton equations gives an evolution system for the variables $\{x_p^\mu, p_\mu\}$. (See system (A13) in Appendix A of [157] for explicit expressions, and Sec. 2.2.1 in this thesis for a description confined to equatorial movement). These EOM can be implemented and integrated straightforwardly using professional ODE-integrators in *matlab* or *mathematica*. Noting that for axisymmetric and stationary spacetimes two momenta are constants of geodesic motion, $p_t = -E$ and $p_\phi = L_z$, one can use the equation $\frac{dt}{d\lambda} = (\ldots)$ to replace the affine parameter λ by the coordinate time t, and, thus, to consider only five variables $\{r_p, \theta_p, \phi_p, p_r, p_\theta\}$. A complete family of geodesic orbits is given by fixing a fourth constant of motion besides E, L_z, μ, the Carter Constant Q. We follow [60] in the definition of Q, but note that any combination of E, L_z, μ, Q gives a fourth constant that can replace Q, so the definition is not unique. Prescribing the four constants of motion plus initial data for the variables defines a unique member-orbit of this family. While the integration of the EOM is unproblematic, the specification of the "correct" initial data, yielding the desired orbits, can be onerous. An especially simple

---

[1]Note that such Hamiltonian approach leads to an advantageous form of the geodesic equations. Instead writing out the geodesic equations as a system for $\{r_p, \theta_p, \phi_p\}$, one obtains $\dot{x}_p = \pm\sqrt{(..)}$ expressions which represent motions in positive or negative direction respectively. Non-monotonic motion in r and θ, then, requires clever case distinctions for picking the correct root, see Sec. II of [60].

case is the circular equatorial motion. In this case $Q = 0$, and it is enough to specify just the radial coordinate r_p to compute $E(r_p)$ and $L_z(r_p)$ according to the conditions for circular motion $\frac{dr_p}{d\lambda} \equiv 0 \equiv \frac{d}{d\lambda}\frac{dr_p}{d\lambda}$ (see Eq's. (2.6) in [60]). In angular directions we always start the orbit at $\theta_p = \pi/2$ and $\phi_p = 0$. To obtain the missing initial data for $\hat{p}_r, \hat{p}_\theta$, insert $(r_p, \theta_p, E, L_z, Q)$ into the geodesic equations $\Sigma\hat{p}^r = \pm\sqrt{R(\mu, E, L_z, Q, r, \theta)}$ and $\Sigma\hat{p}^\theta = \pm\sqrt{\Theta(\mu, E, L_z, Q, r, \theta)}$, cf. (A3) in [157] for explicit expressions of R and Θ; then, just lower the indices, $\hat{p}_r = \frac{\Sigma}{\Delta}\hat{p}^r$ and $\hat{p}_\theta = \Sigma\hat{p}^\theta$, cf. Eq.'s (A7) in [157]. If everything is correct, for circular equatorial orbits $\hat{p}_r(t = 0) = 0$ and $\hat{p}_\theta(t = 0) = 0$ should be satisfied.

Now, let us come to inclined circular orbits, where the situation is a bit more complicated. A nice procedure is given in Sec. II B of [60], which, instead of prescribing Q directly, aims at providing initial data for a given r_p and inclination angle $i = \cos^{-1}\left(\frac{L_z}{\sqrt{L_z^2 + Q}}\right)$. This inclination angle is not trivial to be interpreted. Following the discussion in [113], it corresponds to the intuitive inclination of the orbital axis only strictly for $\hat{a} = 0$, but holds approximately in general (cf. Sec. II of [158]). Let us discuss how to find initial data corresponding to a given i. First, note that this inclination is $0°$ or $180°$ for equatorial motion, i.e. for $Q = 0$. Second, note that at a given r_p there is a range of inclinations (i_i, i_f) which allow stable circular motion. Maximally the range is $(0°, 180°)$. The most stable inclination is $i = 0°$, i.e. prograde equatorial motion. For $i = 0°$ and $i = 180°$ we can use Eq.'s (2.6) of [60] to find L_z of prograde and retrograde equatorial motion respectively. $L_z(i = 0°)$ provides a maximum stable value, $L_{z,\text{max}}$. Starting from $L_{z,\text{max}}$ one gradually decreases[2] L_z and checks if one reaches $L_z(i = 180°)$ without the stability condition $\frac{d^2}{dr_p^2}\text{RHS}(r_p(t)) < 0$ being violated. In case of violation, only a confined range $(L_z(i = 0°), L_{z,\text{min}})$ is stable or equivalently $i \in (0°, i_f)$ with $i_f < 180°$. If the desired inclination i lies within the stable region, one can find the suitable values of L_z, Q in the following way. The conditions for circular motion allow the derivation of expressions for $Q(r_p, L_z)$ and $E(r_p, L_z)$ (see Eq.'s (2.8) and (2.9) in [60]). Thus, one can evaluate $Q(r_p, L_z)$ and $i(L_z, Q)$ for all stable L_z and interpolate to the desired inclination and its associated L_z and Q values. This way one finds initial data which produces circular motion for a desired (r_p, i). After integrating the EOM, one can check the conservation of r_p and the conservation of the Hamiltonian to convince oneself of the result.

We have investigated a few such inclined circular orbits by measuring the emitted energy fluxes. The first test regards an $i = 60°$ orbit at $\hat{r} = 10$ on Schwarzschild. The appro-

---

[2]Note that in this thesis we mainly use the convention $L_z > 0$ and $\hat{a} \in [-1, 1]$. Instead Hughes [60] uses $\hat{a} > 0$ and switches from prograde to retrograde motion by the sign of L_z. The latter convention will be adopted here as an exception since it simplifies Hughes' procedure for finding initial data for inclined orbits. This means $L_z(i = 180°)$ will be < 0.
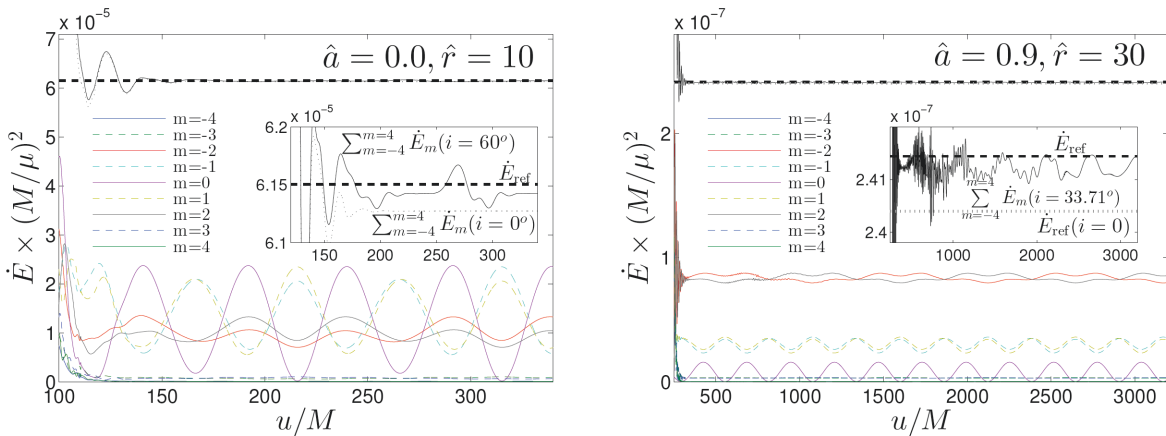
Figure 5.3: Comparison of energy fluxes for inclined circular orbits. The coloured lines are the different m-mode contributions between $m_{\min} = -4$ and $m_{\max} = 4$. The solid black line is the sum of those. The dashed and dotted black lines are certain reference solutions. On Schwarzschild $\hat{a} = 0$ (left) we consider an orbit at $\hat{r} = 10$ with $i = 60°$. The computed total energy flux is constant in time and agrees with the reference solution of Hughes [60] and a corresponding run with $i = 0°$ (the small difference between our $i = 0°$ and $i = 60°$ results is due to different resolutions employed in these test runs). On Kerr $\hat{a} = 0.9$ (right) we consider a case covered by Shibata [87], i.e. $\hat{r} = 30$ with $i = 33.71°$. Our result for the total energy flux (solid black) agrees with the reference solution of Shibata (dashed black). A comparison with Hughes' $i = 0°$ result (dotted) reveals that the impact of inclination is small. This is explained by the large distance, which makes the background relatively spherical and also reflects in the constancy of the total flux over time.

priate initial data[3] is $\hat{E} = 0.9562$, $\hat{L}_z/M = 1.8898$ and $\hat{Q}/M^2 = 10.7143$. The employed resolution is 4000×400 and we use a Gaussian-representation of the particle. One expects the total energy flux to possess two main features due to the spherical symmetry of the background, that is (i) to be constant at every instant of time, and (ii) to coincide with the equatorial flux. As shown in the left panel of Fig. 5.3, the *teukode* results meet the expectations for the total energy flux computed from $m_{\min} = -4$ to $m_{\max} = 4$. Note how the different m-mode contributions (coloured lines) oscillate in time while their sum (solid black) gives approximately the constant flux obtained from the respective equatorial run (dotted). The remaining small oscillations in the solid black line, highlighted in the insets, must be attributed to numerical inaccuracies, probably accumulated through the sums of the mode projections. The target solution of Hughes [60] is shown as a dashed black line. Furthermore, it is interesting to see that the sign of the m-mode matters, i.e. it causes a phase shift between $+$ and $-$ modes. As a second test we consider a spinning BH with $\hat{a} = 0.9$. For comparison with Shibata's results [87], we pick a fairly distant location of the particle, $\hat{r} = 30$ (the minimal value considered in [87]). We pick the $i = 33.71°$ case of

---

[3]Recall that here the hat is used to denote particle specific quantities, like momenta per unit mass $\hat{p}^\mu = \frac{p^\mu}{\mu} = \frac{dX^\mu}{d\lambda}$ (with λ the proper time), i.e. they are reduced with respect to the particle's mass μ. That is we have $\hat{E} = -\hat{p}_t = E/\mu$, $\hat{L}_z = \hat{p}_\phi = L_z/\mu$ and $\hat{Q} = Q/\mu^2$, cf. [60]. Note that this does not necessarily mean hatted quantities are dimensionless. For example, for $\hat{a} = 0$ we have $\hat{L}_z = \hat{p}_\phi = r^2 \hat{p}^\phi = r^2 \frac{d\phi}{d\lambda}$, i.e. the dimension $[\hat{L}_z] = [M]$. From $[Q] = [L_z^2]$ it follows that $[\hat{Q}] = [Q/\mu^2] = [L_z^2/\mu^2] = [\hat{L}_z^2] = [M^2]$, while $\hat{E} = (1 - 2M/r)\frac{dt}{d\lambda}$, i.e. the dimension is $[\hat{E}] = [1]$.
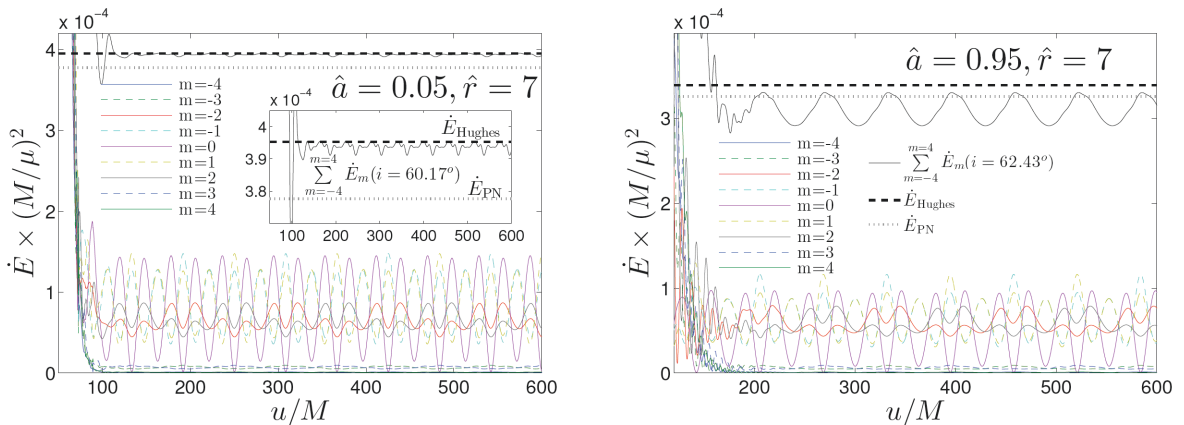
Figure 5.4: Comparison of energy fluxes for inclined circular orbits in the strong-field at $\hat{r} = 7$ as covered by Hughes [60]. For $\hat{a} = 0.05$ (left) we find very good visual agreement with the target solution (dashed). The PN-result due to Ryan [159] (dotted) is shown for comparison. At such low spins the total energy flux is approximately constant in time. For $\hat{a} = 0.95$ (right) the agreement between the three black lines with analogous meaning is rather poor. The origin of these differences is unclear at the moment, but maybe due to remaining differences in the dynamics (see discussion in text) or actual discrepancies in the implementations. Notably the oscillation of the total energy flux is physical and reflects the θ-dependence of the background.

Table I in [87], and find as initial data $\hat{E} = 0.9837$, $\hat{L}_z/M = 4.7379$ and $\hat{Q}/M^2 = 9.9917$. At large $\hat{r}$ the frequencies of motion Ω_ϕ and Ω_θ are very small so that we had to lower the resolution to 4000×260 to simulate several periods at reasonable runtimes. The right panel of Fig. 5.3 shows that the *teukode* (solid black line) again approximately reproduces the correct total energy flux of Shibata (dashed black line). As expected, at large $\hat{r}$ the background is approaching spherical symmetry and therefore it comes as no surprise that the non-inclined circular orbit $i = 0°$ (value taken from Hughes) has approximately the same energy (dotted). In a third test, we consider a small spin $\hat{a} = 0.05$ and a strong-field orbit at $\hat{r} = 7$. Such an orbit was investigated in [60] for $i = 60.17°$. We find initial data $\hat{E} = 0.9445$, $\hat{L}_z/M = 1.7322$ and $\hat{Q}/M^2 = 9.1263$. The left panel of Fig. 5.4 shows the comparison between Hughes (dashed), a quadrupole-order PN-result of Ryan [159] (dotted) and the *teukode* (solid black) at resolution 3600×300. Evidently, the low spin does not lead to significant θ-dependence and the total flux is approximately constant in time. All three lines are in good agreement. Finally, our most challenging test is the second case shown in [60], i.e. $\hat{a} = 0.95$ and $\hat{r} = 7$ at $i = 62.43°$. We find initial data $\hat{E} = 0.9372$, $\hat{L}_z/M = 1.4757$ and $\hat{Q}/M^2 = 7.9888$ and use a resolution of 4000×300. In contrast to the previous configurations, the total flux as computed from the *teukode* (solid black) exhibits a visible oscillation. This oscillation is physical. It reflects the θ-dependence of the background and the inherent change of instantaneous radiation emission along the orbit. The reference lines from Hughes (dashed black) and Ryan (dotted) have to be understood as average numbers as well. The agreement is reasonable also in this test, but not perfect. Thus, for inclined strong-field orbits on a highly spinning

background it cannot be excluded that the *teukode* produces a result significantly different from the reference code of Hughes. Searching for reasons, the comparison of the found frequencies $\hat{\Omega}_\phi = 5.4765\text{e-}02$ and $\hat{\Omega}_\theta = 4.9812\text{e-}02$, where $\hat{\Omega} = M\Omega$, with the stated values ($\hat{\Omega}_\phi = 5.424\text{e-}02$, $\hat{\Omega}_\theta = 4.954\text{e-}02$) indicates that there are non-negligible differences in the dynamics, which could explain the deviations. Further tests are needed to unambiguously validate the code for investigations of non-equatorial motions (not further covered here).

Radial infalls in the equatorial plane

A complementary test to the circular motion is the radial infall. Bernuzzi, Nagar and Zenginoğlu have set up a 1+1-RWZ-equation-solver [130, 131, 132, 133], which gives us the great opportunity to check the *teukode* for arbitrary trajectories with $\hat{a} = 0$. First, we shall consider a head-on-collision with $\phi_p = 0$ in the equatorial plane (cmp. also Martel [160, 161]). Further, we shall skim through the topic of particle-BH scattering experiments by comparison of energy spectra for exemplary plunge trajectories, which includes the complication of $\phi_p = \phi_p(\tau)$, with data kindly provided to us by Berti et al. [156]. Finally, though not discussed here, we mention that waveforms obtained from particle-BH scattering provide important insights also for full numerical relativity; for remnants of spinning neutron star collapses the qualitative features of the waveforms were shown to be in complete accord with our data [162].

Let us begin by considering a radial trajectory which starts from rest at $\hat{r}_0 = 25$ and falls along the x-axis. We focus on the $\ell = 2$, $m = 0$ multipole. Note that the axis of the infall is, in principle, irrelevant for a spherically symmetric background, but the usage of spin-weighted spherical harmonics for mode decomposition fixes the axes. Therefore, infall along the x-axis triggers other multipoles than infall along the z-axis; in our case $m \neq 0$ multipoles are present, whereas analogous calculations for the radial plunge along the z-axis [160] only have to account for the polar $m = 0$ multipoles. In Fig. 5.5 we compare the outcome of the *teukode* with the RWZ-solver [130] in the $\ell = 2$, $m = 0$ RWZ variable $\Psi_{20}(u)$ (left) and in the Weyl mode $\Psi_{4\ 20}(u)$ (right). Recall that we can convert our evolution variables to the RWZ-normalised strain and vice versa using Eq.'s (A.9) and (4.6). We find visual agreement with quantitative differences below a few percent. Notably, the $\Psi_{4\ 20}(u)$ variables (right panel) agree also during the tail phase, and both codes capture the correct tail decay. Instead, repeating the tail comparison in the RWZ-normalised variable Ψ_{20} (not shown), tiny errors appear and the tail cannot be captured as well. The compilation of the correct tail is very sensitive and is one of the few cases which require artificial dissipation. The remaining differences at the few percent level can be assigned to the differences in the setups of the independent codes. For instance, the waveforms from the RWZ code were, in this case, not extracted at scri but at large finite radius $\hat{r} \sim 2200$. Furthermore, the RWZ code solves the linearized Hamiltonian
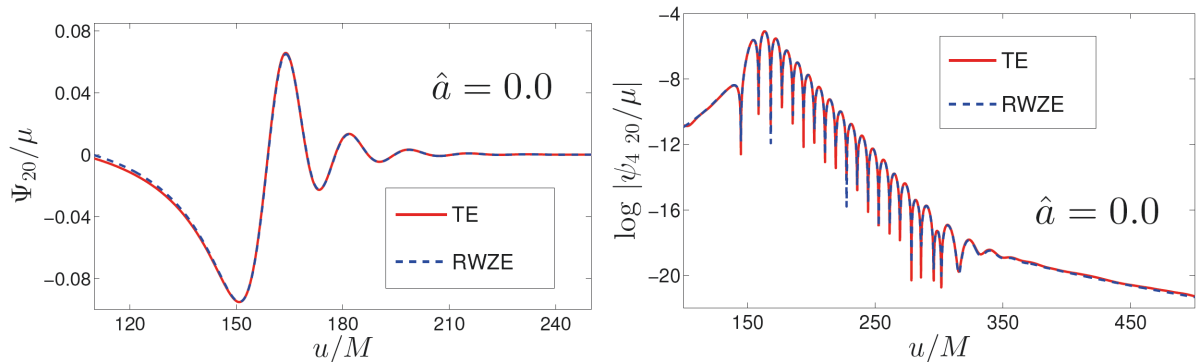
Figure 5.5: Comparison of waveforms for geodetic radial infall dynamics obtained from solving the 2+1 TKEQ (here labelled TE) and the 1+1 RWZ-equation (RWZE) respectively. The particle is falling from $\hat{r}_0 = 25$ along the x-axis onto a Schwarzschild black hole. Left: The $\ell = 2$, $m = 0$ waveform in the RWZ-normalised strain $\Psi_{20}(u)$ at $\mathcal{J}$ (*teukode*) and large finite radius (RWZE code). Right: The $\ell = 2$, $m = 0$ component of the Weyl scalar $\Psi_4{}_{20}$ at $\mathcal{J}$ (*teukode*) and large finite radius (RWZE code) in logarithmic scale. Plots adopted from [H2].

constraint [160] and imposes physical initial data. On the contrary, the *teukode* starts from $\psi = \dot{\psi} = 0$, which is an unphysical choice in the presence of a matter perturbation; an initial burst of junk radiation pollutes the simulation for at least $\sim 200M$.

Dropping the $\phi_p(\tau) = 0$ condition, one can do more generic scattering experiments. We investigate these by measuring the energy spectra, which are especially interesting for ultra-relativistic collisions with $v \sim c$. The work of Berti et al. [156] provides a description of the topic and serves as a target solution for us. The authors integrate the geodesic EOM starting with $r_p \approx \infty$, and solve the inhomogeneous Sasaki-Nakamura equation (cf. Sec. (3.2)) on a Schwarzschild background to calculate the GWs. The considered "shooting" experiments are typically classified as either plunging or scattering. A useful characterisation is given by the impact parameter b, which describes the distance of the central BH to the initially straight motion of the particle (artificially continued until perpendicularly meeting a radial coordinate line). Further, one can argue in terms of the energy of the particle, E, with respect to the maximum of the effective potential for the radial motion $V_{\text{eff}}(L_z)$. Unbound orbits with $E^2 > V_{\text{eff}}^{\max}$ are captured, while those with $E^2 < V_{\text{eff}}^{\max}$ are scattered. Solving $E^2 = V_{\text{eff}}^{\max}$ for L_z, gives a critical value $L_{z,\text{crit}}$ with the condition for plunge being $L_z < L_{z,\text{crit}}$. The critical impact parameter can be found by the relation $b = L_z(E^2 - 1)^{-1/2}$. Finally, trajectories can be classified by (E, L_r), where $L_r = L_z/L_{z,\text{crit}}$. Here we settle with a qualitative comparison for two exemplary $\hat{E} = 1$ trajectories with $L_r = 0, 0.9999$. The obtained *teukode* waves are converted to RWZ-normalised variables $\Psi_{\ell m}$ and Fourier-transformed within *matlab*. The energy spectra is found following Eq. (20) of [163]

$$\frac{dE_{\ell m}}{d\omega} = \frac{1}{16\pi^2} \frac{(\ell + 2)!}{(\ell - 2)!} \cdot \omega^2 \cdot |\text{FFT}(\Psi_{\ell m})|^2 \quad , \tag{5.2}$$
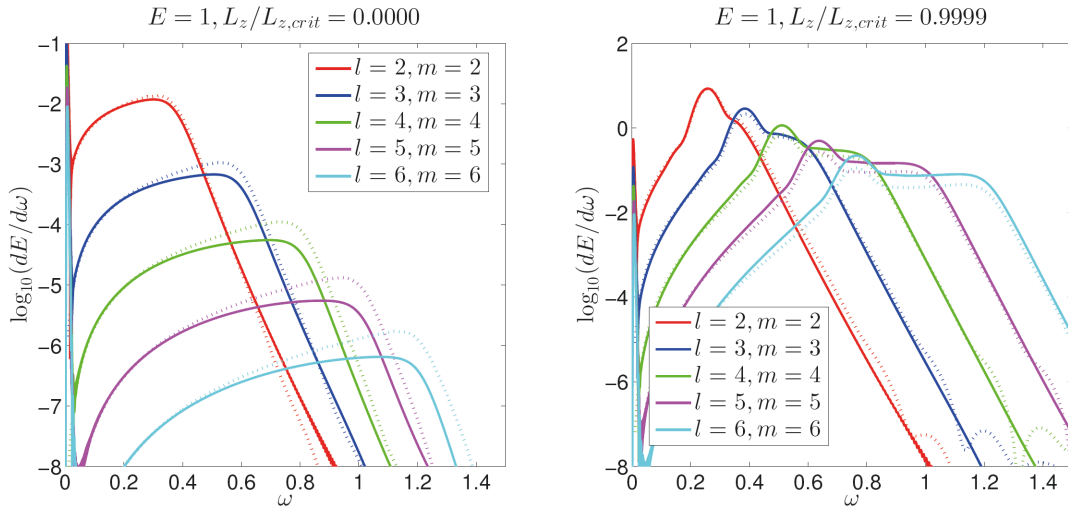
Figure 5.6: Energy spectra for particle-BH collisions without spins. Comparison of the multipolar energy spectra for the dominant modes between the *teukode* (solid lines) and the target data of Berti et al. [156] (dotted lines) for a direct plunge $L_z = 0$ (left panel), and an indirect plunge with $L_r = 0.9999$ (right panel). The agreement is qualitatively convincing, but an arbitrary scale factor was used for the *teukode* data (see text); the reason is as yet unclear.

where ω is obtained in our data sets as $\omega_k = k\, 2\, \pi/d\tau$ with $k \in \{1, \cdots, k_{\max}\}$ and $k_{\max}$ the number of data points used for the Fourier transformation. Fig. 5.6 compares the results from the *teukode* (solid lines), scaled with a not, as yet, understood factor of 10^{-2} to obtain agreement, with the target data of [156]. The left panel shows the head-on-collision and the right panel the indirect plunge with $L_r = 0.9999$. Apart from the scale factor, the agreement is qualitatively nice. The reasons for remaining deviations are potentially (i) the low resolution 2400×60 employed in our tests, (ii) the underresolution of large radii $\hat{r} > 50$ in our hyperboloidal coordinates, and (iii) the junk radiation due to the unphysical initial data; we observed that the here used large initial separations, $\hat{r} \sim 500$, significantly amplify the spurious radiation. Note also that, motivated from the condition that scattering orbits for $\hat{E} > 1$ only exist for $L_z > 4M$, we used $L_{z,\text{crit}} = 4M$ as a rough approximation. The exact solution for $L_{z,\text{crit}}$ is different, unless $\hat{a} = 0$, and would have to be found numerically. This is surely another reason for the deviations seen in the indirect plunge case. In summary, the qualitative agreement is satisfactory at this stage of testing. When the reason for the disagreement can be identified, the interesting plunges with $\hat{E} \gg 1$ and $\hat{a} \neq 0$ are a promising direction of future research.

5.2.3   Realistic inspiral trajectories from EOB-dynamics

A final test is the treatment of realistic inspiral trajectories created within the EOB-formalism (see Sec. (2.2)). For the dynamics we use a mass ratio of $\mu/M = 10^{-3}$. Note that the mass ratio is just a scale parameter for geodesics, but for EOB-dynamics it determines the deviation of the RR from the particle limit. Starting at $\hat{r} = 7$, the chosen
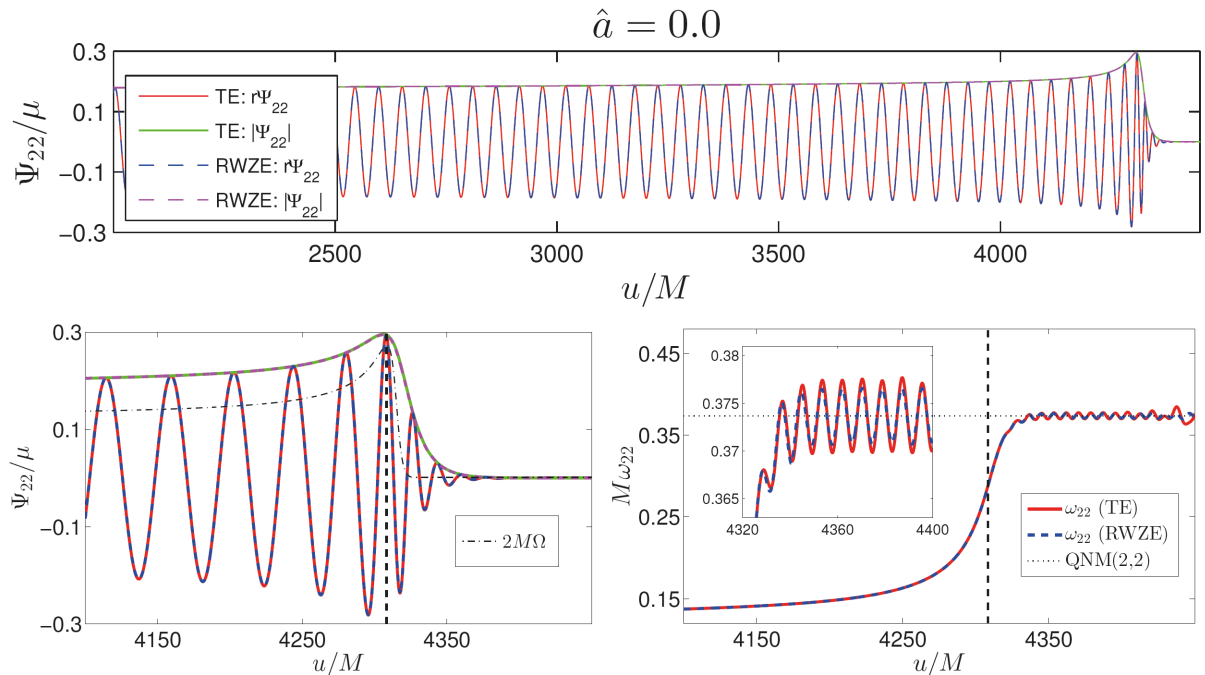
Figure 5.7: Case $\hat{a} = 0$: comparison between the inspiral-merger-ringdown waveforms with $\mu/M = 10^{-3}$ obtained from solving the 2+1 TKEQ (here labelled TE) and the 1+1 RWZ-equation (RWZE) respectively. Shown is the real part of the Ψ_{22} metric waveform (in the RWZ-convention), extracted at $\mathcal{J}^+$, together with its amplitude and frequency. The vertical lines mark the time of the light-ring crossing ($t_{\text{LR}} = u_{\text{LR}} = u_{\Omega^{\max}} = 4308.39M$). Twice the orbital frequency $2\hat{\Omega} = 2M\Omega$ is represented with a dash-dotted black line (bottom left panel). The dotted horizontal line in the right panel marks the fundamental QNM frequency [72]. Plots adopted from [H2].

mass-ratio yields ~ 37 orbits during the quasi-circular motion, which slowly descends to a plunge, with the particle crossing the light-ring (LR) at $r_{\text{LR}} = 3M$ at $u_{\text{LR}} = 4308.39M$. This is the same dynamics already used for the convergence test in Sec. 5.2.1. This dynamics was already extensively studied in [130, 131, 132, 133] by means of the RWZ-solver. Our next check is to reproduce those results. Note that in this case the RWZ-code was already developed to use the hyperboloidal layer technique [126], and thus we can compare the two wave-signals directly at scri.

Figure 5.7 shows the complete (inspiral-plunge-ringdown) waveform in the RWZ-normalised variable Ψ_{22}. The figure proves the excellent visual agreement of both waveforms also during the ringdown. To assess the absolute differences in phase and amplitude no time/phase alignment is required when employing the retarded time u (see Sec. B.2) because both sets of waveforms are extracted at scri and generated from the same dynamics. We measured phase differences of $\Delta\phi_{\ell m} = |\phi_{\ell m}^{\text{TE}} - \phi_{\ell m}^{\text{RWZ}}| \lesssim 10^{-3}$ rad until the time of the light ring crossing ($u_{\text{LR}} = 4308.39M$), and below 0.01 during the ringdown ($u > u_{\text{LR}}$). The relative amplitude differences $\Delta A_{\ell m}/A_{\ell m}$ are at the order of 0.25% until u_{LR} and remain $\lesssim 1.25\%$ during the ringdown. These numbers are illustrated for the dominant multipoles in Fig. 9 of [H2]. The agreement between the independent codes is small enough to be neglected
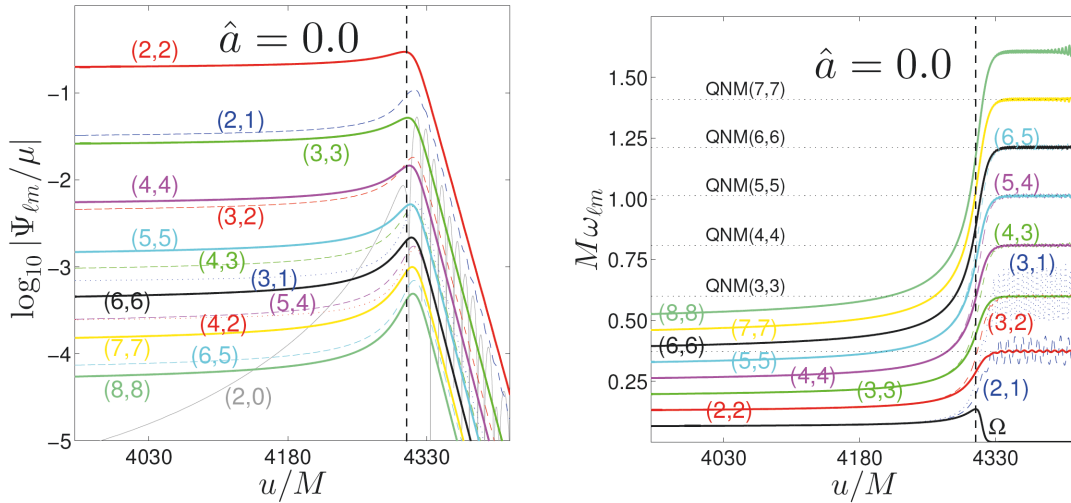
Figure 5.8: Multipolar structure around merger of the $\Psi_{\ell m}$ waveforms for $\mu/M = 10^{-3}$ and $\hat{a} = 0$ as obtained from the *teukode*. Amplitudes (left) and GW frequencies (right). The vertical lines correspond to the maximum of the orbital frequency $u_{\Omega^{\max}} = u_{\mathrm{LR}} = 4308.39M$ (the orbital frequency $\hat{\Omega}$ is also shown as a black line in the right panel). The horizontal lines in the right panel mark the QNM frequencies of the black hole [72]. Plots adopted from [H2].

for many practical purposes. In particular, the phase differences $\Delta\phi_{\ell m}$ are significantly smaller than the differences between the RWZ-waveforms and the EOB-waveforms as found in [131, 164]. Still, one has to mention that the differences in phase and amplitude are larger than those estimated from the self-convergence test shown above. Consequently, they must be of systematic origin and are not expected to disappear with resolution. The reason is likely to reside in one of the conceptual differences between the independent codes, like, e.g., (i) the different coordinate systems and their implied numerical features, (ii) the treatment of different equations (1+1 vs. 2+1), and (iii) many different details in the implementation and the source treatment. Furthermore, the strain-variables $h_{\ell m}$ or $\Psi_{\ell m}$ have to be reconstructed from the *teukode* evolution variable ψ by integration.

Besides the obvious comparison of the strain variables, we compare the multipolar amplitudes and frequencies near merger in Fig. 5.8. The analysis is visually in agreement with the analysis of the multipolar structure performed in [130] (see Fig. 3 therein). Note in particular the oscillations in the quasi-normal mode (QNM) frequencies; e.g., in modes $(2, 1), (2, 2)$ and $(3, 1)$. As explained in [52, 130], these oscillations arise from the interference between positive and negative QNM frequencies triggered during the plunge (cf. also [76]). Going quantitative, one can measure characteristics of the waveform at merger, where it contains most structure. For instance, in [131] it was reported for the first time that the peak of the $\ell = m = 2$ multipole is located earlier in time than the peak of the orbital frequency (for $\hat{a} = 0$ this peak coincides with u_{LR}, i.e. $u_{\mathrm{LR}} = u_{\Omega^{\max}}$), which we can confirm here. Table L.1 in Appendix L presents our measurements of such characteristic

features like (i) the time lags $\Delta t_{\ell m}$ between the time when the amplitude of the ℓm-mode peaks $u_{A_{\ell m}^{\max}}$ and the time when the orbital frequency peaks $u_{\Omega^{\max}}$, (ii) the peak value of the amplitude $A_{\ell m}^{\max}$, and (iii) the wave's frequency at the time $u_{A_{\ell m}^{\max}}$. The *teukode* values and the RWZ-code ones (in brackets) agree nicely.

In conclusion, the results of the RWZ-code can be fully confirmed with the *teukode*. This gives great confidence that the implementation is correct, at least for $\hat{a} = 0$. Analogous confirmations for $\hat{a} \neq 0$ EOB-inspirals will be given in Sec. 7.1, in the analysis of the waveform characteristics over a set of spin parameters $\hat{a}$.

5.2.4 Comparison of different δ-representations

In Sec. 4.3.3 we have introduced the discrete δ-representations with 2-point-support from [91]. This representation shall be labelled as option (a) in order to compare it with other options derived in [91]. We omit the explicit prescriptions since irrelevant for the argument, but distinguish those options by their essential property, i.e. the number of points involved. We call the 4-point option "(b)" and the variable $2n$-point option "(c)". Options (a),(b) and (c) shall be contrasted with the simple, narrow Gaussian method with respect to the criteria of stability and accuracy.

Fig. 5.9 shows the waveforms obtained with the different δ options in the case of an EOB-inspiral trajectory (left panel) and a circular equatorial orbit at $\hat{r} = 10$ (right panel) respectively. As revealed by the left panel, a fast motion of the source in radial direction, as experienced here towards merger, can be problematic when the particle is modelled with the discrete representations. Severe numerical instabilities in the evolution variable ψ_m (shown for $m = 2$) are visible for options (a), (b) and (c) with $n = 4$. A larger support makes the discrete representation smoother, but only for $n \gtrsim 6$ option (c) gives noise-free results comparable to using the smooth, analytical Gaussian. On the contrary, in case of circular orbits (right panel) all options are unproblematic. In fact, options (a) and (b) are most accurate and efficient. The accuracy of the circular fluxes is here evaluated against a reference solution taken from the frequency domain results of Ref. [91] shown as a black solid line. Notably, the Gaussian is more accurate than option (c) with $n = 6$.

Summarising our findings, the tests indicate that the few-point discrete δ methods are efficient and accurate for simulating a source that is effectively *not* moving on the computational domain; e.g., for circular orbits. In case the particle is moving in r or θ the respective δ must contain enough points ($n \gtrsim 6$) to avoid instabilities. Alternatively one has to apply filtering of the high-frequency noise (not done here, see [112]). For such large a support, the discrete delta results in lower accuracy than the simple Gaussian. Thus, we conclude that, choosing between these methods, a generically moving particle
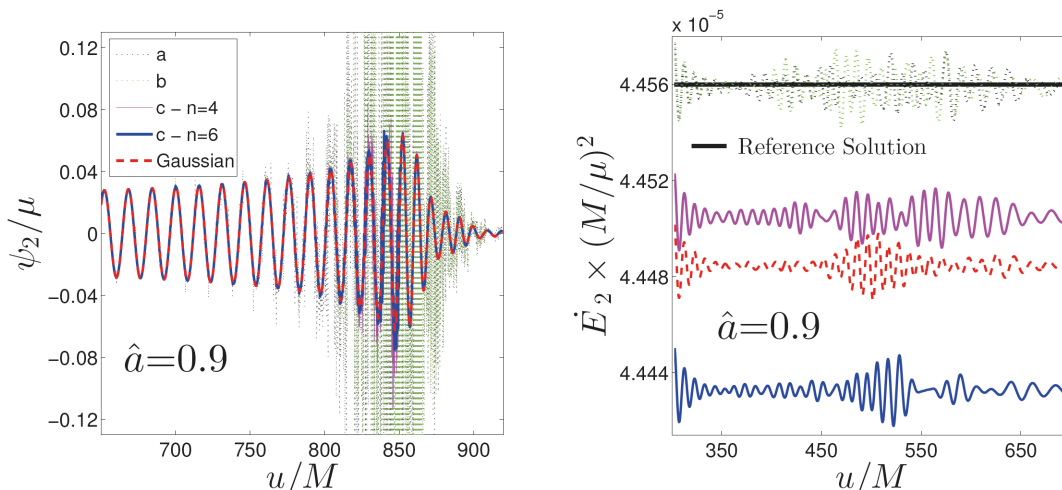
Figure 5.9: Weaknesses (left) and strengths (right) of the $2n$-points discrete δ-representations [91] in comparison with the narrow Gaussian method (see Sec. 4.3.3). The left panel refers to an EOB-inspiral trajectory. Instabilities in the evolution variable ψ_m, here $m = 2$, occur when the δ comprises too few points. The label (a) refers to the 2-point prescription discussed in Sec. 4.3.3. Label (b) is a 4-point option, label (c) a variable $2n$ option (both are not quoted explicitly in the text, see [91] for details). The results are noise-free when enough points are employed, i.e. $2n \gtrsim 12$. The right panel considers a different kind of trajectory: circular motion at fixed $r_p = 10M, \theta_p = \pi/2$. In this effectively non-moving case a particle can be modelled stably by all tested δ-options. We compare the accuracy in the resulting $m = 2$ GW fluxes. Options (a) and (b) come closest to the reference solution taken from the frequency domain results of Ref. [91], shown as a black solid line. Option (c) with $n \gtrsim 6$ is less accurate than the Gaussian representation. Plots adopted from [H2].

is modelled most efficiently with the Gaussian method. Finally, note that one can mix the representations, i.e. for equatorial motion, as considered in this thesis, the best option is to use a Gaussian representation in radial direction and a discrete representation in θ direction (we adopted option (b) in most cases).

5.3 Remaining limitations

So far, this chapter was dedicated to attesting the new approach to solve the TKEQ in the time-domain capability and applicability, and our implementation in the *teukode* correctness and accuracy. Still, there are some minor flaws which deserve short comments.

First, let us point out a certain drawback which comes along with the extensively mentioned benefits of using hyperboloidal coordinates; this drawback is, of course, much smaller than the benefits. As discussed in [H1] for the late-time tail experiments, one observes that the decay is "slower" at scri than at finite radii. This leads to the decaying perturbation pile up at the last grid point, creating a shock-like shape of ψ in radial direction. Numerically, this introduces inaccuracies in the derivatives and, especially for spectral methods, this behaviour is suboptimal. One might be able to conceive more optimal coordinates that prevent such piling up. Note, however, that this is a detail in a very special application and the approach, as it is, performed extraordinary well in the

measurement of late-time decay rates. For the waveforms of point-particle simulations the late-time tail behaviour is not of interest. In this context, another minor problem appears. On the hyperboloidal grid large radii $r_p \gtrsim 50M$ are underresolved. For us those weak-field orbits are only interesting to compare with infalls from "infinity" or with Post-Newtonian results. The main focus is the strong-field regime, where the hyperboloidal coordinates demonstrate their full power. In that sense, one might call our approach "strong-field".

While the above issues are small details, there is one major technical limitation. For too large ratios N_θ/N_ρ the simulations go unstable, in the sense that at some point the solution starts to grow without bound. A rough ratio of 1 : 12 turns out to be stable in most cases, but the ratio is sensitive to the considered values of m and $\hat{a}$. For the challenging $\hat{a} = 0.9999$ case we had to increase the ratio to 1 : 30 to attain well-behaved numerics at $m = 6$. Dissipation and fine-tuning of the CFL-factor can help to enhance the range of stable ratios, but not drastically. For equatorial motion this is not a severe problem because the few points discrete δ-prescriptions can be applied and yield excellent accuracy at low θ resolutions of ~ 150 points. For non-equatorial motion, however, we have to use the Gaussian method (see Sec. 5.2.4). For comparable accuracy we then have to increase the resolution to $N_\theta \sim 400$ points. This, in turn, requires to increase the radial resolution to at least $N_\rho = 4800$ to obey the ratio for stability, though 2400 would probably be enough in terms of accuracy. This seems to be the main limitation of the whole approach and the only issue one should really improve if possible. In fact, it might be an intrinsic problem of the TKEQ because, judging from the ratios of points stated in the works that follow Krivan et al.'s original approach (e.g., 64000×64 in [117] or 3125×32 in [75]), one might suspect that it suffers from the same limitation in the ratio of points. As a first option to alleviate the problem, we implemented the 3rd order partially-implicit Runge-Kutta (PIRK) scheme as described in [165]. In [166] this method has been used successfully for wavelike equations in spherical coordinates to suppress instabilities which usually arise at the coordinate singularities $r = 0$ and $\theta = 0, \pi$. The idea is to separate off the problematic terms in the evolution equations into an operator called $\mathcal{L}_2$, which is then treated implicitly. We suspect our instabilities to arise from the axis and, therefore, choose $\mathcal{L}_2 = C_0\,\psi + C_\theta\partial_\theta\psi$, cf. Eq. (4.3) and the coefficients in App. C. Indeed, we observe that the ratio N_θ/N_ρ of stable simulations can be enhanced to some extent when using a PIRK scheme. Unfortunately, this success comes with the cost of a reduction of the CFL factor, i.e. the time stepping. Effectively, the gained stability from the PIRK scheme therefore relied on a similar increase of the computational costs, but with the collateral effect of dropping from fourth to third order in the time integration. At that point we decided to just accept the high resolutions needed for high θ accuracy, and to leave this problem for future work, possibly addressing the boundary condition in θ.

CHAPTER 6

Vacuum Teukolsky-Equation

The vacuum TKEQ describes the evolution of some initial perturbation on a BH background. Physically, a perturbed BH can be viewed as an approximation of, for example, the end state of a compact binary system after merger, or of a collapsing hypermassive neutron star. Following the no-hair theorems, the body would radiate off the acquired higher multipoles and leave behind a settled BH solution. Naturally two questions arise, (i) what are the characteristic features of a typical decay, and (ii) does, indeed, every perturbation radiate away, i.e. is the Kerr BH stable against linear perturbation, especially in the nearly-extremal regime. We have performed analyses in both these directions.

In this chapter the investigations of [H0] are completed with the continuative studies published in [H1]. Note that, in contrast to the point-particle simulations (mainly discussed in this thesis), the following results were obtained with a spectral version of our *teukode* (as recalled in Sec. 5.1.1). Thus, the reader should not be confused when encountering the RT-coordinates T, R instead of the otherwise used HH-coordinates τ, ρ.

6.1 Late-time decay rates

The structure of the decay of perturbations on BH spacetimes is well-known. After the initial burst of radiation, one measures, for a certain time, an exponential decay modulated with frequencies characteristic of the BH's mass and angular momentum ("quasi-normal-modes (QNM) phase") $\psi \propto e^{i\omega t}$, where ω is complex. The real part of ω determines the characteristic frequency; the imaginary part the damping time. At some point, the oscillations die out, and a phase of polynomial decay $\psi \propto t^{-\mu}$, with μ an integer power, follows. This is called the late-time "tail" phase.

Starting from the pioneering work of Price [167], the evolution pattern of vacuum perturbations has been observed in uncountable studies of decays since to be universal for any spin weight s. Fig. 6.1 shows a typical evolution of a $s = -2$ perturbation on a BH background. The different lines correspond to different observers along the radial direction of the used RT-grid (see Sec. B.3). One clearly recognises the mentioned QNM-phase
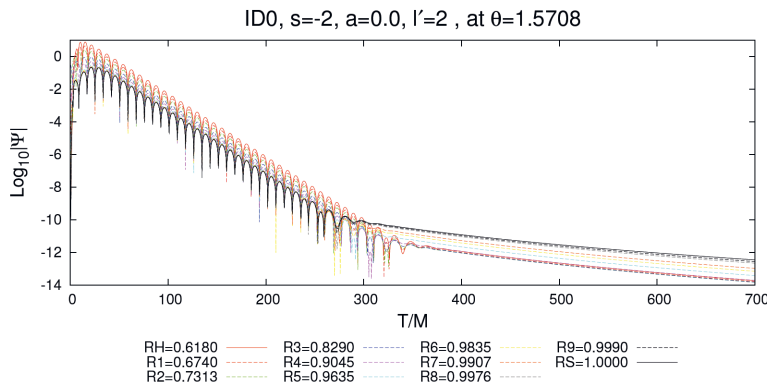
Figure 6.1: A typical decay of some perturbation field ψ on a BH spacetime, illustrated at the example of a gravitational $s = -2$ perturbation on Schwarzschild with an initial Gaussian profile in radial direction and a Y_{-220} profile in angular direction (see text for meaning of initial data ID0). The different lines refer to different observers distributed along the hyperboloidal RT-grid in the equatorial plane (see Sec. B.3), from the horizon R_H to scri R_S. The logarithmic scale reveals the exponential decay in the quasi-normal-mode phase. Counting the peaks over time allows to measure the characteristic frequencies of the oscillations. The late-time tail phase starts in this case at $T \sim 300M$. For $T > 300M$ the decay rates μ could be read-off in a log-log plot as the gradients of straight lines.

for $T \lesssim 300M$, and a subsequent tail phase. Detailed analyses of such data allows to measure the characteristic QNM-frequencies and the decay rates. In addition, analytical computations can provide a cross-check, see [H1] for the relevant literature. We checked a few QNM-frequencies for confirming our simulations and found discrepancies at the order of 1% compared to the tables of Berti et al. [72].

The main goal of our work on vacuum perturbations of a rotating Kerr BH was to set up compilations for the decay rates μ in dependence of several parameters; the considered ℓ-component (with respect to $Y_{s\ell m}$) of the field variable ψ_m, the spin-weight s of the perturbation, and the initial angular distribution specified by a $Y_{s\ell'm}$ profile. Furthermore, we studied the influence of four different kinds of initial data, labelled by ID0, ID1, ID2, ID3 and defined by

$$
\text{ID0 / ID2} : \begin{cases} \psi(0, R) & = G(R) \,/\, 1 \\ \partial_T \, \psi(0, R) & = 0 \end{cases} \tag{6.1}
$$

$$
\text{ID1 / ID3} : \begin{cases} \psi(0, R) & = 0 \\ \partial_T \, \psi(0, R) & = G(R) \,/\, 1 \,, \end{cases} \tag{6.2}
$$

where $G(R) = e^{-(w/2)\,(R-R_0)^2}$ with $w > 0$, and, mentioned to avoid confusion, the slashes denote case distinction rather than division. These initial data are commonly used in the literature, in which they are referred to as stationary (ID0, ID2) or non-stationary (ID1, ID3), and compact (ID0, ID1) or non-compact (ID2, ID3) support initial data. We verified that the Gaussian reasonably models a compact support initial data by checking

that, with the typical parameters for w and R_0, the field values reach below the round-off level at radii well away from the horizon and $\mathcal{J}^+$; for example, setting $w = 3000$ and $R_0 = 0.8$, $G(R) \sim 10^{-38}$ at the horizon (for $a = 0.9$ $R_+ \approx 0.5222$) and at $R = 1$.

The decay rates of a $\psi_{\ell m}$ field are different for $\hat{a} = 0.0$ and $\hat{a} \neq 0$ because in the spherically symmetric case the $Y_{s\ell m}$ modes completely decouple. The larger is $|\hat{a}|$ the stronger is the coupling between different ℓ-modes (of the same parity) and, therefore, small spins might lead numerically to in-between results for the decay rates. Only for $t \to \infty$ all (non-extremal) rotating BHs will share the same values. We focused on a Kerr BH with $\hat{a} = 0.9$ and the axisymmetric $m = 0$ modes. The measured decay rates were predicted to be different at finite radii and scri, and for the special case $s > 0, m = 0$ to even take a distinct value at the horizon. This fact is referred to as "splitting" of decay rates. In [H1] we were able to verify numerically, for the first time, the splitting into three distinct values if $s > 0, m = 0$. Additionally, we verified the possibility of an intermediate behaviour of decay rates, i.e. one which is different at early and late times, so one should distinguish between splitting in time and space. For brevity, more details on this phenomenon are omitted here but can be found in [168, 169, 127, H1]. The results of our computations on decay rates are summarised in Tables H.3 and H.4 in the Appendix H. We stress that the usage of quadruple-precision was essential in finding many of the stated values. This is one reason why these tables are among the most detailed of their kind presented in the literature. In the conclusion of [H1] the found decay rates were abstracted into empirical formulas. Meanwhile, [170] confirmed many of the measured decay rates and the mentioned splitting phenomenon with an independent implementation, which is based as well on the hyperboloidal approach to the TKEQ of Ch. 4, albeit in a modified coordinate system. Notably, our experiments also confirm Hod's analytic predictions [102, 103, 104] for the values of decay rates, with only a small discrepancy for the $\ell' = \ell_0 + 1$ cases, where ℓ_0 labels the lowest allowed ℓ-mode following $\ell \geq \max(|s|, |m|)$. Encouraged by a small set of comparative simulations for $m \neq 0$ (see Tab. H.2), for which the values surprisingly agreed also in the problematic cases, we were able to find the origin of the discrepancy for $m = 0$. Following Hod's derivation (based on a Green's function approach to the TKEQ) it turned out that the final formulas missed a small case distinction for the $s \neq 0, m = 0$ case. The correction yielded, indeed, the numerical results obtained from our simulations, see Appendix B of [H1] for our explicit calculation.

6.2   (Nearly-)Extremal Kerr backgrounds

The study of nearly-extremal black holes $\hat{a} \to 1$ is astrophysically less relevant but interesting from a theoretical point of view. For instance, one would like to prove dynamical stability of the Kerr BH against linear perturbations, and find out how the decay might
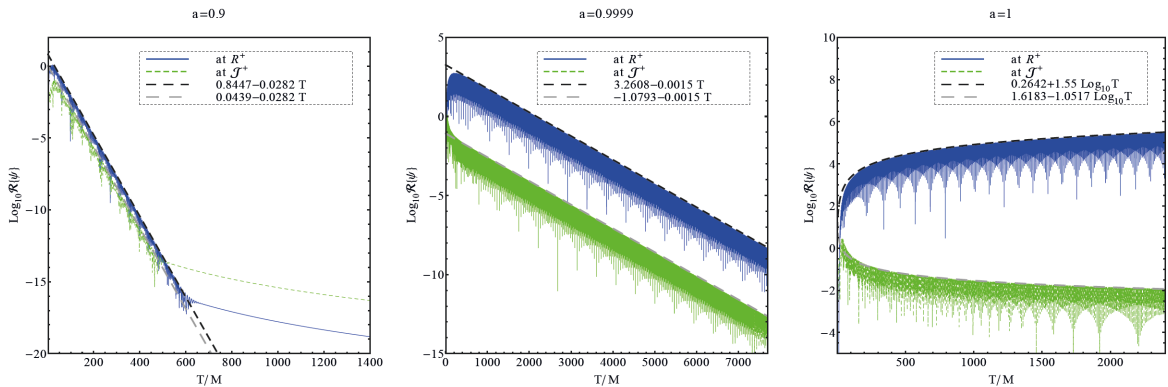
Figure 6.2: Late time decay of $s = -2$ non-axisymmetric perturbations for highly spinning backgrounds. The plots show the field variable $\Re\{\psi\}$ extracted at $R = R_+$ and $R = 1$ (i.e. at $\mathcal{J}^+$) and $\theta = \pi/2$ for $a \in \{0.9, 0.9999\}$ (setting $M = 1$ here) and $\theta = 1.1345$ for $\hat{a} = 1$. Initial data are ID1 and $l' = m = 2$. From left to right the field decays with a power law tail ($\hat{a} = 0.9$), or with an oscillatory behaviour damped by either a slow exponential ($a = 0.9999$) or a power law $1/T$ ($\hat{a} = 1$). Plots taken from [H1].

change in this limit. References [95, 96] have investigated the problem both analytically and numerically using the original time-domain Teukolsky code discussed in [90, 80, 94] (cf. Sec. 3.3). They found that $\ell = m$ QNM-modes could become extremely long-lived on a nearly-extremal Kerr background and that, in the extreme case, the late-time tail is replaced by an oscillatory signal with amplitude decaying as t^{-1}. These observations were explained in terms of a "superradiance resonance cavity". That is to say, near the BH, the effective potential of the background features a peak, which acts reflective for frequencies close to $\omega \approx m\,\omega_H$ (the horizon frequency). QNMs of such frequencies are produced in the nearly-extremal case and are subsequently trapped between the BH and the peak. Only by leakage through the potential barrier escape is possible, which explains the very long-lived and characteristic decay features for $\hat{a} \to 1$.

This section presents a cross-check of the results of [95, 96] against results from our implementation (as published in [H1]). We analysed the evolution for $s = -2, m = 2$ and $s = 0, m = 1$ perturbations as the angular momentum of the background approaches the extremal value $\hat{a} = 1$. The feasibility of such challenging parameters supports, again, the robustness of our approach.

Indeed, our results seem to confirm the investigations of [95, 96]. Varying the angular momentum $\hat{a}$ in the range $\{0.9, 0.99, 0.999, 0.9999, 1\}$ in otherwise identical simulations, we observe qualitative alterations in the decay behaviour. The signal is more and more dominated by a gradually prolonged oscillatory QNM phase, i.e. the damping time increases. For $\hat{a} \to 1$ the amplitude of the oscillating field grows by a few orders of magnitude near R_+ at the beginning of the simulation (especially for $s = -2$), before the exponential decay in a typical QNM-phase begins. For three representative values $\hat{a} \in \{0.9, 0.9999, 1\}$ the evolution of the field variable ψ for $s = -2$, $m = 2$ and ID $\ell' = 2$ is illustrated in

Fig. 6.2 at the horizon (blue lines) and $\mathcal{J}^+$ (green lines). On the simulated timescale, a power law tail is observed for values $\hat{a} \leq 0.999$, see $\hat{a} = 0.9$ case in the left panel. For larger values, like $\hat{a} = 0.9999$ (central panel), an oscillatory and exponentially damped behaviour dominates at both the horizon and $\mathcal{J}^+$. For $\hat{a} = 0.9999$ a power law tail is not observed up to $T \sim 8000M$, but may eventually arise at later times. This behaviour is consistent with the findings of [95, 96], and with the given explanation in terms of modes trapped in the superradiance resonance cavity. For $\hat{a} = 1$ the field remains oscillatory, but it does not decay exponentially during the simulated time. At the horizon the field amplitude is still growing at $T = 2500M$, while at $\mathcal{J}^+$ the decay departs from an exponential law. A similar qualitative behaviour is observed in the case $s = 0$, $m = 1$ with ID $\ell' = 1$ (not shown here).

To convince oneself of the correctness of the results, it is instructive to compare the complex QNM-frequencies $\omega = (\omega_r, \omega_i)$ extracted from the $s = -2$ simulations with the data of Berti et al. [72] (listed there up to $\hat{a} = 0.9999$). The real part corresponds to the frequency of oscillation while the imaginary part gives the damping time. We measure the frequency of the fundamental (longest lived) QNM by counting the periods of the signal for long times. Damping times (or ω_i) are extracted by fitting the envelope (maxima) of the field. For instance, the envelope of the field for $\hat{a} = 0.9999$ is well represented by the fit $\log_{10} |\Re\psi| = c - 0.0015064\,T$, where c is some constant. Note that the fitting coefficient proportional to T needs to be divided by $\log_{10}(e)$ to obtain $\omega_i = 0.0035$. Analogous measurements for $\hat{a} = 0.9$ yield $\omega \sim (0.6827, 0.0649)$ both at R_+ and $\mathcal{J}^+$, which agrees very well with the target values $(0.6715, 0.0649)$. For $\hat{a} = 0.99$ we find $\omega \sim (0.8747, 0.0294)$ compared to the target values of $(0.8709, 0.0294)$, and for $\hat{a} = 0.999$ we get $\omega \sim (0.9584, 0.0105)$ compared to $(0.9558, 0.0105)$. For $\hat{a} = 0.9999$ we obtain $\omega \sim (0.9862, 0.0035)$, again in agreement with $(0.9857, 0.0035)$. These results, also, agree with the analytical formulas for QNM frequencies of nearly-extremal BHs proposed in [171, 172]; the discrepancy is $(\sim 1\%, \sim 5\%)$ for $\hat{a} = 0.99$ and $(\sim 0.02\%, \sim 0.5\%)$ for $\hat{a} = 0.9999$. Note that for $\hat{a} \to 1$ the frequencies of the overtones accumulate around the same value, which reduces errors when counting the peaks. In the extreme case, we measure slightly different values at $\mathcal{J}^+$, $\omega_r \sim 0.9970$, and at R_+, $\omega_r \sim 1.0015$. It is interesting to notice that both are very close to the superradiance frequency $\omega_+ = m\,a/(2\,M\,r_+) \xrightarrow{a \to M} m/2|_{M=1}$. (This holds, by the way, for the extreme-case result for $s = 0$ with $m = 1$ as well; we measure $\omega_r \sim 0.5011$ both at R_+ and $\mathcal{J}^+$). The envelope of the field is best fitted by the power law $\log_{10} |\Re\psi| = c - 1.05 \log_{10} T$, for some constant c. Thus, our numerical results support the expected late-time $\psi \sim T^{-1}$ behaviour for $s = -2$ [96].

Finally, let us comment on the numerical challenges connected to such (nearly-)extremal

setups. As mentioned above, close to the horizon the evolution of the field starts with a strong growth, which does not propagate to the rest of the grid. This leads to a step-like shape of ψ in radial direction which makes numerical differentiation difficult. If the number of radial grid points N_R is too small, the convergence is then corrupted and instabilities may arise. Therefore, we had to employ exorbitantly high number of points for a spectral evolution; $N_R \sim 281$ points for non-extreme cases, and, in the extreme case, $N_R = 561$ for $s = 0$ and $N_R = 701$ for $s = -2$. In addition, the interesting transition from the QNM-phase to the tail phase is progressively postponed to $T \to \infty$, i.e. we need to simulate for long times. For this reason, further technical development, like a parallelisation or a mesh-refinement, would seem desirable to perform more detailed numerical studies of the extremal regime.

GWs from a non-spinning particle

The major goal of this thesis was to develop an accurate GW-laboratory, appropriate to study binary BH mergers numerically in the test-particle limit. The *teukode* provides such a tool. In Ch. 5 it was already described in detail, and validated against plenty of numerical results available in the literature on GWs from a nonspinning particle. In this chapter we present those results which exceed previous knowledge on the topic (cmp. [H2, H3]); notably, the novel results span almost the complete range of Kerr spin parameter values $\hat{a} \in (-0.9999, 0.9999)^1$.

In Sec. 7.1 we start with a multipolar analysis of merger waveforms on Kerr. Such analysis was shown for Schwarzschild in [130] and repeated in Sec. 5.2 here, and for Kerr, in a more restricted range of spin parameters, in [135]. Second goes a study of the fluxes which are emitted during the inspiral, both to the horizon and scri. In this context, we devise a numerical procedure for the construction of a consistent numerical RR. The third topic is the exploration of kick and antikick velocities in the test-particle limit, over the whole parameter range $\hat{a} \in (-0.9999, 0.9999)$.

All the following results relate to particle trajectories that describe realistic inspiral motion, i.e. from adiabatically shrinking circular orbits over a plunge to merger. These trajectories are created from EOB-dynamics with a RR which in the $\mu \rightarrow 0$ limit resembles the circular orbits fluxes from a test-particle. Here, to obtain shorter inspirals, we use a mass ratio $\mu/M = 10^{-3}$, which implies a certain deviation of the RR from the test-particle limit (see Sec. 2.2). We have performed inspiral simulations for all ψ_m-fields in $m \in \{0, 1, .., 8\}$ for a number of background spins $\hat{a} \in (-0.9999, 0.9999)$. Table J.1 in App. J collects detailed information on the used dynamics; e.g., the time when the particle crosses the light-ring (LR) u_{LR}, etc.. The simulations featured resolutions of 3600×160 points and sixth order finite differencing. The angular δ function was modelled by the 4-point δ prescription called option (b) in Sec. 5.2.4, the radial δ by a narrow Gaussian.

---

[1]Even higher spins $\hat{a}$, up to the extremal case, are, in principle, feasible with our approach, but require progressively larger resolutions to avoid instabilities. As explained for the vacuum TKEQ in Sec. 6.2, a spectral implementation requires ~ 700 collocation points to allow extremal simulations, so the here used finite-differencing version would devour costs too high for going beyond $\hat{a} = 0.9999$.

The nearly-extremal simulations were exceptionally challenging so that we employed the resolution 3600×100 and artificial dissipation to guarantee well-behaved numerics, in the sense that no unbounded growth of the numerical solution is observed (see Sec. 5.3).

7.1   Multipolar analysis of merger waveforms

The waveform from a compact binary system consists of the inspiral, plunge, merger and the ringdown to a settled BH solution. The plunge happens on a rather short timescale compared to the inspiral, i.e. the gradual advance through a series of shrinking circular orbits (~ 25 in most of our simulations). Yet, the merger signal, which is understood here as the segment of the waveform $\sim \pm 100M$ around the time when the particle crosses the horizon, is very interesting; it is the strongest part of the signal and it can exhibit complicated structure, which may convey additional physical information. In this section the simulations of GWs from EOB-dynamics are analysed with respect to the multipolar hierarchy and multipolar frequencies at merger. Further, characteristic numbers are measured and discussed, possibly useful for building waveform models (cf. [H2]).

7.1.1   Multipolar amplitudes

Let us first discuss qualitatively the relative importance of the dimensionless amplitudes $\hat{A}_{\ell m} \equiv A_{\ell m}/\mu \equiv |\Psi_{\ell m}|/\mu = |h_{\ell m}|/\left(\mu\sqrt{\frac{(\ell+2)!}{(\ell-2)!}}\right)$, where the $\Psi_{\ell m}$ are the RWZ-normalised strain variables and $h_{\ell m} = h_{+,\ell m} - \mathrm{i}\, h_{\times,\ell m}$ (cf. Eq. (4.6)). These amplitudes are collected for the six representative cases $\hat{a} = \{\pm 0.9999, \pm 0.9, \pm 0.5\}$ in Fig. 7.1. The use of the advanced time u allows the connection of the dynamics with the waveform (see Sec. B.2). For instance, the vertical dashed lines indicate the time when the particle crosses the light-ring (LR); except for $\hat{a} = 0.9999$, in which case it marks the end of the trajectory, slightly before the LR. The reason for not reaching the LR is the inaccuracy of the used RR for fast prograde orbits $\hat{a} \to 1$, as examined below in Sec. 7.2. In these cases unphysically high losses of angular momentum lead to a corruption of the dynamics close to the merger. Note, though, that the LR for $\hat{a} = 0.9999$ is at $r = 1.05M$, and thus we do expect to not miss a significant part of the wave creation.

Surveying Fig. 7.1, let us concentrate first on the relative importance of the modes during the inspiral. Above all, it is striking that in all six panels of Fig. 7.1, i.e. over the whole range of $\hat{a}$, the 22-mode is the most dominant. The relative ordering for other modes can change with the spin $\hat{a}$. For $\hat{a} = -0.9999$ the hierarchy reads 22, 21, 33, 44, 32, 55. Instead, for $\hat{a} = 0.9999$ the rearranged hierarchy reads 22, 33, 44, 21, 32, 55. Diagonal modes like the 33 and the 44 are more dominant for $\hat{a} = 0.9999$. It is an overall conclusion to be drawn that for $\hat{a} \to -1$ the sub-diagonal modes become increasingly important. For concreteness, look at the retrograde orbits in the top row of Fig. 7.1; the 21 is clearly
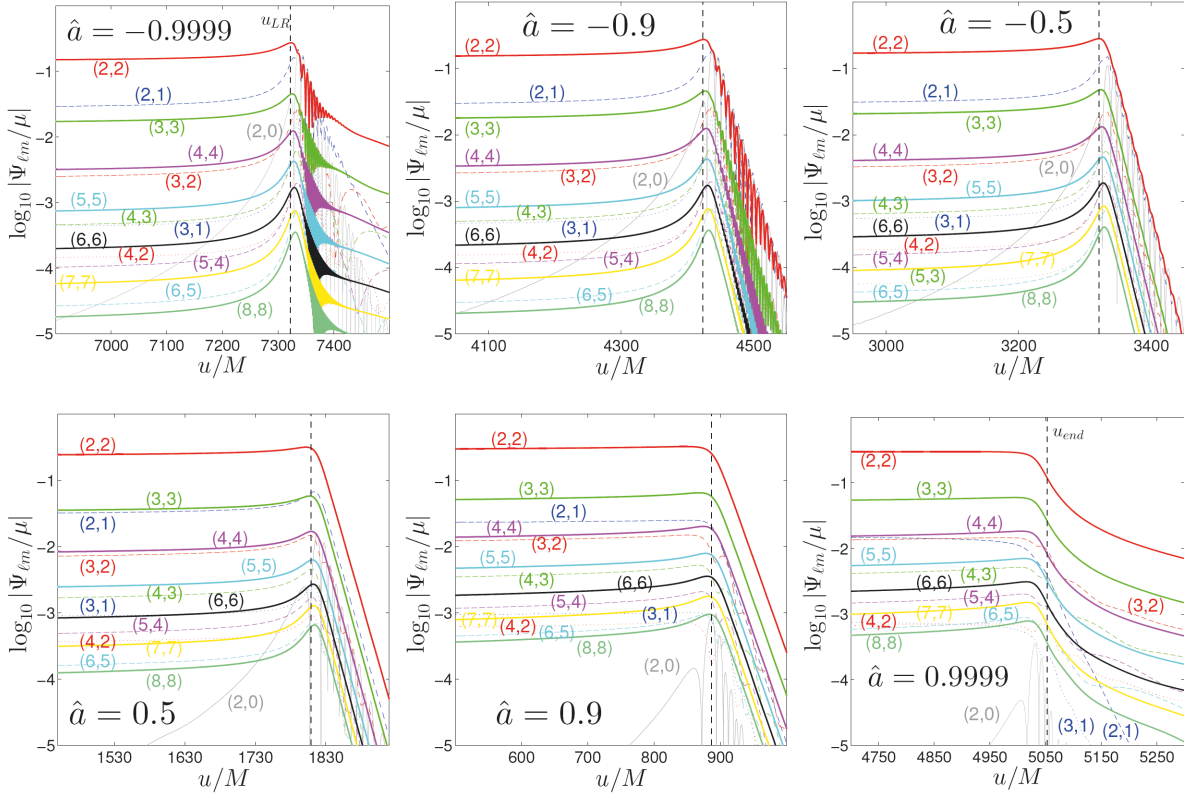
Figure 7.1: Multipolar amplitudes of the $\Psi_{\ell m}$ waveforms for six representative values of $\hat{a}$ and the mass ratio $\mu/M = 10^{-3}$. The vertical line on each plot marks the time when the particle crosses the LR, except for $+0.9999$, in which case it marks the end of the trajectory (in this case our trajectory stops slightly before the LR, see text). The $\hat{a} = 0.9$ case can be compared with Fig. 3 of [135]. Plots adopted from [H2].

stronger than the 33, and, at merger, even close to the 22 for $\hat{a} \to -1$. The situation is gradually reversed for the prograde orbits, shown in the three bottom panels; the 33 becomes stronger than the 21. For $\hat{a} = 0.9999$ even the 44 is strong enough to fight with the 21 for the third place, whereas for $\hat{a} = -0.9999$ the 44 is smaller than the 21 by an order of magnitude. Monitoring the absolute values, it is noticeable that part of the modes, mostly the diagonal ones, display a rather large increase from retrograde to prograde orbits. For example, $\hat{A}_{88}$ grows from $\sim 10^{-4.9}$ at $\hat{a} = -0.9999$ to $\sim 10^{-3.2}$ at $\hat{a} = 0.9999$. Also, some off-diagonal modes grow strongly in absolute value with $\hat{a}$. For example, $\hat{A}_{32}$ from $\sim 10^{-2.6}$ to $\sim 10^{-1.9}$, and $\hat{A}_{43}$ from $\sim 10^{-3.2}$ to $\sim 10^{-2.3}$. For other modes the growth with $\hat{a}$ is much less pronounced. For example, the 22 grows from $\sim 10^{-0.9}$ to $\sim 10^{-0.5}$. Similarly, the 21 and the 31 remain rather constant.

Including now the merger part to the discussion, another interesting observation is that the amplitudes of all the modes are extremely flat over time for $\hat{a} \to 1$. For example, the 22 mode in the bottom right panel of Fig. 7.1 very clearly misses the usual ascent at

merger. This observation was made first by Taracchini et al. [76] in a similar[2] analysis of test-particle Teukolsky-waveforms, using the latest version of the Khanna et al. code (cf. Sec. 3.3). Taracchini et al. give a convincing explanation of the flattening in terms of the dynamics. The relative closeness of the LSO and the LR to the horizon for $\hat{a} \rightarrow 1$ results in a gradually shorter final plunge phase. In other words, for $\hat{a} \rightarrow 1$ we basically consider a quasi-circular inspiral from $\hat{r}_0$ all the way to the horizon. The amount of non-circularity in the dynamics can be nicely quantified by looking at the radial momentum p_{r*} around the LR crossing time. Fig. 15 of [H2] reveals the strong magnification of p_{r*} for $\hat{a} \rightarrow -1$, i.e. we see a sudden change in the motion due to acceleration in radial direction, which is absent for $\hat{a} \rightarrow 1$ dynamics. The resulting uniformity in the dynamics is simply translated to the waveform.

Let us now have a closer look at the actual merger-signal. For $\hat{a} \rightarrow 1$, the mentioned flattening of the waveforms greatly simplifies the analysis because the hierarchy of the modes basically remains the same at merger as during the inspiral. Comparing the bottom row of Fig. 7.1, this holds more or less for all prograde orbits. Even for $\hat{a} = 0.5$, which contains a clearly distinguished plunge phase, the growth of the signal at merger is shallow and very homogeneous for all modes. One exception is given by the 20 mode (gray), which arises out of nothing to play a significant role at merger. In general, one may record that the articulate plunge in retrograde orbits (top row) seems to introduce more prominent reallocations in the relative importance of the modes at merger than for prograde orbits (bottom row). For example, looking at the top middle panel for $\hat{a} = -0.9$, the off diagonal modes seem to grow stronger at merger than the diagonal ones. The 32 and the 31 overtake the 44; the 43 the 55 (also the 54 the 66 etc.). To conclude our discussion of hierarchies at merger, the picture is complemented by the illustration of the factual maximum values $\hat{A}_{\ell m}^{\max} = \max(\hat{A}_{\ell m})$ in Fig. 7.2, which can be compared with the $\hat{a} = 0$ case in Appendix A of [131]. The left plot shows the variation of $\hat{A}_{\ell m}^{\max}$ versus $(\ell, m, \hat{a})$ in a 3d figure. The right panel is a 2d projection over $\hat{a}$. A similar plot can be found in the Appendix of [76]. The most surprising feature, which can be added to the discussion in [76], is the enormous importance of $m = 0$ modes for fast retrograde orbits. For $\hat{a} = -0.9999$ the maxima of the amplitudes follow the ranking 22,21,20,33,32,31,30, whereas for $\hat{a} = 0.9999$ the order reads 22,33,44,21,32,43. Apart from the $m = 0$ modes, other off-diagonal modes become increasingly important at merger for $\hat{a} \rightarrow -1$, similarly to the discussion for the inspiral. This observation is highlighted in the 2d-cut in Fig. 7.2. A reasonable explanation, similarly to the discussion of the flattening of the waveforms, can be given in

---

[2]A major difference to our study is in the radiation reaction used in the dynamics. Taracchini et al. use highly accurate numerical energy fluxes, found from the frequency domain code of Hughes [91, 62, 60], instead of applying resummed analytical PN-information. Thus, horizon fluxes are included, which become very important due to superradiance for $\hat{a} \rightarrow 1$ at $r_p \rightarrow r_{\mathrm{LR}}$ (see Fig. 5 of [76]). The range of spins considered in [76] is $\hat{a} \in (-0.99, 0.99)$.
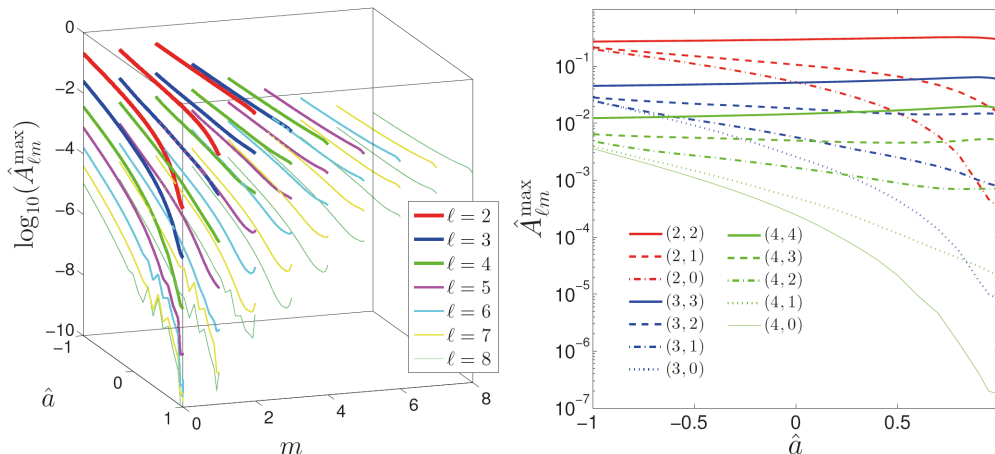
Figure 7.2: Peaks of multipolar amplitudes as functions of the black hole spin. Left: 3D visualisation of all the data up to $\ell = m = 8$. Different ℓ-modes are classified by colours, the spin dependence is shown by solid lines. Right: peaks of the dominant multipoles as functions of the spin. This plot is a 2D cut of the left panel (restricting to $\ell \leq 4$). The $m = 0$ and $m = 1$ modes have the largest amplitudes for $\hat{a} \to -1$. The diagonal modes have weak dependence on the spin and attain a maximum for spin values $0.8 < \hat{a} < 1$. The right panel can be compared with Fig. 14 in [76]. Plots adopted from [H2].

terms of the last part of the dynamics, which are progressively dominated by the plunge for $\hat{a} \to -1$.

Coming to the subsequent ringdown phase, we have omitted a detailed analysis so far. Visually, it is obvious from Fig. 7.1 that for nearly-extremal cases the trapping of modes, as discussed for the vacuum TKEQ in Sec. 6.2 (see also [95, 96, 72, H1, 20]), leads to very weakly damped QNMs. In the nearly-extremal regime the exponential decay holds for much longer times than shown in the plots. For $\hat{a} = 0.9999$ we made an exemplary computation of the damping time by fitting over the interval $u \in [5400M, 6800M]$. For $(\ell, m) = \{(2, 2), (2, 1), (3, 3)\}$ the resulting damping exponents of the dominant overtones are $\{-3.52, -39.11, -3.61\} \times 10^{-3}$ respectively. These numbers match at $\lesssim 4\%$ with the corresponding values for free QNM ringing [72].

7.1.2 Multipolar frequencies

Further physical insights can be gained by monitoring the frequencies $M\omega_{\ell m}$ of the multipolar waveforms around merger. These can be determined numerically by extracting the phase and subsequent differentiation. Alternatively, one can use use $\omega_{\ell m} = -\mathcal{I}(\dot{h}_{\ell m}/h_{\ell m})$, which is usually more accurate in our case. A collection of these frequencies for the six representative cases $\hat{a} = \{\pm 0.9999, \pm 0.9, \pm 0.5\}$ is given in Fig. 7.3. The vertical dashed lines mark again the time of the LR-crossing, except for $\hat{a} = 0.9999$, in which case the trajectory stops before the LR (see discussion in Sec. 7.1.1). The dotted horizontal lines represent the BH QNM-frequencies, as stated in [72]. In addition, there is the orbital frequency Ω of the particle, shown as a solid black line. One immediately notices two
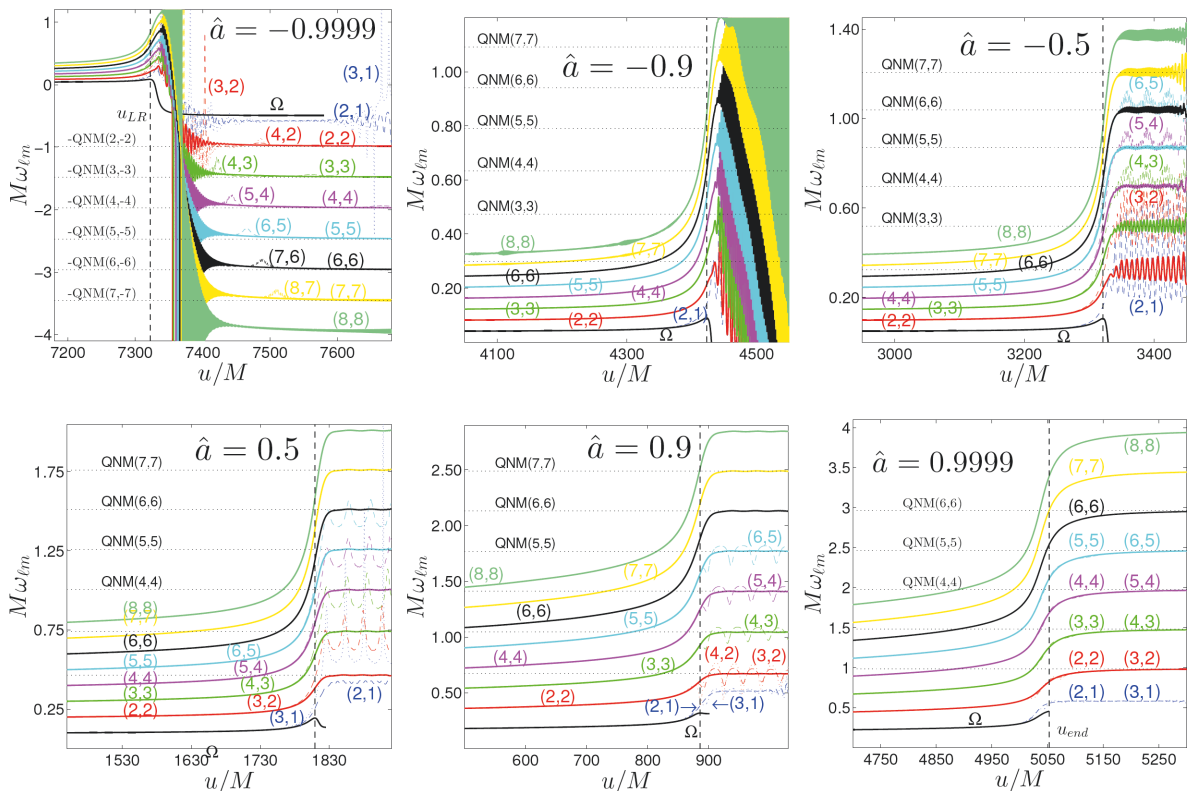
Figure 7.3: Multipolar GW frequencies of the $\Psi_{\ell m}$ waveforms for six representative values of $\hat{a}$ and the mass ratio $\mu/M = 10^{-3}$. The vertical line on each plot marks the crossing of the LR, except for $+0.9999$, where it marks the end of the trajectory (in this case our trajectory stops slightly before the LR, see discussion in text). Horizontal lines are the QNM frequencies of [72]. For nearly-extremal negative $\hat{a}$ we find negative frequencies due to the inversion of the trajectory after the LSO-crossing. The panels can be compared with Fig's. 7-10 in [76] and Fig. 4 of [135]. Plots adopted from [H2].

general features, (i) during the inspiral the multipolar frequencies are characterised by $\omega_{\ell m} = m\,\Omega$, i.e. just multiples of the particle's frequency, and (ii) after the LR-crossing, any ℓm-mode assumes some fundamental ($n = 0$) QNM-frequency $\sigma_{\ell'm'}$. For the prograde $\hat{a} \to 1$ cases, to which we count the $\hat{a} = 0.9$ case here, the frequencies ω_{mm} and $\omega_{m+1,m}$ assume the QNM value σ_{mm}. The $\hat{a} = 0.5$ case reveals a slight alteration. Though also featuring ω_{mm} approach σ_{mm}, we observe $\omega_{m+1,m}$ oscillate around $\sigma_{m+1,m+1}$; e.g, the ω_{65} around the σ_{66} value, and, accordingly, the ω_{54} around the σ_{55} value. Altogether, these findings confirm the analysis of [76], where, for $\hat{a} = 0.99$, Fig. 7 shows the ω_{32} approach σ_{22}, and for $\hat{a} = 0.0$, instead, σ_{32} . Notably, the small oscillations of the multipolar frequency around some QNM-value are a generic feature, and were already observed for $\hat{a} = 0.0$ in [52, 130] (cf. also Fig. 5.7 in this thesis). References [52, 130] explained that the oscillations have a physical reason, namely the interference of $\pm m$-modes. During the plunge both of them can be triggered, which explains why the oscillations vanish for $\hat{a} \to 1$. In this case the inspiral is quasi-circular until the very end, a plunge is basically absent. To understand the effect, we follow the argument given in Sec. V of [76]. The an-

gular part of the TKEQ, explicitly separable in the frequency domain, Eq. (3.6), admits a pair of QNM-solutions $\sigma_{\ell \pm m}$ for the eigenvalue $\mathcal{E}_{s\ell m}$. In other words, $\sigma_{\ell \pm m}$ are two possible solutions that can be superposed. Thus, if we solve for a given $S_{s\ell m}$-mode, we may, in principle, see both $\pm m$-frequency contributions. If, due to a change in the rotation sense of the orbit, both are triggered, we observe interference. The argument holds, similarly, for a $Y_{s\ell m}$ mode because it contains contributions from all S_{sjm} modes (in many cases, though, $Y_{s\ell m} \approx S_{s\ell m}$). The dramatic change of the pictures, from right to left in the top row of Fig. 7.3, reflects this interference of $\pm m$ modes in a fascinating and illuminating way. For $\hat{a} \to -1$ the trajectories develop a turning point due to the increasing strength of the frame dragging as the particle approaches the BH. At the turning point the motion of the particle stops being retrograde and follows, instead, the BH rotation, as depicted for $\hat{a} = -0.9$ in Fig. 2.1. Note that for $\hat{a} = -0.9999$ several prograde orbits are traversed after the turning point. This switched rotation mainly triggers the opposite sign m-mode and, since our ℓm-projection is open to both $\pm m$-frequency solutions, we see $\omega_{\ell m}$ approach $-\sigma_{m,-m}$ in the top left panel. Moreover, for $\hat{a} \neq 0$ the multipolar ℓm-frequencies can possess further structure due to the "mode-mixing" phenomenon; a given $Y_{s\ell m}$ mode projection does not decouple from other Y_{sjm} contributions, i.e. an ℓm-mode in the Y-basis can be influenced by other jm-modes (see [H1] for a discussion of this effect in the context of late-time tail decay rates). Only the eigenfunctions of Eq. (3.6), the $S_{s\ell m}$, would decouple upon evolution. Further fine-structure in the ringdown originates from the subdominant overtones ($n > 0$), which can modulate the signal at early times after merger, but die out faster than the fundamental one.

7.1.3 Characteristic numbers for waveform modelling

Waveform modelling, i.e. the (semi-)analytic representation of waveforms, is an extremely important topic. GW-detectors will require vast amounts of templates which cannot entirely be produced by numerical simulations. Our data may be useful in the future in this context. Therefore, we have measured some characteristic numbers usually employed within the EOB-model to describe the waveforms. In addition, the collection of these numbers provides a further cross-check with the corresponding literature.

The extracted values are (i) the dimensionless maxima of the amplitudes $\hat{A}_{\ell m}^{\max}$, and (ii) the frequencies of the multipolar waveforms at the time when that amplitude maximum is assumed $\omega_{\ell m}^{A_{\ell m}^{\max}}$. In addition, to match the possibly different waveform descriptions for inspiral+merger and the ringdown parts, models need anchor points. In the EOB-model the time at which the particle's frequency Ω peaks is assigned such role; one demands that h_{22} peaks at $t_{\Omega^{\max}}$. Other ℓm-modes are demanded to peak at slightly different times. These times are found by comparing the numerically obtained times at which an ℓm-mode

peaks with the time $t_{\Omega^{\mathrm{max}}}$ (see, e.g., discussion around Eq. (42) in [135]). We, therefore, evaluated the time-lag $\Delta t_{\ell m} = u_{A^{\mathrm{max}}_{\ell m}} - u_{\Omega^{\mathrm{max}}}$. Table L.1 lists our results for $\hat{a} = 0.0$, and Table L.2 for $\hat{a} \neq 0$. Note the remarkable agreement in the extracted key numbers with [135] (values in brackets), despite the differences in the totally independent codes and in the dynamics, due to the different RRs used.

7.2 Fluxes for realistic inspirals

Let us proceed with the discussion of energy and angular momentum fluxes. These are extracted from the waveforms using the time-domain formulas gathered in Sec. 4.2.2.

7.2.1 Horizon fluxes

Horizon fluxes are somewhat less thoroughly studied than the fluxes at scri. Probably because circular orbits experiments show that the absorbed fluxes are orders of magnitude smaller than those at scri, except for nearly-extremal spins and small distances to the lighting-ring (LR), cf. Fig. 1 of [62]. This section compares horizon fluxes with infinity fluxes for inspirals on Kerr backgrounds with $\hat{a} = \pm 0.9$ (cmp. [133] for $\hat{a} = 0.0$).

Surprisingly, the horizon fluxes for a complete inspiral of a particle on Kerr spacetime seem to be a missing piece in the literature. The reason is likely the unwieldiness of the only available practical formalism devised by Poisson [149] (cf. Sec. 4.2.2). Major complications of the formalism reside in the facts that (i) it relies on the ingoing radiation encoded in the Weyl-scalar $\Psi_{0,\mathrm{Hawk}}$ ("Hawk" for "Hawking-Hartle" tetrad, see Sec. 4.2.2), and (ii) on global in time information. The evolution of $\Psi_{0,\mathrm{Hawk}}$ follows the $s = +2$ instead of the $s = -2$ TKEQ. Of course, also the source terms are different and have to be computed independently. Maybe that is why $s = +2$ point particle simulations with the TKEQ are totally absent from the literature. The following study breaks new grounds in two aspects. For the first time, we (i) numerically evolve the $s = +2$ TKEQ with a point particle source term, and (ii) apply Poisson's formalism to compute the associated energy fluxes absorbed by the horizon during a realistic inspiral motion of a particle. Note that the time-domain horizon fluxes are computed in post-processing (cf. Sec. 5.1), and were cross-checked to be accurate for the case of circular orbits (cf. Sec. 5.2.2).

Fig. 7.4 compares the $m = 2$ horizon flux (red) with the infinity flux (blue) for EOB-inspirals on $\hat{a} = -0.9$ (left panel) and $\hat{a} = 0.9$ (right panel). The top panels show the most interesting segment around the merger; the bottom panels include the whole inspiral. Note that the horizon fluxes are scaled by arbitrary factors for this visual comparison. The first (second) vertical line marks the crossing of the LSO (LR). The horizontal lines show the circular orbits fluxes at the initial separation. It is reassuring to note that both
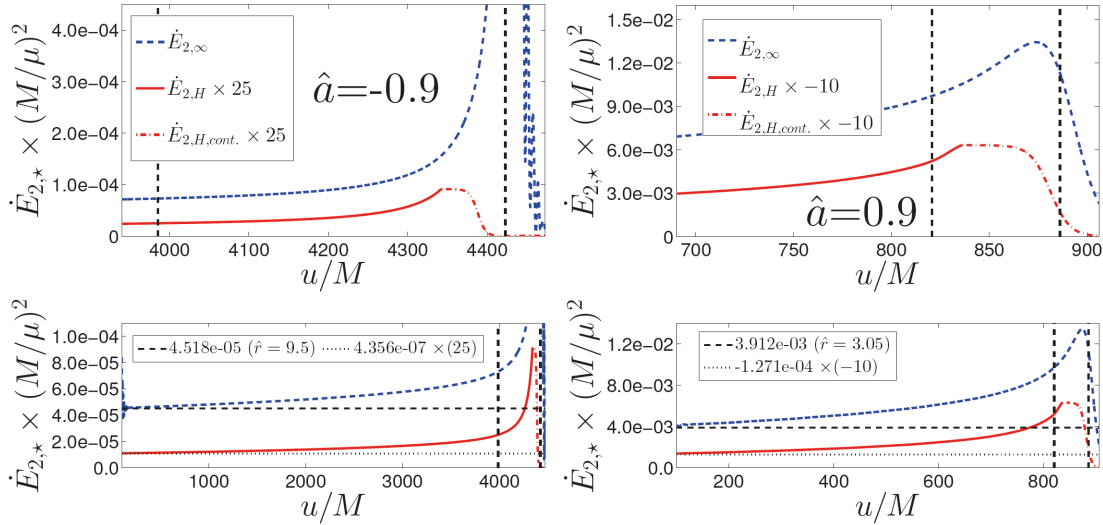
Figure 7.4: Comparison of $m = 2$ energy fluxes at the horizon (red) and scri (blue dashed) for $\hat{a} = -0.9$ (left panel) and $\hat{a} = 0.9$ (right panel). The time coordinate u refers to the retarded time for scri and the advanced time v for the horizon. The first (second) vertical line marks the crossing of the LSO (LR). The horizontal lines show the circular orbits fluxes at the initial separation. Note the absorbed fluxes are scaled by multiplicative factors, and, in the right panel, the factor is negative, i.e. the two fluxes have different signs. The relative importance of horizon fluxes to infinity fluxes remains at $\sim 1\%$ ($\sim 3\%$) for $\hat{a} = -0.9$ (0.9). The waveforms at the horizon are contaminated by the source at late times. As a consequence, the horizon fluxes are reliable until $v \approx v_{r_+} - 100M$, as marked by the solid linestyle (see discussion in the text). The dash-dotted linestyle illustrates the part which is analytically continued in order to build a self-consistent radiation reaction (see Sec. 7.2.3). Plots adopted from [H2].

horizon and infinity fluxes approach the circular orbits fluxes at the beginning of the inspiral (which starts from quasi-circular motion). The main observation in the present plots is that nothing surprising happens. Throughout the inspiral the horizon fluxes stay at the level of $\sim 1\%$ (3%) for $\hat{a} = -0.9$ ($\hat{a} = 0.9$) as expected from circular orbits experiments. Unfortunately, the most interesting part of the trajectory close to the merger cannot be analysed within the present formalism. The reason is twofold. First, note that the field variable ψ is singular at the particle's position (even though the singularity is smeared out in our Gaussian approximation). The energy flux can, therefore, not reliably be measured at the particle's position. Consequently, once the Gaussian reaches the horizon our waveform at the horizon is corrupted (see analogous discussion of the same problem in Sec. IV and Fig. 3 of [133]). While this issue alone would only spoil a negligible part of the late plunge, the Poisson formalism breaks down $\Delta v \sim 50M - 100M$ before the corruption of the horizon waveform. This early corruption is due to a second problem. At (advanced) time v the energy flux is computed from the waveform at times $v \in (v - \Delta v, v + \Delta v)$; the formalism looks to the past and, in particular, to the future. Thus, we can only measure the absorbed fluxes until some time Δv before the corruption of the waveform at merger. That is why without a further development of Poisson's formalism we can not deal with the interesting question of how important the horizon fluxes become

close to merger, especially for nearly-extremal backgrounds. For the time being, we can nevertheless work with the obtained energy fluxes (see Sec. 7.2.3) by continuing them in a reasonable manner. We choose to smoothly switch off the horizon fluxes with a hyperbolic tangent, as indicated in Fig. 7.4 by the dash-dotted red lines.

7.2.2 Consistency of the radiation reaction

Our setup allows an important cross-check of the analytical RR used in the EOB-dynamics (see Sec. 2.2.3). For consistency, one wants the angular momentum fluxes from a point particle, measured *a posteriori* from a TKEQ-simulation, to coincide with the *a priori* assumed energy losses which drive the particle away from the initial circular motion. Such an analysis was already performed for $\hat{a} = 0.0$ in [52, 130, 132], and yielded consistency up to the level of a few percent until merger (employing 5PN information for the RR). In [55], for $\hat{a} \neq 0$, the analytical RR was found to significantly overestimate the numerically found circular orbits fluxes for prograde orbits with $\hat{a} > 0.7$ (see also follow-up works [74, 135, 62, 76]). In Appendix C of [62] the analytic RR was enhanced by a fit to numerical circular orbits data, which drastically improved the agreement (see Fig. 13 therein). Here we will not employ the fit in order to check how the deviations present in the purely analytic information translate to the inspiral waveforms.

In our consistency check we test two prescriptions for producing the EOB-dynamics. They are basically the same, except for slightly different forms of the analytical RR. To understand the difference, recall that EOB-RRs are built from PN information, which are, in turn, expansions in the characteristic velocity v of the considered system. More concretely, the RR is built from several multiplicative factors, among them the Newtonian waveform $h_{\ell m}^{(\mathrm{N},\epsilon)}(v)$ and the "amplitude corrections" $\rho_{\ell m}(v)$ (see Sec. 2.2.3). A particle orbiting a Schwarzschild-BH on circular orbit is known to satisfy the "Kepler-constraint" $M = \Omega^2 r^3$ (see [173]). With a certain reinterpretation of the radius this constraint remains true for the Kerr background (see Eq. (53) in [H2]). For circular motion the implied orbital velocity $v = \Omega r$ provides a natural choice for the expansion parameter v. Instead, once the particle starts to deviate from circular motion and turns towards the plunge, the constraint has to be relaxed and some choice for v has to be made. A careful inspection of the literature reveals that two different choices have been made. On the one hand, there is the original prescription of reference [174] (and references therein), and, on the other hand, there is the suggestion of references [135, 129, 76]. We label the former choice by v_ϕ or "EOB(A)" and the latter by v_Ω or "EOB(B)". Heuristically, the v_ϕ prescription is less-Keplerian due to the complete relaxation of the constraint during the plunge, while v_Ω still imposes the constraint in some form. For explicit definitions of v_ϕ and v_Ω, and for a more detailed discussion of the subtle differences in their usage for the

Figure 7.5: Consistency of numerical and EOB fluxes for $\hat{a} = -0.9$ (left) and $\hat{a} = +0.9$ (right). The top panels show the two analytical EOB-flux-prescriptions (A), i.e. $-\hat{\mathcal{F}}_\phi^{v_\phi}$, and (B), i.e. $-\hat{\mathcal{F}}_\phi^{v_\Omega}$ (see text) and the respective numerical fluxes produced from the *teukode* (labelled here TE) when using those prescriptions. The vertical lines correspond to the LSO and the LR crossing. The horizontal line is the circular flux corresponding to the initial separation. The bottom panels show the difference between the numerical and the analytical flux when using prescription (A) (the respective line for (B) would lie on top in the plotted sector). Looking at the bottom left panel, the analytical prescriptions for $\hat{a} = -0.9$ match the numerical fluxes within $\lesssim 1\%$ until well beyond the LSO. Instead, for $\hat{a} = 0.9$ the analytical information is less accurate ($\sim 100\%$ off at LSO). The numerical fluxes (A) and (B) are visually the same in both plots, though close to the LR the flux prescriptions differ. Plots adopted from [H2].

RR the reader is referred to Sec. 5 of [H2]. In all experiments, apart from the tests in this section, we employed the v_ϕ prescription as our standard choice. The associated RR was built in [55] for modes $\ell, m \leq 4$ from the $\rho_{\ell m}$ stated up to 5.5PN in the nonspinning part and 4PN in the spinning part (cf. Tab. 1 in [55]), and augmented with the nonspinning 5.5PN expressions from [59] for modes $\ell, m \leq 8$.

For the consistency check we create two dynamics with the two slightly different flux prescriptions. For both we perform a set of nine simulations to obtain the ψ_m with $m \in \{0, 1, .., 8\}$; we are not performing $m < 0$ runs because for equatorial motion they are equivalent to the $m > 0$ ones, so we obtain the total flux by multiplying the $m > 0$ results by a factor two. The respective m-mode angular momentum fluxes to infinity, $\dot{J}_m$, are computed from the ψ_m (cf. Sec. 4.2.2), and summed up to a total flux $\dot{J}$. The total flux $\dot{J}$ is, then, contrasted with the analytical RRs employed for the dynamics, $-\hat{\mathcal{F}}_\phi^{v_\phi}$ and $-\hat{\mathcal{F}}_\phi^{v_\Omega}$. Fig. 7.5 shows this comparison for $\hat{a} = -0.9$ (left) and $\hat{a} = 0.9$ (right) in the relevant time interval before merger. The two vertical dashed lines on the plots indicate, from left to right, the LSO and the LR crossing; the horizontal lines show the circular orbits flux at the initial separation. Concentrating on the left panel, the main observation is the nice coincidence of all compared fluxes up to well beyond the LSO ($\sim 4000M$). More precisely, we conclude that, (i) $-\hat{\mathcal{F}}_\phi^{v_\phi}$ (green) and $-\hat{\mathcal{F}}_\phi^{v_\Omega}$ (magenta dashed) are visually on top of each other except for some $\sim 5M$ close to the LR, (ii) the two obtained TKEQ fluxes (red and blue dashed) agree perfectly, as will be quantified at the end of this paragraph, throughout the evolution, and (iii) the deviations between the "input" $-\hat{\mathcal{F}}_\phi^{v_\phi}$ and the
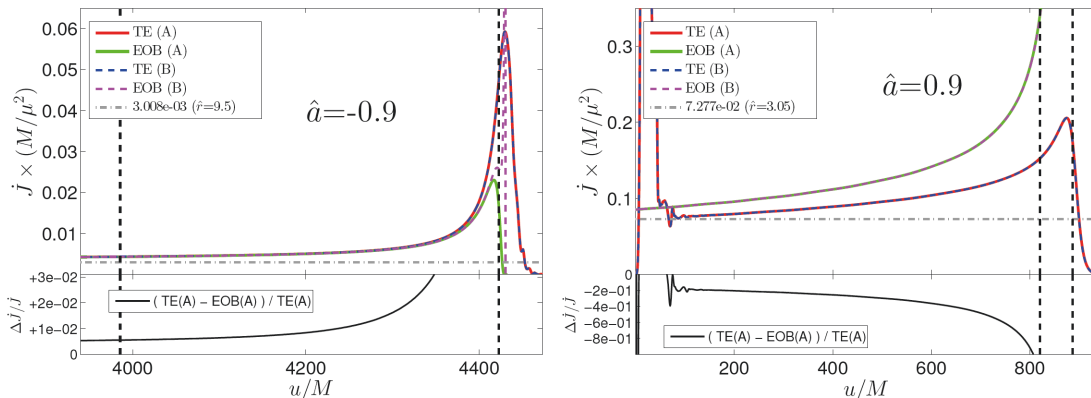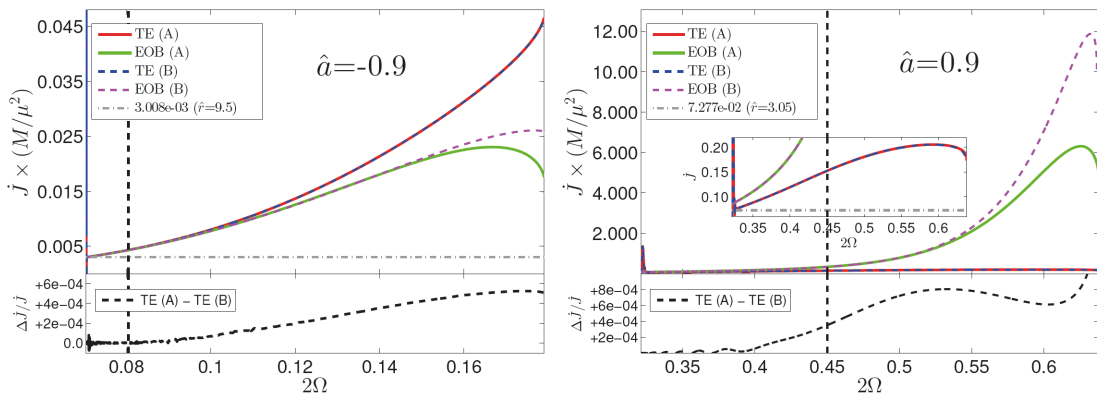
Figure 7.6: Consistency of numerical and EOB analytical fluxes for $\hat{a} = -0.9$ (left) and $\hat{a} = +0.9$ (right). The two major panels show the EOB-fluxes as obtained with prescriptions (A), i.e. $-\hat{\mathcal{F}}_\phi^{v_\phi}$, and (B), i.e. $-\hat{\mathcal{F}}_\phi^{v_\Omega}$, and the two respective numerical fluxes as functions of twice the orbital frequency $\hat{\Omega} = M\Omega$. The bottom panels show the difference between the numerical flux as produced with prescription (A) and (B). The vertical lines correspond to the LSO, the plots terminate at the LR. The horizontal line is the circular flux corresponding to the initial separation, which was chosen to provide ~ 25 orbits before merger. Note that all orbits are spent before the LSO, $\hat{\Omega} < \hat{\Omega}_{\mathrm{LSO}}$. Plots adopted from [H2].

"output" $\dot{J}$ lie at the level of $\sim 3\%$ almost up to the LR crossing, as highlighted in the small bottom panel. In summary, the retrograde case $\hat{a} = -0.9$ is excellently modelled with both the $(5.5 + 4)$PN accurate EOB-RRs. This demonstrates the fact that both, essentially, produce the same dynamics. The unphysical spike in $-\hat{\mathcal{F}}_\phi^{v_\Omega}$ (magenta) appears shortly after the LR, where the dynamics is quasi-geodesic and not sensitive to the RR. Therefore, it is a little bit academic to be bothered with discerning which of the two is actually the better choice. Nevertheless, we briefly investigated what happens for $\hat{a} \to -1$, and found the unphysical spike become more and more pronounced (cf. Fig. 5 in [H2] for the $\hat{a} = -0.99$ case). The reason is the behaviour of v_Ω, also shown in Fig. 5 in [H2] and discussed in the text around. Therefore, from a conceptual point of view, $-\hat{\mathcal{F}}_\phi^{v_\phi}$ is likely the advisable starting point for further improvements on the RR. Coming to the right panel of Fig. 7.5 for the prograde case, the agreement of both fluxes with the numerical outcome seems less convincing. One immediately notices the coincidence of $-\hat{\mathcal{F}}_\phi^{v_\phi}$ and $-\hat{\mathcal{F}}_\phi^{v_\Omega}$ on the one hand, and the two respective TKEQ fluxes on the other hand. But the agreement between the "input" and the "output" is poor, with $\sim 100\%$ deviation at the LSO crossing. Surveying the tendencies of the analytic RRs towards the horizontal line indicates already that even the circular orbits flux is not accurately reproduced. Probably this happens because the orbit starts at $\hat{r} = 3.05$, i.e. well in the strong-field regime. The comparison is complemented by Fig. 7.6, which illustrates the fluxes versus the particle's frequency Ω (instead of the more intuitive time coordinate). This produces a close-up of the LSO-LR regime (the plots end at the LR) because Ω sweeps through most of its range on that timescale and remains rather constant during the inspiral. One clearly perceives the good agreement of all curves in the $\hat{a} = -0.9$ case (left), while for $\hat{a} = 0.9$ (right)

the TKEQ-curves are not even comparable with the RRs on the same scale. The failure originates from the character of the dynamics for $\hat{a} \to 1$, in which case they start at small separations and are very circular until the end. Thus, the RR plays a significant role, also in the strong-field regime, where it is not accurate. Furthermore, the bottom panels of Fig. 7.6 show that the resulting TKEQ-fluxes (red and blue-dashed) agree at a level of $\leq 0.1\%$ throughout the whole evolution, which confirms the insensitivity of the dynamics on the slight differences in the RRs.

In conclusion, for fast prograde orbits the consistency check confirms the lack of higher order PN information for the $\rho_{\ell m}$'s to improve the RR used in the EOB-dynamics. Possibly, the effective fits to numerical data given in [62] can help until the available information at 22 PN for the nonspinning case [175] and 20 PN for the spinning case [57] have been incorporated into the model. Two slightly different versions of the RR are found to be equivalent at the practical level, but the $-\hat{\mathcal{F}}_\phi^{v_\phi}$ version seems better-behaved from a conceptual point of view.

7.2.3   Iterative procedure for improved radiation reaction

Motivated by the poor performance of the analytical RR for $\hat{a} = 0.9$ (see Sec. 7.2.2), one is inclined to search for improvements. A natural idea is to perform an iteration procedure which starts from the analytical RR, computes the TKEQ-fluxes for the obtained dynamics, and uses these TKEQ-flux as a new RR to produce slightly different dynamics. Then, iterate. If a fixed point exists and the first guess is close enough, we expect convergence against a RR which is self-consistent at linear order in the mass ratio ν. When the initial guess of the EOB-fluxes is not accurate enough, one can encounter problems. For example, for $\hat{a} = +0.9$ we were only able to obtain iterative convergence when the initial EOB trajectory was computed incorporating the refined $\rho_{\ell m}$'s obtained in Ref. [62] by fitting the RR to numerical data. Preliminary tests for higher spins $\hat{a} > 0.9$ were not successful.

In this section we present the performance of the procedure for a case study with $\hat{a} = 0.9$ (as published in [H2]). Differently from the $\hat{a} = 0.9$ dynamics used in other sections and described in Table J.1, here the dynamics start at $r_0 = 4M$ to obtain ~ 120 orbits before merger. The resolution was lowered to 1200×60 to ease the computational costs. This resolution is sufficient for our purpose here. A higher resolution would only be necessary to make high accuracy runs with the finally obtained form of the RR. In order to include both the horizon fluxes and the infinity fluxes, we actually have to render 16 simulations at each iteration step, i.e. for $s = \pm 2$ and $m = 1, ..., 8$ ($m = 0$ is negligible, see Fig. 7.1). As discussed in Sec. 7.2.1, the very last parts of the horizon fluxes are smoothly continued to zero. At early times $\lesssim 200M$, our numerical fluxes are corrupted by "junk radiation"
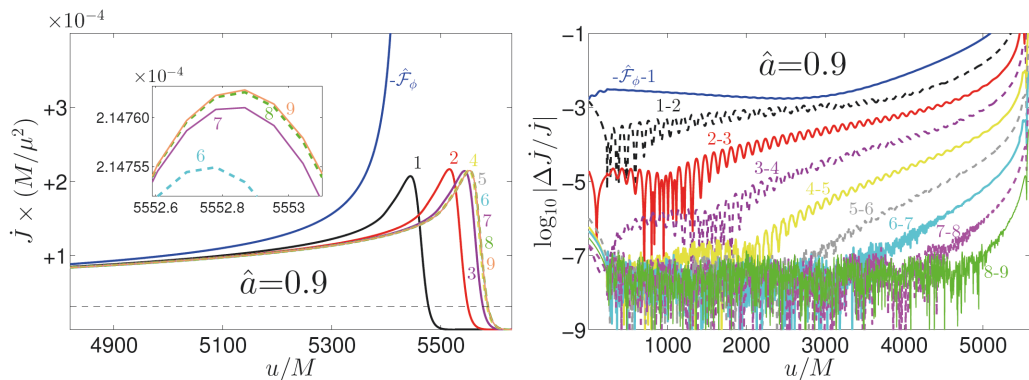
Figure 7.7: Convergence of the iterative self-consistent procedure for the radiation reaction (RR) along inspiral dynamics with $\hat{a} = 0.9$ and $r_0 = 4M$. Left: GW fluxes after each iteration. Note the large differences with respect to iteration 0, i.e. the EOB-RR, $-\hat{\mathcal{F}}_\phi$, even though we used the refining fit given in [62]. Right: Convergence of the fluxes after each iteration. After 9 iterations we obtain a self-consistent RR including both infinity and horizon fluxes. Plots adopted from [H2].

due to the crude initial data; we complete our fluxes at early times by linear extrapolation from $u/M \in [500, 250]$ to $u = 0$. To check that this does not introduce a significant error, we compared the value extrapolated to $u = 0$ with the circular flux at the relative radius, and found an agreement of $\sim 0.2\%$.

The result of the iterative procedure is summarised in Fig. 7.7. The left panel shows the complete (scri and horizon) GW flux $\dot{J}$ at each iteration. The peak position of the flux significantly changes for the first iterations and in total from $u_{peak} \approx 5450M$, at the 0th iteration, to $u_{peak} \approx 5553M$, after the 9th iteration. On the contrary, the peak amplitude remains approximately the same after the first iteration (see inset). This is consistent with the intuition that the amplitude at merger is not a RR-driven effect, but, rather, the merger waveform depends on the plunge phase. The right panel shows that the relative differences in the fluxes between the previous and the next iteration converge very rapidly to zero. At iteration 9 the relative flux differences saturate around 10^{-7} during most of the evolution, and the radiation emitted during the inspiral is well-consistent with the one used for the particle's dynamics.

The impact of using the consistent flux on the GW modelling is quantified by considering the difference in the number of GW-cycles, $\Delta N_{\rm gw}$, between the final waveform (after 9 iterations) and the starting one (iteration 0): $\Delta N_{\rm gw} \sim 6.7$. Note, however, that our 0th iteration dynamics is already different from the usual EOB-dynamics due to the use of the fit of [62] for the RR. The latter difference amounts to $\Delta N_{\rm gw} \sim 28.8$; so, overall, the self-consistent simulation differs from the corresponding EOB one by about $\Delta N_{\rm gw} \sim 35.5$.

We also tested the importance of horizon absorbed fluxes by performing another self-consistent calculation which neglects these contributions. We found that the final tra-

jectory is *shorter*, and the particle reaches the horizon $\sim 117M$ earlier compared to the final trajectory that includes horizon absorption. The fact that in presence of horizon absorption effects the inspiral is longer is explained by superradiance. The net effect of horizon-absorption for $\hat{a} = 0.9$ is essentially an *emission* of energy/angular momentum from the horizon. The differences in the dynamics correspond to $\Delta N_{\mathrm{gw}} \sim 5.4$, i.e. ~ 127.1 instead of ~ 124.4 orbits before merger. This result highlights the importance of including horizon-absorbed fluxes during the inspiral.

7.3   Kick and antikick velocities

A strong-field phenomenon as surprising as fascinating, revealed by the first fully nonlinear simulations of binary BH mergers, is the recoil of the remnant, potentially at speeds of $\sim 1000km/s$ (see, e.g., [176, 177] for recent works and a collection of references). The effect is explained by the anisotropic emission of GWs, and with them linear momentum, which leads to a kick of the center-of-mass by virtue of momentum conservation. By tracing the emission of linear momentum through the evolution one can measure the instantaneous recoil velocity $v(t)$, i.e. the potential recoil that would result if the process of emission was stopped at the time t. For some spins and mass ratios the shape of $v(t)$ was found to attain a maximum around the merger and to decrease to a smaller final value [178, 179]. The drop from the maximum v_{max} to the final recoil velocity v_{end}, $\Delta v = v_{\mathrm{max}} - v_{\mathrm{end}}$, was called "unkick" or "antikick" (see, e.g., Fig. 1 in [179]). In the particle limit the recoil was recently investigated by reference [130] for $\hat{a} = 0.0$ solving the RWZ-equations, and by Sundararajan, Khanna and Hughes [115] (hereafter SKH) for $\hat{a} \neq 0$ solving the TKEQ. The latter study considered spin magnitudes $|\hat{a}| \leq 0.9$ and found that the antikick is strong for large spin prograde orbits and "essentially non-existent" for large spin retrograde coalescences (see Fig. 5 in [115]). Using the *teukode*, we revisited the recoil in the particle limit and extended the SKH-analysis of [115] to nearly extremal spin-values $|\hat{a}| \leq 0.9999$. The following results and further details were published in [H3].

Working with RWZ-normalised variables $\Psi_{\ell m}^{(\epsilon)}$, the GW linear momentum flux can be computed following

$$\mathcal{F}^{\mathbf{P}} = \mathcal{F}_x^{\mathbf{P}} + \mathrm{i}\mathcal{F}_y^{\mathbf{P}} = \sum_{\ell=2}^{\ell_{max}} \mathcal{F}_\ell^{\mathbf{P}} \tag{7.1}$$

$$= -\frac{1}{8\pi} \sum_{\ell=2}^{\ell_{max}} \sum_{m=-\ell}^{\ell} \left[\mathrm{i}a_{\ell m}\dot{\Psi}_{\ell m}^{(0)}\dot{\Psi}_{\ell,m+1}^{(1)*} + b_{\ell m} \sum_{\epsilon=0,1} \dot{\Psi}_{\ell m}^{(\epsilon)}\dot{\Psi}_{\ell+1,m+1}^{(\epsilon)*} \right],$$

where ϵ is the parity of $(\ell + m)$, and the asterisk indicates complex conjugation. Note that Eq. (7.1) already implements the fact that the motion is planar so that even-parity modes with $\ell + m = $ odd and odd-parity modes with $\ell + m = $ even are zero. We extracted

GW multipoles up to $\ell_{max} = 8$. The real-valued coefficients $(a_{\ell m}, b_{\ell m}) > 0$ can be found in [130]

$$a_{\ell m} = 2(\ell - 1)(\ell + 2)\sqrt{(\ell - m)(\ell + m + 1)}, \tag{7.2}$$

$$b_{\ell m} = \frac{(\ell + 3)!}{(\ell + 1)(\ell - 2)!}\sqrt{\frac{(\ell + m + 1)(\ell + m + 2)}{(2\ell + 1)(2\ell + 3)}}. \tag{7.3}$$

From the linear momentum fluxes accumulated by the system up to a certain time t the instantaneous recoil velocity can be computed as the magnitude of the complex velocity vector $\mathbf{v} \equiv v_x + \mathrm{i}v_y$, defined by

$$\mathbf{v}(t) = -\frac{1}{M}\int_{-\infty}^{t} dt' \left(\mathcal{F}_x^{\mathbf{P}} + \mathrm{i}\mathcal{F}_y^{\mathbf{P}}\right) = \mathbf{v}_0 - \frac{1}{M}\int_{t_0}^{t} dt' \left(\mathcal{F}_x^{\mathbf{P}} + \mathrm{i}\mathcal{F}_y^{\mathbf{P}}\right). \tag{7.4}$$

The complex integration constant $\mathbf{v}_0$ accounts for the velocity that the system has acquired in evolving from $t = -\infty$ to $t = t_0$. In practice, $\mathbf{v}_0$ is unknown of course. If it is set arbitrarily to zero, unphysical oscillations show up in the time evolution of the modulus of the velocity $v(t) \equiv |\mathbf{v}(t)|$. Note that in the ring-down, after the peak of $v(t)$, oscillations in the modulus are physical, whereas oscillations before the peak are typical for a crude integration constant (see, e.g., Fig. 5 in [115]). Though the effect is small, it can eventually result in an inaccurate estimate of the final recoil velocity. Therefore, we determine the vectorial integration constant $\mathbf{v}_0$ by finding the center of the hodograph of the velocity in the complex plane following [180, 130]. This procedure is tuned iteratively until the time evolution of $v(t)$ grows monotonically during inspiral, without spurious oscillations. The correct determination of the integration constant is especially important when $\hat{a} \to +1$, as it can strongly influence the rather small value of the final recoil velocity. Fig. 4 of [H3] shows the evolution of $v(t)$ for some examples, and proves that we were able to remove the spurious oscillations, at least visually.

The results of our recoil computations for v_{end} are summarised in Tab. M.1 in App. M; the table also contains $v_{\max}$, the associated antikick Δv, and certain analysis numbers, which will be discussed in a moment. The results for $\hat{a} \geq 0.95$ are separated to indicate that they are uncertain, in view of the inaccuracy of the employed analytical RR for $\hat{a} \to 1$ (see discussion in Sec. 7.2.2). The left panel of Fig. 7.8 visualises the data from Tab. M.1 for the different recoil quantities, with the uncertain $\hat{a} \geq 0.95$ data points shown in gray. One clearly sees the nice agreement between our recoil velocities $v(t)$ (red circles) with the fit representing the SKH-results (dashed black). The small deviations are remarkable, given the differences between the SKH-study and ours. Among others the main differences are (i) the restriction to $m_{\max} = 6$ in SKH, (ii) probably different choices for the integration constants, and (iii) the usage of numerical circular orbits fluxes for $\mu = 10^{-4}M$ in SKH, in contrast to the analytical EOB-RR, deformed at mass ratio $\mu = 10^{-3}M$, here.
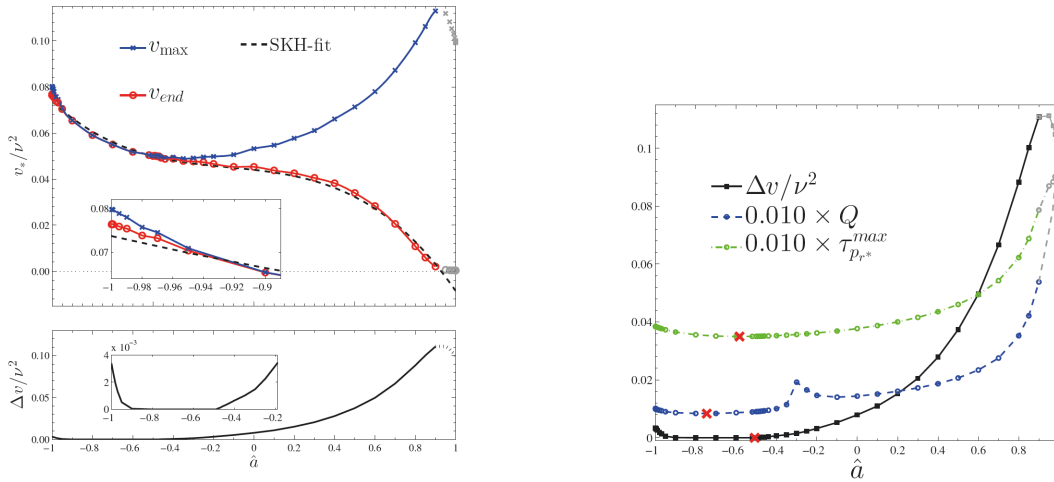
Figure 7.8: Summary of kick/antikick data and analysis. Left: Dependence of the maximum (blue, crosses) and the final (red, circles) recoil velocities on the spin $\hat{a}$ for mass ratio $\nu = 10^{-3}$. The dashed black line refers to the fit of [115]. Although the antikick is suppressed in the interval $-0.9 \leq \hat{a} \leq -0.5$, it strikes back for large negative spins, i.e. for $\hat{a} \lesssim -0.9$ we find again that $v_{max} > v_{end}$. The data points for $\hat{a} > 0.9$ are plotted in gray to indicate that they are affected by larger systematic uncertainties due to inaccuracy of the radiation reaction as $\hat{a} \to +1$. Right: The analysis quantities $\tau_{\dot{p}_{r*}}^{\max}$ and Q resemble globally the behaviour of Δv, and even predict the return of the antikick for $\hat{a} \to -1$. Red crosses mark the minima of each quantity, cf. Tab. M.1. Plots adopted from [H3].

In order to get an impression of the antikick, the plot additionally shows $v_{\max}$ (blue crosses), and the resulting Δv, separately depicted in the small bottom panel (solid black line). We can confirm the SKH results that the antikick is strongest for $\hat{a} \to 1$, and apparently vanishing for $-0.9 \leq \hat{a} \leq 0.2$. But in the previously unreachable regime of $\hat{a} \leq -0.9$, we make an exciting discovery: the antikick behaves non-monotonically in $\hat{a}$. Instead of continuing to zero for $\hat{a} \to -1$, it gradually rises again for $\hat{a} < -0.9$, reaching at $\hat{a} \approx -1$ values which are comparable with $\hat{a} = -0.2$ (cf. the inset in the bottom panel). Similarly interesting is the finding that, as $\hat{a} \to 1$, the final recoil velocity seems to vanish; this result, though, requires future investigations to rule out artificial effects from the inaccuracy of the RR in that regime.

Trying to get some grasp of our results, especially with respect to the antikick, one can employ a variety of analysis tools. In the test-particle limit it is natural to connect the waveforms to the trajectories. As argued in [181, 182], it is simply the form of the trajectory that determines the kick/antikick and not the spacetime in which the waves are generated and propagated. To follow the argument, recall that the velocity is computed as an integral over the linear momentum flux. If the latter is smoothly oscillating towards a final zero amplitude, one expects that its integral vanishes. For the quasi-circular inspiral for $\hat{a} \to 1$ this is the case. For retrograde orbits, however, the clean oscillation is modified with a burst-like structure during the plunge, which results in a net emission of linear

momentum (cf., e.g., Fig's. 8, 9 of [182]). In order to quantify the circularity of the plunge, we have studied the radial momentum p_{r*} with respect to $\hat{a}$. The time derivative $\dot{p}_{r*}$ is found to have a bell-like peak around the merger (see Fig. 1 in [H3]). One can quantify the width of the peak by its characteristic variation time $\left(\tau^{\max}_{\dot{p}_{r*}}\right)^2 = -\frac{\dot{p}_{r*}}{\dddot{p}_{r*}}\big|_{t=t^{\dot{p}_{r*}}_{\max}}$, where $t^{\dot{p}_{r*}}_{\max}$ corresponds to the peak of $-\dot{p}_{r*}$. Before discussing the performance of $\tau^{\max}_{\dot{p}_{r*}}$ in analysing the antikick, let us introduce another tool proposed in the literature. Following Damour and Gopakumar [173], the kick and the antikick can be directly connected to the short timescale of non-adiabatic emission of linear momentum during the plunge, i.e. to the peak of the modulus of the linear momentum flux. The antikick, as a function of $\hat{a}$, can then be understood in terms of a "quality factor" Q, associated to that maximum of the GW linear momentum flux, $\mathcal{F}^{\max}_{\mathbf{P}} = \max|\mathcal{F}_{\mathbf{P}}|$. At time t, the accumulated kick velocity is given by the complex integral Eq. (7.4). The integrand can be split into amplitude and phase to write $\mathbf{v} = -\int_{-\infty}^{t}|\mathcal{F}_{\mathbf{P}}(t')|e^{i\varphi(t')}dt'$, where $\varphi(t)$ is the phase of the linear momentum flux. Expanding around the time $t_{\max}$ corresponding to $\mathcal{F}^{\max}_{\mathbf{P}}$, one gets an approximation for $v(t)$ (see Eq. (9) in [H3]). The important quantities are the characteristic time scale of the peak of the flux $\tau^2_{\max} \equiv -\mathcal{F}^{\max}_{\mathbf{P}}/(|\ddot{\mathcal{F}}_{\mathbf{P}}|)^{\max}$ and the phase derivative at the time of the peak $\omega_{\max} = \dot{\varphi}(t)|_{t=t_{\max}}$. The quality factor is defined as $Q = \omega_{\max}\tau_{\max}$.

The right panel of Fig. 7.8 compares the behaviour of the two mentioned analysis tools, $\tau^{\max}_{\dot{p}_{r*}}$ (green) and Q (blue), with the found antikick (black) over $\hat{a}$. Red crosses mark the respective minima. The associated data is listed in Tab. M.1, which additionally contains an analytic estimate of the final recoil velocity (cf. Eq. (11) in [H3], not discussed here). The global behaviour is similar in all three quantities, with a strong growth towards $\hat{a} \to 1$, a minimum in the range $-0.8 \leq \hat{a} \leq -0.5$, and, compellingly, a small increase towards $\hat{a} \to -1$. Hence, both analysis tools actually predict the surprising return of the antikick for nearly extremal negative spin values. The small spike in Q around $\hat{a} \sim -0.3$ reveals that it does not yet work perfectly. Q only surveys the maximum of the GW linear momentum flux $\mathcal{F}^{\max}_{\mathbf{P}}$. While, normally, $\mathcal{F}^{\max}_{\mathbf{P}}$ has a very distinct peak (cf. Fig. 2 of [H3]), in the region $\hat{a} \sim -0.3$ it exhibits two rather equal maxima, close together. This behaviour cannot be captured in the current form of Q. Still, we draw the conclusion that the quality factor is a very efficient and functional tool. In fact, it might also be useful for comparable mass binaries, where a clean "trajectory" is not defined, but the analysis of the peak of the linear momentum flux is still possible.

GWs from a spinning particle

A crucial missing piece of technology in our point particle laboratory is the "spin". The honest effect of non-extremal, realistic spins of binaries which can be described quantitatively in the point-particle limit is expected to be, at best, relevant for the secular dynamics [30, 183]. Nonetheless, the investigation of spins in the particle approximation, especially at extremal values $\mathcal{O}(|\vec{S}_2|) \sim \mu M$, can provide interesting qualitative information [40] on spin(1)-spin(2) and spin(2)-orbit coupling effects. To the best of our knowledge, a spinning particle has never been considered as a source term for time-domain TKEQ studies. Consequently, results on GWs from a spinning particle on a spinning BH background are restricted to a hand full of frequency-domain studies for conservative motions like (i) radial infalls [184, 185], and (ii) circular, equatorial orbits [56, 186] (cf. the small review in App. D).

As discussed in Sec. 4.3, we have derived the TKEQ source term for a spinning particle within Mathisson's pole-dipole approximation (see Sec. 2.1). The associated equations of motion are the Mathisson-Papapetrou equations (MPEQs) (see Eq.'s 2.6). A promising future prospect is the recapitulation of all experiments presented in this thesis with respect to the effect of spin. As a first step, we have investigated circular equatorial orbits with aligned or anti-aligned spins. This section presents preliminary results, which show, at large radial distances, a nice confirmation of the PN-results obtained in [56]. This indicates that our implementation is correct (or at least agrees with the one in [56]), and paves the way for future experiments. The dynamics are kindly provided by Dr. Lukes-Gerakopoulos [21]. Below we follow the convention to include into the multipolar energy flux $\dot{E}_{\ell m}$ both contributions $\pm m$ because they are equivalent for equatorial motion; more precisely, the quantity $\frac{d}{dt}E_{\ell m}$ contains both the (ℓ, m)- and the $(\ell, -m)$-contributions. Leaning on this convention, we will mean the summed flux including both $\pm m$ contributions when speaking of an ℓm-flux. This is consistent with the definition of the $F_{\ell m}$ in Eq. (2) of [54], which is used below for defining the leading-order fluxes. Further, we use the dimensionless spin parameter $\sigma = S/(\mu\,M)$, with $S \equiv |\vec{S}_2|$ the spin-magnitude of the particle's spin (cf. Sec. 2.1.3).

8.1 2.5PN result of Tanaka et al.

For the ℓm-modes $\in (22, 21, 33, 31, 32, 44, 42)$ Eq.'s (5.16) of [56] state the normalised energy fluxes of a spinning particle in circular equatorial orbit about a Kerr BH at 2.5PN-order. These normalised fluxes are defined as $\eta_{\ell m} = \frac{d}{dt} E_{\ell m} / \frac{d}{dt} E_{22}^N$, where $\frac{d}{dt} E_{22}^N = \frac{32}{5} v^{10}$ is the Newtonian-flux of the 22-mode within the quadrupole formula. Following Tanaka, we set the characteristic velocity to $v = \sqrt{M/r}$. In our notation the 2.5PN-formulas read

$$
\begin{aligned}
\eta_{22}(\hat{a}, \sigma, v) &= 1 - \frac{107}{21} v^2 + \left(4\pi - 6\hat{a} - \frac{19}{3}\sigma \right) v^3 + \left(\frac{4784}{1323} + 2\hat{a}^2 + 9\hat{a}\sigma \right) v^4 \\
&\quad + \left(-\frac{428}{21}\pi + \frac{4216}{189}\hat{a} + \frac{2134}{63}\sigma \right) v^5 , \\
\eta_{21}(\hat{a}, \sigma, v) &= \frac{1}{36} v^2 + \left(-\frac{1}{12}\hat{a} + \frac{1}{12}\sigma \right) v^3 + \left(-\frac{17}{504} + \frac{1}{16}\hat{a}^2 - \frac{1}{8}\hat{a}\sigma \right) v^4 \\
&\quad + \left(\frac{1}{18}\pi - \frac{793}{9072}\hat{a} - \frac{535}{1008}\sigma \right) v^5 , \\
\eta_{33}(\hat{a}, \sigma, v) &= \frac{1215}{896} v^2 - \frac{1215}{112} v^4 + \left(\frac{3645}{448}\pi - \frac{1215}{112}\hat{a} - \frac{10935}{896}\sigma \right) v^5 , \\
\eta_{32}(\hat{a}, \sigma, v) &= \frac{5}{63} v^4 + \left(-\frac{40}{189}\hat{a} + \frac{20}{63}\sigma \right) v^5 , \\
\eta_{31}(\hat{a}, \sigma, v) &= \frac{1}{8064} v^2 - \frac{1}{1512} v^4 + \left(\frac{1}{4032}\pi - \frac{17}{9072}\hat{a} - \frac{1}{8064}\sigma \right) v^5 \quad ,
\end{aligned}
\tag{8.1}
$$

where we have omitted the 44 and 42 results because they do not exhibit spin-dependence at 2.5PN. Unfortunately, the 31-mode is too weak to be measured accurately in our numerics, especially for orbits in the weak-field, which we rely on for the validation of our data. Consequently, we restrict the comparison to the $22, 21, 33, 32$ modes. There are several other important remarks to be made here, i.e. , (i) the formulas are linear in the dimensionless spin $\sigma = |\vec{S}_2|/(\mu M)$ (called $\hat{s}$ in [56]), (ii) $\eta_{\ell m}$ is understood here as twice the actual flux in a given ℓm-mode, in accord with $\dot{E}_{\ell m}$, (iii) the expansion parameter v of Tanaka et al. [56] is defined as $x \equiv v^2 = M/r$; note that this is not strictly the orbital velocity (only for $\hat{a} = \sigma = 0$), and (iv) the $\eta_{\ell m}$ refer to the projection onto spin-weighted spheroidal harmonics $S_{s\ell m}$ (cf. [18, 64]), which only for $\hat{a} = 0.0$ coincide with the well-known spin-weighted spherical harmonics $Y_{s\ell m}$. For our comparison we find it convenient to further divide the $\eta_{\ell m}$ by their leading-order term. In fact, we consider the completely Newton-normalised quantities $\tilde{\eta}_{\ell m} = \frac{d}{dt} E_{\ell m} / \frac{d}{dt} E_{\ell m}^N$, where $\frac{d}{dt} E_{\ell m}^N$ is the leading order flux defined by Eq. (2) and Eq. (4) in [54]. The relevant fluxes, called $F_{\ell m}^N$ in [54], are

$$
\dot{E}_{21}^N = \frac{8}{45} v^{12} , \quad \dot{E}_{33}^N = \frac{243}{28} v^{12} , \quad \dot{E}_{32}^N = \frac{32}{63} v^{14} , \quad \dot{E}_{31}^N = \frac{1}{1260} v^{12} .
$$

Thus, the quantities $\tilde{\eta}_{\ell m}$ are all of the form $\tilde{\eta}_{\ell m} = 1 + \mathcal{O}(x)$.

8.2   Energy fluxes at scri: numerics vs. analytics

We have computed the energy fluxes to infinity from a spinning particle in circular equatorial orbit on Schwarzschild for particle spin values $\sigma \in \{\pm 0.9, \pm 0.7, \pm 0.5, \pm 0.3, \pm 0.1\}$ and for radii $r_p \in \{5, 6, 7, 8, 10, 12, 15, 20\}$. There are two references to compare with, (i) the 2.5PN results of Tanaka et al. [56] (cf. Eq.'s 8.1 above), and (ii) Fig.'s 4-6 of Han [186], which show the energy fluxes vs. σ for $\hat{r} = 10$.

In order to validate the numerics, one would first like to observe an unambiguous trend towards the PN result for $r \to \infty$, or, equivalently, as the inverse radial distance $x \equiv 1/\hat{r} \to 0$. Hence, we consider orbits in the weak-field regime, up to $\hat{r} = 20$. Unfortunately, two obstacles prevent us from examining arbitrarily huge radii $\hat{r}$; (i) the energy fluxes become smaller, eventually beyond our numerical precision, and (ii) our hyperboloidal coordinates drastically loose resolution as $\hat{r} \to \infty$. The latter issue can be mediated by higher computational expenses, of course, but $\hat{r} = 20$ suffices, as shown below, to observe the trend. Fig. 8.1 shows plots of the normalised energy-fluxes versus x, for $\sigma = -0.9$ (left column) and $\sigma = 0.9$ (right column). In all cases, we observe, as $x \to 0$, the expected trend of our results towards the PN-prediction. While the agreement usually reaches $\sim 1\%$ at $\hat{r} = 20$, independently of the considered σ, the worst case is a bit farther off, with $\sim 15\%$, namely, the 32-mode for $\sigma = 0.9$ (bottom right panel). This offset is not surprising because the PN information for the 32-mode only go one term beyond the leading-order (cf. Eq.'s (8.1)). Overall, the plots indicate that our data converge towards the PN-results. As a final test, we plan to perform an extremely high resolved simulation of even larger radius to further support the hypothetical agreement. In [H4] we plan on repeating the comparison of the energy fluxes for $\hat{a} \neq 0$.

Building on the reasonable behaviour of our data in the weak-field, we assume their correctness and discuss the dependence on σ for some fixed radial distances. Fig. 8.2 shows, at the fixed radii $\hat{r} = 20$ (left column) and $\hat{r} = 5$ (right column), the normalised fluxes for the modes 22, 21, 33, 32; on the one hand, as obtained from the *teukode* (red with dots) and, on the other hand, the PN results (blue). For $\hat{r} = 20$ we observe, in all modes, qualitative agreement between the *teukode* and the 2.5PN formula. One can make several observations for the four investigated modes at $\hat{r} = 20$ and $\hat{r} = 5$,

(i) in most cases, for $\sigma < 0$ the fluxes are stronger than at $\sigma = 0$; for $\sigma > 0$ they are weaker than at $\sigma = 0$; exceptions are the 32- and 21-mode at $\hat{r} = 20$,

(ii) in most cases, the fluxes are monotonic in σ; exceptions are the 32- and 21-mode at $\hat{r} = 5$,

(iii) for the 22- and the 33-mode the dependence on σ is roughly the same at $\hat{r} = 20$ and $\hat{r} = 5$, whereas for the 32- and 21-mode the behaviour changes drastically,
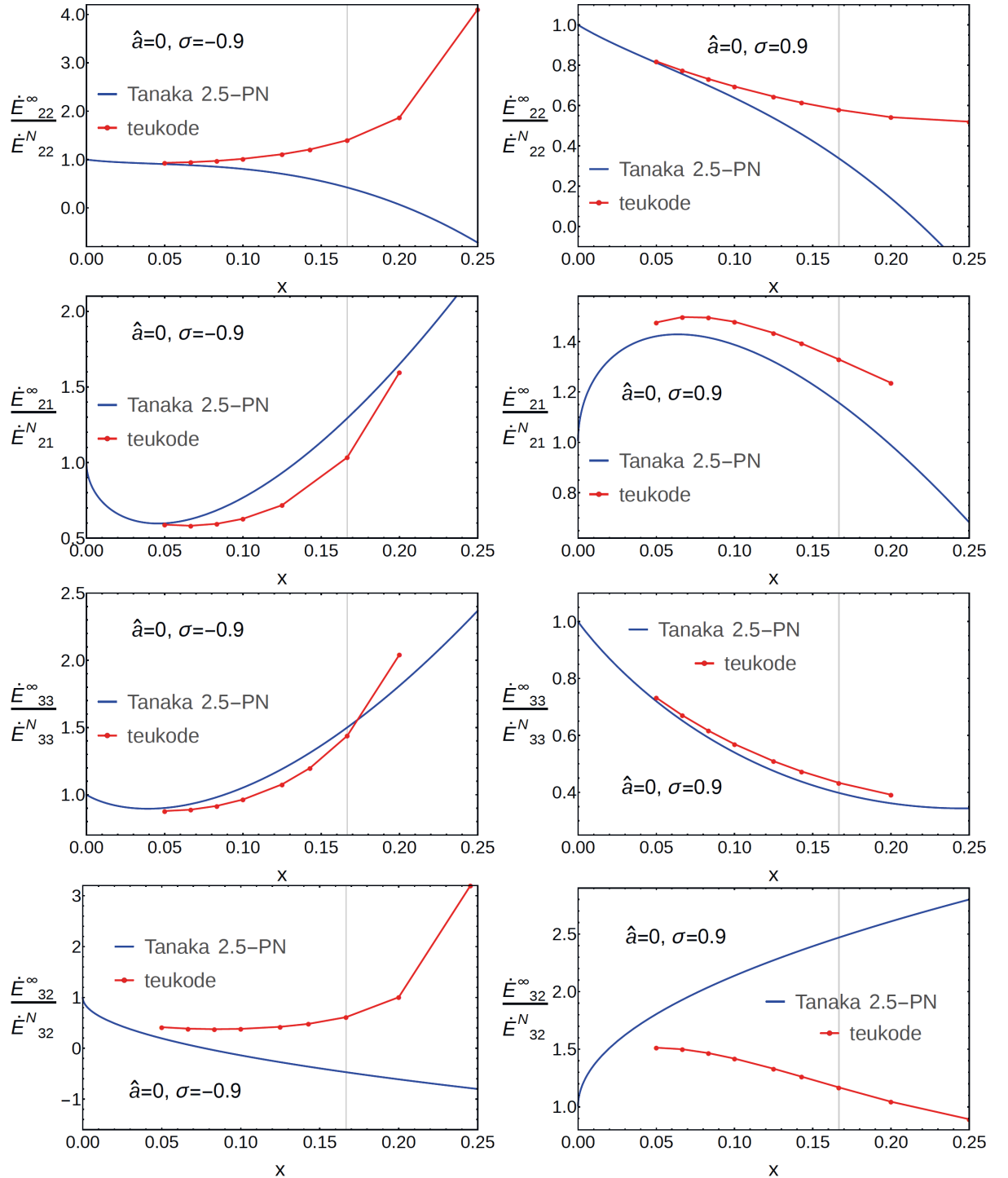
Figure 8.1: Convergence of numerics against analytics as $x \to 0$. The plots show the multipolar energy fluxes in the Y_{-222} (top), Y_{-221} (top middle), Y_{-233} (bottom middle), and Y_{-232} (bottom) modes for a spinning particle with $\sigma = -0.9$ (left) and $\sigma = 0.9$ (right) on circular, equatorial orbit on Schwarzschild. The vertical line shows the LSO for $\sigma = 0.0$. At $\hat{r} = 20$ the agreement is at the order of $\sim 1 - 5\%$, only the 32-mode is farther off, $\sim 15\%$ for $\sigma = 0.9$. The reason is, likely, that the PN-information in this mode only reaches the next-to-leading order term.
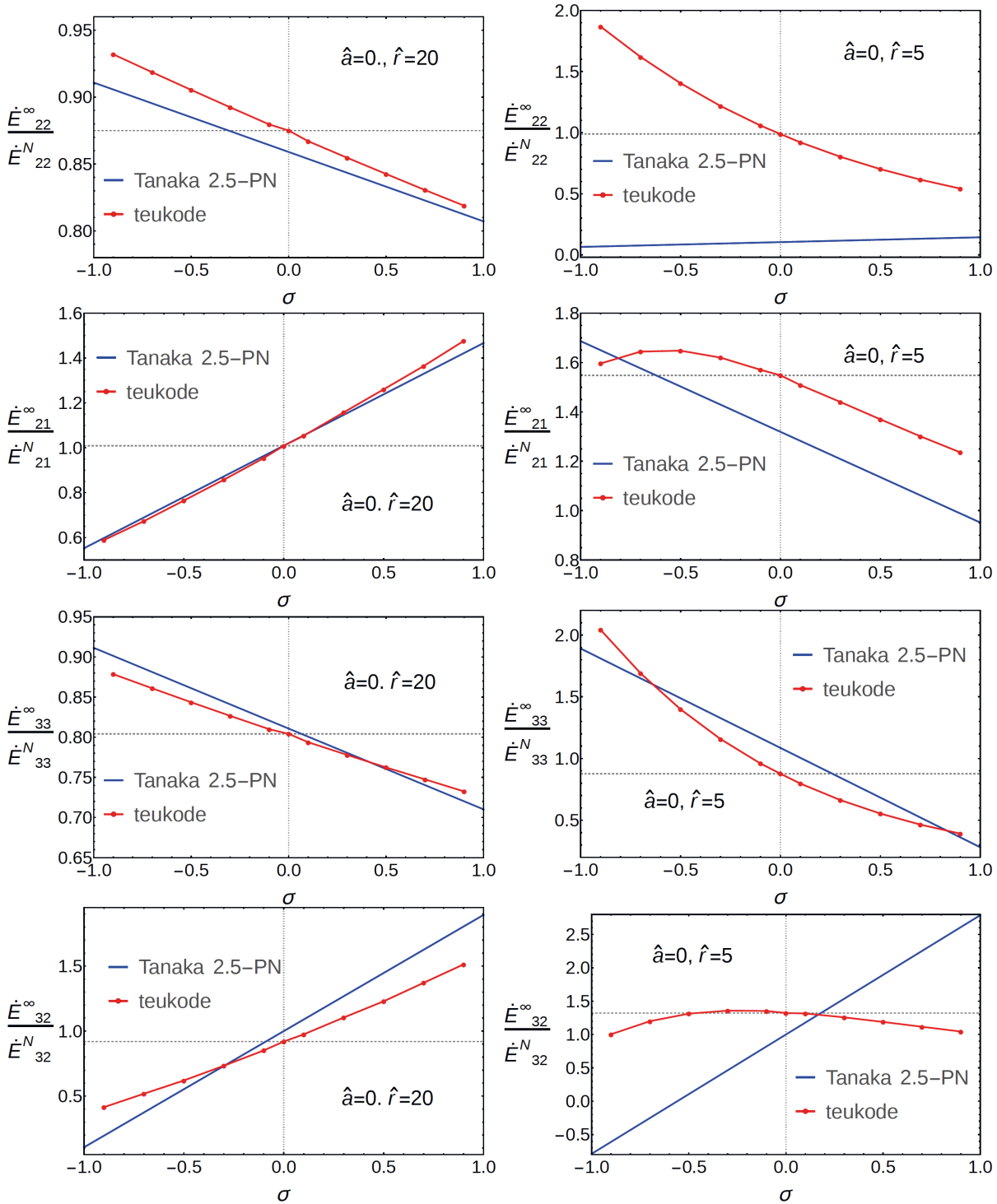
Figure 8.2: Multipolar energy fluxes in the Y_{-222} (top), Y_{-221} (top middle), Y_{-233} (bottom middle), and Y_{-232} (bottom) modes for a spinning particle on circular, equatorial orbit at $\hat{r} = 20$ (left) and $\hat{r} = 5$ (right) on Schwarzschild. The horizontal dotted lines are the reference points for a non-spinning particle from the frequency-domain data of Hughes [60]. Our $\sigma = 0.0$ data points were produced at higher accuracy and, therefore, we see a small kink in the red lines.

(iv) in the strong-field we observe non-linear dependence on σ in all four modes,

(v) in the weak-field we observe linear dependence on σ in all four modes, and

(vi) for the 21 and the 33 modes the PN-formulas capture the qualitative dependence on σ rather well even in the strong field

Going through the list of statements, we can draw some conclusions. In this context, one often argues in terms of "couplings" between different angular momenta, which refers to effects that disappear when either of them disappears; e.g., if a term in a PN-formula contains a product $\sigma \cdot \hat{a}$, it is counted as a spin(2)-spin(1) coupling. So, first, point (i) must be attributed to the spin(2)-orbit coupling because on Schwarzschild spin(1)-orbit and spin(1)-spin(2) couplings are excluded. As a consequence of point (i), we expect slower (faster) inspirals when the spin and the orbital momentum are (anti-)aligned. Intuitively, this can be interpreted as "aligned moments repel" while "antialigned moments attract" each other. This was found to be different for plunging orbits in the equatorial plane [185], which supports the claim that the amount of radiation does not simply depend on σ, but, also, on the type of the trajectory. Observations (iv) and (v) must be interpreted as reflections of the degree of non-linearity in the dynamics. The TKEQ-source term depends only linearly on the spin; any non-linearity that we observe must reside intrinsically in the dynamic quantities. Apparently, far away from the BH the dynamics do not sense the $\mathcal{O}(S^2)$ term introduced to the EOM by the TUL-SSC (cf. Eq. 2.9). This seems reasonable, as the $\mathcal{O}(S^2)$-terms appear in combination with the curvature tensor, which vanishes as $\hat{r} \to \infty$. Instead, in the strong-field its influence becomes significant for the dynamics and thus we can observe a non-linear effect in the fluxes. Finally, point (vi) indicates that the behaviour on σ can be captured rather well by the PN-formulas. This is very encouraging because non-spinning PN-information are available up to 22-PN [175] on Schwarzschild and 20-PN on Kerr [57]. Their inclusion could possibly suffice to remove the major part of the offset between numerics and analytics.

Coming to the second reference [186], unfortunately, numerical values are not given explicitly, so we can only compare our data visually. Thus, we prefer to spare a detailed discussion here. We only mention that we made the comparison for the example of the 22-energy-flux for $\hat{a} = 0$ at the fixed radius $\hat{r} = 10$. We found fluxes which disagree qualitatively with the numerical results of [186]. At $\hat{r} = 10$ we observe a rather linear dependence of the fluxes on σ, whereas [186] shows a quadratic dependence. The agreement of our data with the 2.5PN prediction at that radius appeared, instead, very reasonable (comparable to the results for $\hat{r} = 20$), especially when sorting out the offset due to missing PN information for the non-spinning case at $\sigma = 0.0$. A similar confirmation was not shown in [186], so there is some reason to trust our results over those of [186]. A detailed analysis on the origin of the deviations with respect to [186] is left to the future.

Conclusions and outlook

Conclusions

In this work we have presented a novel, numerical approach to compute gravitational waves (GWs) from black hole (BH) binaries in the point-particle limit. The realisation of this approach in the *teukode* has proved to be a useful test-suite, in which we can model GWs from BH mergers at low cost, with high-accuracy and for nearly-extremal spins.

Our new approach relies on a reformulation of the Teukolsky-Equation (TKEQ) within horizon-penetrating, hyperboloidal coordinates (HH-coordinates [20]). The approach is in some aspects advantageous over the 20-years-old algorithm introduced by Krivan et al. [80], even though the latter was improved over the years to be equally accurate and efficient [75, 127]. Potential sources of error like unphysical numerical boundary conditions and extrapolation to future null infinity are superseded due to the advantageous coordinates. In the traditional approach, these problems can be resolved as well [127] by attaching layers that connect a Boyer-Lindquist (BL) interior to the horizon and future null infinity. The remaining limitations of the traditional scheme are the second-order convergence inherited from the special Lax-Wendroff time-advancing algorithm and the use of non-horizon penetrating coordinates, which prevents the extraction of horizon fluxes for generic trajectories. Both problems are resolved in our scheme; it works with a standard Runge-Kutta integrator of fourth order, and allows extraction of horizon fluxes.

Several obstacles had to be removed to enhance the approach, previously known only for the homogeneous TKEQ (cf. [H0, H1]), to the point-particle setup. A major problem was the artificial singularity of the TKEQ source term at the horizon, which we were able to resolve by rederiving the TKEQ in the Campanelli et al.-tetrad [99] instead of the originally used Kinnersley-tetrad. A minor complication was the computation of the dynamics of a point-particle in HH-coordinates.

Our implementation in the *teukode* was found to be numerically convergent with the expected order, and could be validated against a number of results in the literature;

among them, our previous spectral code for the homogeneous TKEQ [H1], a Regge-Wheeler-Zerilli-code [132, 133], waveform characteristics from the prevailing Teukolsky-solver [76, 135], and frequency domain Teukolsky data from [60], [156] and [87]. All these tests were passed consistently, and, moreover, confirmed the efficiency of the approach.

After the validation of the *teukode*, we produced several new results. First, extending previous knowledge from Schwarzschild to Kerr, we studied the consistency of the commonly used effective-one-body radiation reaction (RR) force. We found problematic inconsistencies in the case of fast prograde spins $\hat{a} \sim +0.9$; for retrograde spins $\hat{a} < 0$ we could confirm the model. Another interesting new insight was the previously unnoticed importance of the axisymmetric $m = 0$ modes in the merger waveforms of BH binaries in the point-particle approximation for $\hat{a} \to -1$. Here, m refers to the projection against spin-weighted spherical harmonics $Y_{s\ell m}$. Also, we performed the first, to the best of our knowledge, $s = +2$ TKEQ simulations in the time domain for a point particle source term. In analysing these runs, the horizon penetrating coordinates allowed us to apply the time-domain formalism proposed by Poisson [149], and thus to measure energy fluxes down the event horizon in realistic inspiral simulations. This, in turn, allowed to build a fully self-consistent in the mass ratio μ/M numerical RR by an iterative procedure. This numerical RR does not suffer from the problems of the analytic RR for fast prograde spins, and even includes the effects of horizon fluxes. In a subsequent study we revisited the computation of BH recoil velocities in the particle limit and discovered an unexpected growth of the anti-kick for $\hat{a} \to -1$. Interestingly, a comparison with analytical considerations on the fluxes revealed that the "quality-factor" of [173] actually predicts this result. This finding motivates the application of the quality-factor also in comparable mass binaries. Finally, we enhanced the applicability of our approach to consider the spin of the small companion, which means we were dealing with spinning particles in GR. To our knowledge, the *teukode* is the first successful time-domain Teukolsky solver that allows to investigate the GWs from a spinning particle. In a study of circular equatorial orbits we provided a first check of energy fluxes to infinity, and found discrepancies with the only other published numerical study [186]. Our results are supported by approximative Post-Newtonian results [56], and thus useful for further analyses.

Outlook

The point-particle laboratory which was established in this thesis provides several possibilities for subsequent studies.

Without further development the *teukode* can be used in different directions. For instance, more generic geodesic motions could be studied in detail. The preliminary tests for

non-equatorial movement presented here (Sec. 5.2.2) seem to indicate the capability to investigate inclined circular orbits. Also the investigation of inspiral motions that leave the equatorial plane [187] seems within reach. Furthermore, one could consider eccentric orbits, or even a combination, i.e. inclined eccentric orbits [60, 188, 189]. Possibly, one could also revisit the interesting zoom-whirl orbits studied in [110, 190]. For sure, a focus of future research should lay on scattering experiments with ultra-relativistic collisions as performed in [156]. The preliminary tests shown here (Sec. 5.2.2) are promising, but it is yet unclear whether the infall from "infinity" can be accurately approximated by large-distance infalls in our hyperboloidal coordinates.

With respect to the inspiral simulations investigated here, there are two main perspectives which call for immediate attention. On the one hand, one would like to find out whether the available high order PN information for energy fluxes of a particle [57] can be used to obtain an accurate model for the RR, also for $\hat{a} \to +1$. For this one would just have to perform standard resummation procedures (Sec. 2.2.3), create modified dynamics and repeat our consistency analysis. Especially the interesting question whether the antikick vanishes as $\hat{a} \to +1$ can only be answered if the consistency is confirmed. On the other hand, one would like to stretch the limits of the point-particle approximation and find out how much information can actually be gained for the comparable mass case. Possibly, extrapolation could even be quantitative as demonstrated in [191] for $\hat{a} = 0.0$.

Of course, the most obvious prospect is the investigation of effects of the spin. The implementation is completed and the first tests, shown in Sec. 8.2, are very promising. The ultimate goal is to repeat the whole procedure of creating a RR, checking its consistency, producing inspiral dynamics and corresponding merger waveforms, and, finally, to analyse how the spin influences the waveforms. This would allow to break completely new grounds. One could, e.g., investigate, for the first time, recoil velocities and the antikick from a spinning particle.

Finally, once all the immediate applications are covered, one can think about other matter perturbations like a ring of particles, or a disk of dust in the equatorial plane. Also, further technical development could be useful. For example, a mesh refinement around the particle could drastically alleviate the computational costs, or one could improve the scaling on multiple processors to speed up the code.

Derivation of the Teukolsky Equation

This Appendix shall convey a basic understanding of how the TKEQ (3.3) can be derived. The discussion given below follows the reasoning in the original papers [17, 18], and Sec.'s (8.4-8.5) from Alcubierre's book [6] in the description of the tetrad calculus. The main idea is the linearization and clever combination of certain Newman-Penrose equations. Details on the Newman-Penrose (NP) formalism, which leads to the mentioned NP-equations, and the complete derivation of the TKEQ can be found in the original works [63] and [18] respectively.

A.1 From metric to curvature perturbations

Let us forget for a moment that there exists such a thing as the TKEQ and start from scratch. If we were given the task to linearize the Einstein Equations around the Kerr solution, we would probably start by adding a small extra term to the Kerr metric

$$g_{\mu\nu} \rightarrow g_{\mu\nu}^{Kerr} + \epsilon\, h_{\mu\nu} \tag{A.1}$$

with the assumption that $\epsilon \approx 0$, and then insert this to Eq.'s (1.1). Differentiating with respect to ϵ and setting $\epsilon = 0$ leads to equations linear in $h_{\mu\nu}$. Indeed, in the non-rotating limit, this logic was followed by Regge-Wheeler [15] and Zerilli [16] to obtain their famous Regge-Wheeler-Zerilli (RWZ) Equations, which describe the evolution of spin-weighted spherical harmonic modes of linear perturbations about a non-rotating BH as a PDE in two coordinates, the Schwarzschild-(t, r) (cf., also, [146]). The same procedure would also work for a rotating BH background (cf., e.g., [192]), but one expects much higher algebraic complexity. Also, the transition from spherical symmetry to axi-symmetry would have one believe that there remains no chance of separating the θ-dependency to obtain simpler equations. However, Teukolsky succeeded in finding completely separable equations following a different route of attack based on the Bianchi-equations and tetrad calculus.

As Teukolsky vividly shared in his review on the Kerr metric [82], see Sec. 8 therein, he was a second-year graduate student at Caltech at the time, and inspired by the works of his local colleagues, like Price, Fackerell, Ipser, and Press, then likewise a graduate student at Caltech. All of them had worked with a special tetrad calculus as introduced by Newman-Penrose [63], later called the "NP-formalism". Price employed the NP-formalism in a simpler rederivation of the RWZ equations, which enabled his pioneering work on the late-time decay of BH perturbations [167]. Fackerell and Ipser followed the NP-formalism in their study of the Maxwell-Equations on a Kerr background [193]. Bardeen and Press had derived decoupled equations for the Weyl scalars Ψ_0 and Ψ_4 on Schwarzschild, extending Price's study [194]. As depicted by Teukolsky in [82], it was apparently no problem to transfer Bardeen&Press' result to Kerr. The struggle was to find the rescaling of the field variable, $\Psi_4 \rightarrow \Psi$, such that the resulting explicit equation would actually allow, once the variable Ψ is mode decomposed, a separation of the four dimensional PDE; surprisingly, not just into simpler PDEs but even into ordinary differential equations (ODEs).

A.2 A tetrad basis

In GR a tetrad basis can be a very useful tool. It provides a basis which is freely specifiable to the respective needs and independent of the chosen coordinates. This means, in particular, that tetrad components of tensors are invariant under coordinate transformations, which gives rise to the name "tetrad scalars" for components of tensors in the tetrad basis (we will come back to this feature in App. G.1).

A tetrad basis is defined as a set of four, linearly independent vectors $\{\vec{e}_a\}$ that maintain the same angles in a given metric at each point of spacetime. More precisely, the scalar products of the tetrad vectors have to be constant

$$\vec{e}_a \cdot \vec{e}_b = e_a^{\ \mu} e_b^{\ \nu} g_{\mu\nu} \overset{!}{=} \eta_{ab} \quad , \tag{A.2}$$

where the indices $a, b, c...$ run over the tetrad vectors, while $\mu, \nu, ...$ run over the components with respect to the coordinate basis, η_{ab} is a matrix with everywhere constant components, and the $e_a^{\ \mu}$ are called "tetrad legs". The name η_{ab} already suggests that the tetrad basis vectors are often chosen orthonormal so that one gets Minkowski form $\eta_{ab} = diag(-1, 1, 1, 1)$.

Having introduced a tetrad basis, all tensors can be projected onto that basis. For instance the constant relations between the tetrad legs can be reformulated from a new perspective to the demand that the metric in the tetrad basis reduce to the Minkowski metric

$$g_{ab} = e_a^{\ \mu} e_b^{\ \nu} g_{\mu\nu} \overset{!}{=} \eta_{ab} \quad . \tag{A.3}$$

For us the Ricci rotation coefficients

$$\gamma_{abc} := e_a^{\ \mu} e_c^{\ \nu} \nabla_\nu (e_b)_\mu \tag{A.4}$$

are of special interest since the Riemann tensor can be written as a combination of Ricci rotation coefficients and their directional derivatives along the tetrad legs (cf. Eq. (2.6) in [63]). The knowledge of all Ricci rotation coefficients and derivatives thus encodes the information on the geometry.

A.3 Newman-Penrose spin coefficient formalism

The Newman-Penrose (NP) formalism is a tetrad approach to GR, which is especially useful in the study of gravitational radiation in asymptotically flat spacetimes. It relies on a special "null-tetrad", which is a tetrad in the sense described above, with the additional feature that the four legs are null vectors, $||\vec{e}_a|| = 0$. To construct four linearly independent null vectors one needs to allow them to be complex. The legs of a null-tetrad are commonly called $\{\vec{l}, \vec{n}, \vec{m}, \vec{m}^*\}$, with $\vec{l}, \vec{n}$ being real, and $\vec{m}^*$ being the complex conjugate of $\vec{m}$. These null vectors can be constructed by superposition once one has found an orthonormal tetrad, i.e. one that yields g_{ab} in Minkowski form,

$$l^\mu = \frac{e_0^\mu + e_1^\mu}{\sqrt{2}}, \quad n^\mu = \frac{e_0^\mu - e_1^\mu}{\sqrt{2}}, \quad m^\mu = \frac{e_2^\mu + \mathrm{i}\, e_3^\mu}{\sqrt{2}}, \quad m^{*\mu} = \frac{e_2^\mu - \mathrm{i}\, e_3^\mu}{\sqrt{2}} \quad . \tag{A.5}$$

In the null tetrad basis the orthonormality relations take the slightly different form

$$\eta_{ab} = \begin{pmatrix} 0 & -1 & 0 & 0 \\ -1 & 0 & 0 & 0 \\ 0 & 0 & 0 & +1 \\ 0 & 0 & +1 & 0 \end{pmatrix} \quad . \tag{A.6}$$

Newman and Penrose used such a tetrad and spinor calculus to derive a set of equations, later called "NP-equations", which provide relations between the different Ricci rotation coefficients, the "Weyl-scalars" (see below) and the "Ricci-scalars", see Eq.'s (4.2a-r) in [63]. These equations are the central ingredients to the derivation of the TKEQ. Notably, the NP-equations partly stem from the Bianchi-identities $R_{\alpha\beta[\gamma\delta;\mu]} = 0$, which take rather simple form when written in tetrad notation (cf., e.g., the first one of Eq.'s (4.5) in [63] with Eq. (2.2) in [18]). These differential relations for the Riemann tensor, i.e. in vacuum equivalently for the Weyl tensor, can be interpreted as containing the propagation equation of GWs. The considered fields are the five complex-valued Weyl-scalars $\Psi_0, \Psi_1, \Psi_2, \Psi_3, \Psi_4$. As suggested from the name, these scalars are built from contractions of the Weyl tensor with the tetrad legs. The two most important ones are

$$\Psi_0 = C_{0202} = C_{\alpha\beta\mu\nu}\, l^\alpha\, m^\beta\, l^\mu\, m^\nu \qquad , \qquad (A.7)$$

$$\Psi_4 = C_{1313} = C_{\alpha\beta\mu\nu}\, n^\alpha\, m^{*\beta}\, n^\mu\, m^{*\nu} \qquad , \qquad (A.8)$$

and the remaining $\Psi_1 = C_{0103}$, $\Psi_2 = C_{0231}$, $\Psi_3 = C_{0131}$. Any other contraction of the Weyl tensor with the tetrad legs vanishes or can be expressed from these five contractions, which, therefore, represent all 10 independent components of the Weyl tensor. Loosely speaking, one may think of Ψ_0 and Ψ_4 as representing ingoing and outgoing radiation respectively, with the other scalars vanishing for a suitable choice of the tetrad basis. In the weak field limit, $r \to \infty$, the GW metric perturbations $h_{\mu\nu}$ satisfy the Einstein Eq.'s linearized about flat space time. In this region the linearized Riemann tensor coincides with the Weyl tensor and there we get a direct relation between $h_{\mu\nu}$ and the Weyl scalars. In the transverse-traceless gauge with the usual labels h_+ and $h_\times$ for the two independent components one gets

$$h = h_+ - ih_\times = 2 \int_{-\infty}^{t} \int_{-\infty}^{t'} \Psi_4 \, dt'' dt' \quad , \qquad (A.9)$$

see Sec.'s (1.14) and (8.9) in [6] for more details.

As mentioned above tetrad scalars like the Weyl scalars are invariant under coordinate transformations. Nevertheless, they are, of course, dependent on the choice of the null tetrad or equivalently on the choice of the orthonormal tetrad used for its construction. In fact, the orthonormality relations (A.6) are preserved under spatial rotations and Lorentz-boosts of the orthonormal tetrad. This corresponds to six degrees of freedom, which are usually wrapped into two complex parameters, d and e and two real parameters, Λ and Θ. The transformations are often sorted into three classes of "null rotations", see Sec. 8.5.2 in [6] or Appendix A of [18]. It is useful to note that these null rotations can be exploited in order to make one or more Weyl scalars vanish. The transformation behaviour of the Weyl scalars also leads to the *Petrov-classification* of spacetimes. The fact that in this classification both Schwarzschild and Kerr are of the same "type D" was a major motivation for Teukolsky to believe in the possibility of transferring Bardeen&Press's result of decoupled equations for Ψ_0 and Ψ_4 from Schwarzschild to Kerr, see Sec. 8 in [82].

Here we mention only one of the three null rotations, namely the one of class three,

$$l^\mu \to \Lambda\, l^\mu \quad , \quad n^\mu \to \Lambda^{-1}\, n^\mu \quad , \quad m^\mu \to e^{\mathrm{i}\Theta}\, m^\mu \qquad , \qquad (A.10)$$

which is used to define the "conformal weight" and the "spin-weight" of a NP-tetrad-scalar. A tetrad scalar Z that transforms like $Z \to \Lambda^c e^{i s \Theta} Z$ under a transformation (A.10) is ascribed the conformal weight c and the spin-weight s, see, e.g., Sec. 3.3 in [145]. As can be easily checked for the two interesting Weyl scalars we have

$$\Psi_0 \to \Lambda^2\, e^{2\mathrm{i}\Theta}\, \Psi_0 \qquad , \qquad \Psi_4 \to \Lambda^{-2}\, e^{-2\mathrm{i}\Theta}\, \Psi_4 \qquad , \qquad (A.11)$$

which means Ψ_4 is of spin-weight $s = -2$, while Ψ_0 of spin-weight $s = +2$. Note that

such a transformation is needed in our approach to the TKEQ for obtaining fields that are regular on the horizon and future null infinity (cf. Ch. 4).

Before proceeding, let us introduce some naming conventions of the NP-formalism, as they were also adopted by Teukolsky. Directional derivatives along tetrad legs get their own names

$$D = l^\mu \partial_\mu \,, \qquad \underline{\Delta} = n^\mu \partial_\mu \,, \qquad \delta = m^\mu \partial_\mu \,, \qquad \delta^* = m^{*\mu} \partial_\mu \,, \tag{A.12}$$

see Eq.'s (2.12) in [63]. Note that we use $\underline{\Delta}$ for what was called Δ by NP because we use $\Delta = r^2 - 2\,M\,r + r^2$. In addition, we use the asterisk for complex conjugation instead of an overbar. Furthermore, the Ricci-rotation coefficients are called "spin coefficients" in the context of a null tetrad and they get their own names,

$$\begin{aligned} \kappa &:= \gamma_{200} \,, &\quad \tau &:= \gamma_{201} \,, &\quad \sigma &:= \gamma_{202} \,, &\quad \rho &:= \gamma_{203} \,, \\ \pi &:= -\gamma_{310} \,, &\quad \nu &:= -\gamma_{311} \,, &\quad \mu &:= -\gamma_{312} \,, &\quad \lambda &:= -\gamma_{313} \,, \\ \epsilon &:= \frac{\gamma_{100} - \gamma_{320}}{2} \,, &\quad \gamma &:= \frac{\gamma_{101} - \gamma_{321}}{2} \,, &\quad \beta &:= \frac{\gamma_{102} - \gamma_{322}}{2} \,, &\quad \alpha &:= \frac{\gamma_{103} - \gamma_{323}}{2} \,. \end{aligned} \tag{A.13}$$

These 12 complex quantities describe the 24 independent components of γ_{abc} (the antisymmetry of the first two indices reduces the independent components to $6 \cdot 4 = 24$).

A.4 Tetrad perturbations

In order to find his famous equations, Teukolsky essentially linearised certain NP equations. These equations deal with tetrad-scalars and it is somewhat natural to deviate from the intuitive linearisation procedure of Eq. (A.1). Instead, consider a perturbed tetrad-scalar $\Psi = \Psi^A + \Psi^B$, where the perturbation is labelled with the superscript B and the unperturbed quantity with the superscript A. Intuitively one assigns the perturbation to the field that the tetrad scalar is built of. However, such a perturbation can be equivalently obtained when the unperturbed field is expressed in a perturbed tetrad basis. Such perturbed tetrad basis can be the result of perturbations of the metric $g_{\mu\nu}$ that was used to define the tetrad in Eq. (A.2). Then the tetrad can be decomposed into

$$\vec{l} = \vec{l}^{\,A} + \vec{l}^{\,B} \,, \qquad \vec{n} = \vec{n}^{\,A} + \vec{n}^{\,B} \,, \qquad \vec{m} = \vec{m}^{\,A} + \vec{m}^{\,B} \,, \tag{A.14}$$

with, for example, $\vec{l}^{\,A}$ being the fixed tetrad leg and $\vec{l}^{\,B}$ a small perturbation to it that accounts for dynamical changes of the metric. From this point of view a perturbation of a field $\Psi = \Psi^A + \Psi^B$ is explained as a perturbation of the underlying tetrad, which directly leads to perturbations in all tetrad related quantities like the Ricci-rotation-coefficients of Eq.'s (A.4) and in tetrad related equations like the NP-equations. In the context of the (gravitational) TKEQ, the perturbed field Ψ is a Weyl scalar and, therefore, one also speaks of "curvature perturbations" in contrast to metric perturbations. Notably, it seems a non-trivial and not fully solved problem to reconstruct the full metric perturbation (needed in the Lorenz-gauge for the self-force problem) from the curvature perturbations that are attained by solving the TKEQ, see Sec. 8.4 in [82].

A.5 Decoupled gravitational perturbation equations

Having introduced the idea of tetrad perturbations, all concepts for the derivation of decoupled gravitational perturbation equations are at hand. In essence, the procedure can be described as a clever superposition of certain NP-equations that are linearized in terms of a tetrad perturbation, plus an advantageous choice of the underlying null-tetrad, which leads to the vanishing of many NP quantities; more precisely, $\Psi_0^A = \Psi_1^A = \Psi_3^A = \Psi_4^A = 0$

and $\kappa^A = \sigma^A = \nu^A = \lambda^A = 0$ [1]. To get an impression of the NP-equations let us display explicitly one of them used by Teukolsky

$$
\begin{aligned}
&(\delta^* - 4\,\alpha + \pi)\,\Psi_0 - (D - 4\,\rho - 2\,\epsilon)\Psi_1 - 3\,\kappa\,\Psi_2 \\
&= (\delta + \pi^* - 2\alpha^* - 2\beta)\Phi_{00} - (D - 2\,\epsilon - 2\,\rho^*)\Phi_{01} + 2\sigma\Phi_{01} - 2\kappa\Phi_{11} - \kappa^*\,\Phi_{02} \quad , \quad (A.15)
\end{aligned}
$$

where the Φ_{ab} are contractions of the Ricci tensor with the tetrad legs, see Eq.'s (4.3) in [63]. They are intentionally on the right-hand-side of the equation because by virtue of the Einstein field equations they represent the matter terms; e.g., $\Phi_{00} = -\frac{1}{2}\,R_{\mu\nu}\,l^\mu\,l^\nu = 4\pi\,T_{\mu\nu}\,l^\mu\,l^\nu =: 4\,\pi\,T_{ll}$.

Inserting the decompositions of the fields $\Psi = \Psi^A + \Psi^B$, and accordingly the Ricci-contractions $\Phi = \Phi^A + \Phi^B$ and all the NP-operators like $\sigma = \sigma^A + \sigma^B$, into three such NP-equations like Eq. (A.15) yields a system of equations, which can be linearised in order to get equations for the perturbations Ψ^B. The particular case shown by Teukolsky in more detail in [18] is $\Psi^B = \Psi_0^B$ and we will follow the derivation for this case. First, note that the Φ^A vanish identically due to the demand that we consider a vacuum background metric. Second, the background spin coefficients, like, e.g., σ^A, can simply be computed given the background metric. Following Sec. II of [18], the only obstacles in obtaining the desired equation for Ψ_0^B are a few remaining NP-operator perturbations, like, e.g., σ^B, and a few appearances of the Ψ_1^B field. By a clever combination of further NP-equations Teukolsky was able to eliminate Ψ_1^B, and to replace the remaining NP-operator perturbations in favour of $\Psi_2^A\Psi_0^B$. The final result, Eq. (2.12) in [18], omitting the superscript A on all the background quantities, reads

$$
\begin{aligned}
\big[\, & (D - 3\,\epsilon + \epsilon^* - 4\,\rho - \rho^*)(\underline{\Delta} - 4\,\gamma + \mu) \\
& - (\delta + \pi^* - \alpha^* - 3\,\beta - 4\,\tau)(\delta^* + \pi - 4\,\alpha) - 3\,\Psi_2 \big]\,\Psi_0^B = 4\,\pi\,T_0 . \quad\quad (A.16)
\end{aligned}
$$

Here, T_0 means the perturbation T_0^B but, because $T_0^A = 0$, the distinction is not necessary. The source term T_0 contains all the matter contributions, and reads

$$
\begin{aligned}
T_0 =& (\delta + \pi^* - \alpha^* - 3\,\beta - 4\,\tau)\,[(D - 2\,\epsilon - 2\rho^*)\,T_{lm} - (\delta + \pi^* - 2\,\alpha^* - 2\,\beta)\,T_{ll}] \\
& + (D - 3\,\epsilon + \epsilon^* - 4\,\rho - \rho^*)\,[(\delta + 2\,\pi^* - 2\,\beta)\,T_{lm} - (D - 2\,\epsilon + 2\,\epsilon^* - \rho^*)\,T_{mm}] \quad . \\
& \hspace{13cm} (A.17)
\end{aligned}
$$

The corresponding decoupled equation for Ψ_4^B is found by exploiting the fact that the NP-equations are invariant under the change $\vec{l} \longleftrightarrow \vec{n}$, $\vec{m} \longleftrightarrow \vec{m}^*$. Consequently, Eq. (A.16) holds under the interchange of tetrad legs and we obtain the equation for Ψ_4^B as a corollary

$$
\begin{aligned}
\big[\, & (\underline{\Delta} + 3\,\gamma - \gamma^* + 4\,\mu + \mu^*)(D + 4\,\epsilon - \rho) \\
& - (\delta^* - \tau^* + \beta^* + 3\,\alpha + 4\,\pi)(\delta - \tau + 4\,\beta) - 3\,\Psi_2 \big]\,\Psi_4^B = 4\,\pi\,T_4 \quad\quad (A.18)
\end{aligned}
$$

with the source term

$$
\begin{aligned}
T_4 =& (\underline{\Delta} + 3\gamma - \gamma^* + 4\mu + \mu^*)\,[(\delta^* - 2\tau^* + 2\alpha)T_{nm^*} - (\underline{\Delta} + 2\gamma - 2\gamma^* + \mu^*)T_{m^*m^*}] \\
& + (\delta^* - \tau^* + \beta^* + 3\alpha + 4\pi)\,[(\underline{\Delta} + 2\gamma + 2\mu^*)T_{nm^*} - (\delta^* - \tau^* + 2\beta^* + 2\alpha)T_{nn}] \quad . \\
& \hspace{13cm} (A.19)
\end{aligned}
$$

---

[1] We are mainly interested in gravitational perturbations here, but the discussion is similar for electromagnetic perturbations. In that case one considers the Maxwell-equations on the Kerr background written in terms of NP quantities, see Eq.'s (3.1-3.4) in [18].

Since in the final result, Eq.'s (A.16)&A.18), the only remaining non-matter perturbation quantities are the fields Ψ_4^B and Ψ_0^B, the superscript B is usually dropped as well. The decoupled equations for Ψ_0 and Ψ_4 (A.16-A.19) hold for any vacuum, Petrov-type-D background metric. In particular for a Schwarzschild background they reduce to the Bardeen-Press equations [194]. It is interesting to read in [82] how Teukolsky derived these decoupled equations in "a few hours" after he was told by Press that Bardeen&Press had succeeded in obtaining such decoupled equations for Schwarzschild. The trouble was that the above equations did not allow, once specified to the Kerr spacetime and written out explicitly using the Kinnersley null tetrad in BL coordinates (cf. Eq. (3.2)), a separation of variables, as Teukolsky had hoped for [82]. It took several months until he realised that, instead of Ψ_4, the quantity $\rho^{-4}\Psi_4^B$ leads to the celebrated separable equations. In Sec. 3 we quoted the explicit TKEQ, Eq. (3.3). Deriving the gravitational parts of Eq. (3.3) from Eq.'s (A.16)-(A.19) is just a matter of computing the respective spin coefficients Eq.'s (A.13), and the directional derivatives Eq.'s (A.12). One only has to mind to consider suitably rescaled variables as listed in Table 1 of [18].

As a side note, it is interesting to mention that our approach in Ch. 4 actually starts from the Eq.'s (A.16)-(A.19) above. In fact, for our purpose of a time-domain solution the effort of finding separable equations, which seem to be the most celebrated result of the 1973 Teukolsky paper, would (likely) not have been necessary. In our approach we do not exploit the full separability to ODEs. The decoupled equations given above are enough in the sense that they can simply be written out explicitly for Kerr spacetime and solved numerically in 3+1 form, or in 2+1 form exploiting the trivial decomposition in azimuthal direction, possible in suitable coordinates. In Ch. 4 we have started from the decoupled equations (A.16-A.19) and chosen a different tetrad and different coordinates to derive an advantageous reformulation. Nevertheless, note that in order to start from the same explicit equation as usual, we have followed Teukolsky to rescale the field according to $\rho^{-4}\Psi_4^B$ on top of additional rescalings needed in our approach. Therefore, we cannot exclude that dropping the rescaling needed for separability might lead to unexpected numerical side effects.

Hyperboloidal compactification technique

The first part of this Appendix, Sec. B.1, provides the basic ideas on the topic of hyperboloidal foliations of spacetimes, i.e. the representation of the spacetime as a set of hypersurfaces with the defining properties to be spacelike everywhere, but to still extend through future null infinity $\mathcal{J}^+$. Two specific hyperboloidal foliations shall be introduced, the HH-coordinates in Sec. B.2, and the RT-coordinates in Sec. B.3. Finally, Sec. B.4 discusses briefly why we pick HH-coordinates as our standard choice. To avoid confusion with other parts of this thesis, we mention that in this Appendix the symbol S is used to denote the flexible coordinate value of future null infinity in HH-coordinates. In general, we loosely follow Sec. 2.9 of [195], and a series of works of Zenginoğlu [121, 123, 124, 126, 196], which are recommended for a rigorous introduction to the topic, and for further references to pioneering works of, e.g., Penrose [197, 198], Friedrich [199, 200], Frauendiener [201], and Moncrief [202].

Hyperboloidal foliations are relevant for their conceptual strength to allow a clean extraction of radiation information. Conventional 3+1-foliations have to extrapolate the signal to future null infinity because the radiation signal measured there is expected to be the best approximation for observers at large distances from the astrophysical sources[1] (see Sec. 4.1.2 in [122] and end of Sec. 5 in [203]). Such a foliation implies automatically beneficial effects on the issue of boundary treatment in computational simulations of unbounded domains [126]. This conceptual elegance makes hyperboloidal foliations a very promising strategy also for full numerical relativity simulations. This thesis deals only with BH perturbation theory and the below discussion is conducted with respect to this special application. Nonetheless, the successful application of hyperboloidal compactification observed here can certainly reinforce the motivation of studying the concept of hyperboloidal foliations in the context of the full Einstein Equations (see, e.g., [204, 205]).

B.1 Ideas of hyperboloidal foliations

In order to understand the ideas of constructing hyperboloidal coordinates let us consider one-dimensional flat spacetime in standard coordinates (t, x) with metric $\eta_{\mu\nu} = diag(-1, 1)$. In the search for foliations adapted to radiation extraction the most intuitive approach considers null rays. Outgoing gravitational radiation (travelling at the speed of light $c = 1$) will traverse $t = +x + $ const. lines, while ingoing radiation $t = -x + $ const. lines, both of which are "null". Visualising these as 45° lines in a (t, x) diagram one can easily imagine that the translation of either of these lines foliates the spacetime just as well as the conventional $t = const.$ foliation. This is basically the idea of the "characteristic approach". It turns out that in practice such foliation is prone to the formation of caustics in regions of strong gravitational fields (see Sec. 2.9 in [195] and [121]). This drawback leads to the idea of slices that are spacelike everywhere, i.e. not suffering from caustics, but still asymptotically reach $\mathcal{J}^+$. They are called "hyperboloidal slices". In the picture

---

[1]Note that the signal itself will obviously have died out at infinity, but assuming a certain fall-off behaviour like r^{-1} one can consider the suitably rescaled signal, see below in this section for our rescaling of the field variables.

of the (t, x) diagram such slices are nothing else but the well-known $t(x) = \pm\sqrt{k^2 + x^2}$ hyperbolae for some constant $k > 0$, which flatten in the limit of $k \ll x$ to the light cone. Again the translation along t of these hyperbolae provides a slicing of flat spacetime of the form $\tau(t, x) = \pm\sqrt{k^2 + x^2} + t$. A nice visualisation of such hyperboloidal slicing for a non-trivial BH spacetime can, e.g., be found in Fig. 1 of [196].

Hyperboloidal slices reach out to $\mathcal{J}^+$, but in order to exploit this fact a further step is needed. A spatial compactification must pull $\mathcal{J}^+$ to a finite coordinate value that can be part of a computational domain. It is advantageous to make the spatial coordinate value of $\mathcal{J}^+$ independent of the time function so that it is constantly represented by the same grid point in a numerical evolution [121]. Altogether, the procedure is called "hyperboloidal compactification". One should be aware of the positive effect of a hyperboloidal time coordinate on the "compactification problem", which would be entailed in a purely spatial compactification [126]. Imagine a wave travelling towards $\mathcal{J}^+$ (hyperbolic equations typically feature wavelike solutions $\sim e^{i(kx-\omega t)}$). There will be infinitely many oscillations on the way. A rash spatial compactification will, therefore, squeeze infinitely many oscillations into a finite coordinate domain, which can obviously not be resolved (see Fig. 2 in [126] for a nice visualisation). This problem is surmounted by a suitable transformation of the time coordinate, as a matter of fact, a hyperboloidal foliation. As explained in [206], the "bending up" of the slices is necessary to guarantee also in the asymptotic region a finite outgoing radial coordinate light speed, which allows to resolve the outgoing radiation.

Consider now the Kerr spacetime in standard BL-coordinates (t, r, θ, ϕ). In general Zenginoğlu summarises the hyperboloidal compactification technique (see Eq.'s (12) of [126]) as

$$\tau(t, r) = t - h(r) \quad , \quad r = \frac{\rho}{\Omega(\rho)} \qquad , \qquad (\text{B.1})$$

where h is called the height function and Ω the conformal factor. The zero set of Ω determines the coordinate value of ρ corresponding to spatial infinity, with the demand that $\Omega \neq 0$ elsewhere. One requires that $|\frac{d}{dr}h(r)| < 1$ (for $c = 1$) and $\frac{d}{d\rho}\Omega|_{\Omega(\rho)=0} \neq 0$. Usually Ω is chosen such that $\mathcal{J}^+$ is at the fixed coordinate position $\rho = S$ by simply setting $\Omega = 1 - \rho/S$. Here S is freely specifiable, except $S > \rho(r_+)$, but the choice affects the numerical features of the foliation (the name S is used because $\mathcal{J}^+$ is often called "scri"). The attribution of the label "conformal factor" to Ω can be understood by inspecting the metric in the compactified coordinates. There will be singularities at $\Omega = 0$ corresponding to $r \to \infty$, which require a conformal transformation of the physical metric $\tilde{g}_{\mu\nu} = \Omega^{-2} g_{\mu\nu}$ for regularity at scri. The height function becomes more intuitive when the foliation is examined in a conformal Penrose diagram, where it literally governs the offset of the hyperboloidal $\tau = const.$ slices from the original $t = const.$ ones. Note that the above prescriptions (B.1) are not unique but likely the most simple ones. Note, also, that the time transformation satisfies $\partial_\tau = \partial_t$. This means that if ∂_t was adapted to the timelike Killing field of some stationary spacetime ∂_τ remains so, and thus one avoids to introduce time-dependence in the metric coefficients.

A main motivation for hyperboloidal foliations is the resolution of the outer boundary problem, which refers to the spurious unphysical effects produced when employing standard outgoing boundary conditions called transparent or radiative (also absorbing or nonreflecting). The possibility to include $\mathcal{J}^+$ as the outer boundary in a computational domain removes that problem because the coordinate light speed is by construction purely outgoing at $\mathcal{J}^+$. Speaking more technically, any strongly hyperbolic system of equations can be decomposed into advection like equations for the characteristic variables (see, e.g., Sec. 5.3 in [195]), and the therein appearing speeds of ingoing fields vanish at $\mathcal{J}^+$. This means nothing physical will ever enter the computational domain from the outer boundary

(in general, gauge effects could still be superluminal, and thus have non-zero coordinate speeds with respect to a null coordinate system). This removes, in particular, the unphysical numerical reflections which decrease the accuracy. This fact is visualised in Fig. B.2 of the next subsection for a special choice of such coordinates, the "HH-coordinates".

B.2 "HH-coordinates"

After emphasising the motivation of hyperboloidal coordinates as an elegant way to handle the outer boundary problem, one might wonder about the inner boundary problem. Indeed, standard coordinates suffer from the same problem of unphysical numerical reflections at the inner boundary. It does not get as much attention because there is a well-known and simple solution: horizon-penetrating coordinates. These can be viewed as the counterpart to hyperboloidal coordinates. Since the inner region of the horizon is causally disconnected from the outer region, the inclusion of the horizon to the covered domain as the innermost grid point leads by construction to the suppression of outgoing radiation at the inner boundary. Combining both coordinate transformations yields a grid which constitutes a causally closed domain. Thus, no spurious radiation can propagate from the boundaries into the domain.

One such realisation is the "HH"-coordinate system $(\tau, r, \theta, \varphi)$ (HH for horizon-penetrating, hyperboloidal), which was first introduced in [20], and adopted in this thesis and the associated publications [H2, H3] as the standard choice for the algorithm. The horizon-penetration is achieved by using the ingoing-Kerr (iK) coordinates

$$d\tilde{t} = dt + \frac{2Mr}{\Delta}dr, \qquad d\varphi = d\phi + \frac{a}{\Delta}dr \qquad (B.2)$$

$$\Leftrightarrow \quad \tilde{t} = t - r + \int \frac{a^2 + r^2}{\Delta} dr, \quad \varphi = \phi + a \int \frac{dr}{\Delta} . \qquad (B.3)$$

The level sets of the iK-slicing are visualised as dotted, green lines in the conformal diagram Fig. B.1. For clarity let us point out a maybe obvious subtlety; namely, after the transformation (B.2) a Fourier-decomposition of a field variable refers to $e^{im\varphi}$- instead of $e^{im\phi}$-modes (cf. Eq. (3.9)). Applying the transformations to the Kerr metric (3.1) results in the line element

$$ds^2_{\mathrm{iK}} = -\left(1 - \frac{2Mr}{\Sigma}\right) d\tilde{t}^2 - \frac{4aMr}{\Sigma}\sin^2\theta \, d\tilde{t} \, d\varphi - 2a\sin^2\theta \left(1 + \frac{2Mr}{\Sigma}\right) dr d\varphi + \qquad (B.4)$$

$$+ \frac{4Mr}{\Sigma} d\tilde{t} dr + \left(1 + \frac{2Mr}{\Sigma}\right) dr^2 + \Sigma d\theta^2 + \left(r^2 + a^2 + \frac{2Ma^2 r \sin^2\theta}{\Sigma}\right) \sin^2\theta d\varphi^2 \quad ,$$

where $\Sigma \equiv r^2 + a^2 \cos^2\theta$ and $\Delta \equiv r^2 + a^2 - 2Mr$ as defined after Eq. (3.1).

On top of these first transformations comes the hyperboloidal compactification. Following the insights gained in [132], a favourable choice for the height function satisfies the demand that the coordinate expression of the outgoing radial coordinate light speed be asymptotically the same in the old as in the hyperboloidal coordinate system. Before computing the outgoing characteristics, note that we can ignore angular dependencies and set $a = 0$ since we are only interested in the asymptotic behaviour of the characteristics. For the iK-system we then find $\frac{d\tilde{t}}{dr} = \pm\frac{r+2M}{r-2M}$ from $ds^2 = 0$ for radial null curves. After integration this yields $\tilde{t} = r + 4M \ln(r - 2M)$, which motivates the retarded time $u = \tilde{t} - (r + 4M \ln(r - 2M))$. We can drop the $2M$ subtraction in the logarithmic term because, again, we are interested in an asymptotic condition. Denoting the new coordinates by (τ, ρ), we, therefore, demand

$$\tilde{t} - (r + 4M \ln r) \stackrel{!}{=} \tau - (\rho + 4M \ln \rho) . \qquad (B.5)$$
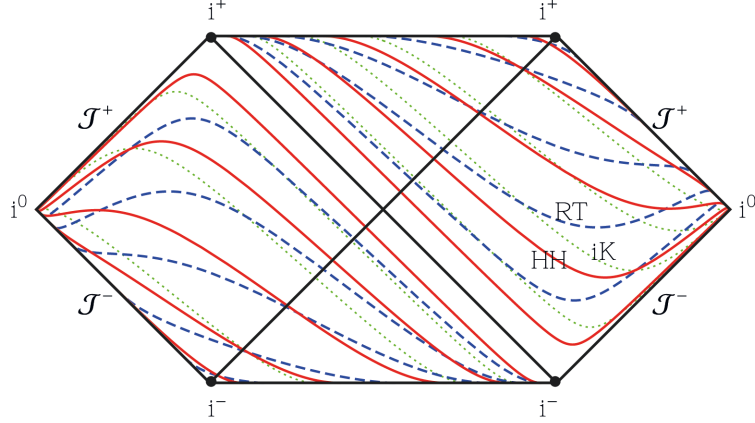
Figure B.1: Foliations of Schwarzschild spacetime ($a = 0$): ingoing Kerr (iK; green dotted; see Sec. B.2), Rácz–Tóth (RT; blue dashed; see Sec. B.3), and horizon-penetrating-hyperboloidal (HH; red solid; see Sec. B.2) coordinates with $S = 10$. Plot adopted from [H2].

Rearranging terms according to (B.1), we find the height function $h(\rho)$. Imposing the simplest choice for the compress function Ω, we arrive at

$$h(\rho) = \frac{\rho}{\Omega} - \rho - 4M \ln \Omega, \qquad \Omega(\rho) = 1 - \frac{\rho}{S} \quad . \tag{B.6}$$

The horizon in the new coordinates is located at $\rho_+ = \frac{a^2 S + M S^2 + \sqrt{M^2 S^4 - a^2 S^4}}{a^2 + 2MS + S^2}$. The resulting foliation of Kerr spacetime for $S = 10$ is shown as solid red lines in Fig. B.1; together with the iK-slices, and another hyperboloidal, horizon-penetrating foliation (labelled RT), which is introduced in the next section. The conformal diagram shows that the foliation is manifestly horizon-penetrating and smoothly reaches scri. In the following we denote the choice of the flexible parameter S by an indexed suffix HH_S. To get an idea of the effect of S one can argue that it is inversely correlated with the mean curvature along the slice [121]. Large S are therefore connected with small mean curvature, and vice versa. Furthermore, vanishing mean curvature is asymptotically given on Cauchy surfaces while infinite mean curvature is related to characteristic surfaces. In this picture large S are pulling the hyperboloidal surfaces towards a more Cauchy-like behaviour, whereas small S are pushing the surface to more characteristic-like behaviour. The behaviour of the characteristics $c_\pm$ for some choices of S (HH_1, HH_{10} and HH_{20}) is illustrated in Fig. B.2. As expected, the outgoing radial coordinate speeds c_+ vanish at the horizon and the ingoing radial coordinate speeds c_- vanish at scri. This allows simulations without imposing any boundary conditions and it is the reason for the excellent accuracy of the approach (prove of which is given in Ch. 5). After several tests, as discussed in Sec. B.4, we made $S = 10$ our standard choice.

In practical applications it is useful to assign features of the waveforms to the responsible event in the dynamics. The dynamics are computed within BL-coordinates and, hence, the time parameter is associated to an observer at infinity. The waves at future null infinity can be connected to this observer's time by accounting for the required travel time[2], i.e. by applying a retarded time coordinate. GWs travel along null geodesics and for our purpose it is enough to approximate them in Schwarzschild. Thus, we introduce the tortoise coordinate $r^* = r + 2M \ln \left(\frac{r}{2M} - 1 \right)$, which allows to characterise radial null curves by $t = \pm r^*$. We can define retarded and advanced time coordinates by $u = t - r_*$ and $v = t + r_*$. Setting in the transformations to iK-$\tilde{t}$ and the subsequent transformation

---

[2]Note that in the hyperboloidal coordinates a wave reaches scri in a finite coordinate time $\Delta\tau$.
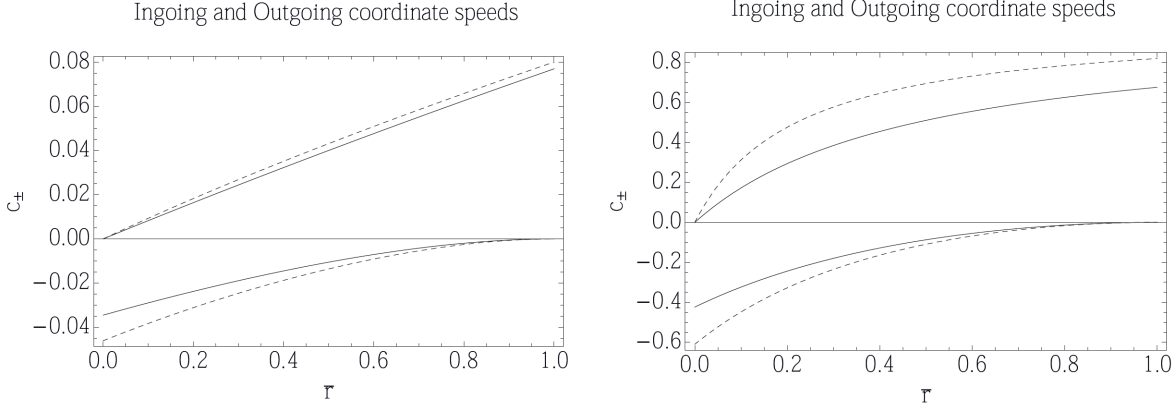
Figure B.2: Visualisation of ingoing (c_-, negative) and outgoing (c_+, positive) radial coordinate light speeds, when $a = 0$. On the left panel we use HH_1 (solid) and RT (dashed) coordinates (RT for Rácz and Tóth [168], see Sec. B.3). On the right panel we use HH_{10} (solid) and HH_{20} (dashed) coordinates. The incoming (with respect to the domain) characteristic speeds vanish at both boundaries (horizon and scri), so no boundary conditions are needed. Note the radial domains are rescaled to $[0, 1]$ for the comparison. Plot adopted from [H2], credits are due to Dr. Zenginoğlu.

to HH-coordinates we can compute the retarded time

$$u(\tau, \rho) = \tau - \rho - 4M \ln \left(\frac{S\rho + 2M\rho - 2MS}{S} \right) + 2M \ln 2M \ , \tag{B.7}$$

and the advanced time

$$v(\tau, \rho) = \tau + \rho \frac{S + \rho}{S - \rho} - 4M \ln \left(\frac{S - \rho}{S} \right) - 2M \ln(2M) \ . \tag{B.8}$$

The constant term $2M \ln 2M$ comes from our convention for the integration constant of the tortoise coordinate. We use $u(\tau, S)$ to visualise waveforms at scri and $v(\tau, \rho_+)$ at the horizon. Then $u = 0$ and $v = 0$ correspond to the start of the dynamics, and one does not have to align by hand waveforms and dynamical quantities (like, e.g., the orbital frequency of the point-particle).

B.3   "RT-coordinates"

Another important hyperboloidal foliation was introduced already in 2011 by Rácz and Tóth [168], hereafter RT-coordinates, and used in a study of late-time tail decay rates for the scalar wave equation on Kerr. We adopted these coordinates in our continuative study of decay rates of gravitational and electromagnetic perturbations in [H0, H1]. In this thesis only the results shown in Ch. 6 were obtained within the RT-coordinate system.

The RT-coordinates are very similar to Moncrief's scri-fixing coordinates in Minkowski spacetime (see slide 4 in [202], with $\kappa = 1$, and [207, 208]), but with an additional logarithmic term, necessary to satisfy the asymptotic properties presented in [121]. As done for the HH-coordinates, one starts with a transformation to iK-coordinates to obtain horizon-penetrating coordinates. Subsequently, one adds a hyperboloidal compactification. Denoting the time and space RT-coordinates by $\{T, R\}$, the height function and the conformal factor are given by

$$h(R) = \frac{1 + R^2}{2\Omega} - 4M \ln 2\Omega \ , \qquad \Omega(R) = \frac{1 - R^2}{2} \ , \tag{B.9}$$

which results in the explicit transformations

$$\tilde{t} = T - 4M \ln\left(1 - R^2\right) + \frac{1 + R^2}{1 - R^2} \ , \quad r = \frac{2R}{1 - R^2} \ . \tag{B.10}$$

Note that the height function blows up at infinity, where the conformal factor vanishes in a suitable way. The first term in the height function is the same term as in Minkowski spacetime; the second term is needed due to the presence of the BH. The resulting hyperboloidal foliation of Kerr spacetime is horizon penetrating and smoothly reaches scri at $R = 1$. The event horizon R_+ in the new radial coordinate R is located at $R_+ = \frac{2\sqrt{2M\sqrt{M^2-a^2}-a^2+2M^2+1}-2}{2\left(\sqrt{M^2-a^2}+M\right)}$. Figure B.1 shows the time surfaces of the RT coordinates in a conformal diagram for the non-rotating $a = 0$ case (blue lines). The characteristics $c_\pm$ vanish at scri and the horizon respectively and are similar to the HH_1 characteristics as displayed in Fig. B.2. Note that RT-coordinates can also be modified to allow a prescribed scri position [H1], but this choice does not seem to affect the numerical properties.

B.4 Numerical comparison: "RT" vs. "HH"

Let us conclude with a comparison of RT- and HH-coordinates with respect to their numerical efficiency in solving the TKEQ. Both of the coordinate systems have the desired properties of hyperboloidal coordinates, i.e. (i) no boundary conditions are needed, and (ii) no extrapolation is needed for clean wave extractions at the horizon and scri. Still, in a numerical implementation there can be differences in stability and efficiency. In particular the flexible parameter S in the HH-coordinates affects the numerical properties and can be fine-tuned towards maximal efficiency.

We compared RT-coordinates with HH_S coordinates for $S = 1, 10, 20$ for $a = 0$. RT and HH_1 coordinates behave very similarly numerically, which can be expected from the similarity of the coordinate speeds shown in the left panel of Fig. B.2. Increasing S allows to use larger time stepping and, thereby, increases the efficiency. But the number of waves that have to be resolved on the spatial grid becomes larger as well (remember that large S means slices that are more Cauchy-like). For too large S this blue-shifting of the wave (cf. Fig.2 of [126]) leads to wavelengths which cannot be resolved anymore near the compactification boundary. In practice, one has to find a good balance between the resolution at this boundary and the time stepping, which is restricted by a Courant-Friedrichs-Lewy condition, and, therefore, depends on the characteristic speeds. From our numerical experiments we found that $S = 10$ allows a doubling of the time stepping, compared with $S = 1$ and RT-coordinates, without any sign of instability. Values of $S \geq 20$ can, in principle, be even faster, but require artificial dissipation to guarantee stable simulations, which reduces the accuracy and, moreover, slows down the code again. The effect is not yet understood at a quantitative level in terms of a physical argumentation, but it is certainly related to the connection between S, the mean extrinsic curvature and the characteristic speeds. Therefore, we just settle for $S = 10$ as our standard choice motivated from its performance in the numerical experiments.

Explicit coefficients of the TKEQ in HH-coordinates

For completeness, this Appendix provides the explicit expressions for the coefficients of Eq. (4.3) in HH-coordinates (see [H1] for RT-coordinates). Remember that Eq. (4.3) is the 2+1 reduced form of the full equation, i.e. φ derivatives have been processed to im factors. We separate real and imaginary part for the complex-valued coefficients. Denoting the mass of the central BH M, its specific angular momentum a, the spin-weight of the considered field s, the coordinate location of scri in the HH-coordinates S, and the radial coordinate ρ, the coefficients read

$$
\mathcal{R}(C_0) = -\frac{2a^2 S^2}{\rho^2} + \frac{4a^2 S}{\rho} - 2a^2 + m^2 S^2 \csc^2(\theta) + 2ms S^2 \cot(\theta) \csc(\theta)
$$
$$
+ \frac{2Ms S^2}{\rho} - 2Ms S + \frac{2MS^2}{\rho} - 2MS + s^2 S^2 \cot^2(\theta) - s S^2 \;,
\tag{C.1}
$$

$$
\mathcal{I}(C_0) = \frac{2amS(S-\rho)}{\rho} \;,
\tag{C.2}
$$

$$
\mathcal{R}(C_\tau) = -\frac{2}{\rho S^2} \left\{ a^2 \left(2M(\rho + 2S)(\rho - S)^2 + \rho \left(\rho^3 + S^3 - 2\rho^2 S \right) \right) \right.
$$
$$
\left. + \rho S \left(4M^2(\rho - S)(\rho + sS + S) + M \left(2\rho^3 - (s+1)S^3 + 2\rho s S^2 + \rho^2(s-1)S \right) + \rho S(\rho - S)(\rho + sS) \right) \right\} \;,
\tag{C.3}
$$

$$
\mathcal{I}(C_\tau) = 2a \left(s S^2 \cos(\theta) - m(4M(\rho - S) + \rho(\rho - 2S)) \right) \;,
\tag{C.4}
$$

$$
\mathcal{R}(C_\rho) = -\frac{2(\rho - S) \left(a^2(\rho + S)(\rho - S)^2 + \rho S(M(\rho - S)(2\rho + sS + S) + \rho S(\rho + sS)) \right)}{\rho S^2} \;,
\tag{C.5}
$$

$$
\mathcal{I}(C_\rho) = -2am(\rho - S)^2 \;,
\tag{C.6}
$$

$$
C_\theta = -S^2 \cot(\theta) \;,
\tag{C.7}
$$

$$
C_{\tau\tau} = -\frac{1}{S^2} \left\{ \left(4M(\rho - S) + \rho^2 - S^2 - 2\rho S \right) \cdot \right.
$$
$$
\left. \left(a^2(\rho - S)(4M + \rho - S) + \rho S \left(8M^2 + 2M(\rho + S) + \rho S \right) \right) + a^2 S^4 \sin^2(\theta) \right\} \;,
\tag{C.8}
$$

$$
C_{\rho\rho} = -\frac{(\rho - S)^2 \left(a^2(\rho - S)^2 + \rho S(2M(\rho - S) + \rho S) \right)}{S^2} \;,
\tag{C.9}
$$

$$
C_{\theta\theta} = -S^2 \;,
\tag{C.10}
$$

$$
C_{\tau\rho} = -\frac{2 \left(a^2(\rho - S)^2(4M(\rho - S) + \rho(\rho - 2S)) + \rho S \left(8M^2(\rho - S)^2 + 2M(\rho - S)^2(\rho + S) + \rho^2 S(\rho - 2S) \right) \right)}{S^2} \;.
\tag{C.11}
$$

Review: GWs from spinning particles

In this Appendix we provide a short literature review on GWs produced with the TKEQ from spinning particle matter perturbations. The TKEQ is the standard tool to compute the GWs of binaries in the point-particle limit when the spin of the central object needs to be taken into account (cf. Ch. 3). The spin of the test-particle, however, is usually ignored by virtue of the argument that the body be too small to have measurable spin [19]. Theoretical considerations exclude large values of the spin in astrophysical configurations (cf. [40]); more precisely, $S/(\mu M) \sim \mathcal{O}(1)$ is unphysical if $\mu \ll M$. But, the spin of the particle might become more important if (i) the mass ratio is mildly extreme, $\mathcal{O}(10^{-3})$ [183], or (ii) one considers secular evolutions [30]. In addition, investigations of spin effects are of theoretical interest and conclusions for comparable mass binaries can be drawn at least qualitatively. Therefore, it is highly desirable to have a GW algorithm which accounts for both the central object's and the particle's spins.

The literature on GWs from a SP orbiting about a Kerr background is far less extensive than that on the dynamics. Basically, there is only a hand full of studies to be used as a guide line [184, 185, 56, 186]. In order to not repeat recurrent discussions let us summarize what all of them bear in common, (i) the direction of the spin vector is limited to be parallel or anti-parallel to the rotation axis of the central Kerr BH, which is necessary for particular motions like equatorial orbits or radial plunges as investigated in these works, (ii) the MPEQs (2.6) are closed with the TUL-SSC, and simplified for the restricted class of orbits, (iii) theoretically too high spin magnitudes $S/(\mu M) \sim \mathcal{O}(1)$ are considered, and (iv) the obtained dynamics are used to build the source term for the $s = -2$ TKEQ; the TKEQ is transformed to the Sasaki-Nakamura Equation and the GWs are computed in the frequency domain (cf. Sec. 3.2).

Let us now have a more detailed look at the respective results. The first study of Mino et al. [184] dates in 1995 and considers radial infalls along the z-axis with the spin-vector parallel to the z-axis. The main result is that the energy fluxes can significantly depend on the spin-magnitude and its direction. For large aligned, with respect to the spin of the central BH, spins the flux is comparable to the nonspinning case, whereas for large anti-aligned spins the flux is larger by a factor three. The authors also point out that the changes in the GWs of a SP compared to those of a nonspinning particle originate from two effects, (i) the different dynamics due to spin(1)-spin(2) and spin(2)-orbit interactions, and (ii) the appearance of spin dependent terms in the source term of the TKEQ. They find out that the second effect is the dominant one. Chronologically next is the analytic study of circular equatorial orbits due to Tanaka et al. [56] in 1996. The authors compute, within the PN framework, the energy fluxes to infinity and their projections, therein $\eta_{\ell m}$, on spin-weighted spheroidal harmonics up to 5PN. The PN parameter v is chosen as $v^2 := M/r_0$, i.e. it is not the orbital velocity unless $a = S = 0$. The results for $\eta_{\ell m}$ are our target solution; for large orbital radii our numerical solutions should reproduce the PN formulas. In addition, the authors estimate the RR from the found fluxes, and show an interesting plot on the position of the ISCO depending on a and S (see, also, [209] for a study of the ISCO for SPs). Next comes the work of Saijo et al. [185] in 1998, which complements reference [184], in the sense that here radial infalls in the x-y-plane are

considered. Throughout the study, the conserved total energy of the particle is restricted to $E = \mu$ (cf. Eq. (2.7)). Orbits are parameterised by the "orbital angular momentum", which they define as the conserved total angular momentum (z-component only, as usual) minus the spin $L_z = J_z - S$. As mentioned by Semerak et al. [30] (cf. discussion after Eq. (34) therein), for some trajectories obtained within the MPEQs and the TUL-SSC the tangent stops being timelike. This failure is interpreted as an indication of the insufficiency of the pole-dipole approximation, and of the MPEQs, for too large spins or/and for too inhomogeneous gravitational fields. Saijo et al. mention the same problem; especially for $S/(\mu M) \sim \mathcal{O}(1)$, the region of L_z which results in reasonable trajectories is highly restricted (cf. Fig. 2 in [185]). The main results of the paper are imparted in plots, among these, e.g., (i) the total radiated energy versus L_z for spin(1) values $\hat{a} \in \{0, 0.3, 0.6, 0.9\}$ and spin(2) magnitudes in $S/(\mu M) \in \{-0.9, 0.0, 0.9\}$, (ii) energy spectra for different combinations of a, S at fixed L_z, and (iii) the gravitational strain $h_\times$ and h_+ for different L_z and S at fixed $\hat{a} = 0.6$. Contrarily to infalls along the z-axis [184], for infalls in the equatorial plane, parallel spins $(a\,S > 0)$ are found to enhance the energy fluxes compared with the nonspinning case; anti-aligned spins $(a\,S < 0)$, instead, decrease the fluxes (see Fig. 3 in [185]). Note that a is chosen strictly positive, with the sign of L_z defining the sense of the orbit (instead in this thesis we allow $a < 0$ with L_z always positive). Furthermore, the gravitational fluxes are found to become maximal when spin(1), spin(2) and the orbital angular momentum are aligned. In 2010, almost 15 years later, the recent study of Wen-Biao Han appears [186]. Therein fluxes from a SP in circular, equatorial orbits are computed, but differently from [56] the GWs are found numerically. The main results are three plots for energy fluxes to infinity and down the horizon for $a = \pm 0.996, 0$ at $r = 10M$. In principle, these plots should be as well target solutions for our work. But, as mentioned in Ch. 8, our results disagree significantly. While the origin of the discrepancies is not entirely clear, one may notice that reference [186] only cross-checks the results against PN solutions for $S = 0$.

Other spin supplementary conditions

In Sec. 2.1.3 we have introduced the TUL-SSC as our choice for fixing the notion of spin. Since it is useful to know a few other important SSCs, this Appendix shall quote a few relevant possibilites. Following the notation of Sec. 2.1 a dot denotes $v^\alpha \nabla_\alpha$.

First, there is the Pirani SSC (in [32] called "Frenkel" [27] respectively) condition [210]

$$v_\mu S^{\mu\nu} = 0 \qquad , \tag{E.1}$$

which, following [23], was also used in the early works [27, 28, 29]. This SSC features the strict conservation of $m = -p_\mu v^\mu$ and allows the definition of the spin-vector

$$s^\mu = \frac{1}{2} \, \epsilon^{\mu\nu\rho\sigma} \, v_\nu \, S_{\rho\sigma} \quad , \tag{E.2}$$

with a conserved spin measure $2S^2 = 2 \, s^\mu s_\mu = S^{\mu\mu} S_{\mu\nu}$. Condition (E.1) does not constrain a unique relation between the tangent and the specific linear momentum and the spin-tensor. While a unique relation can be found for $\dot{v}^\mu$ [31], one is left with the freedom of the initial values for v_i^μ, and the choice obviously influences the obtained dynamics. In particular, if v_i^μ is not chosen parallel to p^μ with respect to the initial choice for the reference point, one will observe helical motion[1] of the reference point on top of the overall motion [31]. As already argued by Tulczyjew [34, 38], restricting to linear in spin considerations allows to spare the quadratic term in Eq. (2.9). In that case, typically seen in PN-expansions [153, 211], the Pirani- and the TUL-SSC are equivalent, and $v^\alpha \nabla_\alpha S^{\mu\nu} = 0$.

For completeness, three other useful SSC are mentioned here. First, there is the coordinate dependent SSC suggested by Corinaldesi and Papapetrou [212], $S^{0i} = 0$. This SSC might be applicable if one has some preferred coordinate system like the one adapted to a fixed BH background. The COM which serves as the reference point for the worldline could then be the one measured in the background coordinates, i.e. in the rest frame of the source of the gravitational field. This choice results in a unique relation for $v^\mu, p^\mu, S^{\mu\nu}$ and, consequently, in a unique worldline [31]. Second, there is the generalized Newton-Wigner [213] SSC as introduced by [214]. The condition chooses the four velocity with respect to which the spin shall vanish as the sum of the specific linear momentum and a timelike tetrad leg. It allows the construction of a Hamiltonian with variables which are canonical at linear order in the particle's spin [214]. Finally, there is the recent Kyrian-Semerak SSC [31], which demands only $\dot{\omega}^\mu = 0$, and $\omega_\mu \omega^\mu = -1$, without specifying ω_μ further. This SSC leads to a particularly simple form of the evolution equations because it implies $m = \mu$ and $u^\mu = v^\mu$. Consequently, the MPEQs simplify to $\dot{S}^{\mu\nu} = 0$. In this case, the worldline is, obviously, not unique unless ω_i^μ is specified, respecting $\dot{\omega}^\mu = 0$ and $\omega_\mu \omega^\mu = -1$.

---

[1]Note that [48] explains such helical motions as pure gauge effects without physical influence on the overall motion. Therefore, such motion is viewed as an equally valid description of the same motion, only a more complicated one.

Algorithm to compute the $S_{s\ell m}$

It can be useful to compute the $S_{s\ell m}^{a\omega}$ functions defined by Eq. (3.6), even when not working in the frequency-domain. For circular equatorial orbits, for example, the solution consists of a single frequency ω; thus, $a\omega$ is fixed and we have a unique set of basis functions $S_{s\ell m}$. The $S_{s\ell m}$ can be used, (i) as a projection basis in order to compare against frequency domain results employing that basis, and (ii) to exploit the "Starobinsky-Teukolsky" identities, saving computation time (cf. Sec. 4.2.1).

A nice algorithm to compute the $S_{s\ell m}$ is presented in App. A.1 of [60] (cf. also [55]). The idea is to expand the $S_{s\ell m}(\theta, \phi)$ in terms of the well-known $Y_{s\ell m}(\theta, \phi)$; more precisely, noting the same $e^{i\,m\,\phi}$ terms,

$$\tilde{S}_{s\ell m}^{a\omega}(\theta) = \sum_{j=l_{\min}} b_j^{a\omega} \tilde{Y}_{sjm}(\theta) \quad, \tag{F.1}$$

where $Y_{s\ell m}(\theta, \phi) = \tilde{Y}_{sjm}(\theta)\, e^{im\phi}$ and $\ell_{min} = \max(|m|, |s|)$. It remains to compute the expansion coefficients $b_j^{a\omega}$ for a given $a\omega$ up to sufficiently large j. A way to get some equation determining these coefficients is to, (i) insert the expansion Eq. (F.1) into the definition equation (3.6), (ii) note that the $\tilde{Y}_{sjm}$ satisfy the equation for $a\omega = 0$, and (iii) finally, to integrate the remaining pieces against $\tilde{Y}_{s\ell m}^*$. The appearing integrals can be expressed in terms of Clebsch-Gordan coefficients. Their properties are known and reveal that the different integrals in the obtained sum are nonvanishing only for those $\tilde{Y}_{sjm}$ with $j \in \{\ell-2, \ell-1, \ell, \ell+1, \ell+2\}$. For a given m this yields a relation between the coefficient $b_\ell^{a\omega}$ and the five other coefficients $b_j^{a\omega}$ for $j \in \{\ell-2, \ell-1, \ell, \ell+1, \ell+2\}$. Repeating this for all ℓ, and collecting the equations as lines into a (infinite) matrix, one obtains an eigenvalue-problem $\mathbf{M}_m \vec{b}_m^{a\omega} = \mathcal{E}_m \vec{b}_m^{a\omega}$ (see Eq. (A6) in [60]). Truncating at $\ell = \ell_{\max}$ restricts the matrix to $n \times n$ with $n = \ell_{\max} - \ell_{\min} + 1$. One just has to solve this eigenproblem to get as solutions the desired eigenvalues $\mathcal{E}_m$ and the coefficients-vector $\vec{b}_m$. Since the matrix is band-diagonal with nonzeros only at $\{(i, i-2), (i, i-1), (i, i), (i, i+1), (i, i+2)\}$, where $i \in \{1, .., n\}$, it is quickly solvable with standard methods.

Our implementation restricts to $s = \pm 2$. We avoid the cumbersome development of a Clebsch-Gordan calculator by employing *mathematica* for precomputing the matrix $\mathbf{M}_m$ with $\ell_{\max} = 20$ and unspecified $a\omega$. At simulation time, when $a\omega$ is known, we determine the numerical values for $\mathbf{M}_m$, and solve the eigenproblem by means of the *gnu scientific library* <gsl_eigen.h> [215]. As a crosscheck, the results for the $S_{s\ell m}$ can be inserted back in the definition equation, or compared to the polynomial fits given by Press&Teukolsky in [64]. It is interesting to look at some example for the ℓ'th eigenvector $\vec{b}_{\ell m}^{a\omega}$. For $s = -2$, $a = 0.9$, $m = 2$, $r_0 = 4$ and $\Omega(a, r_0) = 0.11236$, e.g., we have $a\omega = 0.202247$. We get $\vec{b}_{22}^{a\omega} = (0.999273, -0.0381148, 0.00113455, -0.0000262984, 5.02749 \cdot 10^{-7}, -8.11421 \cdot 10^{-9}, 1.13519 \cdot 10^{-10}, \sim 0, ..)$ with eigenvalue $\mathcal{E}_{-222}(a\,\omega = 0.202247) = 5.43011086$. This indicates that, for some modes (but not all!), $\tilde{S}_{-2\ell m}$ is dominated by $\tilde{Y}_{-2\ell m}$ for most $a\omega$, whereas the eigenvalue is rather different from the $a = 0$ value $\mathcal{E}_{-222}(a\,\omega = 0) = 6$.

Further Comments

In this appendix two less important, though possibly useful, conclusions drawn in the course of this thesis shall be mentioned. Both refer to the point particle treatment within the TKEQ. The first comment, Sec. G.1, describes the possibility to perform the source computation in BL-coordinates even when the HH-TKEQ is used ("mixed approach"). The second comment, Sec. G.2, points out certain ambiguities in the calculation of a distributional source. The content here could be thought of as continuing the discussions of Sec. 4.3.

G.1 Coordinate invariance of the source

It seems useful to highlight the possibility of choosing other coordinates for the evolution than for the source term computation. One may notice that the source term S_s is a tetrad scalar and, therefore, theoretically invariant from the choice of coordinates. Yet, in practice, it is clear that the coordinates are crucial; e.g., a source in BL-coordinates cannot be regular at the horizon. Still, if one is only interested in configurations in which the matter perturbation does not reach the horizon it is tempting to employ a mixed approach, i.e. the HH-TKEQ with a simple source term in BL-coordinates. One such scenario is the investigation of fluxes from a point-particle in circular orbit. In this case the mixed approach proved highly useful to extinguish implementation errors. Therefore, some caveats and the limitations that have to be taken into account in the mixed approach shall be explained here.

Imagine to use a grid in hyperboloidal coordinates to evolve the TKEQ (4.3), but having performed the source calculation in BL-coordinates; this means, in particular, to have the ∂_μ refer to $(\partial_t, \partial_r, \partial_\theta, \partial_\phi)$ and time-dependencies in the δ's to refer to t. In BL-coordinates the corresponding $T_{\mu\nu}$ will contain delta-functions like $\delta(r - r_p(t))$. The first problem is the representation of a δ-function in BL-r on a HH-ρ grid. For example, considering the Gaussian one could try to evaluate the δ at every ρ_i like $\delta_\sigma(r - r_p(t)) \sim e^{-0.5\,\sigma^{-2}\,(r(\rho_i) - r_p(t(\tau,\rho_i)))^2}$. This would, though, significantly deteriorate the approximation of the delta on the evolution grid because a Gaussian narrow in BL-r can be smeared out in HH-ρ. For a good δ approximation we have to insist on representing the δ directly on the evolution grid. A way out is to exploit the known transformation behaviour of δ-distributions [91]

$$\delta(r - r_p(t)) = \frac{\delta(\rho - \rho_p(t))}{\left|\frac{dr(\rho)}{d\rho}\right|} \quad . \tag{G.1}$$

It is important to note that, (i) the particle position ρ_p remains a time-dependent quantity (more explicitly BL t dependent), and (ii) in a BL source computation this δ is hit only by BL-t derivatives, so we have to compute the BL-t derivative of the HH-ρ position of the particle $\partial_t \rho_p(t) = \partial_t \frac{Sr_p(t)}{S + r_p(t)}$. A second minor issue arises from the use of BL-ϕ in the source while the HH-φ is used for the homogeneous part of the TKEQ. The overall factor $e^{-im\varphi}$, which is multiplied to the equation to erase φ dependencies in the homogeneous part, appears in the source term. When the source term is computed in BL-coordinates the δ in azimuthal direction refers to BL-ϕ and the decompo-

sition in modes reads $\delta(\phi - \phi_p(t)) = \frac{1}{2\pi} \sum_m e^{i\,m\,(\phi - \phi_p(t))}$. Using the relation between ϕ and φ, Eq. (3.10), we observe that the φ and ϕ dependences still disappear because of $e^{im(\phi - \varphi)} = e^{-im\,(a/(r_+ - r_-))\,\log((r-r_+)/(r-r_-))}$. Accounting for this remaining factor is important to get the correct result. The third issue is the most subtle one. At each time slice $\tau = const.$ one will be traversing the computational grid points ρ_i to compute pointwise the source term S_s needed for the evolution. This source term requires knowledge of the particle's position $(r_p(t), \theta_p(t), \phi_p(t))$. The crucial point is that the extraction of these positions from the precomputed dynamics implies to compute $t(\tau, \rho_i)$. Thus, at a fixed evolution time τ, each point of the evolution grid ρ_i possesses a different BL-t, and, as a consequence, each ρ_i observes the particle at a different BL-position. In particular, observers close to the horizon suffer from $t(\tau, \rho) \xrightarrow[\rho \to \rho_+]{} \infty$ because $r_p(t) \xrightarrow[t \to \infty]{} r_+$.

In our first tests we followed this mixed procedure. It turned out that it is working well as long as the particle is far enough away from the horizon; e.g., on a circular orbit. As expected, the source term on the hyperboloidal grid takes exactly the same form no matter if calculated in BL- or HH-coordinates. Yet, in general, the BL-approach is disadvantageous for two reasons. First, the computational costs are drastically higher if we have to interpolate the particle's position at every ρ_i again. It is much more convenient to have a unique particle's position at a given slice $\tau = const.$. This is only possible when the source is computed in HH-coordinates (or, more precisely, in the same coordinates as used for the evolution). In addition, for realistic infall trajectories one has to track the particle until close before the horizon. Most of the GW signal is already produced before the actual merger, but for high accuracy throughout the quasi-normal ringing and tail phase our tests indicated that one needs to monitor the motion until the very end. Unfortunately, in this mixed approach, grid points ρ_i which are moderately separated from ρ_+ may see so far into the future that the singular behaviour of the source written in BL-coordinates is triggered significantly far away from the horizon.

In summary, the mixed approach of evolving the TKEQ on a hyperboloidal grid with a source in BL-coordinates is appealing for its simplicity; as an example, the explicit source term in BL coordinates for a radial infall on Schwarzschild is provided below. The mixed approach provides an unvalueable tool for debugging the code since it works for the important case of circular orbits. In this case it allows to remove a possible source of error in the implementation; namely, in the transformation of the dynamics to the HH-system. Yet, in general, the source in BL-coordinates is impracticle. Thus, in our simulations we always compute the source term in HH-coordinates, using Eq.'s (A.17) and (A.19) respectively, with the tetrad-legs represented in the HH-coordinate basis and written in HH-coordinates, and with the corresponding NP-operators.

G.1.1   Example: radial infall with $a = 0$ and $S^{\mu\nu} = 0$

In restricted cases the source calculation results in very simple expressions when performed in the BL-coordinate system and with the Kinnersley tetrad.

Let us consider the radial plunge of a non-spinning test-particle along the x-axis onto a Schwarzschild BH. The particle has constant coordinates $\theta_p = \pi/2, \phi_p = 0$, and the constant momenta $p_t = -E$, $p_\theta = 0$, $p_\phi = 0$. Thus, the angular parts of the energy-momentum tensor vanish, $T_{\theta\mu} = T_{\phi\mu} = 0$. In the case $a = 0$ the tetrad legs simplify to $n^\mu = 0.5(1, -(1 - 2M/r), 0, 0)$, and $m^\mu = (\sqrt{2}r)^{-1}(0, 0, 1, i\csc\theta)$. Due to $m^t = m^r = 0$, we find $T_{m^*m^*} = T_{m^*n} = 0$. Also, the Newmann-Penrose operators simplify significantly for $a = 0$; e.g., $\tau = \pi = 0$ and $\alpha = -\beta = -\beta^*$. The only terms that survive are

$$T_4 = -(\delta^* + 2\alpha)\delta^* T_{nn} \quad , \tag{G.2}$$

where T_{nn} is given by

$$T_{nn} = \frac{\mu \ \delta^{(3)}(...)}{4r^2 \ \sin\theta \ dt/d\lambda} \left[E^2 + 2\left(1 - \frac{2M}{r}\right) E \ p_r + \left(1 - \frac{2M}{r}\right)^2 p_r^2 \right] \ . \qquad \text{(G.3)}$$

The derivative operator δ^* reduces to $\delta^* = m^{*\alpha}\partial_\alpha = (\sqrt{2}r)^{-1}(\partial_\theta + \mathrm{i}\csc\theta \ \partial_\phi)$. In the 2+1 decomposition the ϕ derivative amounts to a factor im. If one further specifies to $m = 0$, one is left with the very simple source term

$$T_4 = -\frac{\mu}{8 \ r^4 \ \sin^3\theta \ dt/d\lambda} \left[E^2 + 2A_S \ E \ p_r + A_S^2 p_r^2 \right] \times$$

$$\left[(2\cos^2\theta + 1)\delta^{(3)} - 3\cos\theta \ \sin\theta \ \partial_\theta\delta^{(3)} + \sin^2\theta \ \partial_\theta^2 \ \delta^{(3)} \right] \ , \qquad \text{(G.4)}$$

where $A_S(r) = (1 - \frac{2M}{r})$.

G.2 Ambiguities for a pointlike source

There is one more subtle issue which deserves a short comment. Working with a pointlike source, we are faced with ambiguities due to the impossibility of treating a δ-distribution numerically. The smearing out of the δ over a few grid points implies that the energy-momentum tensor $T^{\mu\nu}$ is nonvanishing in some region around the wordline. The following discussion holds in any coordinate system.

The ambiguity enters when one wants to raise/lower indices. Let us look at an easy example. Set $a = 0$ and consider a nonspinning particle in circular equatorial orbit $p_\mu = (-E, 0, 0, L_z)$. In the source term one encounters pieces like $p_\mu n^\mu$ (coming from T_{nn}). Using the Kinnersley tetrad, we have $n^\mu = \left(\frac{1}{2}, -(1 - \frac{2M}{r}), 0, 0\right)$. That is, $p_\mu n^\mu = -\frac{E}{2}$. Now look at the theoretically equivalently expression $p^\mu n_\mu$. Given only data for p_μ in the dynamics, one might compute p^μ like $p^\mu(\lambda) = g_p^{\mu\nu}(\lambda)p_\nu(\lambda)$, with $g_p^{\mu\nu}(\lambda)$ the metric at the particle's position (motivated by the fact that p^μ is only defined along the worldline). The result reads $p^\mu(\lambda) = \left(-E\left(1 - \frac{2M}{r_p(\lambda)}\right)^{-1}, 0, 0, -L_z \ r_p(\lambda)^{-2}\right)$. Instead, n_μ is defined over the whole spacetime; in particular, it is needed at all the points with nonvanishing δ-function around the particle's position. Naturally, it is lowered with the background metric, and we get $n_\mu = \left(\frac{1 - \frac{2M}{r}}{2}, 1, 0, 0\right)$. This results in two different expressions

$$p_\mu n^\mu = -\frac{E}{2} \qquad \neq \qquad p^\mu n_\mu = -\frac{E}{2} \frac{1 - \frac{2M}{r}}{1 - \frac{2M}{r_p(\lambda)}} \quad , \qquad \text{(G.5)}$$

which coincide if the source term is exactly computed at the field point $r = r_p(\lambda)$. Since we are computing the source in a finite region around the r_p, the two expressions will evaluate slightly differently. In addition, note the implications for the subsequent calculations in terms of derivatives hitting these pieces. In the example we have $\partial_r(p_\mu n^\mu) = 0$, whereas $\partial_r(p^\mu n_\mu) \neq 0$. The same holds for time derivatives. One could be alarmed that the different final expressions in the source calculation might lead to ambiguos numerical results. However, we have tested in a few examples that the different expressions are pleasingly converging with resolution to the exact same form of the source term. Therefore, any choice for lowering/raising the quantities is legitimate when the δ-function is restricting the source to narrow enough a region.

Tables: Decay rates for Kerr

This Appendix collects results of our experiments with the homogeneous TKEQ. More precisely, it contains tables of late-time decay rates found from numerical simulations with the spectral version of the *teukode* (cf. Sec. 5.1.1). The tables complete the studies presented in [H0], and were published in [H1] (see that reference for corresponding plots and discussion).

The tables concern i.) $s = 0, m = 1$, Tab. H.1, ii.) $s = -2, m = 2$, Tab. H.2, iii.) $s = \pm 1, m = 0$, Tab. H.3, and iv.) $s = \pm 2, m = 0$ Tab. H.4. All tables refer to a Kerr background with $\hat{a} = 0.9$. The notation μ_l relates to the late-time decay rate of the Y_{slm} projection of the field, p_l to the local in time measurement of the power index (LPI), l' to the angular profile of the initial data sets ID0, ID1, ID2 and ID3, defined in Sec. 6.1, and R to the hyperboloidal radial coordinate of the RT-system. See Sec. 6.1 for a short reminder of the topic.

Table H.1: Decay rates μ_l for $s = 0$ and $m = 1$ with ID1 at finite radii|null infinity. Brackets point to uncertainties in the LPI assessment due to possible inaccuracies or not verifiable splitting, $\times$ to ambiguous or immeasurable values, $-$ to modes excluded by symmetry. Bold values denote splitting in time, i.e at intermediate times $p_l \neq -\mu_l$ for $R \lesssim 1$. Square brackets point out different values compared to our $m = 0$ tables. Table adopted from [H1].

l'	$l = 1$	$l = 2$	$l = 3$	$l = 4$	$l = 5$
1	5|3	$-$	7|5	$-$	9|7
2	$-$	[7]|4	$-$	[9]|6	$-$
3	5|3	$-$	**7**|5	$-$	**9**|7
4	$-$	(7)|4	$-$	$\times$|6	$-$
5	7|5	$-$	9|5	$-$	$\times$|7

Table H.2: Decay rates μ_l for $s = -2$ and $m = 2$ with ID1 at finite radii|null infinity. Bold values denote splitting in time, i.e at intermediate times $p_l \neq -\mu_l$ for $R \lesssim 1$. Square brackets point out different values compared to our $m = 0$ tables. Table adopted from [H1].

l'	$l = 2$	$l = 3$	$l = 4$	$l = 5$
2	7|6	8|7	9|8	10|9
3	[7]|[6]	[8]|7	[9]|8	[10]|9
4	7|6	8|7	**9**|8	**10**|9
5	8|7	9|7	10|8	**11**|9

Table H.3: Decay rates μ_l for $s = -1$ (left) at finite radii|null infinity and for $s = +1$ (right) at the horizon|finite radii|null infinity. Brackets point to uncertainties in the LPI assessment due to possible inaccuracies or not verifiable splitting, $\times$ to ambiguous or immeasurable values. Bold values denote splitting in time, i.e. at intermediate times $p_l \neq -\mu_l$ for $R \lesssim 1$. Table adopted from [H1].

ID0

l'	$l=1$	$l=2$	$l=3$	$l=4$	$l=5$
1	5|4	6|5	7|6	8|7	9|8
2	5|4	**6**|5	**7**|6	**8**|7	**9**|8
3	6|5	7|5	**8**|6	**9**|7	**10**|8
4	7|6	8|6	9|6	×|(7)	×|(8)
5	8|7	9|7	10|7	(11)|7	×|8

ID0

l'	$l=1$	$l=2$	$l=3$	$l=4$	$l=5$
1	6|5|2	7|6|3	8|7|4	9|8|5	×|9|6
2	6|5|2	7|**6**|3	8|**7**|4	9|**8**|5	×|×|6
3	7|6|3	8|7|3	9|**8**|4	10|**9**|5	×|×|6
4	8|7|4	9|8|4	10|9|4	11|(**10**)|5	×|×|6
5	9|8|5	10|9|5	11|10|5	12|11|5	×|×|6

ID1

l'	$l=1$	$l=2$	$l=3$	$l=4$	$l=5$
1	5|4	6|5	7|6	8|7	9|8
2	6|5	7|5	8|6	9|7	10|8
3	5|4	6|5	**7**|6	**8**|7	**9**|8
4	6|5	7|5	8|6	**9**|7	**10**|8
5	7|6	8|6	9|6	10|7	×|8

ID1

l'	$l=1$	$l=2$	$l=3$	$l=4$	$l=5$
1	6|5|2	7|6|3	8|7|4	9|8|5	×|9|(6)
2	7|6|3	8|7|3	9|8|4	10|9|5	×|10|6
3	6|5|2	7|6|3	8|**7**|4	9|**8**|5	×|×|6
4	7|6|3	8|7|3	9|8|4	10|**9**|5	×|(10)|6
5	8|7|4	9|8|4	10|9|4	11|10|5	×|×|6

ID2

l'	$l=1$	$l=2$	$l=3$	$l=4$	$l=5$
1	4|3	5|4	6|5	7|6	8|7
2	4|3	**5**|4	**6**|5	**7**|6	**8**|7
3	5|4	6|4	**7**|5	**8**|6	**9**|7
4	6|5	7|5	8|5	×|6	×|7
5	7|6	8|6	9|6	×|6	×|7

ID2

l'	$l=1$	$l=2$	$l=3$	$l=4$	$l=5$
1	5|4|1	6|5|2	7|6|3	8|7|4	×|8|5
2	5|4|1	6|5|2	7|6|3	8|7|4	×|8|5
3	6|5|2	7|6|2	8|**7**|3	9| × |4	×|×|5
4	7|6|3	8|7|3	9|8|3	10| × |4	×|×|5
5	8|7|4	9|8|4	10|9|4	11| × |4	×|×|5

ID3

l'	$l=1$	$l=2$	$l=3$	$l=4$	$l=5$
1	4|3	5|4	6|5	7|6	8|7
2	5|4	6|4	7|5	8|6	9|7
3	4|3	5|4	**6**|5	**7**|6	**8**|7
4	5|4	6|4	7|5	(**8**)|6	(**9**)|7
5	6|5	7|5	(8)|5	(9)|×	×|×

ID3

l'	$l=1$	$l=2$	$l=3$	$l=4$	$l=5$
1	5|4|1	6|5|2	7|6|3	8|7|4	×|8|5
2	6|5|2	7|6|2	8|7|(3)	9|8|(4)	×|9|(5)
3	5|4|1	6|5|2	7|**6**|3	8|**7**|4	×|×|5
4	6|5|2	7|6|2	8|7|3	9|**8**|4	×|×|5
5	7|6|3	8|7|3	9|8|3	10|9|×	×|×|5

Table H.4: Decay rates μ_l for $s = -2$ (left) at finite radii|null infinity and for $s = +2$ (right) at the horizon|finite radii|null infinity. Brackets point to uncertainties in the LPI assessment due to possible inaccuracies or not verifiable splitting, $\times$ to ambiguous or immeasurable values. Bold values denote splitting in time, i.e. at intermediate times $p_l \neq -\mu_l$ for $R \lesssim 1$. Table adopted from [H1].

ID0

l'	$l = 2$	$l = 3$	$l = 4$	$l = 5$
2	7|6	8|7	9|8	10|9
3	7|6	**8**|7	**9**|8	**10**|9
4	8|7	9|7	**10**|8	**11**|9
5	9|8	10|8	11|8	$\times$|(9)

ID0

l'	$l = 2$	$l = 3$	$l = 4$	$l = 5$
2	8|7|2	9|8|3	10|9|4	$\times$|10|5
3	8|7|2	9|**8**|3	10|**9**|4	$\times$|**10**|5
4	9|8|3	10|9|3	11|**10**|4	$\times$|**11**|5
5	10|9|4	11|10|4	12|11|4	$\times$|$\times$|5

ID1

l'	$l = 2$	$l = 3$	$l = 4$	$l = 5$
2	7|6	8|7	9|8	10|9
3	8|7	9|7	10|8	11|9
4	7|6	8|7	**9**|(8)	**10**|(9)
5	8|7	9|7	10|8	**11**|9

ID1

l'	$l = 2$	$l = 3$	$l = 4$	$l = 5$
2	8|7|2	9|8|3	10|9|4	$\times$|10|5
3	9|8|3	10|9|3	11|10|4	$\times$|11|5
4	8|7|2	9|8|(3)	10|**9**|4	$\times$|**10**|5
5	9|8|3	10|9|3	11|10|$\times$	$\times$|$\times$|5

ID2

l'	$l = 2$	$l = 3$	$l = 4$	$l = 5$
2	6|5	7|6	8|7	9|8
3	6|5	**7**|6	**8**|7	**9**|8
4	7|6	8|6	**9**|7	**10**|8
5	8|7	9|7	10|7	$\times$|8

ID2

l'	$l = 2$	$l = 3$	$l = 4$	$l = 5$
2	7|6|1	8|7|2	9|8|3	$\times$|9|4
3	7|6|1	8|7|2	9|8|3	$\times$|9|4
4	8|7|2	9|(8)|2	10|$\times$|3	$\times$|$\times$|4
5	9|8|3	10|9|3	11|(10)|(3)	$\times$|$\times$|4

ID3

l'	$l = 2$	$l = 3$	$l = 4$	$l = 5$
2	6|5	7|6	8|7	9|8
3	7|6	8|6	9|7	10|8
4	6|5	7|6	**8**|7	**9**|8
5	7|6	8|6	9|$\times$	$\times$|$\times$

ID3

l'	$l = 2$	$l = 3$	$l = 4$	$l = 5$
2	7|6|1	8|7|2	9|8|3	$\times$|9|4
3	8|7|2	9|8|(2)	10|9|(3)	$\times$|10|$\times$
4	7|6|1	8|7|(2)	9|**8**|3	$\times$|$\times$|4
5	8|7|2	9|8|2	10|(9)|(3)	$\times$|$\times$|4

Tables: Energy fluxes from nonspinning particles on CEOs

Table I.1: GW energy fluxes at scri, $\dot{E}_m^\infty$, and at the horizon, $\dot{E}_m^H$, for circular, equatorial orbits at various $\hat{r}_0$ for $m = 2, 3$ and background rotations $\hat{a} = 0.0, 0.9$. The values are normalized by $(M/\mu)^2$. Radii below the last-stable-orbit (LSO) are marked with $*$. The resolution used for the shown results is $N_x \times N_\theta = 2400 \times 200$. The horizon fluxes are computed with two different methods: the usual frequency domain formula [83] applicable in our time domain setup because of circular orbits, and the time domain formula in Eq. (4.22) (in brackets). $\Delta\dot{E}_m^{\infty,H}/\dot{E}_m^{\infty,H}$ are the percentual relative differences to the frequency domain values of [91, 62]. Note that our results include *all* the ℓ-mode contributions, while the reference solution truncates the sums at $\ell = 8$. Table adopted from [H2].

$\hat{a}$	m	$\hat{r}_0$	$\dot{E}_m^\infty$	$\Delta\dot{E}_m^\infty/\dot{E}_m^\infty[\%]$	$\dot{E}_m^H$		$\Delta\dot{E}_m^H/\dot{E}_m^H[\%]$
0	2	4*	8.580479 e-03	8.33e-03	5.64953e-04	(5.64849e-04)	2.03e-02
0	2	6	7.368338 e-04	3.58e-04	2.62484e-06	(2.62443e-06)	3.91e-03
0	2	8	1.650495 e-04	1.52e-03	1.09970e-07	(1.09953e-07)	4.00e-05
0	2	10	5.373492 e-05	2.75e-03	1.13139e-08	(1.13122e-08)	2.14e-03
0.9	2	4	2.661563 e-03	2.57e-03	-5.28423e-05	(-5.28346e-05)	4.72e-03
0.9	2	6	4.621241 e-04	2.81e-03	-3.98467e-06	(-3.98441e-06)	1.30e-03
0.9	2	8	1.254217 e-04	3.44e-03	-5.68006e-07	(-5.67988e-07)	9.13e-04
0.9	2	10	4.455909 e-05	3.49e-03	-1.19689e-07	(-1.19702e-07)	1.36e-03
0	3	4*	2.710318 e-03	7.95e-03	6.92585e-05	(6.92581e-05)	5.34e-03
0	3	6	1.459721 e-04	1.22e-02	5.41814e-08	(5.41814e-08)	8.86e-03
0	3	8	2.449258 e-05	1.31e-02	8.61375e-10	(8.61376e-10)	1.17e-02
0	3	10	6.434177 e-06	1.34e-02	4.69154e-11	(4.69155e-11)	1.28e-02
0.9	3	4	6.466345 e-04	1.37e-02	-3.00663e-06	(-3.00675e-06)	8.98e-03
0.9	3	6	8.042190 e-05	1.34e-02	-1.17094e-07	(-1.17111e-07)	1.11e-02
0.9	3	8	1.717198 e-05	1.35e-02	-1.00392e-08	(-1.00421e-08)	1.20e-02
0.9	3	10	5.043443 e-06	1.34e-02	-1.40038e-09	(-1.40118e-09)	1.21e-02

Table I.2: GW energy fluxes for a circular, equatorial orbit at $\hat{r}_0 = 6$ for $\hat{a} = 0.9$ in the $\ell = m = 2$ mode at different finite extraction radii, for waves extrapolated using Eq. (5.1) and $K = 2$, and for waves at null infinity. The values are normalized by $(M/\mu)^2$. Table adopted from [H2].

$\hat{r}$	100	200	300	500	740	1000	Extrp. $(K = 2)$	$\mathscr{J}$
$\dot{E}_{22} \times 10^4$	4.546	4.595	4.604	4.608	4.610	4.610	4.611	4.611

APPENDIX J

Table: EOB-dynamics

Using the procedure outlined in Sec. 2.2.3, we have produced and investigated the EOB-dynamics for backgrounds $\hat{a} \in (-0.9999, 0.9999)$. The RR was built from the 5.5PN+4PN (denoting the PN-order for Kerr+Schwarzschild) exact $\rho_{\ell m}$ computed in [55] and augmented with 5.5PN expressions [59] for modes up to $\ell_{\max} = 8$. The obtained RR fails to reproduce the circular orbit fluxes of a particle for fast positive spins in the strong-field. Looking, e.g., at Fig. 5 of [76], which depicts the multipolar 22 energy flux for a particle in circular orbit over the radial distance, it is the sudden drop of the fluxes for $\hat{a} \to 1$ and $r \to r_{\mathrm{LR}}$ due to superradiance which is not captured by our analytical formulas. Due to these inaccuracies we encountered unphysical behaviour of the dynamical quantities close to the merger for $\hat{a} \geq 0.97$; e.g., L_z could become negative due to $\hat{\mathcal{F}}_\phi$ being too large. Therefore, the dynamics for such fast spinning backgrounds do not cover the crossing of the light-ring (LR), which is very close to the horizon for $\hat{a} \to 1$. Note, though, that the particle still reached as close as $\hat{r} \sim 1.05$ in these cases, so we do not expect to miss a significant part of the wave creation.

In Tab. J.1 some key numbers of the used dynamics are listed. Given a value for the background spin $\hat{a}$ the initial radial position $\hat{r}_0$ was tuned to provide at least ~ 20 orbits before merger. Note, however, that we were not very strict in this respect. For instance, $|\hat{a}| \to 1$ simulations need a lot of time, $u \gtrsim 1000M$, to disperse the initial junk radiation (remember the "radiation cavity" for nearly-extremal BH's, Sec. 6.2), so we had to consider longer inspirals in order to have a clean signal at merger. Inspecting the initial positions of the particle shows that they can be rather weak-field for $\hat{a} \to -1$ and strong-field for $\hat{a} \to 1$. The reason is the structure of the spacetime as reflected in the values of the last-stable circular orbit (LSO) $\hat{r}_{\mathrm{LSO}}$ and of the light-ring (LR)[1] $\hat{r}_{\mathrm{LR}}$ also listed in Tab. J.1. Note how large the LSO and the LR are for $\hat{a} \to -1$; e.g., $\hat{r}_{\mathrm{LSO}} = 9$ for $\hat{a} = -0.9999$. Thus, for $\hat{a} \to -1$ initial positions have to be even larger than $\hat{r} = 9$ to allow enough revolutions. Instead, initial positions are small for $\hat{a} \to +1$; e.g., $\hat{r}_{\mathrm{LSO}} = 1.016$ for $\hat{a} = 0.9999$. Furthermore, Tab. J.1 provides the frequencies of the particle at the start, at the LSO and at the LR. Prograde orbits exhibit higher frequencies than retrograde orbits at each of these characteristic positions. Finally, Tab. J.1 includes the LR-crossing time $\hat{t}_{LR}$ and the time of the maximum of the orbital frequency $\hat{t}_{\Omega\mathrm{max}}$. Both coincide for $\hat{a} = 0.0$, which is no longer true for $\hat{a} \to 1$. Note that $\hat{t}_{\Omega\mathrm{max}}$ is often used as an anchor point for analytic models, at which one switches to the ringdown description of the waveform using superposition of QNMs (see, e.g., [76]).

---

[1] See [216] for a nice collection of formulas for the LSO, LR and other test-particle related quantities.

Table J.1: Key numbers for the simulations discussed in this work (see Fig's. 5.1, 5.7, 5.8, 7.1, 7.2, 7.3, 7.4 , 7.8). From left to right: $\hat{r}_0$ is the initial separation, $\hat{\Omega}_0 = \left(\hat{r}^{3/2} + \hat{a}\right)^{-1}$ the initial (circular) orbital frequency; $\hat{\Omega}_{\mathrm{LSO}} \equiv \hat{\Omega}\left(\hat{t}_{\mathrm{LSO}}\right)$ and $\hat{\Omega}_{\mathrm{LR}} \equiv \hat{\Omega}\left(\hat{t}_{\mathrm{LR}}\right)$ refer to the orbital frequency of the particle at the LSO and LR crossing respectively. The last column of the table lists the time corresponding to $\max(M\Omega)$. For $\hat{a} \to 1$ the trajectories stop slightly outside the LR (see discussion in text). Note, how (i) for positive spins the inspiral starts already in the strong-field regime, and (ii) for $\hat{a} \neq 0$, $\hat{t}_{\Omega^{\max}} \neq \hat{t}_{\mathrm{LR}}$ with progressively larger differences as $\hat{a} \to 1$. Table adopted from [H2].

$\hat{a}$	$\hat{r}_0$	$M\Omega_0$	$\hat{r}_{\mathrm{LSO}}$	$M\Omega_{\mathrm{LSO}}$	$\hat{t}_{\mathrm{LSO}}$	$\hat{r}_{\mathrm{LR}}$	$M\Omega_{\mathrm{LR}}$	$\hat{t}_{\mathrm{LR}}$	$\hat{t}_{\Omega^{\max}}$
-0.9999	10.00	0.03266	9.000	0.0385	6858.3	4.000	0.03846	7321.7	7321.3
-0.9995	9.90	0.03317	8.999	0.0385	5541.0	4.000	0.03846	6004.4	6004.0
-0.9990	9.80	0.03369	8.997	0.0385	4382.9	3.999	0.03847	4846.3	4845.8
-0.9950	9.75	0.03396	8.986	0.0385	3963.1	3.996	0.03854	4425.2	4424.8
-0.9900	9.50	0.03535	8.972	0.0386	1931.5	3.991	0.03863	2392.6	2392.2
-0.9700	9.40	0.03591	8.916	0.0390	1629.7	3.973	0.03898	2085.5	2085.1
-0.9500	9.50	0.03530	8.859	0.0393	2747.8	3.955	0.03934	3198.1	3197.7
-0.9000	9.50	0.03523	8.717	0.0403	3985.5	3.910	0.04025	4423.4	4423.0
-0.8000	9.20	0.03689	8.432	0.0422	3668.1	3.819	0.04222	4080.8	4080.4
-0.7000	8.90	0.03868	8.143	0.0444	3397.0	3.725	0.04436	3785.2	3784.8
-0.6000	8.60	0.04062	7.851	0.0467	3168.7	3.630	0.04673	3533.0	3532.7
-0.5000	8.30	0.04271	7.555	0.0493	2980.4	3.532	0.04934	3321.3	3321.0
-0.4000	8.00	0.04499	7.254	0.0522	2829.6	3.432	0.05224	3147.7	3147.5
-0.3000	7.70	0.04747	6.949	0.0555	2714.6	3.329	0.05548	3010.4	3010.2
-0.2000	7.40	0.05018	6.639	0.0591	2634.3	3.223	0.05913	2908.4	2908.3
-0.1000	7.10	0.05314	6.323	0.0633	2588.9	3.113	0.06328	2841.8	2841.8
0.0000	7.00	0.05399	6.000	0.0680	4076.1	3.000	0.06802	4308.4	4308.4
0.1000	6.40	0.06138	5.669	0.0735	2012.0	2.882	0.07352	2224.2	2224.3
0.2000	6.10	0.06551	5.329	0.0800	2088.2	2.759	0.07995	2281.0	2281.1
0.3000	5.80	0.07009	4.979	0.0876	2207.2	2.630	0.08762	2381.0	2381.2
0.4000	5.40	0.07723	4.614	0.0969	1862.8	2.493	0.09694	2018.3	2018.6
0.5000	5.01	0.08537	4.233	0.1085	1671.1	2.347	0.10854	1808.8	1809.2
0.6000	4.70	0.09268	3.829	0.1235	1914.2	2.189	0.12351	2034.5	2035.0
0.7000	4.10	0.11109	3.393	0.1438	1126.9	2.013	0.14379	1230.1	1230.9
0.8000	3.80	0.12184	2.907	0.1736	1571.6	1.811	0.17360	1657.3	1658.5
0.9000	3.05	0.16060	2.321	0.2251	820.7	1.558	0.22514	883.6	886.2
0.9500	3.02	0.16134	1.937	0.2732	1432.9	1.386	0.27316	1472.5	1491.6
0.9700	3.30	0.14358	1.738	0.3037	2813.7	1.296	0.30368	2841.9	2862.4
0.9900	3.01	0.16097	1.454	0.3510	2010.0	1.168	0.35101	2032.6	2058.5
0.9950	3.60	0.12779	1.341	0.3722	4914.9	1.118	0.37215	4941.1	4945.2
0.9990	3.60	0.12772	1.182	0.4137	5018.1	1.052	0.45258	$\times$	5032.5
0.9995	3.60	0.12771	1.140	0.4308	5034.2	1.037	0.45309	$\times$	5043.6
0.9999	3.60	0.12771	1.079	0.4537	$\times$	1.016	0.45368	$\times$	5052.5

Tables: Angular momentum fluxes from spinning-particle on CEOs

As an orientation for further studies, we collect here the angular momentum fluxes obtained from our simulations of a spinning-particle in circular equatorial motion around Schwarzschild. These are related to the energy fluxes plotted in Ch. 8 by relation (4.11) with $\omega = m\Omega_\phi$, where Ω_ϕ is the frequency of the particle. An analytic expression for this frequency is given in Eq. (12) of [186] (though, we have to use $-a$ and $-\sigma$ for agreement).

Table K.1: Multipolar $\ell = 2, m = 2$ angular momentum flux to infinity for a spinning particle in circular, equatorial orbit at different radii about a BH with $\hat{a} = 0.0$. The values are normalized by (M/μ^2).

$r[M]$	-0.9	-0.7	-0.5	-0.3	-0.1	0.1	0.3	0.5	0.7	0.9
04	8.518e-02	6.943e-02	5.645e-02	4.595e-02	3.753e-02	3.081e-02	2.545e-02	2.119e-02	1.779e-02	1.507e-02
05	1.878e-02	1.678e-02	1.499e-02	1.338e-02	1.195e-02	1.068e-02	9.552e-03	8.563e-03	7.693e-03	6.930e-03
06	7.676e-03	7.097e-03	6.559e-03	6.062e-03	5.603e-03	5.181e-03	4.793e-03	4.438e-03	4.113e-03	3.816e-03
07	3.948e-03	3.719e-03	3.503e-03	3.300e-03	3.109e-03	2.930e-03	2.762e-03	2.605e-03	2.457e-03	2.320e-03
08	2.304e-03	2.197e-03	2.095e-03	1.998e-03	1.905e-03	1.817e-03	1.734e-03	1.655e-03	1.580e-03	1.508e-03
10	9.822e-04	9.504e-04	9.196e-04	8.898e-04	8.611e-04	8.334e-04	8.067e-04	7.809e-04	7.561e-04	7.322e-04
12	5.029e-04	4.906e-04	4.787e-04	4.671e-04	4.558e-04	4.448e-04	4.341e-04	4.237e-04	4.136e-04	4.037e-04
15	2.260e-04	2.221e-04	2.183e-04	2.146e-04	2.109e-04	2.073e-04	2.038e-04	2.003e-04	1.969e-04	1.936e-04
20	8.210e-05	8.119e-05	8.030e-05	7.942e-05	7.854e-05	7.768e-05	7.683e-05	7.599e-05	7.516e-05	7.434e-05

Table K.2: Multipolar $\ell = 2, m = 1$ angular momentum flux to infinity for a spinning particle in circular, equatorial orbit at different radii about a BH with $\hat{a} = 0.0$. The values are normalized by (M/μ^2). The $\times$ symbol refers to runs that were not yet performed.

$r[M]$	-0.9	-0.7	-0.5	-0.3	-0.1	0.1	0.3	0.5	0.7	0.9
04	$\times$	$\times$	$\times$	$\times$	$\times$	$\times$	$\times$	$\times$	$\times$	$\times$
05	8.916e-05	9.467e-05	9.773e-05	9.886e-05	9.855e-05	9.723e-05	9.525e-05	9.288e-05	9.034e-05	8.779e-05
06	2.627e-05	2.943e-05	3.211e-05	3.432e-05	3.612e-05	3.754e-05	3.864e-05	3.948e-05	4.011e-05	4.056e-05
07	$\times$	1.224e-05	1.373e-05	1.510e-05	1.634e-05	1.746e-05	1.847e-05	1.937e-05	2.017e-05	2.088e-05
08	5.177e-06	6.033e-06	6.867e-06	7.669e-06	8.434e-06	9.160e-06	9.844e-06	1.049e-05	1.109e-05	1.165e-05
10	1.689e-06	1.985e-06	2.286e-06	2.588e-06	2.890e-06	3.188e-06	$\times$	3.773e-06	$\times$	4.332e-06
12	7.121e-07	8.364e-07	9.647e-07	1.096e-06	1.230e-06	1.365e-06	1.501e-06	1.638e-06	1.774e-06	1.910e-06
15	2.574e-07	3.002e-07	3.449e-07	3.913e-07	4.392e-07	4.883e-07	5.384e-07	5.895e-07	6.414e-07	6.938e-07
20	7.198e-08	8.283e-08	9.421e-08	1.061e-07	1.185e-07	1.313e-07	1.445e-07	1.581e-07	1.720e-07	1.863e-07

Table K.3: Multipolar $\ell = 3, m = 2$ angular momentum flux to infinity for a spinning particle in circular, equatorial orbit at different radii about a BH with $\hat{a} = 0.0$. The values are normalized by (M/μ^2).

$r[M]$	-0.9	-0.7	-0.5	-0.3	-0.1	0.1	0.3	0.5	0.7	0.9
04	3.521e-04	3.697e-04	3.512e-04	3.156e-04	2.750e-04	2.360e-04	2.013e-04	1.720e-04	1.478e-04	1.283e-04
05	3.203e-05	3.947e-05	4.448e-05	4.734e-05	4.852e-05	4.844e-05	4.751e-05	4.604e-05	4.428e-05	4.240e-05
06	7.398e-06	9.650e-06	1.160e-05	1.321e-05	1.448e-05	1.544e-05	1.613e-05	1.659e-05	1.686e-05	1.699e-05
07	2.538e-06	3.382e-06	4.187e-06	4.927e-06	5.590e-06	6.170e-06	6.668e-06	7.090e-06	7.440e-06	7.726e-06
08	1.088e-06	1.458e-06	1.829e-06	2.188e-06	2.529e-06	2.848e-06	3.141e-06	3.407e-06	3.648e-06	3.862e-06
10	2.933e-07	3.906e-07	4.924e-07	5.963e-07	7.007e-07	8.039e-07	9.050e-07	1.003e-06	1.097e-06	1.188e-06
12	1.070e-07	1.404e-07	1.760e-07	2.132e-07	2.515e-07	2.905e-07	3.297e-07	3.688e-07	4.077e-07	4.460e-07
15	3.248e-08	4.167e-08	5.158e-08	6.207e-08	7.306e-08	8.445e-08	9.615e-08	1.081e-07	1.202e-07	1.325e-07
20	7.239e-09	9.002e-09	1.091e-08	1.294e-08	1.508e-08	1.733e-08	1.968e-08	2.211e-08	2.461e-08	2.718e-08

Table K.4: Multipolar $\ell = 3, m = 3$ angular momentum flux to infinity for a spinning particle in circular, equatorial orbit at different radii about a BH with $\hat{a} = 0.0$. The values are normalized by (M/μ^2). The $\times$ symbol refers to runs that were not yet performed.

$r[M]$	-0.9	-0.7	-0.5	-0.3	-0.1	0.1	0.3	0.5	0.7	0.9
04	$\times$	$\times$	$\times$	$\times$	$\times$	$\times$	$\times$	$\times$	$\times$	$\times$
05	5.569e-03	4.751e-03	4.049e-03	3.450e-03	2.940e-03	2.507e-03	2.142e-03	1.834e-03	1.575e-03	1.357e-03
06	1.784e-03	1.590e-03	1.418e-03	1.264e-03	1.127e-03	1.006e-03	8.986e-04	8.036e-04	7.197e-04	6.456e-04
07	7.586e-04	6.942e-04	6.353e-04	5.817e-04	5.327e-04	4.881e-04	4.475e-04	4.106e-04	3.770e-04	3.465e-04
08	3.792e-04	3.531e-04	3.289e-04	3.064e-04	2.855e-04	2.662e-04	2.483e-04	2.316e-04	2.163e-04	2.020e-04
10	1.266e-04	1.204e-04	1.146e-04	1.091e-04	1.038e-04	9.885e-05	9.414e-05	8.967e-05	8.544e-05	8.143e-05
12	5.357e-05	5.160e-05	4.972e-05	4.790e-05	4.616e-05	4.449e-05	4.289e-05	4.135e-05	3.987e-05	3.845e-05
15	1.921e-05	1.871e-05	1.822e-05	1.775e-05	1.729e-05	1.684e-05	1.641e-05	1.599e-05	1.558e-05	1.518e-05
20	5.247e-06	5.159e-06	5.073e-06	4.987e-06	4.904e-06	4.822e-06	4.742e-06	4.663e-06	4.585e-06	4.509e-06

Tables: Characteristic waveform numbers

In this appendix the extracted key numbers measured from our waveforms of a nonspinning particle on realistic EOB-inspiral trajectories are gathererd (see Sec. 7.1.3). These numbers might become useful in the future for waveform modeling. At the moment, they rather provide a further quantitative comparison of the *teukode* with the RWZ-code of [132] for $\hat{a} = 0.0$, and the prevailing Teukolsky-code used in [135].

Table L.1: Properties of multipolar waveforms at merger for $\hat{a} = 0$. The retarded time at the crossing of the light ring u_{LR}, coincides with the time of the maximum of the orbital frequency, $u_{\mathrm{LR}} = u_{\Omega^{\mathrm{max}}} = 4308.39M$ (for $\hat{a} \neq 0$ they can differ, see Table J.1) , with $M\Omega^{\mathrm{max}} = 0.136$. The peak of each multipolar amplitude divided by μ, $\hat{A}_{\ell m}^{\mathrm{max}} \equiv A_{\ell m}^{\mathrm{max}}/\mu$ occurs at another time $u_{A_{\ell m}^{\mathrm{max}}} \neq u_{\Omega^{\mathrm{max}}}$. The table lists the differences $\Delta t_{\ell m} = u_{A_{\ell m}^{\mathrm{max}}} - u_{\Omega^{\mathrm{max}}}$. For completeness, we also state the peak values $\hat{A}_{\ell m}^{\mathrm{max}}$ and the frequencies at that time $M\omega_{\ell m}^{A_{\ell m}^{\mathrm{max}}}$. Values in brackets refer to 1+1 RWZ simulations of [131]. Table adopted from [H2].

ℓ	m	$\Delta t_{\ell m}$	$\hat{A}_{\ell m}^{\mathrm{max}}$	$M\omega_{\ell m}^{A_{\ell m}^{\mathrm{max}}}$
2	2	-2.38 (-2.56)	0.29589 (0.29472)	0.27335 (0.27213)
2	1	9.41 (9.37)	0.10694 (0.10692)	0.29067 (0.29064)
3	3	1.11 (1.00)	0.051673 (0.051456)	0.45462 (0.45321)
3	2	6.85 (6.84)	0.018170 (0.018174)	0.45181 (0.45174)
3	1	10.55 (10.54)	0.0056954 (0.0056872)	0.41176 (0.41129)
4	4	2.90 (2.82)	0.014581 (0.014523)	0.63541 (0.63400)
4	3	7.22 (7.21)	0.0049634 (0.0049653)	0.63686 (0.63668)
4	2	9.54 (9.51)	0.0016570 (0.0016543)	0.62603 (0.62533)
5	5	4.18 (4.12)	0.0052278 (0.0052093)	0.81811 (0.81672)
5	4	7.63 (7.63)	0.0017267 (0.0017277)	0.82170 (0.82148)
6	6	5.20 (5.14)	0.0021703 (0.0021636)	1.00027 (1.00013)
6	5	8.09 (8.09)	0.00069673 (0.00069726)	1.00079 (1.00077)

Table L.2: Properties of multipolar waveforms at merger for representative values of $\hat{a}$. See Table L.1 for definitions. The values in brackets are the numbers found in [135]. Crosses indicate that, for $m = 0$ modes, the phase is not measurable. Table adopted from [H2].

ℓ	m	$\hat{a}$	$\Delta t_{\ell m}$	$\hat{A}^{\max}_{\ell m}$	$M\omega^{A^{\max}_{\ell m}}_{\ell m}$	$\hat{a}$	$\Delta t_{\ell m}$	$\hat{A}^{\max}_{\ell m}$	$M\omega^{A^{\max}_{\ell m}}_{\ell m}$
2	2	0.5	-7.23 (-7.22)	0.3147	0.3396	-0.5	-0.03 (-0.08)	0.2820	0.2378
2	1	0.5	3.83	0.0666	0.2912	-0.5	12.79	0.1508	0.2391
2	0	0.5	8.45	0.0155	$\times$	-0.5	12.81	0.1108	$\times$
3	3	0.5	-1.99	0.0576	0.5678	-0.5	2.76	0.0480	0.3916
3	2	0.5	-1.61	0.0146	0.4262	-0.5	12.15	0.0220	0.4422
3	1	0.5	3.12	0.0025	0.3514	-0.5	12.10	0.0115	0.3162
3	0	0.5	8.94	0.0004	$\times$	-0.5	17.93	0.0091	$\times$
4	4	0.5	0.32	0.0169	0.7954	-0.5	4.40	0.0132	0.5458
4	3	0.5	0.54	0.0046	0.6535	-0.5	10.10	0.0056	0.5934
4	2	0.5	1.06	0.0009	0.5306	-0.5	12.44	0.0027	0.5719
4	1	0.5	4.81	0.0001	0.4958	-0.5	16.38	0.0015	0.4168
4	0	0.5	8.69	2.16e-05	$\times$	-0.5	16.22	0.0011	$\times$
2	2	0.7	-12.74 (-12.77)	0.3228	0.3886	-0.7	0.76 $(\times)$	0.2776	0.2279
2	1	0.7	-0.02	0.0472	0.2950	-0.7	13.62	0.1728	0.2095
2	0	0.7	6.50	0.0061	$\times$	-0.7	13.43	0.1418	$\times$
3	3	0.7	-5.10	0.0611	0.6505	-0.7	3.28	0.0468	0.3729
3	2	0.7	-9.57	0.0143	0.4236	-0.7	13.24	0.0241	0.4015
3	1	0.7	-1.12	0.0018	0.3196	-0.7	18.65	0.0151	0.2230
3	0	0.7	8.30	0.0001	$\times$	-0.7	18.38	0.0138	$\times$
4	4	0.7	-2.12	0.0183	0.9117	-0.7	4.90	0.0128	0.5192
4	3	0.7	-4.66	0.0047	0.6832	-0.7	12.92	0.0058	0.5907
4	2	0.7	-9.29	0.0007	0.4515	-0.7	17.17	0.0032	0.5043
4	1	0.7	-0.39	5.97e-05	0.3849	-0.7	16.79	0.0022	0.3207
4	0	0.7	27.91	4.68e-06	$\times$	-0.7	16.61	0.0018	$\times$
2	2	0.9	-39.16 (-39.09)	0.3212	0.4771	-0.9	1.54 (1.60)	0.2738	0.2198
2	1	0.9	-35.01	0.0249	0.2509	-0.9	14.36	0.1996	0.1738
2	0	0.9	0.09	0.0009	$\times$	-0.9	14.03	0.1788	$\times$
3	3	0.9	-18.03	0.0645	0.8013	-0.9	3.75	0.0459	0.3567
3	2	0.9	-35.46	0.0148	0.4860	-0.9	13.94	0.0267	0.3442
3	1	0.9	-26.01	0.0010	0.2711	-0.9	19.13	0.0209	0.1295
3	0	0.9	5.18	1.75e-05	$\times$	-0.9	18.82	0.0203	$\times$
4	4	0.9	-12.11	0.0201	1.1223	-0.9	5.37	0.0125	0.4960
4	3	0.9	-19.96	0.0052	0.7959	-0.9	13.93	0.0062	0.5318
4	2	0.9	-51.22	0.0007	0.4624	-0.9	17.65	0.0042	0.3645
4	1	0.9	-13.43	3.11e-05	0.3218	-0.9	17.18	0.0032	0.2089
4	0	0.9	21.41	4.17e-07	$\times$	-0.9	16.98	0.0029	$\times$

Table: Recoil velocities

Table M.1: The columns list: the BH spin $\hat{a}$; the magnitude of the maximal and final recoil velocities, v_{max}/ν^2 and v_{end}/ν^2; the magnitude of the antikick $\Delta v/\nu^2$: for $-0.9 \leq \hat{a} \leq -0.5$ no significant antikick is observed; the quality factor Q associated with the maximum of the amplitude of the linear momentum flux, as an indicator of the adiabaticity of the emission of linear momentum: the larger Q is, the more adiabatic is the emission process, the larger is the antikick; the characteristic time scale $\tau_{\dot{p}_{r_*}}^{max}$ of $-\dot{p}_{r_*}$ (see Sec. (7.3)), as a complementary indicator of the adiabaticity of the dynamics; an approximate analytic calculation of the kick velocity, v_{end}^{anal}/ν^2 (not discussed here, see Eq. (11) in [H3]). Minima of $\Delta v/\nu^2, Q, \tau_{\dot{p}_{r_*}}^{max}$ are shown in boldface. The (more uncertain) results for nearly extremal positive spins are separated by a horizontal line. Tab. adopted from [H3].

$\hat{a}$	v_{max}/ν^2	v_{end}/ν^2	$\Delta v/\nu^2$	Q	$\tau_{\dot{p}_{r_*}}^{max}$	v_{end}^{anal}/ν^2
-0.9999	0.07972	0.07634	3.377e-03	1.0060	3.8436	0.04060
-0.9990	0.07967	0.07637	3.303e-03	1.0065	3.8411	0.04091
-0.9950	0.07884	0.07587	2.972e-03	0.9942	3.8302	0.04052
-0.9900	0.07798	0.07539	2.589e-03	0.9639	3.8171	0.04050
-0.9800	0.07571	0.07383	1.883e-03	0.9518	3.7924	0.04017
-0.9700	0.07452	0.07320	1.326e-03	0.9356	3.7696	0.03996
-0.9500	0.07093	0.07040	5.264e-04	0.9015	3.7292	0.03942
-0.9000	0.06545	0.06539	5.589e-05	0.8663	3.6508	0.03855
-0.8000	0.05910	0.05909	9.332e-06	**0.8378**	3.5570	0.03807
-0.7000	0.05501	0.05501	8.223e-07	0.8402	3.5123	0.03910
-0.6000	0.05183	0.05183	1.915e-08	0.8650	**3.4977**	0.04189
-0.5000	0.05003	0.05003	**2.289e-09**	0.9024	3.5044	0.04765
-0.4400	0.04914	0.04879	3.485e-04	0.9491	3.5167	0.05318
-0.4000	0.04948	0.04882	6.618e-04	1.0038	3.5280	0.05801
-0.3500	0.04889	0.04787	1.024e-03	1.1444	3.5456	0.06704
-0.3000	0.04913	0.04766	1.479e-03	1.9191	3.5667	0.09562
-0.2500	0.04956	0.04730	2.255e-03	1.6508	3.5914	0.10402
-0.2000	0.04981	0.04658	3.224e-03	1.4625	3.6198	0.09148
-0.1000	0.05060	0.04534	5.266e-03	1.4011	3.6878	0.07821
0.0000	0.05319	0.04530	7.892e-03	1.4364	3.7722	0.07029
0.1000	0.05471	0.04377	1.094e-02	1.5086	3.8755	0.06279
0.2000	0.05771	0.04252	1.519e-02	1.6045	4.0019	0.05655
0.3000	0.06105	0.04053	2.052e-02	1.7207	4.1580	0.05116
0.4000	0.06606	0.03822	2.785e-02	1.8678	4.3534	0.04578
0.5000	0.07131	0.03398	3.733e-02	2.0643	4.6049	0.03887
0.6000	0.07796	0.02831	4.965e-02	2.3413	4.9426	0.02766
0.7000	0.08719	0.02056	6.663e-02	2.7528	5.4289	0.01406
0.8000	0.09919	0.01085	8.835e-02	3.5249	6.2242	0.00431
0.9000	0.11293	0.00206	1.109e-01	5.3834	7.8682	0.00031
0.9500	0.11186	0.00065	1.112e-01	7.1404	8.6964	0.00015
0.9700	0.10821	0.00046	1.077e-01	7.9190	8.8428	0.00008
0.9800	0.10524	0.00043	1.048e-01	8.7525	9.0199	0.00021
0.9900	0.10307	0.00044	1.026e-01	9.2251	9.4295	0.00045
0.9950	0.10127	0.00038	1.009e-01	9.3933	9.8429	0.00039
0.9990	0.09968	0.00036	9.933e-02	9.2492	10.4124	0.00019
0.9999	0.09914	0.00035	9.878e-02	9.1388	10.5938	0.00031

References

[1] Albert Einstein. Die feldgleichungen der gravitation. *Sitzungsberichte der Königlich Preußischen Akademie der Wissenschaften (Berlin), Seite 844-847.*, 1:844–847, 1915.

[2] Albert Einstein. Zur allgemeinen relativitaetstheorie. *Sitzungsberichte der Königlich Preußischen Akademie der Wissenschaften (Berlin), Seite 778-786.*, 1:778–786, 1915.

[3] Karl Schwarzschild. Über das gravitationsfeld eines massenpunktes nach der einsteinschen theorie. *Sitzungsberichte der Königlich Preußischen Akademie der Wissenschaften (Berlin), 1916, Seite 189-196*, 1:189–196, 1916.

[4] Roy P. Kerr. Gravitational field of a spinning mass as an example of algebraically special metrics. *Phys. Rev. Lett.*, 11:237–238, 1963.

[5] Richard C. Tolman. Static solutions of einstein's field equations for spheres of fluid. *Phys. Rev.*, 55:364–373, 1939.

[6] Miguel Alcubierre. *Introduction to 3+ 1 numerical relativity.* Oxford Univ. Press, 2008.

[7] Thomas W Baumgarte and Stuart L Shapiro. *Numerical relativity: solving Einstein's equations on the computer.* Cambridge University Press, 2010.

[8] Sebastiano Bernuzzi, Marcus Thierfelder, and Bernd Brügmann. Accuracy of numerical relativity waveforms from binary neutron star mergers and their comparison with post-Newtonian waveforms. *Phys.Rev.*, D85:104030, 2012.

[9] Sebastiano Bernuzzi, Tim Dietrich, Wolfgang Tichy, and Bernd Bruegmann. Mergers of binary neutron stars with realistic spin. *Phys.Rev.*, D89:104021, 2014.

[10] SpEC - Spectral Einstein Code, Code Homepage.

[11] R. A. Hulse and J. H. Taylor. Discovery of a pulsar in a binary system. *Astrophys. J.*, 195:L51–L53, 1975.

[12] LIGO - Laser Interferometer Gravitational Wave Observatory.

[13] KAGRA, Large-scale Cryogenic Gravitational Wave Telescope Project.

[14] Virgo/EGO, European Gravitational Observatory.

[15] Tullio Regge and John A. Wheeler. Stability of a Schwarzschild singularity. *Phys. Rev.*, 108:1063–1069, 1957.

[16] Frank J. Zerilli. Effective potential for even parity Regge-Wheeler gravitational perturbation equations. *Phys. Rev. Lett.*, 24:737–738, 1970.

[17] S.A. Teukolsky. Rotating black holes - separable wave equations for gravitational and electromagnetic perturbations. *Phys.Rev.Lett.*, 29:1114–1118, 1972.

[18] Saul A. Teukolsky. Perturbations of a rotating black hole. 1. Fundamental equations for gravitational electromagnetic and neutrino field perturbations. *Astrophys. J.*, 185:635–647, 1973.

[19] Leor Barack and Curt Cutler. LISA capture sources: Approximate waveforms, signal-to-noise ratios, and parameter estimation accuracy. *Phys. Rev.*, D69:082005, 2004.

[20] Huan Yang, Aaron Zimmerman, Anil Zenginoğlu, Fan Zhang, Emanuele Berti, et al. Quasinormal modes of nearly extremal Kerr spacetimes: spectrum bifurcation and power-law ringdown. *Phys.Rev.*, D88(4):044047, 2013.

[21] Georgios Lukes-Gerakopoulos, Jonathan Seyrich, and Daniela Kunst. Investigating spinning test particles: spin supplementary conditions and the Hamiltonian formalism. *Phys.Rev.*, D90(10):104019, 2014.

[22] Alessandro Nagar, Thibault Damour, and Angelo Tartaglia. Binary black hole merger in the extreme mass ratio limit. *Class. Quant. Grav.*, 24:S109–S124, 2007.

[23] Jan Steinhoff. Canonical formulation of spin in general relativity. *Annalen Phys.*, 523:296–353, 2011.

[24] Gordon N. Fleming. Covariant position operators, spin, and locality. *Phys. Rev.*, 137:B188–B197, Jan 1965.

[25] C Møller. Sur la dynamique des systemes ayant un moment angulaire interne. In *Annales de l'institut Henri Poincaré*, volume 11, pages 251–278. Presses universitaires de France, 1949.

[26] Robert M. Wald. Gravitational spin interaction. *Phys.Rev.*, D6:406–413, 1972.

[27] J. Frenkel. Die elektrodynamik des rotierenden elektrons. *Zeitschrift fuer Physik*, 37(4-5):243–262, 1926.

[28] Cornel Lanczos. Ueber eine invariante formulierung der erhaltungssaetze in der allgemeinen relativitaetstheorie. *Zeitschrift fuer Physik*, 59(7-8):514–539, 1930.

[29] Myron Mathisson. Neue mechanik materieller systemes. *Acta Phys.Polon.*, 6:163–2900, 1937.

[30] O. Semerak. Spinning test particles in a Kerr field. 1. *Mon.Not.Roy.Astron.Soc.*, 308:863–875, 1999.

[31] K Kyrian and O Semerak. Spinning test particles in a Kerr field. *Mon.Not.Roy.Astron.Soc.*, 382:1922, 2007.

[32] Eva Hackmann, Claus Laemmerzahl, Yuri N. Obukhov, Dirk Puetzfeld, and Isabell Schaffer. Motion of spinning test bodies in Kerr spacetime. *Phys.Rev.*, D90(6):064035, 2014.

[33] Myron Mathisson. Republication of: New mechanics of material systems. *General Relativity and Gravitation*, 42(4):1011–1048, 2010.

[34] W.G. Dixon. A covariant multipole formalism for extended test bodies in general relativity. *Il Nuovo Cimento*, 34(2):317–339, 1964.

[35] W.G. Dixon. Dynamics of extended bodies in general relativity. I. Momentum and angular momentum. *Proc.Roy.Soc.Lond.*, A314:499–527, 1970.

[36] W.G. Dixon. Dynamics of extended bodies in general relativity. II. Moments of the charge-current vector. *Proc.Roy.Soc.Lond.*, A319:509–547, 1970.

[37] William G Dixon. Dynamics of extended bodies in general relativity. iii. equations of motion. *Philosophical Transactions of the Royal Society of London A: Mathematical, Physical and Engineering Sciences*, 277(1264):59–119, 1974.

[38] W Tulczyjew. Motion of multipole particles in general relativity theory. *Acta Phys. Pol*, 18:393, 1959.

[39] Achille Papapetrou. Spinning test particles in general relativity. 1. *Proc.Roy.Soc.Lond.*, A209:248–258, 1951.

[40] Michael D. Hartl. Dynamics of spinning test particles in Kerr space-time. *Phys. Rev.*, D67:024005, 2003.

[41] K. S. Thorne. Multipole Expansions of Gravitational Radiation. *Rev. Mod. Phys.*, 52:299–339, 1980.

[42] S. Carroll. *Spacetime and Geometry: An Introduction to General Relativity*. Always learning. Pearson Education, Limited, 2013.

[43] A. H. Taub. Motion of test bodies in general relativity. *Journal of Mathematical Physics*, 5(1):112–119, 1964.

[44] Jan Steinhoff and Dirk Puetzfeld. Influence of internal structure on the motion of test bodies in extreme mass ratio situations. *Phys. Rev.*, D86:044033, 2012.

[45] Donato Bini, Pierluigi Fortini, Andrea Geralico, and Antonello Ortolan. Quadrupole effects on the motion of extended bodies in Kerr spacetime. *Class.Quant.Grav.*, 25:125007, 2008.

[46] Donato Bini and Andrea Geralico. Deviation of quadrupolar bodies from geodesic motion in a Kerr spacetime. *Phys.Rev.*, D89(4):044013, 2014.

[47] Donato Bini and Andrea Geralico. Extended bodies in a Kerr spacetime: exploring the role of a general quadrupole tensor. *Class.Quant.Grav.*, 31:075024, 2014.

[48] Filipe Costa, Carlos A. R. Herdeiro, Jose Natario, and Miguel Zilhao. Mathisson's helical motions for a spinning particle: Are they unphysical? *Phys. Rev.*, D85:024001, 2012.

[49] Thibault Damour and Alessandro Nagar. A new effective-one-body description of coalescing nonprecessing spinning black-hole binaries. 2014.

[50] A. Buonanno and T. Damour. Effective one-body approach to general relativistic two- body dynamics. *Phys. Rev.*, D59:084006, 1999.

[51] Donato Bini and Thibault Damour. Gravitational radiation reaction along general orbits in the effective one-body formalism. *Phys.Rev.*, D86:124012, 2012.

[52] Thibault Damour and Alessandro Nagar. Faithful Effective-One-Body waveforms of small-mass-ratio coalescing black-hole binaries. *Phys. Rev.*, D76:064028, 2007.

[53] Thibault Damour and Alessandro Nagar. Comparing Effective-One-Body gravitational waveforms to accurate numerical data. *Phys. Rev.*, D77:024043, 2008.

[54] Thibault Damour, Bala R. Iyer, and Alessandro Nagar. Improved resummation of post-Newtonian multipolar waveforms from circularized compact binaries. *Phys. Rev.*, D79:064004, 2009.

[55] Yi Pan, Alessandra Buonanno, Ryuichi Fujita, Etienne Racine, and Hideyuki Tagoshi. Post-Newtonian factorized multipolar waveforms for spinning, non-precessing black-hole binaries. *Phys.Rev.*, D83:064003, 2011.

[56] Takahiro Tanaka, Yasushi Mino, Misao Sasaki, and Masaru Shibata. Gravitational waves from a spinning particle in circular orbits around a rotating black hole. *Phys.Rev.*, D54:3762–3777, 1996.

[57] Abhay G Shah. Gravitational-wave flux for a particle orbiting a Kerr black hole to 20th post-Newtonian order: a numerical approach. 2014.

[58] Ryuichi Fujita. Gravitational Waves from a Particle in Circular Orbits around a Rotating Black Hole to the 11th Post-Newtonian Order. *PTEP*, 2015(3):033E01, 2015.

[59] Ryuichi Fujita and Bala R. Iyer. Spherical harmonic modes of 5.5 post-Newtonian gravitational wave polarizations and associated factorized resummed waveforms for a particle in circular orbit around a Schwarzschild black hol. *Phys. Rev.*, D82:044051, 2010.

[60] Scott A. Hughes. The Evolution of circular, nonequatorial orbits of Kerr black holes due to gravitational wave emission. *Phys.Rev.*, D61:084004, 2000.

[61] Hideyuki Tagoshi, Masaru Shibata, Takahiro Tanaka, and Misao Sasaki. PostNewtonian expansion of gravitational waves from a particle in circular orbits around a rotating black hole: Up to O (v**8) beyond the quadrupole formula. *Phys. Rev.*, D54:1439–1459, 1996.

[62] Andrea Taracchini, Alessandra Buonanno, Scott A. Hughes, and Gaurav Khanna. Modeling the horizon-absorbed gravitational flux for equatorial-circular orbits in Kerr spacetime. *Phys.Rev.*, D88:044001, 2013.

[63] Ezra Newman and Roger Penrose. An Approach to gravitational radiation by a method of spin coefficients. *J. Math. Phys.*, 3:566–578, 1962.

[64] William H. Press and Saul A. Teukolsky. Perturbations of a Rotating Black Hole. II. Dynamical Stability of the Kerr Metric. *Astrophys. J.*, 185:649–674, 1973.

[65] J.B. Hartle and D.C. Wilkins. Analytic properties of the teukolsky equation. *Commun. Math. Phys.*, 38:47–63, 1974.

[66] J.M. Stewart. On the stability of kerr's space-time. *Proc. R. Soc. London, Ser. A*, 344:65–79, 1975.

[67] B. F. Whiting. Mode stability of the Kerr black hole. *Journal of Mathematical Physics*, 30:1301–1305, June 1989.

[68] Steven L. Detweiler. BLACK HOLES AND GRAVITATIONAL WAVES. III. THE RESONANT FREQUENCIES OF ROTATING HOLES. *Astrophys. J.*, 239:292–295, 1980.

[69] E. W. Leaver. An Analytic representation for the quasi normal modes of Kerr black holes. *Proc. Roy. Soc. Lond.*, A402:285–298, 1985.

[70] Edward Seidel and Sai Iyer. BLACK HOLE NORMAL MODES: A WKB APPROACH. 4. KERR BLACK HOLES. *Phys. Rev.*, D41:374–382, 1990.

[71] K. D. Kokkotas. Normal modes of the Kerr black hole. *Class. Quant. Grav.*, 8:2217–2224, 1991.

[72] Emanuele Berti, Vitor Cardoso, and Andrei O. Starinets. Quasinormal modes of black holes and black branes. *Class. Quant. Grav.*, 26:163001, 2009.

[73] K. Glampedakis. Extreme mass ratio inspirals: LISA's unique probe of black hole gravity. *Class. Quant. Grav.*, 22:S605–S659, 2005.

[74] Nicolas Yunes, Alessandra Buonanno, Scott A. Hughes, Yi Pan, Enrico Barausse, et al. Extreme Mass-Ratio Inspirals in the Effective-One-Body Approach: Quasi-Circular, Equatorial Orbits around a Spinning Black Hole. *Phys.Rev.*, D83:044044, 2011.

[75] Anil Zenginoğlu and Gaurav Khanna. Null infinity waveforms from extreme-mass-ratio inspirals in Kerr spacetime. *Phys.Rev.*, X1:021017, 2011.

[76] Andrea Taracchini, Alessandra Buonanno, Gaurav Khanna, and Scott A. Hughes. Small mass plunging into a Kerr black hole: Anatomy of the inspiral-merger-ringdown waveforms. 2014.

[77] Wen-Biao Han. Gravitational waves from extreme-mass-ratio inspirals in equatorially eccentric orbits. *Int.J.Mod.Phys.*, D23(7):1450064, 2014.

[78] Sam R. Dolan, Leor Barack, and Barry Wardell. Self force via m-mode regularization and 2+1D evolution: II. Scalar-field implementation on Kerr spacetime. *Phys.Rev.*, D84:084001, 2011.

[79] Leor Barack. Gravitational self force in extreme mass-ratio inspirals. *Class.Quant.Grav.*, 26:213001, 2009.

[80] William Krivan, Pablo Laguna, Philippos Papadopoulos, and Nils Andersson. Dynamics of perturbations of rotating black holes. *Phys. Rev.*, D56:3395–3404, 1997.

[81] William Kinnersley. Type D Vacuum Metrics. *J. Math. Phys.*, 10:1195–1203, 1969.

[82] Saul A. Teukolsky. The Kerr Metric. *Class.Quant.Grav.*, 32(12):124006, 2015.

[83] S.A. Teukolsky and W.H. Press. Perturbations of a rotating black hole. III - Interaction of the hole with gravitational and electromagnetic radiation. *Astrophys.J.*, 193:443–461, 1974.

[84] Misao Sasaki and Takashi Nakamura. Gravitational Radiation From a Kerr Black Hole. 1. Formulation and a Method for Numerical Analysis. *Prog.Theor.Phys.*, 67:1788, 1982.

[85] S. Chandrasekhar and Steven L. Detweiler. Equations governing gravitational perturbations of the Kerr black-hole. *Proc. Roy. Soc. Lond.*, A350:165–174, 1976.

[86] Steven L. Detweiler. Resonant oscillations of a rapidly rotating black hole. *Proc. Roy. Soc. Lond.*, A352:381–395, 1977.

[87] Masaru Shibata. Gravitational waves induced by a particle orbiting around a rotating black hole: Effect of orbital precession. *Prog. Theor. Phys.*, 90:595–614, 1993.

[88] Yasushi Mino, Misao Sasaki, Masaru Shibata, Hideyuki Tagoshi, and Takahiro Tanaka. Black hole perturbation: Chapter 1. *Prog.Theor.Phys.Suppl.*, 128:1–121, 1997.

[89] Shuhei Mano, Hisao Suzuki, and Eiichi Takasugi. Analytic solutions of the Teukolsky equation and their low frequency expansions. *Prog.Theor.Phys.*, 95:1079–1096, 1996.

[90] William Krivan, Pablo Laguna, and Philippos Papadopoulos. Dynamics of scalar fields in the background of rotating black holes. *Phys. Rev.*, D54:4728–4734, 1996.

[91] Pranesh A. Sundararajan, Gaurav Khanna, and Scott A. Hughes. Towards adiabatic waveforms for inspiral into Kerr black holes: I. A new model of the source for the time domain perturbation equation. *Phys. Rev.*, D76:104005, 2007.

[92] Enrique Pazos-Avalos and Carlos O. Lousto. Numerical integration of the Teukolsky equation in the time domain. *Phys.Rev.*, D72:084022, 2005.

[93] William Krivan. Late time dynamics of scalar fields on rotating black hole backgrounds. *Phys. Rev.*, D60:101501, 1999.

[94] Nils Andersson, Pablo Laguna, and Philippos Papadopoulos. Dynamics of scalar fields in the background of rotating black holes. 2. A Note on superradiance. *Phys. Rev.*, D58:087503, 1998.

[95] Nils Andersson and Kostas Glampedakis. A Superradiance resonance cavity outside rapidly rotating black holes. *Phys.Rev.Lett.*, 84:4537–4540, 2000.

[96] Kostas Glampedakis and Nils Andersson. Late time dynamics of rapidly rotating black holes. *Phys.Rev.*, D64:104021, 2001.

[97] Manuela Campanelli, William Krivan, and Carlos O. Lousto. The imposition of Cauchy data to the Teukolsky equation II: Numerical comparison with the Zerilli-Moncrief approach to black hole perturbations. *Phys. Rev.*, D58:024016, 1998.

[98] William Krivan and Richard H. Price. Formation of a rotating hole from a close limit head-on collision. *Phys. Rev. Lett.*, 82:1358–1361, 1999.

[99] Manuela Campanelli, Gaurav Khanna, Pablo Laguna, Jorge Pullin, and Michael P. Ryan. Perturbations of the Kerr space-time in horizon penetrating coordinates. *Class.Quant.Grav.*, 18:1543–1554, 2001.

[100] Gaurav Khanna. Evolution of Kerr-Schild type initial data for binary black holes using the horizon penetrating Teukolsky equation. *Phys. Rev.*, D65:124018, 2002.

[101] Lior M. Burko and Gaurav Khanna. Radiative falloff in the background of rotating black hole. *Phys.Rev.*, D67:081502, 2003.

[102] Shahar Hod. Mode coupling in rotating gravitational collapse of a scalar field. *Phys.Rev.*, D61:024033, 2000.

[103] Shahar Hod. Mode coupling in rotating gravitational collapse: Gravitational and electromagnetic perturbations. *Phys.Rev.*, D61:064018, 2000.

[104] Shahar Hod. The Radiative tail of realistic gravitational collapse. *Phys.Rev.Lett.*, 84:10–13, 2000.

[105] Leor Barack and Amos Ori. Late time decay of scalar perturbations outside rotating black holes. *Phys.Rev.Lett.*, 82:4388, 1999.

[106] Leor Barack. Late time decay of scalar, electromagnetic, and gravitational perturbations outside rotating black holes. *Phys.Rev.*, D61:024026, 2000.

[107] Leor Barack and Amos Ori. Late time decay of gravitational and electromagnetic perturbations along the event horizon. *Phys.Rev.*, D60:124005, 1999.

[108] Lior M. Burko and Gaurav Khanna. Universality of massive scalar field late time tails in black hole space-times. *Phys. Rev.*, D70:044018, 2004.

[109] Ramon Lopez-Aleman, Gaurav Khanna, and Jorge Pullin. Perturbative evolution of particle orbits around Kerr black holes: Time domain calculation. *Class.Quant.Grav.*, 20:3259–3268, 2003.

[110] Lior M. Burko and Gaurav Khanna. Accurate time-domain gravitational waveforms for extreme-mass-ratio binaries. *Europhys. Lett.*, 78:60005, 2007.

[111] Gaurav Khanna. Teukolsky evolution of particle orbits around Kerr black holes in the time domain: Elliptic and inclined orbits. *Phys.Rev.*, D69:024016, 2004.

[112] Pranesh A. Sundararajan, Gaurav Khanna, Scott A. Hughes, and Steve Drasco. Towards adiabatic waveforms for inspiral into Kerr black holes: II. Dynamical sources and generic orbits. *Phys.Rev.*, D78:024022, 2008.

[113] Jonathan R Gair and Kostas Glampedakis. Improved approximate inspirals of test-bodies into Kerr black holes. *Phys. Rev.*, D73:064037, 2006.

[114] Stanislav Babak, Hua Fang, Jonathan R. Gair, Kostas Glampedakis, and Scott A. Hughes. 'Kludge' gravitational waveforms for a test-body orbiting a Kerr black hole. *Phys. Rev.*, D75:024005, 2007. [Erratum: Phys. Rev.D77,04990(2008)].

[115] Pranesh A. Sundararajan, Gaurav Khanna, and Scott A. Hughes. Binary black hole merger gravitational waves and recoil in the large mass ratio limit. *Phys.Rev.*, D81:104009, 2010.

[116] Lior M. Burko and Gaurav Khanna. Late-time Kerr tails revisited. *Class.Quant.Grav.*, 26:015014, 2009.

[117] Lior M. Burko and Gaurav Khanna. Late-time Kerr tails: Generic and non-generic initial data sets, 'up' modes, and superposition. *Class.Quant.Grav.*, 28:025012, 2011.

[118] Gaurav Khanna and Justin McKennon. Numerical modeling of gravitational wave sources accelerated by OpenCL. *Comput. Phys. Commun.*, 181:1605–1611, 2010.

[119] Justin McKennon, Gary Forrester, and Gaurav Khanna. High Accuracy Gravitational Waveforms from Black Hole Binary Inspirals Using OpenCL. 2012.

[120] Tyler Spilhaus and Gaurav Khanna. Brief note on high-multipole Kerr tails. 2013.

[121] Anil Zenginoğlu. Hyperboloidal foliations and scri-fixing. *Class. Quant. Grav.*, 25:145002, 2008.

[122] Anil Zenginoğlu. A hyperboloidal study of tail decay rates for scalar and Yang-Mills fields. *Class. Quant. Grav.*, 25:175013, 2008.

[123] Anil Zenginoğlu, Dario Nunez, and Sascha Husa. Gravitational perturbations of Schwarzschild spacetime at null infinity and the hyperboloidal initial value problem. *Class. Quant. Grav.*, 26:035009, 2009.

[124] Anil Zenginoğlu and Manuel Tiglio. Spacelike matching to null infinity. *Phys. Rev.*, D80:024044, 2009.

[125] Anil Zenginoğlu. Asymptotics of Schwarzschild black hole perturbations. *Class. Quant. Grav.*, 27:045015, 2010.

[126] Anil Zenginoğlu. Hyperboloidal layers for hyperbolic equations on unbounded domains. *J.Comput.Phys.*, 230:2286–2302, 2011.

[127] Anil Zenginoğlu, Gaurav Khanna, and Lior M. Burko. Intermediate behavior of Kerr tails. *Gen.Rel.Grav.*, 46:1672, 2014.

[128] Yi Pan, Alessandra Buonanno, Luisa T. Buchman, Tony Chu, Lawrence E. Kidder, et al. Effective-one-body waveforms calibrated to numerical relativity simulations: coalescence of non-precessing, spinning, equal-mass black holes. *Phys.Rev.*, D81:084041, 2010.

[129] Andrea Taracchini, Alessandra Buonanno, Yi Pan, Tanja Hinderer, Michael Boyle, et al. Effective-one-body model for black-hole binaries with generic mass ratios and spins. 2013.

[130] Sebastiano Bernuzzi and Alessandro Nagar. Binary black hole merger in the extreme-mass-ratio limit: a multipolar analysis. *Phys. Rev.*, D81:084056, 2010.

[131] Sebastiano Bernuzzi, Alessandro Nagar, and Anil Zenginoğlu. Binary black hole coalescence in the extreme-mass-ratio limit: testing and improving the effective-one-body multipolar waveform. *Phys.Rev.*, D83:064010, 2011.

[132] Sebastiano Bernuzzi, Alessandro Nagar, and Anil Zenginoğlu. Binary black hole coalescence in the large-mass-ratio limit: the hyperboloidal layer method and waveforms at null infinity. *Phys.Rev.*, D84:084026, 2011.

[133] Sebastiano Bernuzzi, Alessandro Nagar, and Anil Zenginoğlu. Horizon-absorption effects in coalescing black-hole binaries: An effective-one-body study of the non-spinning case. *Phys.Rev.*, D86:104038, 2012.

[134] Nicolas Yunes, Alessandra Buonanno, Scott A. Hughes, M. Coleman Miller, and Yi Pan. Modeling Extreme Mass Ratio Inspirals within the Effective-One-Body Approach. *Phys. Rev. Lett.*, 104:091102, 2010.

[135] Enrico Barausse, Alessandra Buonanno, Scott A. Hughes, Gaurav Khanna, Stephen O'Sullivan, et al. Modeling multipolar gravitational-wave emission from small mass-ratio mergers. *Phys.Rev.*, D85:024046, 2012.

[136] Andrea Taracchini, Yi Pan, Alessandra Buonanno, Enrico Barausse, Michael Boyle, et al. Prototype effective-one-body model for nonprecessing spinning inspiral-merger-ringdown waveforms. *Phys.Rev.*, D86:024011, 2012.

[137] Kristen A. Lackeos and Lior M. Burko. Self-forced gravitational waveforms for Extreme and Intermediate mass ratio inspirals. *Phys. Rev.*, D86:084055, 2012.

[138] Enrico Barausse, Vitor Cardoso, and Gaurav Khanna. Test bodies and naked singularities: Is the self-force the cosmic censor? *Phys.Rev.Lett.*, 105:261102, 2010.

[139] Enrico Barausse, Vitor Cardoso, and Gaurav Khanna. Testing the Cosmic Censorship Conjecture with point particles: the effect of radiation reaction and the self-force. *Phys.Rev.*, D84:104006, 2011.

[140] Lior M. Burko and Gaurav Khanna. Self-force gravitational waveforms for extreme and intermediate mass ratio inspirals. III: Spin-orbit coupling revisited. *Phys.Rev.*, D91(10):104017, 2015.

[141] Vitor Cardoso and Gaurav Khanna. Black holes in anti–de Sitter spacetime: Quasinormal modes, tails, and flat spacetime. *Phys.Rev.*, D91(2):024031, 2015.

[142] Bertil Gustafsson, Heinz-Otto Kreiss, and Joseph Oliger. *Time dependent problems and difference methods*, volume 24. John Wiley & Sons, 1995.

[143] S.W. Hawking and J.B. Hartle. Energy and angular momentum flow into a black hole. *Commun.Math.Phys.*, 27:283–290, 1972.

[144] S. Chandrasekhar. *The mathematical theory of black holes.* Oxford Univ. Press, Oxford, 1983.

[145] Bernd Brügmann. A pseudospectral matrix method for time-dependent tensor fields on a spherical shell. *Journal of Computational Physics*, 235(0):216–240, 2013.

[146] Alessandro Nagar and Luciano Rezzolla. Gauge-invariant non-spherical metric perturbations of Schwarzschild black-hole spacetimes. *Class. Quant. Grav.*, 22:R167, 2005.

[147] P. C. Peters. Gravitational Radiation and the Motion of Two Point Masses. *Phys. Rev.*, 136:B1224–B1232, 1964.

[148] Tim Dietrich, Niclas Moldenhauer, Nathan K. Johnson-McDaniel, Sebastiano Bernuzzi, Charalampos M. Markakis, Bernd Bruegmann, and Wolfgang Tichy. Binary Neutron Stars with Generic Spin, Eccentricity, Mass ratio, and Compactness - Quasi-equilibrium Sequences and First Evolutions. 2015.

[149] Eric Poisson. Absorption of mass and angular momentum by a black hole: Time-domain formalisms for gravitational perturbations, and the small-hole / slow-motion approximation. *Phys.Rev.*, D70:084044, 2004.

[150] A.A. Starobinsky and S.M. Churilov. Amplification of electromagnetic and gravitational waves scattered by a rotating black hole. *Sov.Phys.-JETP*, 38:1–5, 1974.

[151] James M. Bardeen, B. Carter, and S.W. Hawking. The Four laws of black hole mechanics. *Commun.Math.Phys.*, 31:161–170, 1973.

[152] R.H. Price and K.S. Thorne. Membrane Viewpoint on Black Holes: Properties and Evolution of the Stretched Horizon. *Phys.Rev.*, D33:915–941, 1986.

[153] Guillaume Faye, Luc Blanchet, and Alessandra Buonanno. Higher-order spin effects in the dynamics of compact binaries. I. Equations of motion. *Phys.Rev.*, D74:104033, 2006.

[154] A.-K. Tornberg and B. Engquist. Numerical approximations of singular source terms in differential equations. *Journal of Computational Physics*, 200:462–488, November 2004.

[155] B. Engquist, A.-K. Tornberg, and R. Tsai. Discretization of Dirac delta functions in level set methods. *Journal of Computational Physics*, 207:28–51, July 2005.

[156] Emanuele Berti, Vitor Cardoso, Tanja Hinderer, Madalena Lemos, Frans Pretorius, et al. Semianalytical estimates of scattering thresholds and gravitational radiation in ultrarelativistic black hole encounters. *Phys.Rev.*, D81:104048, 2010.

[157] Janna Levin and Gabe Perez-Giz. A Periodic Table for Black Hole Orbits. *Phys. Rev.*, D77:103005, 2008.

[158] Kostas Glampedakis, Scott A. Hughes, and Daniel Kennefick. Approximating the inspiral of test bodies into Kerr black holes. *Phys. Rev.*, D66:064005, 2002.

[159] Fintan D. Ryan. Effect of gravitational radiation reaction on nonequatorial orbits around a Kerr black hole. *Phys. Rev.*, D53:3064–3069, 1996.

[160] Karl Martel and Eric Poisson. A one-parameter family of time-symmetric initial data for the radial infall of a particle into a Schwarzschild black hole. *Phys. Rev.*, D66:084001, 2002.

[161] Karl Martel. Gravitational waveforms from a point particle orbiting a Schwarzschild black hole. *Phys. Rev.*, D69:044025, 2004.

[162] Tim Dietrich and Sebastiano Bernuzzi. Simulations of rotating neutron star collapse with the puncture gauge: end state and gravitational waveforms. *Phys. Rev.*, D91(4):044039, 2015.

[163] Sebastiano Bernuzzi and Alessandro Nagar. Gravitational waves from pulsations of neutron stars described by realistic Equations of State. *Phys. Rev.*, D78:024024, 2008.

[164] Thibault Damour, Alessandro Nagar, and Sebastiano Bernuzzi. Improved effective-one-body description of coalescing nonspinning black-hole binaries and its numerical-relativity completion. *Phys.Rev.*, D87:084035, 2013.

[165] Isabel Cordero-Carrion and Pablo Cerda-Duran. Partially implicit Runge-Kutta methods for wave-like equations in spherical-type coordinates. 2012.

[166] Pedro J. Montero and Isabel Cordero-Carrion. BSSN equations in spherical coordinates without regularization: vacuum and non-vacuum spherically symmetric spacetimes. *Phys. Rev.*, D85:124037, 2012.

[167] Richard H. Price. Nonspherical Perturbations of Relativistic Gravitational Collapse. II. Integer-Spin, Zero-Rest-Mass Fields. *Phys. Rev.*, D5:2439–2454, 1972.

[168] Istvan Rácz and Gabor Zsolt Tóth. Numerical investigation of the late-time Kerr tails. *Class.Quant.Grav.*, 28:195003, 2011.

[169] Michael Jasiulek. Hyperboloidal slices for the wave equation of Kerr-Schild metrics and numerical applications. *Class.Quant.Grav.*, 29:015008, 2012.

[170] Rodrigo Panosso Macedo and Marcus Ansorg. Axisymmetric fully spectral code for hyperbolic equations. *J. Comput. Phys.*, 276:357–379, 2014.

[171] Shahar Hod. Slow relaxation of rapidly rotating black holes. *Phys.Rev.*, D78:084035, 2008.

[172] Shahar Hod. Black-hole quasinormal resonances: Wave analysis versus a geometric-optics approximation. *Phys.Rev.*, D80:064004, 2009.

[173] Thibault Damour and Achamveedu Gopakumar. Gravitational recoil during binary black hole coalescence using the effective one body approach. *Phys. Rev.*, D73:124006, 2006.

[174] Thibault Damour and Alessandro Nagar. An improved analytical description of inspiralling and coalescing black-hole binaries. *Phys. Rev.*, D79:081503, 2009.

[175] Ryuichi Fujita. Gravitational Waves from a Particle in Circular Orbits around a Schwarzschild Black Hole to the 22nd Post-Newtonian Order. *Prog.Theor.Phys.*, 128:971–992, 2012.

[176] James Healy, Carlos O. Lousto, and Yosef Zlochower. Remnant mass, spin, and recoil from spin aligned black-hole binaries. 2014.

[177] Luciano Rezzolla, Rodrigo P. Macedo, and Jose Luis Jaramillo. Understanding the 'anti-kick' in the merger of binary black holes. *Phys.Rev.Lett.*, 104:221101, 2010.

[178] John G. Baker, Joan Centrella, Dae-Il Choi, Michael Koppitz, James R. van Meter, et al. Getting a kick out of numerical relativity. *Astrophys.J.*, 653:L93–L96, 2006.

[179] Jeremy D. Schnittman et al. Anatomy of the binary black hole recoil: A multipolar analysis. *Phys. Rev.*, D77:044031, 2008.

[180] Denis Pollney, Christian Reisswig, Luciano Rezzolla, Bela Szilagyi, Marcus Ansorg, et al. Recoil velocities from equal-mass binary black-hole mergers: A Systematic investigation of spin-orbit aligned configurations. *Phys.Rev.*, D76:124002, 2007.

[181] Richard H. Price, Gaurav Khanna, and Scott A. Hughes. Systematics of black hole binary inspiral kicks and the slowness approximation. *Phys.Rev.*, D83:124002, 2011.

[182] Richard H. Price, Gaurav Khanna, and Scott A. Hughes. Black hole binary inspiral and trajectory dominance. *Phys.Rev.*, D88(10):104004, 2013.

[183] E. A. Huerta and Jonathan R Gair. Importance of including small body spin effects in the modelling of extreme and intermediate mass-ratio inspirals. *Phys. Rev.*, D84:064023, 2011.

[184] Yasushi Mino, Masaru Shibata, and Takahiro Tanaka. Gravitational waves induced by a spinning particle falling into a rotating black hole. *Phys.Rev.*, D53:622–634, 1996.

[185] Motoyuki Saijo, Kei-ichi Maeda, Masaru Shibata, and Yashushi Mino. Gravitational waves from a spinning particle plunging into a Kerr black hole. *Phys.Rev.*, D58:064005, 1998.

[186] Wen-Biao Han. Gravitational Radiations from a Spinning Compact Object around a supermassive Kerr black hole in circular orbit. *Phys.Rev.*, D82:084013, 2010.

[187] Scott A. Hughes. Evolution of circular, nonequatorial orbits of Kerr black holes due to gravitational wave emission. 2. Inspiral trajectories and gravitational wave forms. *Phys.Rev.*, D64:064004, 2001.

[188] Takahiro Tanaka, Masaru Shibata, Misao Sasaki, Hideyuki Tagoshi, and Takashi Nakamura. Gravitational wave induced by a particle orbiting around a Schwarzschild black hole. *Prog. Theor. Phys.*, 90:65–84, 1993.

[189] Masaru Shibata. Gravitational waves by compact stars orbiting around rotating supermassive black holes. *Phys. Rev.*, D50:6297–6311, 1994.

[190] Roman Gold and Bernd Bruegmann. Radiation from low-momentum zoom-whirl orbits. *Class. Quant. Grav.*, 27:084035, 2010.

[191] Alessandro Nagar. Gravitational recoil in nonspinning black hole binaries: the span of test-mass results. *Phys.Rev.*, D88:121501, 2013.

[192] David Brizuela, Jose M. Martin-Garcia, and Guillermo A. Mena Marugan. xPert: Computer algebra for metric perturbation theory. *Gen. Rel. Grav.*, 41:2415–2431, 2009.

[193] E. D. Fackerell and J. R. Ipser. Weak electromagnetic fields around a rotating black hole. *Phys. Rev.*, D5:2455–2458, 1972.

[194] J. M. Bardeen and W. H. Press. Radiation fields in the schwarzschild background. *J. Math. Phys.*, 14:7–19, 1973.

[195] M. Alcubierre. *Introduction to 3+1 Numerical Relativity*. Oxford University Press, 2008.

[196] Anil Zenginoğlu. A Geometric framework for black hole perturbations. *Phys. Rev.*, D83:127502, 2011.

[197] Roger Penrose. Asymptotic properties of fields and space-times. *Phys. Rev. Lett.*, 10:66–68, 1963.

[198] R. Penrose. Zero rest mass fields including gravitation: Asymptotic behavior. *Proc. Roy. Soc. Lond.*, A284:159, 1965.

[199] Helmut Friedrich. Cauchy problems for the conformal vacuum field equations in general relativity. *Comm. Math. Phys.*, 91:445–472, 1983.

[200] Helmut Friedrich. On the existence of n-geodesically complete or future complete solutions of Einstein's field equations with smooth asymptotic structure. *Comm. Math. Phys.*, 107:587–609, 1986.

[201] Jorg Frauendiener. Numerical treatment of the hyperboloidal initial value problem for the vacuum Einstein equations. 2. The Evolution equations. *Phys.Rev.*, D58:064003, 1998.

[202] Vincent Moncrief. Conformally regular ADM evolution equations, 2000. Talk at Santa Barbara, `http://online.itp.ucsb.edu/online/numrel00/moncrief`.

[203] Michael Purrer, Sascha Husa, and Peter C. Aichelburg. News from critical collapse: Bondi mass, tails and quasinormal modes. *Phys. Rev.*, D71:104005, 2005.

[204] Anil Zenginoğlu. Hyperboloidal evolution with the Einstein equations. *Class. Quant. Grav.*, 25:195025, 2008.

[205] Alex Vañó-Viñuales, Sascha Husa, and David Hilditch. Spherical symmetry as a test case for unconstrained hyperboloidal evolution. *Class. Quant. Grav.*, 32(17):175010, 2015.

[206] Gioel Calabrese, Carsten Gundlach, and David Hilditch. Asymptotically null slices in numerical relativity: Mathematical analysis and spherical wave equation tests. *Class.Quant.Grav.*, 23:4829–4846, 2006.

[207] Sascha Husa. Numerical relativity with the conformal field equations. *Lect.Notes Phys.*, 617:159–192, 2003.

[208] Gyula Fodor and Istvan Racz. What does a strongly excited 't Hooft-Polyakov magnetic monopole do? *Phys. Rev. Lett.*, 92:151801, 2004.

[209] Shingo Suzuki and Kei-ichi Maeda. Innermost stable circular orbit of a spinning particle in Kerr space-time. *Phys.Rev.*, D58:023005, 1998.

[210] F.A.E. Pirani. On the Physical significance of the Riemann tensor. *Acta Phys.Polon.*, 15:389–405, 1956.

[211] Lawrence E. Kidder. Coalescing binary systems of compact objects to postNewtonian 5/2 order. 5. Spin effects. *Phys.Rev.*, D52:821–847, 1995.

[212] E. Corinaldesi and Achille Papapetrou. Spinning test particles in general relativity. 2. *Proc. Roy. Soc. Lond.*, A209:259–268, 1951.

[213] T.D. Newton and Eugene P. Wigner. Localized States for Elementary Systems. *Rev.Mod.Phys.*, 21:400–406, 1949.

[214] Enrico Barausse, Etienne Racine, and Alessandra Buonanno. Hamiltonian of a spinning test-particle in curved spacetime. *Phys. Rev.*, D80:104025, 2009.

[215] GSL: the GNU scientific library. Code Homepage.

[216] James M. Bardeen, William H. Press, and Saul A Teukolsky. Rotating black holes: Locally nonrotating frames, energy extraction, and scalar synchrotron radiation. *Astrophys. J.*, 178:347, 1972.

Abbreviations

BH - black hole

BL - Boyer-Lindquist

CEO - circular, equatorial orbit

CFL - Courant-Friedrichs-Lewy

COM - center of mass

GR - general relativity

GW - gravitational wave

EOM - equations of motion

EOB - effective-one-body

HH - hyperboloidal and horizon penetrating

ID - initial data

NP - Newman-Penrose (formalism)

NR - numerical relativity

MPEQs - Mathison-Papapetrou-Equations

ODE - ordinary differential equation

PDE - partial differential equation

PIRK - partially implicit Runge-Kutta

QNM - quasi normal mode

RR - radiation reaction

RT - Rácz and Tóth

RWZ - Regge-Wheeler-Zerilli

RWZE - Regge-Wheeler-Zerilli Equation

SKH - Sundararajan, Khanna, Hughes

SP - spinning particle

SSC - spin supplementary condition

TE - Teukolsky Equation

TKEQ - Teukolsky Equation

TUL-SSC - Tulczyjew spin-supplementary-condition

List of contributed works

[H0] E. Harms, "Numerical solution of the 2+1 Teukolsky equation on a hyperboloidal foliation of Kerr spacetime", Master Thesis, FSU Jena, TPI

[H1] E. Harms, S. Bernuzzi and B. Brügmann, "Numerical solution of the 2+1 Teukolsky equation on a hyperboloidal and horizon penetrating foliation of Kerr and application to late-time decays," Class. Quant. Grav. **30** (2013) 115013 [arXiv:1301.1591 [gr-qc]].

[H2] E. Harms, S. Bernuzzi, A. Nagar and A. Zenginoglu, "A new gravitational wave generation algorithm for particle perturbations of the Kerr spacetime," Class. Quant. Grav. **31** (2014) 24, 245004 [arXiv:1406.5983 [gr-qc]].

[H3] A. Nagar, E. Harms, S. Bernuzzi and A. Zenginoglu, "The antikick strikes back: recoil velocities for nearly-extremal binary black hole mergers in the test-mass limit," Phys. Rev. D **90** (2014) 12, 124086 [arXiv:1407.5033 [gr-qc]].

[H4] E. Harms, A. Nagar, S. Bernuzzi and G. Lukes-Gerakopoulos, "Infinity fluxes for a spinning particle in circular, equatorial orbit" *in preparation*

List of presentations

05.11.2012 - SFB/TR7 Videoseminar in Jena
Numerical solution of the 2+1 Teukolsky equation on a hyperboloidal foliation of the Kerr spacetime

27.02.2013 - DPG Tagung Jena
Numerical solution of the 2+1 Teukolsky equation on a hyperboloidal and horizon penetrating foliation of Kerr

04.09.2013 - International Conference on Mathematical Modeling in Physical Science in Prague
Numerical solution of the 2+1 Teukolsky equation on a hyperboloidal and horizon penetrating foliation of Kerr

04.12.2014 - SFB/TR7 conclusion workshop Jena
A new gravitational wave generation algorithm for particle perturbations of the Kerr spacetime

19.03.2015 - DPG Tagung Berlin
A new gravitational wave generation algorithm for particle perturbations of the Kerr spacetime

Acknowledgements

I want to thank my supervisor Prof. Bernd Brügmann for always being open to questions and helpful with problems, and, in particular, for supporting me in doing research in the topic of black hole perturbation theory, which fascinated me personally though it was not at the center of the group's work.

I want to thank Dr. Sebastiano Bernuzzi, who initiated this project with me and helped me from the beginning until now with his invalueable explanations, ideas and also many personal advises. As well, I want to thank Dr. Alessandro Nagar, who also supported me over the whole project with his advises, ideas and with his deep analytical understanding. I want to thank Dr. David Hilditch (even though he is rather a mathematician) for always taking a lot of time to explain any kind of general relativity question in a comprehensible way, for tolerating, without complaint, me discussing with Seba in his office, for learning a high-level language which allows to discuss science, and for his encouragment when things were not working. I want to thank my former flat mate Dr. Bolek Lukes-Gerakopoulos for discussing any kind of live or work problem, and, especially, for introducing me to the topic of the "spinning particle". Also, I want to thank Dr. Andreas Weyhausen for being very helpful and friendly in including me to the group and for many useful conversations. Furthermore, I want to thank Prof. Gerhard Schäfer for being happy to discuss any kind of physical or philosophical question, in particular, about the "spinning particle".

Of course, I also want to thank my office mates, Niclas Moldenhauer, Tim Dietrich and Marcus Bugner, who always helped me with any kind of problem, and lived with me through lots of nice events over the years. In particular, I want to thank my President Niclas Moldenhauer for helping me over the whole 8 years of studying by explaining homework and uncountable many questions, and by always improving my work with invalueable ideas and suggestions. Special thanks also to T. Dietrich, B. Gerakopoulos, D. Hilditch, N. Moldenhauer, S. Bernuzzi, A. Nagar for useful comments on the manuscript. I also want to thank McBuggiMCachine for being a MCachine, just like me, and for driving the garbage boat to clean the Saale from time to time. Thanks, also, to Martin Fruhnert and Moritz FeYerabend who also helped me master the studies with their joyful presence.

And, of course, I want to thank my family and my girlfriend Elli for supporting and encouraging me throughout my whole studies.

Ehrenwörtliche Erklärung

Ich erkläre hiermit ehrenwörtlich, dass ich die vorliegende Arbeit selbständig, ohne unzulässige Hilfe Dritter und ohne Benutzung anderer als der angegebenen Hilfsmittel und Literatur angefertigt habe. Die aus anderen Quellen direkt oder indirekt übernommenen Daten und Konzepte sind unter Angabe der Quelle gekennzeichnet.

Bei der Auswahl und Auswertung dieser Arbeit haben mir die nachstehend aufgeführten Personen in der jeweils beschriebenen Weise unentgeltlich geholfen:

Prof. Brügmann - beratend

Dr. Bernuzzi - beratend

Dr. Nagar - beratend

Dr. Hilditch - beratend

Dr. Lukes-Gerakopoulos - beratend

Prof. Schäfer - beratend

Weitere Personen waren an der inhaltlich-materiellen Erstellung der vorliegenden Arbeit nicht beteiligt. Insbesondere habe ich hierfür nicht die entgeltliche Hilfe von Vermittlungs- bzw. Beratungsdiensten (Promotionsberater oder andere Personen) in Anspruch genommen. Niemand hat von mir unmittelbar oder mittelbar geldwerte Leistungen für Arbeiten erhalten, die im Zusammenhang mit dem Inhalt der vorgelegten Dissertation stehen.

Die Arbeit wurde bisher weder im In- noch im Ausland in gleicher oder ähnlicher Form einer anderen Prüfungsbehörde vorgelegt.

Die geltende Promotionsordnung der Physikalisch-Astronomischen Fakultät ist mir bekannt.

Ich versichere ehrenwörtlich, dass ich nach bestem Wissen die reine Wahrheit gesagt und nichts verschwiegen habe.

Ort, Datum: ....   Unterschrift: ....

Lebenslauf

Enno Harms

06.05.1987 geboren in Wittingen

1993-1997 Grundschule Hankensbüttel

1997-1999 Orientierungsstufe Hankensbüttel

1999-2006 Gymnasium Hankensbüttel

2006 Abitur

2006-2007 Zivildienst im Otterzentrum Hankensbüttel

2007-2010 Bachelor Sc. Physik, Nebenfach Mathematik, TU Braunschweig

2010-2012 Master Sc. Physik, Nebenfach Mathematik, FSU Jena

30.9.2012 MSc. Physik

2012-... wiss. Mitarbeiter am Theoretisch-Physikalischen-Institut FSU Jena

Lehrtätigkeiten an der FSU Jena

WS 2012/13	Projektbetreuung **Computational Physics 3**, Prof. Brügmann
2013-14	Projektbetreuung **Fortgeschrittenen Praktikum**, Dr. Schröter
WS 2013/14	Übungsleiter **Computational Physics 2**, Prof. Skupin
SS 2014	Übungsleiter **Quantenmechanik**, Prof. Brügmann
WS 2014/15	Übungsleiter **Allgemeine Relativitätstheorie**, Prof. Brügmann
SS 2015	Übungsleiter **Numerische Relativitätstheorie**, Prof. Brügmann

Ort, Datum: ....   Unterschrift: ....

Zusammenfassung

Das Thema dieser Arbeit war die numerische Berechnung von Gravitationswellen eines allgemein relativistischen Zweikörpersystems bestehend aus schwarzen Löchern. Die Ergebnisse beziehen sich auf die Test-Teilchen-Näherung, in welcher man das System als eine Punktteilchenstörung auf der festen Hintergrundmetrik eines supermassiven schwarzen Lochs betrachtet. Somit sind die Ergebnisse quantitativ nur für extreme Massenverhältnisse ($M_1 \gg M_2$) gültig, qualitativ jedoch im Allgemeinen nützlich. Insbesondere wurde der Einfluss des "Spin" des zentralen schwarzen Lochs analysiert.

Die relevante Gleichung, die eben genannte Punktteilchenstörungen auf der Hintergrundmetrik eines schwarzen Lochs beschreiben kann, wurde 1972 von Teukolsky hergeleitet. Traditionell wird ein Schema von Krivan aus dem Jahr 1997 zur numerischen Lösung der Gleichung verwendet. Hier jedoch wurde die Teukolsky-Gleichung in einem für unsere Zwecke günstigeren Koordinatensystem neu hergeleitet. Genauer gesagt handelt es sich dabei um Horizont-angepasste, hyperboloidale Koordinaten. Diese beinhalten den Horizont und das lichtartig Unendliche als Randpunkte der Domäne und stellen damit ein abgeschlossenes Gebiet dar. Weil somit keine Information von außen eindringen kann benötigen wir keine unphysikalischen Randbedingungen in unseren Simulationen. In vielen Fällen bedeutet dies eine deutliche Verbesserung der Genauigkeit.

Ein Großteil der Arbeit bestand in der Entwicklung des Computercodes *teukode*, welcher die Teukolsky-Gleichung in den neuen Koordinaten für eine Punktteilchenstörung numerisch löst. Zunächst wurde der *teukode* in einfachen Situationen, wie z.B. der Bewegung des Teilchens entlang zirkulärer Bahnen in der Equatorialebene, gegen bestehende Ergebnisse der Literatur validiert. In allen Fällen waren die Daten konsistent. In Spezialfällen, welche in der Literatur mit extremer Genauigkeit gelöst werden können, zeigte sich die hervorragende Effizienz unserer Herangehensweise.

Nach Bestehen der Literaturvergleiche konnte der *teukode* auch für weiterführende Untersuchungen verwendet werden. Neuartige Ergebnisse wurden bezüglich analytischer Modelle für die Strahlungsrückwirkung eines Punktteilchens, für Wellenformen zur Zeit der Kollision und für den gravitativen Rückstoß gefunden. Als neueste Entwicklung wurde der *teukode* so erweitert, dass der "Spin" des Punktteilchens mit einbezogen werden kann. Damit ist der *teukode* der erste Teukolsky-Löser, der Gravitationswellen eines rotierenden Teilchens auf allgemeiner Bahn berechnen kann. Erste Ergebnisse sind vielversprechend und erlauben eine Fülle von neuen Studien in naher Zukunft.